Transient BEMT models and validation through a sea trial turbine platform

Iestyn Evans

Submitted to Swansea University in fulfilment
of the requirements for the Degree of Doctor of Philosophy

Swansea University
Prifysgol Abertawe

College of Engineering
Swansea University

29th April 2024

Author Declarations

Statement 1

This work has not been previously accepted in substance for any degree and is not being concurrently submitted in candidature for any degree.

Signed: *Iestyn Evans*
Date: 31^{st} of December 2023

Statement 2

This thesis is the result of my own investigations, except where otherwise stated. Other sources are acknowledged by footnotes giving explicit references. A bibliography is appended.

Signed: *Iestyn Evans*
Date: 31^{st} of December 2023

Statement 3

I hereby give consent for my thesis, if accepted, to be available for photocopying and for interlibrary loan, and for the title and summary to be made available to outside organisations.

Signed: *Iestyn Evans*
Date: 31^{st} of December 2023

Statement 4

The University's ethical procedures have been followed and, where appropriate, that ethical approval has been granted.

Signed: *Iestyn Evans*
Date: 31^{st} of December 2023

Abstract

Tidal stream turbines (TSTs) have the potential to contribute significantly to the UK energy needs. Currently, the sector is still in a primitive stage and has a relatively high levelised cost of energy compared to other renewable energy sources. A reduction in their cost can be made by improving their design through numerical modelling and physical testing. This thesis will firstly present the classical blade element momentum theory (BEMT) numerical model which is enhanced with additional features (1. foil shape and Reynolds number dependence, and 2. transient turbulence and wave flow fields), which are incorporated to improve the predictions of loads and performance of TSTs. The improvements to the BEMT numerical model are quantified and validated by comparing to empirical data from laboratory testing of five different TSTs (Magallanes ATIR, Sabella D12, IFREMER, Oxford, and Barltrop). This inclusion of the foil shape and Reynolds number dependence in the numerical model has improved the prediction of rotor loads by up to 20%, whilst the inclusion of transient turbulence and wave flow fields has allowed for simulation of TSTs in flow conditions that were not previously possible. Secondly, the thesis presents the design and testing of a 3.0m diameter TST, named remote river energy system (RRES). The BEMT numerical model was used to predict the loads on the turbine which governed its design. A laboratory test rig was built to test the power take-off and pump assemblies prior to deployment at Warrior Way, Pembrokeshire. Valuable knowledge was gained throughout the design and testing stages of the RRES which will improve future developments of TSTs. The improvements made to the BEMT numerical model and testing of the RRES will help lower the levelised cost of energy and increase the attractiveness of TSTs as generators of clean renewable energy.

Acknowledgements

I would firstly like to thank my supervisors, Ian Masters and Michael Togneri. Their extensive knowledge and experience has been invaluable throughout. I have learnt a lot from you both, thank you.
As with any significant engineering project, it is a team effort and not an individual one. Throughout the RRES project I have enjoyed working with many colleagues and am very grateful for all their invaluable contributions. A special mention must be given to the following; David Glasby for his work on the design, Tom Lake for his work on the electronics, and Ian Masters for his leadership and guidance.
This thesis was supported by the MEECE project funded by the European Regional Development Fund and the Welsh & UK governments through the Swansea Bay City Deal.

Contents

List of Tables

List of Figures

Nomenclature

Acronyms

ADCP	Acoustic Doppler Current Profiler	LLW	Low Low Water
ADV	Acoustic Doppler Velocimeter	MDPE	Medium Density Polyethylene
AL	Actuator Line	META	Marine Energy Test Area
ALM	Additive Layer Manufacture	NRW	Natural Resources Wales
BEMT	Blade Element Momentum Theory	PSD	Power Spectral Density
BR	Blade Resolved	PTO	Power Take-Off
CAD	Computer Aided Design	RPM	Revolutions Per Minute
CFD	Computational Fluid Dynamics	RRES	Remote River Energy System
DES	Detached Eddy Simulation	SF	Safety Factor
DNS	Direct Numerical Simulations	SPI	Sediment Profile Imagery
FBD	Free Body Diagram	SWL	Still Water Level
FMEA	Failure Mode Effect Analysis	TEC	Tidal Energy Converter
GAD-CFD	Generalised Actuator Disk Computational Fluid Dynamics	TI	Turbulence Intensity
		TRL	Technology Readiness Level
GFRP	Glass Fibre Reinforced Polymer	TSR	Tip Speed Ratio
GPS	Global Positioning System	TST	Tidal Stream Turbine
HATT	Horizontal Axis Tidal Turbine	URANS	Unsteady Reynolds Average Navier-Stokes
LCOE	Levelised Cost of Energy		
LDV	Laser Doppler Velocimeter	VATT	Vertical Axis Tidal Turbine
LES	Large Eddy Simulation	VPM	Vortex Particle Method

Symbols

a	Axial induction factor	-	c	Airfoil chord length	m
a	Radial pad width	m	c_f	Coefficient of friction	-
a_{crit}	Critical axial induction factor	-	C_d	Orifice discharge coefficient	-
A	Acceleration of rotor blades	rad/s^2	C_D	Drag coefficient	-
A	Swept area of rotor blades	m^2	C_L	Lift coefficient	-
A_o	Cross-sectional area of orifice	m^2	C_m	Inertia coefficient	-
A_{piston}	Piston head cross-sectional area	m^2	C_P	Power coefficient	-
A_{wave}	Wave amplitude	m	$C_P{}^*$	Scaled power coefficient	-
b	Tangential induction factor	-	C_T	Thrust coefficient	-
b	Length of bearing pad	m	$C_T{}^*$	Scaled thrust coefficient	-
B	Pitch line circumference	m	d	Depth of water	m

dr	Thickness of blade element	m	p_{amb}	Ambient pressure	Pa
D	Drag	N	p_D	Pressure at actuator disk	Pa
D_{anchor}	Depth of anchor	m	p_{jo}	Bearing pressure	Pa
D_{pipe}	Diameter of pipe	m	p_{th}	Bearing pressure capacity	Pa
d_w	Depth of water	m	$\Delta p_{Ball\ valve}$	Pressure drop across ball valve	Pa
E	Modulus of elasticity	Pa	$\Delta p_{orifice}$	Pressure drop across orifice	Pa
f	Friction factor	-	Δp_{valve}	Pressure drop across throttle valve	Pa
F_{anchor}	Force on anchor	N			
$F_{A\text{-}inertia}$	Inertia force on rotor blades	N	p_{pump}	Pump pressure	Pa
$F_{D_{wind}}$	Wind drag force of RRES	N	p_v	Vapour pressure	Pa
$F_{D_{RRES}}$	Drag force of RRES	N	p_W	Pressure downstream of turbine	Pa
F_{hub}	Hub loss correction factor	-	p_∞	Pressure upstream of turbine	Pa
$F_{inertia}$	Inertia force	N	P	Power	W
$F_{mooring}$	Mooring force	N	P_{pump}	Pump power	W
F_{piston}	Piston force	N	P_{rotor}	Rotor power	W
F_{pump}	Pump force	N	Q	Volumetric flow rate	m^3
F_{tip}	Tip loss correction function	-	r	Local radius	m
F_T	Axial force (Thrust)	N	R	Radius of rotor blade	m
$F_{T\text{-}inertia}$	Inertia torque on rotor blades	N	Re	Reynolds number	-
g	Minimisation objective function	-	S_a	Axial source term	N
h_L	Head loss	m	S_i	Source term	N
h_{pump}	Pump head	m	S_t	Tangential source term	N
$h_{turbine}$	Head gain of turbine	m	t	Rotor blade twist	°
H_{wave}	Wave height	m	Δt	Time step of numerical model	s
i	Number of bearing pads	-	T	Torque	Nm
I	Rotor inertia	kg/m^2	T_{crank}	Crankarm torque	Nm
I	Cross-sectional moment of inertia	m^4	$T_{friction}$	Friction torque	Nm
			$T_{generator}$	Generator torque	Nm
k_g	Pad / circumference ratio	-	T_{rotor}	Rotor torque	Nm
K_L	Loss coefficients	-	u_{wave}	Horizontal wave particle velocity	m/s
L	Lift	N	$\dot{u}_{wave}$	Horizontal wave particle acceleration	m/s^2
L_{chord}	Characteristic linear dimension (i.e half the blade chord length)	m	U	Flow stream velocity	m/s
L_{crank}	Crankarm length	m	U_c	Free stream flow velocity	m/s
L_{jo}	Length of journal bearing		U_D	Flow velocity at actuator disk	m/s
$L_{mooringline}$	Length of mooring leg	m	U_W	Flow velocity downstream of turbine	m/s
L_{pipe}	Length of pipe	m			
$L_{pontoon}$	Length of RRES pontoon	m	U_∞	Flow velocity upstream of turbine	m/s
L_{rod}	Piston rod length	m			
L_{wave}	Wave length	m	V	Instantaneous fluid velocity with respect to the rotor blade	m/s
m	Wave number	-			
$\dot{m}$	Mass flow rate	kg/s	V	Volume	m^3
M_A	Added mass	kg	V_{pump}	Pump volume	m^3
M_{anchor}	Mass of anchor	kg	$\dot{V}_{pump}$	Volumetric flow rate of pump	m^3/s
M_{leg}	Mass of mooring leg	kg	V_R	Rotor velocity	m/s
N	Number of rotor blades	-	w_{wave}	Vertical wave particle velocity	m/s
p	Pressure	Pa	$\dot{w}_{wave}$	Vertical wave particle acceleration	m/s^2

W_{jo}	Load on journal bearing	N	ϵ	Roughness of pipe	m
W_m	Weight of mooring leg	N	$\Gamma(\theta)$	Elliptical downwash function	-
W_{th}	Max thrust load on bearing	N	λ	Tip speed ratio	-
z_{wave}	Wave depth	m	ω	Wave frequency	Hz
z_W	Head height downstream of turbine	m	ω_{pump}	Pump rotational rate	rad/s
			Ω	Rotor rotational speed	rad/s
z_∞	Head height upstream of turbine	m	$\dot{\Omega}$	Acceleration of rotor blades	rad/s^2
α	Angle of attack	$^\circ$	ϕ	Inclination of the resultant flow with respect to the rotor blade	$^\circ$
β	Ratio of orifice to pipe diameter	-			
η	Water elevation from SWL	m	ρ	Density	kg/m^3
η_{dt}	Drive train efficiency	-	σ	Cavitation number	-
η_{gear}	Gear ratio	-	θ	Combined pitch and twist of blade	$^\circ$
η_{motor}	Gear ratio of motor	-			
η_{pump}	Pump efficiency	-	υ	Kinematic viscosity	m^2/s

Constants

g	Gravitational constant	$9.81 m/s^2$	π	Ratio of a circle's circumference to its diameter	3.1416...

Prefix

tera	T	10^{12}	milli	m	10^{-3}
giga	G	10^9	micro	μ	10^{-6}
mega	M	10^6	nano	n	10^{-9}
kilo	k	10^3			

Chapter 1

Introduction & Literature Review

1.1 Introduction

The global energy demands of human activities, (i.e. industrial processes, transportation, electricity generation, etc), is increasing year on year. There are many different opinions on how to best fulfil our energy demands, differing greatly between different countries and governments. Since the start of the industrial revolution, burning fossil fuels has been our main source of energy which releases CO_2 into the atmosphere, contributing to climate change. 196 countries have adopted a legally binding international treaty on climate change named the Paris Agreement. Its goal is to limit the increase in the global average temperature to well below 2°C of pre-industrial levels. The United Kingdom government has set a goal of reaching net zero by 2050 by decarbonising all sectors of the economy [20].

The renewable energy sector will play a key part in achieving the UK goal of net zero by 2050. Tidal stream turbines (TST) technology is one potentially important part of the renewable energy sector. Energy is harnessed from fast moving currents in the oceans caused by the rise and fall of the tides as a result of the gravitational pull of the moon and sun. Although tidal energy generation is still in its infancy, it has great potential as it is very predictable compared to other renewable energy sources such as wind, solar or wave [21]. Estimations of potential tidal energy resource in the United Kingdom are between 50.2-95TWh/yr (or around 3-6% of total energy demand), 105.4TWh/yr in Western Europe, and 500-1000TWh/yr worldwide [22, 21].

It was not until the year 2000 that research and development in tidal energy was funded by the UK government, approximately 25 years after they first funded other renewable

energy systems such as wind and solar. This explains the current stage of development in the tidal energy sector and why it is trailing other renewable energy sectors. In the brief time since the inception of the sector, many exciting developments have been made. Several testing centres have been built to enhance prototype testing of tidal turbines, such as NaREC, the European Marine Energy Centre, and Wave hub. The development, deployment, and demonstration of commercial scale devices such as the HS1500 [23] has helped significantly increase the funding into TST research and development. Detail of recent significant deployments of TST are given in Table 1.1.

TSTs, also interchangeably called tidal energy converters (TECs), have the potential to become significant contributors of clean renewable energy, reducing our dependency on fossil fuels [21, 22]. A significant barrier for TSTs is the expense of operations at sea; more specifically the expense of planned and unplanned maintenance [24, 25, 26]. Improving the design of TSTs through numerical modelling, development, and testing will reduce the number of planned and unplanned maintenance and therefore greatly increase their popularity.

Blade Element Momentum Theory (BEMT) is a common numerical model that is used for design and performance evaluation of TSTs [27]. BEMT is often the preferred numerical model as it offers acceptable accuracy for evaluation of turbine design iterations with significant computational saving [28, 29, 30, 31]. In a computationally efficient manner, BEMT calculates the performance of a turbine or propeller by combining two methods; the momentum *"actuator disk"* theory and the blade element theory [32, 33, 9]. A robust BEMT model has been developed at Swansea University [28, 34], which will be the foundation of this thesis. Foil shape and Reynolds number dependency, and transient features are developed and included in the BEMT numerical model to improve its accuracy of predicting TST performance and loads. Any improvements to the BEMT numerical model are quantified by comparison to empirical laboratory experiments. Improvements in the accuracy of the BEMT numerical model will directly enhance the design and evaluation of TSTs. This will reduce the levelised cost of energy (LCOE) and thus increase the popularity of TSTs as generators of clean renewable energy.

This thesis also continues the development and testing of a remote river energy system (RRES) which is based on work from a previous project [35]. The brief for the RRES is that it must be cheap and easily manufactured, particularly aimed towards developing communities, as the development of any new energy solution should be reliable and

Table 1.1: Detail of recent significant deployments of tidal stream turbines.

Developers	Device	Detail
SAE Renewables MeyGen	2 different sea-bed mounted tidal turbines; HS1500 and AR1500. Both are rated to 1.5MW 	Test site: MeyGen 1A at Inner Sound tidal development site, Scotland. Currently the installed capacity is 6MW (4 turbines). Project is planned to develop into a 396MW farm. As of 31st of Dec 2023, the project has generated 61GWh. Both devices are 3 bladed turbines of 18m diameter rated to 1.5MW. The turbines weigh 150t mounted on 1450t gravity foundation.
HydroQuest	OceanQuest 1MW sea-bedmounted vertical axis tidal stream turbine 	Test site: Paimpol-Brehat, France. Successfully tested between 2019-2021. HydroQuest are currently developing a 2.5MW version for a planned 17.5MW farm as part of the flowatt project at Raz Blanchard, Normandy, France.
Orbital Marine Power	Floating tidal stream turbine Orbital 02 2MW 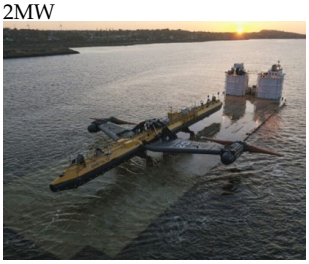	Test site: Fall of Warness at the EMEC test area, Orkney, Scotland. The 02 is a 72m long tubular hull which supports two coaxial two-bladed turbines of 20m diameter, with a combined rated power of 2MW.
Magallanes Renovables	Floating tidal stream turbine ATIR 1.5MW 	Test site: Fall of Warness at the EMEC test area, Orkney, Scotland. The ATIR is a 45m long vessel which has a 25m deep draft which supports two coaxial three-bladed turbines. The turbines have a diameter of 19m with a combined rated power of 1.5MW.
Swansea University	Remote river energy system (RRES) 7kW 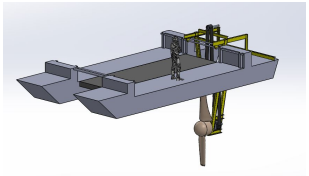	Test site: META Warrior Way, Pembrokshire, UK. The RRES is a 10m long floating tidal stream turbine with a submersible arm which supports a 3m diameter two-bladed turbine. The device is developed with minimal manufacturing and materials cost with the aim for small developing communities.

affordable for all people. The development is done in four stages and follows the guidance of IEC TS 62600-202:2022. Stage one, concept model, has already been completed in a previous project [35]. Development stages 2-4 are presented in this thesis. The second stage is a laboratory test rig that will be used to primarily test the PTO and control system. The third stage is a deployment of the 0.9m diameter RRES at test site which will test the performance, PTO, and control system of the RRES. The last stage is a deployment of the 3m diameter RRES at the test site which aims to demonstrate operability, maintainability, access, and health and safety. Invaluable information is gained through the development and testing of a TST which will help future projects. Increasing the reliability of TSTs can be made by improving their components, which is achieved with better design, manufacturing and assembly techniques, and deployment procedures.

The RRES design presented in this thesis is a platform to facilitate prototype technology trials to further develop the concept. Design of the RRES is dictated by conditions at the chosen test site, at Warrior Way, Milford Haven. The test area is a tidal estuary, with mean depth at high water of 20m and a maximum tidal range of 10m. The current flow velocities commonly range from 0-1.8m/s, with 1.3m/s as the highest reliable speed within a tidal cycle. Under a severe weather event, it is hypothesised that the current flow velocity could reach 2.2m/s.

The RRES version developed and tested in this thesis is designed for installation in a tidal estuary. Energy is harnessed by transfer of rotational power from the rotor blades through a geared system to actuate the power take-off (PTO) system, comprising a dual action piston pump and one way valves. A closed loop control system is used to operate a throttling valve which regulates the flow of water in the pipes and consequently the rotor rotational rate. The system is comprehensively instrumented to allow for system design and testing experiments. The components which are of particular importance are: PTO, valves, chassis, safety braking, rotor blades, mooring, and sensors. Prior to deployment at the Marine Energy Test Area, Wales, UK, a laboratory test rig is used to test the power take off, valves, and sensors, with a motor replacing the rotor. Specification of the rotor blades and performance predictions of the system is achieved using the BEMT numerical model. Final design drawings are openly available which will facilitate application of the design and improvements by other collaborators.

1.2 Aims & Overview

There are two high level aims for the work presented in this thesis;

1. Improve the BEMT numerical model prediction of tidal stream turbines loads and performances through the implementation of 1. element foil shape and Reynolds number dependency, and 2. transient features.

2. Development and testing of the RRES, (stages 2-4 (scaled design model - full scale prototype device)), using the BEMT numerical model throughout as a design tool.

The first part of this thesis presents the improvements and validation of the BEMT numerical model. Two additional features are added; 1. foil shape and Reynolds number dependency, and 2. transient turbulence and wave. Evaluation of the improvements to the BEMT numerical model is made by an extensive comparison against empirical laboratory data from five different rotor blades. The validated BEMT numerical model is then used to predict the loads and performance of the RRES, used as the foundations to the design process. The second part of this thesis presents the design process for the RRES. As previously stated, the design process of the RRES follows the guidance of IEC TS 62600-202:2022 which gives best practices and recommended procedures for the early stage development of a tidal energy converter. The development is split into four stages, with stages 2-4 presented in this thesis. Stage one, concept model, has already been completed in a previous project [35]. Stage 2 is design model (0.9m diameter version), stage 3 is sub-system model (deployment of 0.9m diameter RRES), and stage 4 full scale testing of prototype device (deployment of 3.0m diameter RRES). A laboratory rig is commissioned to test the PTO and pump assemblies, replacing the input power from the rotor blades with an electrical motor. The most important design details of the RRES then follows which include the following; pontoon assembly, rotor blades, blade root bending moment sensor, bearings, control system, and mooring. The last part of this thesis presents the results from both the laboratory rig and deployment of the RRES. The results show that a tidal stream turbine has been successfully designed and manufactured. It provides much valuable information for further iterations of the RRES and to other developers of tidal stream turbines.

In the remainder of this chapter, a review of the literature on general TEC principles and selected test cases are given. Additional background on the literature for specific aspects of the work is summarised elsewhere in the thesis, e.g. numerical methods in Chapter 3.

1.3 Tidal stream energy converters

Tidal stream energy devices capture kinetic energy from ocean currents caused by the rise and fall (flood and ebb) of the tides. Topographical features such as headlands, inlets, straight, and shape of the sea-bed can significantly increase the ocean currents. A location with a large tidal range is necessary to viably produce power at a commercial scale. Many different types of tidal stream energy devices exists, capturing the kinetic energy of ocean currents in various ways. The captured kinetic energy is converted into useful electrical energy by generators.

In addition to tidal stream energy convertors, tidal barrages and lagoons can also generate energy from tidal rise and fall by taking advantage of the height difference between low and high tides [36, 37, 38]. Tidal barrages and lagoons have a dam, (i.e. barrage, wall, barrier), which is constructed across tidal rivers, bays, and estuaries. The dam holds water at high tide and releases the water during low tide through turbines, producing electrical energy. In comparison to tidal current energy convertors, the environmental impact and costs of tidal barrages and lagoons are significantly higher.

Tidal stream energy converters can be categorised under six main means of power capture; horizontal axis turbine, vertical axis turbine, oscillating hydrofoil, enclosed tips venturi, Archimedes screw, and tidal kite.

1.3.1 Horizontal axis turbine

The horizontal axis turbine is by far the most common tidal stream turbine and can be described as a sea version of a conventional wind turbine. For a wind turbine, the flow of air causes the rotors to rotate around the horizontal axis. In the same manner, the flow of water causes the rotors of a tidal horizontal axis turbine to rotate around its horizontal axis, generating power. HS1500 is an example of a 1.5MW horizontal axis tidal stream turbine which is deployed as part of the MeyGen project off the north coast of Scotland [23, 39]. Figure 1.1 shows pictures of the physical turbine and the planned farm layout.

1.3.2 Vertical axis turbine

A vertical axis turbine extracts energy from the current in a similar manner to the horizontal axis turbine, but differs in the orientation of rotor rotation. As the name suggests, the rotors rotate around the vertical axis [40, 41]. A schematic of a vertical axis tidal stream turbine is shown in Figure 1.2a [3]. A French consortium of HydroQuest and Construction Mecaniques de Normandie have successful developed and installed a 1MW vertical

(a) (b)

Figure 1.1: MeyGen horizontal axis turbine, a) photo of the physical turbine, and b) CAD render of the proposed tidal turbine farm.

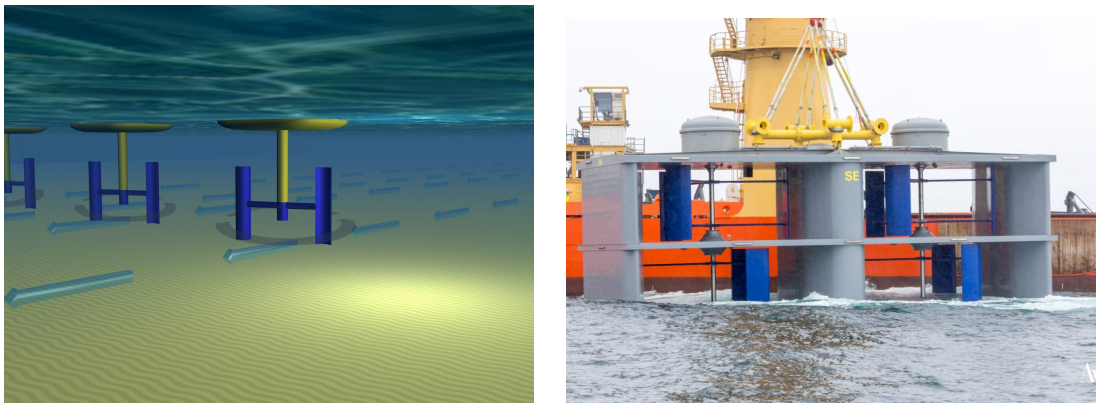

(a) (b)

Figure 1.2: Vertical axis tidal stream turbine; a) Schematic of a vertical axis tidal stream turbine [3] and b) photo of the HydroQuest vertical axis turbine [4].

axis tidal stream turbine (OceanQuest) at Paimpol-Brehat, Brittany [4]. A photo of the OceanQuest being deployed is shown in Figure 1.2b.

A vertical axis turbine has some advantages compared to horizontal axis turbine. The vertical axis turbine has a simpler design due to constant angle of attack across the hydrofoil, resulting in it not requiring blade twist. Due to the simpler design, the maintenance requirements and costs are lower. Vertical axis turbines also have better performance in severe flow conditions. There is limited commercial deployment of vertical axis turbines partially due to their low technology readiness level compared to horizontal-axis designs. Also, at high energetic sites, horizontal axis turbines provide higher power capture than vertical axis turbines [42].

1.3.3 Enclosed tips Venturi

An enclosed tip Venturi tidal device concentrates the current flow to the swept area of the turbine using Venturi duct or diffusers. They are also commonly know as ducted TST. Ducts can be added to both horizontal and vertical axis turbines. The current flow is converged, i.e. increase mass flow rate, towards the rotor and thus ducted turbines can produce the same power as non-ducted turbines from a smaller turbine [43]. However, when comparing total overall size, the ducted turbine is less efficient than an equivalent size non-ducted turbine [44]. Another disadvantage of ducted turbines is the additional wake caused by the structure of the duct, limiting their use in tidal arrays. Figure 1.3 shows photos of ducted tidal stream turbine; a) DCNS-OpenHydro 0.5MW turbine and b) computer aided design (CAD) schematic of planned OpenHydro turbine array with 2MW turbines [5].

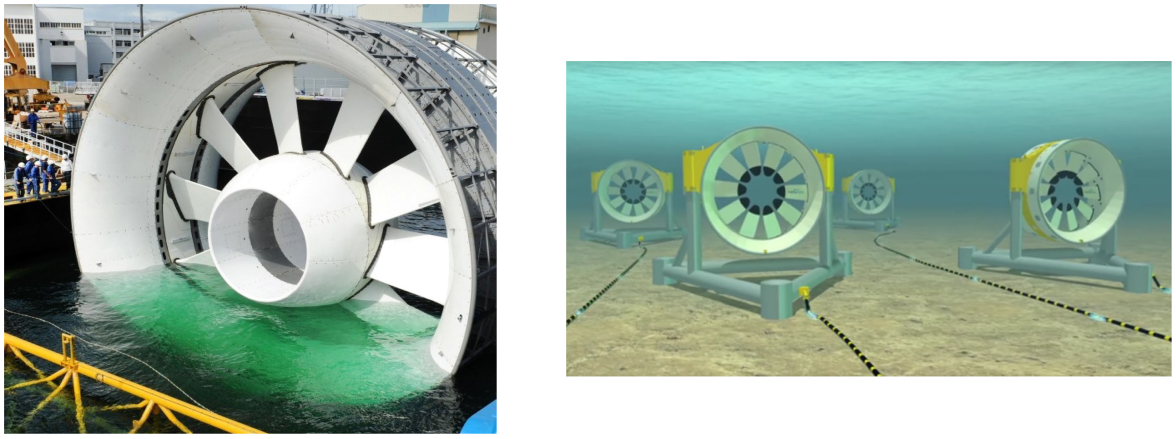

(a) (b)

Figure 1.3: Photos of ducted tidal stream turbine; a) DCNS-OpenHydro 0.5MW turbine and b) CAD schematic of planned OpenHydro turbine array with 2MW turbines [5].

1.3.4 Oscillating hydrofoil

An oscillating hydrofoil tidal device consists of a hydrofoil attached to an extended arm [45]. As the current flows around the hydrofoil it creates lift, causing the arm to rise and fall. The oscillating arm drives a hydraulic system which is used to create electricity. A schematic of an oscillating hydrofoil tidal stream turbine is shown in Figure 1.4 [6].
The relative flow speed, and thus angle of attack is the same across the whole length of the hydrofoil, permitting the hydrofoil of an oscillating turbine to have a straight, non twist profile. This results in an easier and cheaper manufacture compared to axial turbine blades which require a more complex geometry with twist. Due to the rectangular extraction

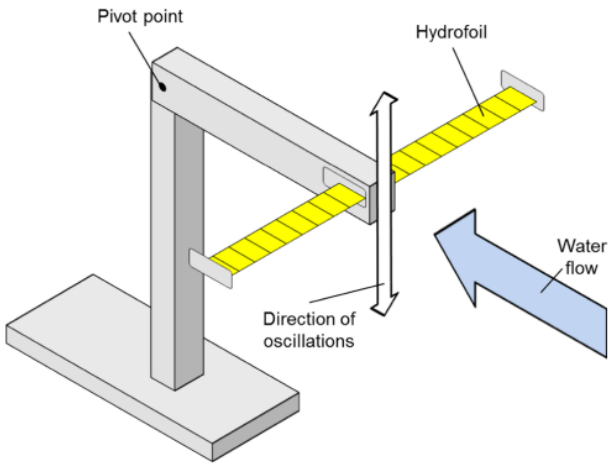

Figure 1.4: Schematic of an oscillating hydrofoil tidal stream turbine [6].

plane, oscillating hydrofoil turbines can be used in shallow waters and riverbeds. The efficiency of oscillating hydrofoil turbines is relatively poor due to the time required to change the direction of oscillation [36]. Currently there is little development of commercial scale oscillating hydrofoil turbines.

1.3.5 Archimedes screw

The Archimedes screw tidal energy device has the shape of a helical surface surrounding a central cylindrical shaft. As the flow of the current moves up and through the helical screw, the turbine is turned producing electricity. The Archimedes screw is fixed to the sea-bed but is allowed to pivot to alter the angle and direction to the incoming flow. Improvements in efficiency are seen by increasing the number of turns, decreasing the horizontal screw angle, and increasing the ratio of inflow depth and radius. An advantage of the Archimedes screw over other TST is its ability to operate well at low flow velocities [46]. The turbulence and wake created from Archimedes screw turbine are minimal meaning that tidal arrays can be more concentrated than other TST. Flumill are a Norwegian company which have developed and deployed a commercial sized 600kW Archimedes screw turbine, shown in Figure 1.5. No efficiency figures are given for this device, but as a low Reynolds number machine, working mostly on drag forces, it is expected to be low.

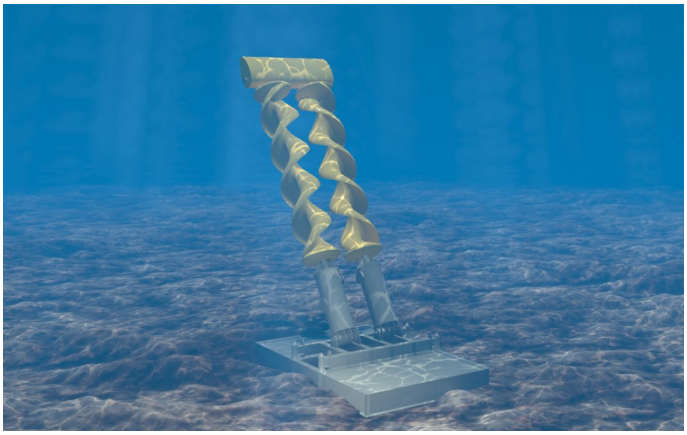

(a)

(b)

Figure 1.5: Photo of Flumill Archimedes screw tidal stream turbine [7], a) CAD model and b) physical device.

1.3.6 Tidal kite

A tidal kite consists of a hydrofoil and a turbine which is tethered to the sea-bed. The flow of the current causes the kit to "fly" in an orbit around the tether location. As the hydrofoil is orbiting, the flow of water moves through the turbine producing power. A rudder is positioned at the rear of the hydrofoil which dictates the orbital path of the tidal kite. The movement of the kite increases the speed of the flow through the turbine, increasing the potential power generation, which makes the tidal kite a particularly attractive option for lower current velocity sites. Minesto are a Swedish developer of a tidal kite device, and claim that their tidal kit moves 10x faster than than the current velocity [8, 6]. Minesto DG-14 tidal kite has a wing span of 14m, rotor diameter of 1.15m, tether length of 110-140m, and installation depth of 90-120m [8]. Figure 1.6 shows schematics of a) Minesto tidal kite with key components labelled, and b) deployment of a tidal kite, which shows the kite assembly tethered to the sea-bed and the path of travel [8]. The tidal kite requires a

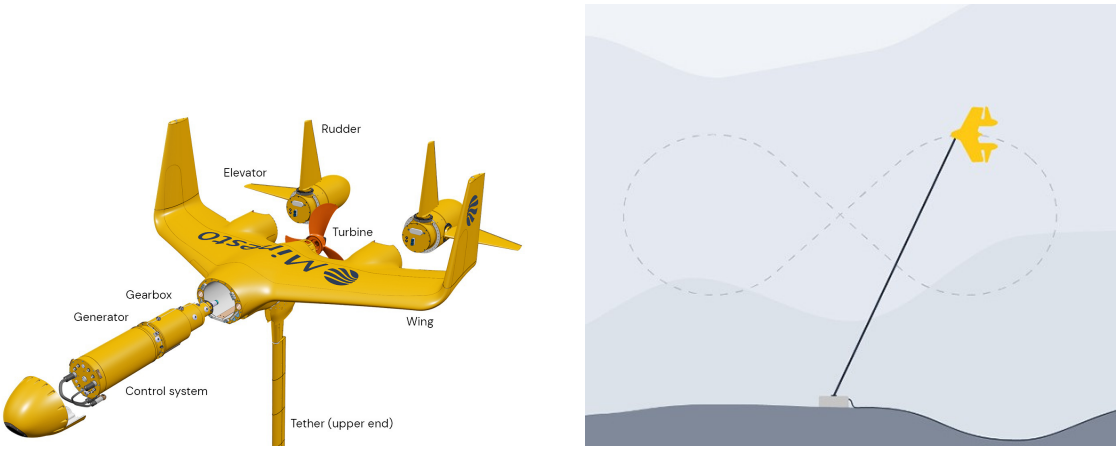

(a) (b)

Figure 1.6: Tidal kite schematics of a) Minesto tidal kite with key components labelled, and b) deployment of a tidal kite which shows the kite assemble tethered to the sea-bed and the path of travel [8].

large swept area to be commercially competitive, which is a weakness of the technology compared to the other more compact TST.

Chapter 2

Blade Element Momentum Theory

Blade element momentum theory and computational fluid dynamics (CFD) are common numerical models that are available for predicting the performance of TST [27]. These numerical methods are established from the wind turbine industry which is considerably more mature than the TST industry. BEMT is often preferred to CFD numerical models as it offers acceptable accuracy for evaluation of turbine design iterations with significant computational saving [28, 29, 30, 31]. BEMT was initially developed in the late 19^{th} century for marine and aviation propellers with the model later applied to wind turbines [32, 33, 9]. In a computationally efficient manner, BEMT calculates the performance of a turbine or propeller by combining two methods; the momentum "actuator disk" theory and the blade element theory.

2.1 Literature Review

The BEMT model minimises its computational cost by making several simplifying assumptions, which are explained in detail in Section 2.2. A consequence of these assumptions is that some important phenomena such as tip vortices and radial flow are neglected which can significantly distort the predicted performance of a TST. Inclusion of loss factors, such as tip, hub and high induction in the BEMT model can significantly improve its accuracy [28, 34, 47, 48, 49, 50, 51, 52]. These typically serve as semi-empirical corrections that account for some of the physical phenomena omitted by the assumptions underpinning the model.

Madsen *et al* [52] compare BEMT and Navier-Stokes CFD solutions to conclude that significant inaccuracies in the BEMT model are limited to the blade root and blade tip.

They present corrections to improve the accuracy of the BEMT model. They show that with the corrections, the BEMT model can be used as an accurate turbine performance predictor. A method for including tip and hub losses in the BEMT model is described by Masters *et al* [28]. They compare the correction factors of hub and tip loss from different methods. Some corrective factors relied on empirical data which significantly increased the computational cost of the BEMT model. Prandtl tip and hub corrections were selected as they improved the accuracy of the BEMT model and did not rely on empirical data, contributing a minimal computational expense to the BEMT model. Chapman *et al* [34] describes a method for including tip, hub and high induction corrections to the BEMT model. At high tip speed ratio (TSR), the axial induction factor predicted by the classical BEMT becomes physically untenable. They propose a modified version of the Buhl high induction correction factor that is used for wind turbines. The BEMT model is compared to experimental data where it predicts power output well, but over predicts the axial force. Lift and drag polars play a primary role in the BEMT numerical model. Masters *et al* presents a comparison of BEMT results against experimental data for three rotors [1]. The sensitivity of the BEMT model to small changes in hydrodynamic properties of the blade profiles (lift and drag properties) are studied. Table 2.1 summarises the changes to maximum power and thrust coefficients and optimum TSR for the three different blades in response to small changes in the lift and drag properties of the blade profiles. Small

Table 2.1: Changes to maximum power and thrust coefficients and optimum TSR for three turbines used in experimental studies at Liverpool, IFREMER, and Manchester in response to small changes in the lift and drag properties of the blade profile [1]

		Liverpool	**IFREMER**	**Manchester**
Max C_P	Original	0.4431	0.4122	0.3350
	$C_L - 10\%$	0.4377 (−1.22%)	0.4035 (−2.12%)	0.3119 (−6.88%)
	$C_D + 50\%$	0.4287 (−3.26%)	0.3848 (−6.66%)	0.2157 (−35.62%)
	Both	0.4213 (−4.92%)	0.3736 (−9.37%)	0.1866 (−44.3%)
Max C_{Fa}	Original	0.8018	0.7531	0.9761
	$C_L - 10\%$	0.7707 (−3.88%)	0.7224 (−4.07%)	0.9175 (−6.00%)
	$C_D + 50\%$	0.8024 (+0.08%)	0.7540 (+0.13%)	0.9643 (−1.21%)
	Both	0.7714 (−3.79%)	0.7234 (−3.95%)	0.9185 (−5.90%)
Optimum TSR	Original	3.64	4.52	4.64
	$C_L - 10\%$	3.84 (+5.50%)	4.62 (+2.21%)	4.54 (−2.15%)
	$C_D + 50\%$	3.52 (−3.30%)	4.32 (−4.42%)	4.10 (−11.64%)
	Both	3.70 (+1.65%)	4.50 (−0.44%)	4.40 (−5.17%)

changes in lift and drag polars has only a small effect on the predicted turbine performance from the BEMT numerical model. This gives them assurance that during operation, when small changes to the blade characteristics may occur due to biofouling or blade erosion, a large drop in rotor performance is unlikely. The change in performance prediction of a TST from the BEMT numerical model is correlated to the change in lift and drag polars, i.e. the greater the change in the lift and drag polars, the greater the change in BEMT predicted turbine performance.

Dynamic loads resulting from wave-current interactions amplify cycling loadings which accelerate fatigue on tidal current rotor blades. El-Shahat *et.al.* have investigated the effect of a wave field and resulting dynamic loads on tidal stream rotor blades, by modifying a BEMT numerical model coupled with linear and non-linear wave theories [53]. They state that the flow field cannot be assumed steady when accounting for wave effect and current shear, and thus the azimuthal position of the rotor blades becomes very important and must be accounted for in the BEMT numerical model. They also include a dynamic stall model in their BEMT numerical model. The standard deviation of hydrodynamic loadings of both in-plane and out-of-plane bending moments were significantly affected by wave period and height.

Unsteady flow corrections have been incorporated into a BEMT numerical model by Perez *et.al.*, using empirical high-frequency data recorded by an ADCP in an energetic tidal site [54]. They couple a classic BEMT numerical model with rotational augmentation and dynamic stall corrections, which they suggest makes the numerical model more suitable for unsteady conditions. The performance of a tidal current turbine in flow fields with various turbulence intensities and integral length scales is estimated by comparing power, thrust, and bending moment coefficients. They showed that standard deviations of the coefficients were more sensitive than their means. They also found that the performance coefficients were influenced more by turbulence intensities than integral length scales.

Vogel *et.al.* have addressed a key difference that exists between the flow field of wind and tidal current turbines due to the density difference between water and air. As water is ~815 times denser than air, a tidal current turbine will experience "volume-flux constrained fluid dynamics", (i.e. blockage effects), which results in a static pressure difference between the upstream and downstream flow fields not seen in the case of wind turbines. The applied thrust and blockage ratio of the turbine affects the flow speed through the rotor plane and in the wake. This is accounted for in their BEMT numerical model by modifying the

momentum theory equations. Their BEMT numerical model was compared to a blade resolved numerical model, with agreement in thrust and torque prediction to within 3%. Horizontal axis tidal turbines (HATT) are by far the most common type of TST but there are vertical axis tidal turbines (VATT) in existence. VATT are often less complex and consequently less expensive than HATT. However, most have significantly lower performance characteristics and therefore have a higher cost. VATT often have higher solidity and loading compared to HATT which causes issues with traditional BEMT models. Mannion *et al* have developed an accurate BEMT model for high solidity VATT [29]. They use a double stream-tube model which employs a graphical approach to determine the axial induction factor compared to the iterative approach used in traditional BEMT models. Power performance for low and high solidity rotors are compared between the BEMT model and experimental data. The BEMT model produced peak efficiency values within 2.5% for the low solidity rotor and 10% for high solidity rotor against experimental data.

2.2 Theory

2.2.1 Steady-state model

This section firstly presents the derivation of the classical BEMT numerical model, which uses two different models to describe the turbine; momentum theory and blade element models. It then details the additional features that the implementation used for this study have added to the classical BEMT numerical model to improve its predictions; transient model, corrections, synthetic turbulence, waves, and foil shape and Reynolds number dependence.

Linear momentum theory

The momentum theory assumes a stream-tube with an actuator disk that represents the rotor as shown in Figure 2.1. One dimensional momentum theory models the turbine as a frictionless permeable actuator disk which is assumed to impart no rotational velocity to the flow. It is assumed that the actuator disk does not interact with the fluid outside of the stream-tube. Energy is removed from the stream-tube by drag force produced by the actuator disk, creating a pressure drop across it. Far upstream and downstream of the stream-tube is assumed to be at ambient pressure, which means that the flow speed must drop to satisfy Bernoulli's Equation 2.1.

$$\frac{p_\infty}{\rho g} + \frac{U_\infty^2}{2g} + z_\infty - h_{turbine} = \frac{p_W}{\rho g} + \frac{U_W^2}{2g} + z_W \tag{2.1}$$

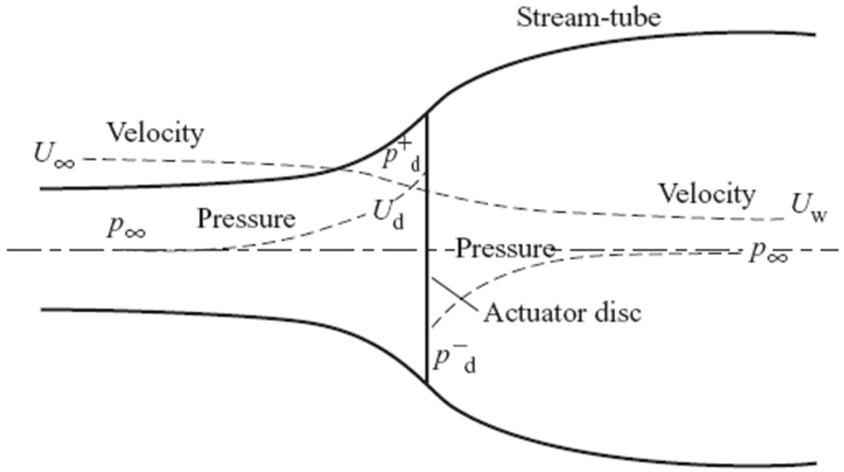

Figure 2.1: Energy extracting actuator disk and stream-tube [9].

The rate of change of momentum due to the actuator disk may be written as Equation 2.2 in terms of flow velocity U, density ρ, and cross sectional area A. The symbol ∞ refers to conditions far upstream, D to conditions at the actuator disk, and W to conditions in the far wake. F_T is the axial force.

$$F_\mathrm{T} = U_\infty(\rho A_\infty U_\infty) - U_\mathrm{W}(\rho A_\mathrm{W} U_\mathrm{W}) \tag{2.2}$$

Mass flow rate $\dot{m}$ is conserved within the stream-tube, thus equation (2.2) can be re-written as Equation 2.3.

$$F_\mathrm{T} = \dot{m}(U_\infty - U_\mathrm{W}) \tag{2.3}$$

Pressure difference immediately upstream and downstream of the actuator disk can also be used to define the axial force, F_T. The static pressure far upstream and downstream of the actuator disk are equal to ambient pressure, p_∞. Bernoulli's equation is applied separately upstream and downstream of the actuator disk which are represented in Equations (2.4) and (2.5) respectively. U_D is the flow speed at the disk, and p_{+D}, p_{-D} as pressures immediately upstream and downstream of the actuator disk.

$$p_\infty + \frac{1}{2}\rho U_\infty^2 = p_\mathrm{+D} + \frac{1}{2}\rho {U_\mathrm{D}}^2 \tag{2.4}$$

$$p_\mathrm{-D} + \frac{1}{2}\rho {U_\mathrm{D}}^2 = p_\infty + \frac{1}{2}\rho {U_\mathrm{W}}^2 \tag{2.5}$$

We can assume that the cross-sectional area of the stream-tube immediately upstream and downstream of the actuator disk are effectively the area of the actuator disk, A_D. From this assumption, F_T based on pressure differential, Equation 2.6, is derived from Equations (2.4) and (2.5).

$$F_{\mathrm{T}} = A_{\mathrm{D}} \frac{1}{2} \rho (U_{\infty}^2 - {U_{\mathrm{W}}}^2) \tag{2.6}$$

Equating Equation 2.6 to Equation 2.3 yields Equation 2.7

$$U_{\mathrm{D}} = \frac{U_{\infty} + U_{\mathrm{W}}}{2} \tag{2.7}$$

The fractional reduction in flow speed from far upstream, U_{∞}, to flow speed at actuator disk, U_D is defined as the axial induction factor, a. Equations (2.8) and (2.9) are relationships between flow speed with respect to the the axial induction factor.

$$U_{\mathrm{D}} = U_{\infty}(1 - a) \tag{2.8}$$

$$U_{\mathrm{W}} = U_{\infty}(1 - 2a) \tag{2.9}$$

Absorbed power, P, is the thrust (axial force) multiplied by the flow velocity at the actuator disk, U_D. Using Equation 2.6, generated power can be written as Equation 2.10. Substituting in the axial induction factor, a, generated power can be rewritten as Equation 2.11. Similarly the axial force, Equation 2.6, can be written in terms of the axial induction factor as in Equation 2.12.

$$P = A_{\mathrm{D}} \frac{1}{2} \rho (U_{\infty}^2 - {U_{\mathrm{W}}}^2) U_{\mathrm{D}} \tag{2.10}$$

$$P = A_{\mathrm{D}} \frac{1}{2} \rho U_{\infty}^3 4a(1 - a)^2 \tag{2.11}$$

$$F_{\mathrm{T}} = A_{\mathrm{D}} \frac{1}{2} \rho U_{\infty}^2 4a(1 - a) \tag{2.12}$$

Rotational momentum theory

In the linear momentum treatment, flow entering the rotor disk has no rotational motion at all. It is apparent that for a real horizontal-axis turbine, some of the axial flow energy is converted to rotational momentum by the rotor disk as it imparts rotational torque

on the fluid, which is done completely across the thickness of the disk. We introduce a tangential induction factor, b, to expresses the change in tangential velocity; Equation 2.13, where ω is the increase in tangential flow velocity and Ω is the tangential speed of the rotor (control volume).

$$b = \frac{\omega}{2\Omega} \tag{2.13}$$

To develop the momentum model to incorporate rotational effects, the stream-tube is divided into annular sections with local radius r and thickness dr. The area of the stream-tube annulus is $2\pi rdr$. Multiplying the change in pressure across the rotor disk by the annular area gives the elemental thrust; Equation 2.14.

$$dF_{\mathrm{T}} = (4b(1+b)\frac{1}{2}\rho\Omega^2 r^2)2\pi r dr \tag{2.14}$$

Torque produced on the rotor disk, dT, disk is equal to the rate of change of angular momentum of the fluid passing through it; Equation 2.15.

$$dT = d\dot{m}(\Omega r)r = \rho U_{\mathrm{D}} 2\pi r dr(\Omega r)r \tag{2.15}$$

Substituting Equations (2.8) and (2.13) into Equation 2.15 we get an expression for elemental torque in terms of upstream flow, rotational velocity, and the induction factors a and b; Equation 2.16. Similarly, the axial force in an annulus of area $2\pi rdr$ is derived from Equation 2.12 and is given in Equation 2.17.

$$dT_1 = 4b(1-a)\rho U_\infty \Omega r^2 \pi r dr \tag{2.16}$$

$$dF_{\mathrm{T1}} = 2\pi r \frac{1}{2}\rho U_\infty^2 4a(1-a)dr \tag{2.17}$$

Blade Element Theory

Due to the axial and tangential induction factors not being know a priori, the equations derived from the momentum theory are of little use on their own. In order to solve for these parameters, we need another representation of the torque and axial force on the rotor blades; this is achieved using blade element theory. The blade element theory divides the rotor blade into two-dimensional elements along its length. There is no fluid interaction between the elements and thus the loads on the blades can be assumed to rely solely on

the lift and drag characteristics of the blade shape.
Figure 2.2 is a diagram showing velocities and forces for a blade element at radius *r* relative to the blade chord line. θ, α, and ϕ represent combined pitch and twist of the blade, angle of attack of the blade from the resultant flow, and inclination of the resultant flow relative to the rotor plane respectively. *dL* and *dD* are the elemental lift and drag forces respectively whilst *U* is the resultant flow.

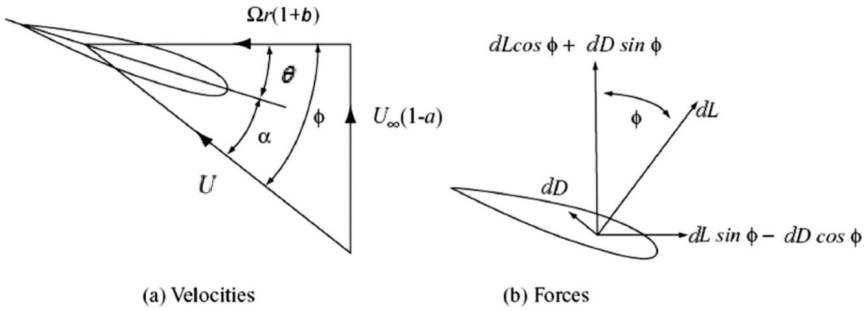

Figure 2.2: Blade element velocities and forces [9].

Blade element axial force and torque can be found by resolving their lift and drag forces. These can be written in terms of their coefficients, C_L and C_D, and *c* the aerofoil chord length and are given in Equations 2.18 and 2.19. N is the number of blades.

$$dF_{\mathrm{T2}} = N\frac{1}{2}\rho U^2 c(C_{\mathrm{L}}cos\phi + C_{\mathrm{D}}sin\phi)dr \tag{2.18}$$

$$dT_2 = N\frac{1}{2}\rho U^2 cr(C_{\mathrm{L}}sin\phi - C_{\mathrm{D}}cos\phi)dr \tag{2.19}$$

Equation 2.20 for the inclination of the resultant flow, ϕ, is derived from Figure 2.2.

$$\phi = tan^{-1}\left(\frac{U_\infty(1-a)}{r\Omega(1+b)}\right) \tag{2.20}$$

Dimensionless local speed ratio, λ, is given in Equation 2.21. Substituting the local speed ratio into Equation 2.20 gives Equation 2.22.

$$\lambda = \frac{r\Omega}{U_\infty} \tag{2.21}$$

$$\phi = tan^{-1}\left(\frac{(1-a)}{\lambda(1+b)}\right) \tag{2.22}$$

Equation 2.23 for the resultant flow, U, can be calculated using Pythagoras' theory.

$$U = U_\infty[\lambda^2(1+b)^2 + (1-a)^2]^{\frac{1}{2}} \tag{2.23}$$

Equations 2.18 and 2.19 can be equated with the momentum theory representations given in Equations 2.16 and 2.17.

Numerical solving

Two formulae for element axial force Equations 2.17 and 2.18 and torque Equations 2.16 and 2.19 now exist, derived from two different theories. The equations are combined in to a single minimisation objective function, g, Equation 2.24. This use of an objective function was first published by Masters *et al* [28]. The objective function is solved iteratively for the axial and tangential induction factors, a and b. *E.g.*, a version of the BEMT numerical model written in MATLAB achieved this with an active-set algorithm through the native fmincon function. Once the induction factors are known, straightforward calculations can be made to determine the performance of the rotor blades.

$$g = (dF_{\mathrm{T1}} - dF_{\mathrm{T2}})^2 + (dT_1 - dT_2)^2 \tag{2.24}$$

Total rotor axial force, $F_{T,rotor}$, and torque, T_{rotor}, are the sum of the elemental axial force, dF_T, and torque, dT respectively.

2.2.2 Transient model

A typical BEMT model runs loops across different rotational speeds, outputting canonical performance curves such as power coefficient vs TSR. Modelling unsteady flow conditions, (e.g turbulent, wave, or tidal) requires a transient time dependent run. Described below are some important modifications to the BEMT numerical model that are necessary for transient simulations [55]:

1. Create 3D flow grid around turbine.
2. Calculate position of rotor blade relative to the flow grid.
3. Find corresponding flow vectors for each element.
4. Resolve flow vector such that turbine components are relative to the rotor blade.

5. Solve elemental loads using BEMT.
6. Store data from time step for post processing.
7. Repeat steps 2-6 for the desired duration.

At every time-step a coarse loop determines the rotor rotational speed, based on the flow field velocity, needed to meet the target C_p, $C_{p,target}$, and target TSR, λ_{target}. The starting rotational speed of the rotor is defined by the user in the input file. At the end of every time-step the rotational acceleration of the rotor, $\dot{\Omega}$, is calculated. The exact equation used to determine the rotational acceleration of the rotor depends on the model used, but it is calculated by subtracting lost torque, e.g friction, $T_{friction}$, and generator, $T_{generator}$, from hydrodynamic torque and dividing by the inertia of the rotor, I, Equation 2.25. Generated torque is calculated using Equation 2.26 whilst frictional torque and inertia are user defined inputs. When a constant rotational rate control scheme is employed for the turbine, the generator torque term is allowed to change to maintain zero acceleration of rotor.

$$\dot{\Omega} = \frac{T_{\text{hydrodynamic}} - T_{\text{lost}}}{I} \tag{2.25}$$

$$T_{\text{generator}} = C_{\text{p,target}} \frac{1}{2\Omega} \rho \pi R^2 \left(\frac{\Omega R}{\lambda_{\text{target}}} \right)^3 \tag{2.26}$$

The new rotational speed of the rotor is calculated using Equation 2.27. Ω is the rotational speed of the rotor, Δt is the duration of the time step, i is the current iteration and $i + 1$ is the subsequent iteration. Depending on the magnitude of the generated and lost torque, rotational acceleration might be positive or negative resulting in acceleration or deceleration of the rotor rotational speed.

$$\Omega(i+1) = \Omega(i) + \dot{\Omega}(i)\Delta t \tag{2.27}$$

The generator model, Equation 2.26, gives the greatest control for user to define the lost torque within the BEMT model. Within the generator model the user can select several different parameters to best represent their problem. Application of braking, the duration of the braking, free or fixed rotation of rotor and friction torque in system are some of the most important parameters in the generator model.
The rotation speed of the rotor can be set to free or constant. Selecting free rotation is similar to selecting no braking as it sets generator torque to zero, allowing the rotational

speed to accelerate up to the freewheel condition - this is a means of investigating loads under failure conditions. When the constant rotation velocity is selected, the generator brake torque is calculated so that the rotational acceleration, A is zero. Another loss torque that can be specified by the user is the friction in the system. This is applied in the same manner as the generator braking torque.

2.2.3 Tip and hub corrections

The pressure difference between the suction and pressure sides of the rotor blades will produce a spanwise flow, resulting in vortices at the tip. The classical BEMT numerical model does not account for this physical phenomena and assumes no flow along the span of the rotor blade. This flow around the span of the rotor blade adversely affects the performance, resulting in BEMT numerical models over-predicting their power production. Correction functions are used to account for these inaccurate assumptions in the BEMT numerical model.

2.2.3.1 Tip loss

There are exact solutions to the tip loss behaviour [9, 56] which are computationally intense, and therefore do not lend themselves to the computational efficiency of the BEMT numerical model. Instead, semi-empirical corrections are used [28]. Prandtl's tip loss correction uses a factor F_{tip} to modify the momentum theory representation of the hydrodynamic force components, i.e., as they appear in Equations 2.16 and 2.17 [57]. The function treats the wake vortices sheets as a series of impermeable discs with mean velocity. Prandtl's tip loss function is given by Equation 2.28 [57], where θ is the inflow angle.

$$F_{\text{tip}} = \frac{2}{\pi}\cos^{-1}(e^{-f}) \tag{2.28}$$

$$f = \frac{N}{2}\frac{R-r}{r\sin(\theta)} \tag{2.29}$$

The momentum equations derived in Section 2.2.1 are updated with the tip correction factor;

$$dT_1 = 4F_{\text{tip}}b(1-a)\rho U_\infty \Omega r^2 \pi r dr \tag{2.30}$$

$$dF_{\text{T1}} = 2F_{\text{tip}}\pi r\frac{1}{2}\rho U_\infty^2 4a(1-a)dr \tag{2.31}$$

They are then combined with the blade element equations, **??** and **??** and solved.

2.2.3.2 Hub loss

The hub loss function is included in the BEMT numerical model to account for vortices shedding near the hub of the rotor blades as suggested by [33]. The hub loss function uses the same underlying theory as the tip loss function and is given in Equation 2.32. It is modified to work outwards from the blade root rather than inwards from the tip.

$$F_{\text{hub}} = \frac{2}{\pi}\cos^{-1} e^{-f} \tag{2.32}$$

$$f = \frac{N}{2}\frac{r - R_{\text{hub}}}{r\sin(\theta)} \tag{2.33}$$

It is slightly adjusted to work outwards from the blade root rather than inwards from the tip. The hub loss function is included in the momentum equations in the same manner as the tip loss function. Simplification of the loss functions is made by using a total loss function, F, which is the product of F_{tip} and F_{hub}. The momentum equations thus become;

$$dT_1 = 4Fb(1-a)\rho U_\infty \Omega r^2 \pi r dr \tag{2.34}$$

$$dF_{\text{T1}} = 2F\pi r\frac{1}{2}\rho U_\infty^2 4a(1-a)dr \tag{2.35}$$

2.2.3.3 High induction

One of the fundamental assumptions of the BEMT is that flow through a disc is bound within a streamtube. When the axial induction factor, a, is greater than 0.5, this indicates that the flow is reversed in the far wake, cf. Equation 2.9, which contradicts the fundamental assumption of the BEMT that the flow is in an enclosed streamtube. This contradiction is fixed through a high induction correction factor. The high induction correction factor gives a new relationship between the axial induction factor and the thrust. The momentum theory gives the following relationship between thrust coefficient and axial induction factor;

$$C_{\text{T}} = 4aF(1-a) \tag{2.36}$$

One high induction correction factor is the Glauert factor [9] Equation 2.37. It is used when the critical axial induction factor, a_{crit}, is reached, which is typically 0.4.

$$a = \frac{1}{F}[0.143 + \sqrt{0.0203 - 0.6427(0.889 - C_{\text{T}})}] \tag{2.37}$$

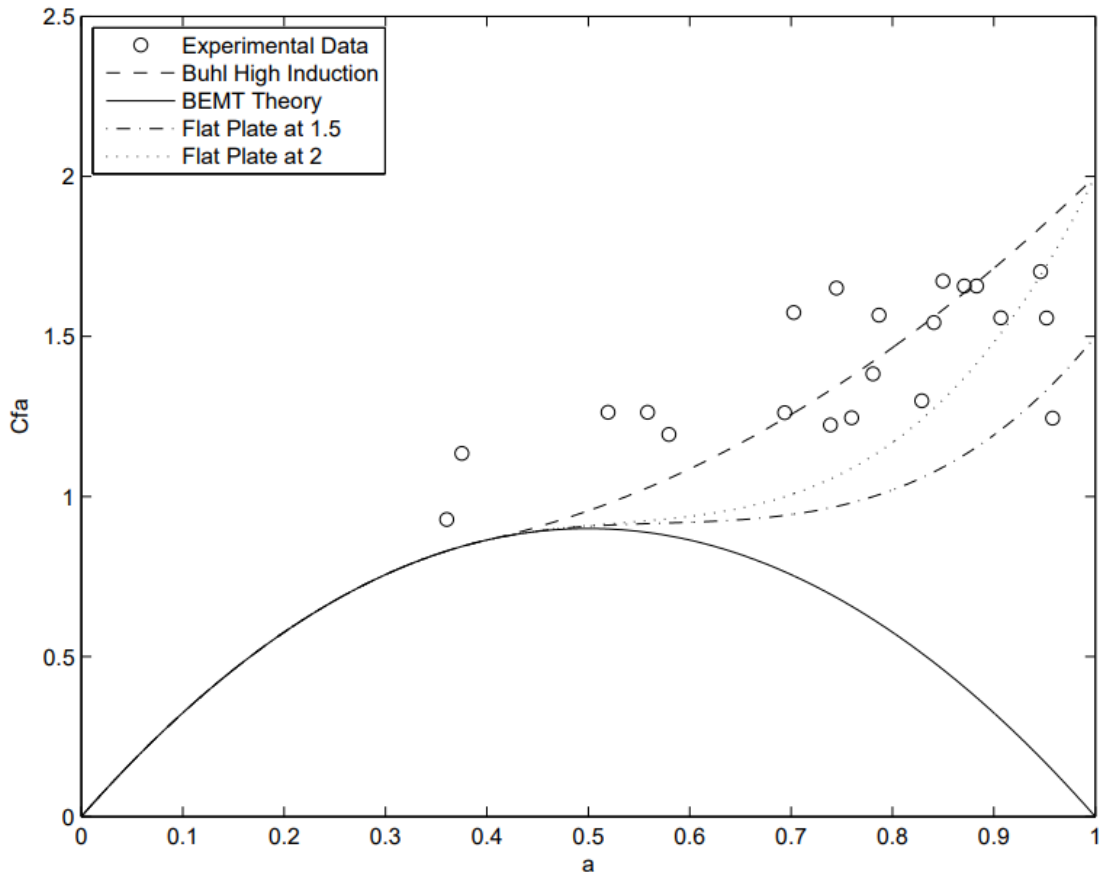

Figure 2.3: Thrust coefficient against axial induction factor for classical momentum theory, Buhl's high induction factor, two proposed induction relations, and experimental data [10].

Near the tip, the high induction correction factors and the tip correction factors are dependent on each other [58]. Buhl [58] modifies Glauert high induction correction factor to incorporate the tip and hub loss effects and is given in Equation 2.38.

$$C_{\mathrm{T}} = \frac{8}{9} + (4F - \frac{40}{9})a + (\frac{50}{9} - 4F)a^2 \tag{2.38}$$

Thrust coefficient against axial induction factor for classical momentum theory, Buhl's high induction factor, two proposed induction relations, and experimental data is plotted in Figure 2.3 [10]. The two proposed induction relations are theoretical solutions of C_T = $C_{T_{MAX}}$ = 1) 1.5 and 2) 2.0 for a flat plate with a_{limit} set to 0.4.
The BEMT numerical model used for the simulations presented in this thesis uses the

classical model up until a critical threshold value which is set to 0.4; for higher values of a, the Buhl correction of Equation 2.38 is implemented.

2.2.4 BEMT input flow fields

There are various flow field configurations available for the BEMT numerical model. Simple flow fields such as uniform velocity "plug flow" or power law have limitations when validating the BEMT results against experimental tests. A flow field which has turbulence and waves gives most accurate and representative results, increasing the robustness of the BEMT. The flow domain in the BEMT is a three-dimensional cuboid running from $\{xmin, ymin, zmin\}$ to $\{xmax, ymax, zmax\}$ with a resolution in each axis determined by the number of x, y, and z points variables. The flow vectors at any point within the flow domain is obtained by linear interpolation [55].
Synthetic turbulence flow fields are created using the Sandia method [59, 60, 61], as described in Section 2.2.4.1. It produces three-dimensional flow fields which are non-physical, but match key statistical properties of real turbulent flows at low computational cost. The flow field turbulence is described using the Von Karman spectrum. The streamwise integral lengthscale is set to 0.2 times the rotor diameter [59, 60, 62, 63], and an anistropic ratio $(\sigma u : \sigma v : \sigma w) = (1.00 : 0.75 : 0.56)$ is used [64].
Including waves in the BEMT input flow field is achieved by firstly calculating the water particle velocities due to the wave, using the Airy wave theory. Then, we simply add the wave flow field to the turbulent flow field. Interaction between waves and currents are second order effects which are strongest at the surface [65]. The interactions have limited effect on flow domain used in the BEMT, thus we ignore it. Care is needed to ensure that both flow field domains are of the same size and have the same number of points in each axis to ensure correct merger. A flow diagram of the methodology for creating BEMT input flow field with turbulence and waves is shown in Figure 2.4. To ensure clarity only two-dimensional slices of the flow field are shown.

2.2.4.1 Synthetic turbulence

Turbulent flow has a significant influence on the peak loads and fatigue life of TSTs [62, 66, 67, 68, 69]. An accurate turbulence model must be used to correctly predict the performance of TST from the BEMT numerical model. Solving governing fluid motion equations for turbulent flow would be computationally expensive and would limit the benefits of the BEMT numerical model. Synthetic turbulence methods produce three-dimensional flow fields that are non-physical, but match statistical properties of real

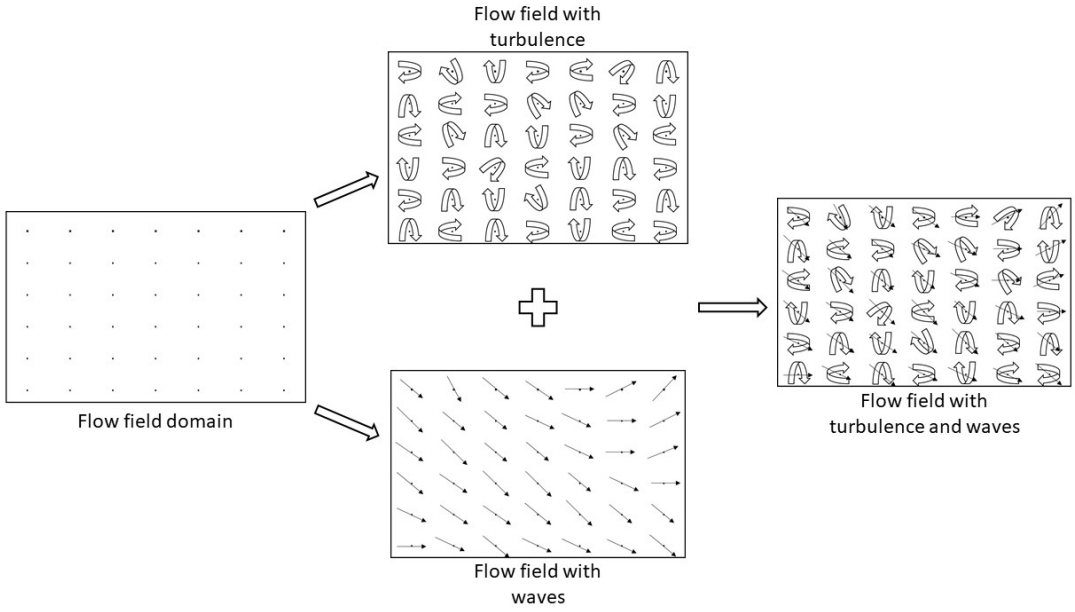

Figure 2.4: A two-dimensional flow diagram of the methodology for creating BEMT input flow field with turbulence and waves.

turbulence at low computational expense [59, 66, 67, 68, 70, 60, 69]. The synthetic eddy and Sandia methods are two common methods for generating synthetic turbulence [70, 60]. The synthetic eddy method was originally developed for the generation of inflow conditions for large eddy simulation [70]. It fills the flow domain with randomly positioned eddies that produce a local velocity. These synthetic eddies are not intended to be realistic representations of physical eddies. Properties, such as magnitude of induced velocity, anisotropy ratios, integral length scales etc, assigned to each eddy are based on measurements from real flows. This will assure that the flow field induced by the eddies will have the same Reynolds stress tensor as the real flow it is based on. Detailed underlying mathematical description of the synthetic eddy method is described by N.Jarrin in his thesis [71].

The Sandia method was originally developed to simulate wind flow fields [60], which has been subsequently extended and applied to tidal stream flow fields [59]. It is a spectral method based on an array whose every diagonal element corresponds to a point in space for which a time-history of turbulence is to be generated. These diagonal elements contains the power spectral densities (PSDs) of turbulence at the corresponding point with randomised phase data; the off-diagonal elements of the array contains cross-spectral

densities to ensure that the turbulent velocity fluctuations are correctly correlated across space. Turbulent flow fields in strong tidal currents are well described by the von Karman spectrum [61], which is used by Togneri *et al* in their analysis of synthetic turbulence [59]. A strength of the Sandia method is that it works well with limited measured data, (i.e., only a PSD distribution and cross-correlation data; an analytic expression for cross-correlation can be implemented where data is unavailable), and any arbitrary spectrum, measured or theoretical. A drawback of the method is that although cross-correlation in space is built into the model, all cross component correlations of velocity will be zero as they are generated independently. Detailed underlying mathematical description of the Sandia method is described by P.Veers [60].

Togneri *et al* [59] compare the Eddy and Sandia synthetic turbulence methods to generate inflow conditions for a BEMT numerical model. Both methods satisfactorily replicate certain statistical properties of real turbulent flow. An issue encountered with the synthetic eddy method was that it produced a flow field whose velocity PSD diverted significantly from that of real flows. They propose a simple modification to permit variable length-scale pseudo-eddies which addresses the issue well [63]. Their simulations indicate that turbine loads are directly proportional to turbulent intensity. They also state that for BEMT simulations using synthetic turbulence the spectral properties of the turbine loads cannot be predicted from knowledge of the corresponding velocity spectra alone.

2.2.4.2 Waves

Due to the location of floating tidal stream turbines (i.e. near the surface of the water), waves have a significant impact on their rotor loads, particularly peak loads. Including waves in the BEMT numerical model input flow fields will allow for quantification of the influence of waves on rotor loads, and consequently their life span. Wave effects are implemented in the BEMT inflow field using linear (Airy) wave theory to give analytic expressions for the wave-induced velocities.

Airy "small amplitude" wave theory

The Airy wave theory, also known as linear wave theory, gives a description of the wave kinematics and dynamics. Based on a simplified approach, it assumes that fluid flow is inviscid, incompressible and irrotational, that the wave height is small compared to the wavelength and water depth, and that the flow field is of uniform depth. Ocean waves are not greatly influenced by viscosity, surface tension, or turbulence and thus a theory derived from idealised two-dimensional fluid flow is justifiable.

A wave of wavelength L and height H in water of depth d, from still water level (SWL), is depicted in Figure 2.5 [11]. η is the water elevation from SWL and m is the wave number. Detailed derivation of the Airy theory is well covered in literature [11, 72], and thus only a few crucial steps will be highlighted here.

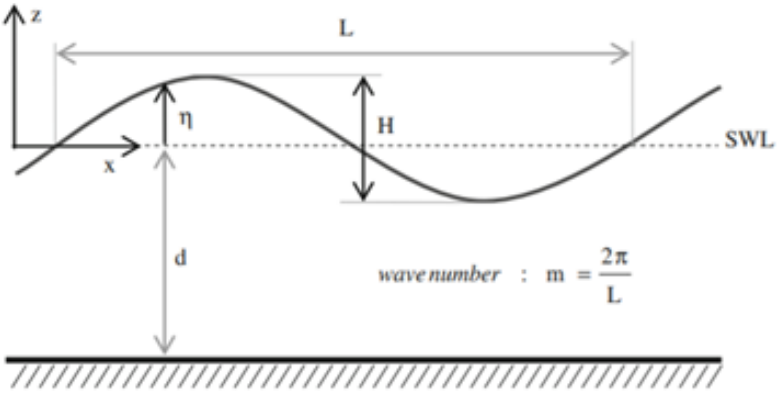

Figure 2.5: Two-dimensional small amplitude wave (Airy wave) theory [11].

Flow potential ϕ, of irrotational flow must obey Equation 2.39. This allows the bottom and free surface boundary conditions to be defined as is written in Equation 2.40 and Equation 2.41.

$$\nabla^2\phi = 0 \tag{2.39}$$

$$\text{At z=-d ...}\frac{\partial\phi}{\partial z} = 0 \tag{2.40}$$

$$\text{At z=0 ...}(\frac{\partial^2\phi}{\partial t^2} + g\frac{\partial\phi}{\partial z}) = 0 \tag{2.41}$$

Deriving from the boundary conditions, the flow potential to be written as,

$$\phi = A\frac{g\cosh m(z+d)}{\omega\cosh md}e^{i(\omega t - mx)} \tag{2.42}$$

where A is the wave amplitude, g is the gravitational constant, z is depth, and ω is wave frequency. Similarly, the water elevation η, can be written as,

$$\eta = -iAe^{i(\omega t - mx)} \tag{2.43}$$

The horizontal and vertical water particle velocities can be calculated from Equation 2.44 and Equation 2.45.

$$u = \frac{\partial \phi}{\partial x} = -iA\omega \frac{\cosh m(z+d)}{\sinh md} e^{i(\omega t - mx)} \tag{2.44}$$

$$w = \frac{\partial \phi}{\partial z} = A\omega \frac{\sinh m(z+d)}{\sinh md} e^{i(\omega t - mx)} \tag{2.45}$$

The water particle accelerations are the time derivatives of those velocities.

$$\dot{u} = \frac{\partial u}{\partial t} = A\omega^2 \frac{\cosh m(z+d)}{\sinh md} e^{i(\omega t - mx)} \tag{2.46}$$

$$\dot{w} = \frac{\partial w}{\partial t} = iA\omega^2 \frac{\sinh m(z+d)}{\sinh md} e^{i(\omega t - mx)} \tag{2.47}$$

Acceleration "added mass" forces

Where there is significant acceleration in the inflow for a submerged body, added mass forces can become significant. Forces exerted on a fully submerged fixed body in oscillatory flow can be described by the Morison equation which is a semi-empirical function [73]. It can be used to estimate the loadings caused by waves on offshore structures, specifically tidal stream turbine rotor blades in this case.

The Morison equation consists of two constituent terms, drag and inertia as shown in Equation 2.48. The drag term accounts for the flow velocity whilst the inertia term accounts for the flow acceleration. Tangential force, $F_{\text{T-inertia}}$, and thrust, $F_{\text{A-inertia}}$, encountered by the rotor blades due to wave accelerations can be calculated using the inertia term. Total turbine tangential force, F_{T}, and thrust, F_{ME}, is the sum of the inertia and drag terms.

$$F_{\text{ME}} = F_{\text{drag}} + F_{\text{inertia}} \tag{2.48}$$

The inertia force per unit length in the wave propagation direction is represented by dF_{inertia} (Equation 2.49). C_{m} is the inertia coefficient (Equation 2.50), A is the cross-sectional area of the rotor blades parallel to the wave flow direction, and u is the local incident velocity.

$$dF_{\text{inertia}} = \rho C_{\text{m}} A \frac{du}{dt} dl \tag{2.49}$$

For non-cylindrical structures, such as rotor blades, the inertia coefficient is made dependent on the added mass coefficient, C_{A} [73, 74, 75]. A_{x} is the cross-sectional area of the rotor blade and M_{A} is the added mass.

$$C_{\mathrm{m}} = 1 + C_{\mathrm{A}} = 1 + \frac{M_{\mathrm{A}}}{\rho A_{\mathrm{x}} dl} \tag{2.50}$$

Theodorsen's theory is used as the basis to calculate the added mass of a rotor blade. Derived from potential flow theory, it describes a thin plate making small amplitude oscillations in both pitch and heave, calculating the lift per unit span. Rotor blades in waves can be compared to Theodorsen's flat plate oscillating in heave if the frame of reference moves with the wave inflow and the blades are fixed at an angle, θ, to the oscillating flow. Fixing the blade angle allows us to replace the chord length with $c\sin(\theta)$. The added mass, $M_{\text{A-axial}}$, for axial oscillatory flow is given by Equation 2.51, similarly the added mass, $M_{\text{A-tangential}}$, for tangential oscillatory flow is given by Equation 2.52.

$$M_{\text{A-axial}} = \rho\pi(\frac{c\sin(\theta)}{2})^2 dl \tag{2.51}$$

$$M_{\text{A-tangential}} = \rho\pi(\frac{c\cos(\theta)}{2})^2 dl \tag{2.52}$$

Combining Equation 2.49, Equation 2.50, and Equation 2.51, Equation 2.52 gives rotor blade thrust, $F_{\text{A-inertia}}$, and tangential force, $F_{\text{T-inertia}}$, due to the inertia "added mass" forces.

$$F_{\text{A-inertia}} = \rho(1 + \frac{\pi(c\sin(\theta))^2}{4A_{\mathrm{x}}})A_{\mathrm{x}}\frac{du}{dt}r \tag{2.53}$$

$$F_{\text{T-inertia}} = \rho(1 + \frac{\pi(c\cos(\theta))^2}{4A_{\mathrm{x}}})A_{\mathrm{x}}\frac{dv}{dt}r \tag{2.54}$$

For a rotor blade element, Equations (2.53) and (2.54) can be written as,

$$dF_{\text{A-inertia}} = \rho(1 + \frac{\pi(c\sin(\theta))^2}{4A_{\mathrm{x}}})A_{\mathrm{x}}\frac{du}{dt}dr \tag{2.55}$$

$$dF_{\text{T-inertia}} = \rho(1 + \frac{\pi(c\cos(\theta))^2}{4A_{\mathrm{x}}})A_{\mathrm{x}}\frac{dv}{dt}dr \tag{2.56}$$

2.2.5 Foil shape & Reynolds number dependence

One of the main strengths of the BEMT numerical model is its low computational demands, and thus care is needed when introducing additional features. Assigning each element in the representation of the rotor is a significant step towards higher-fidelity modelling and can be achieved with a relatively simple and minimal code. A brief description of each step in the BEMT numerical model is included below with emphasis placed on the

additional geometry modelling feature. The core of the BEMT numerical model used in this work follows the same procedure as any other basic BEMT numerical model and thus detailed descriptions of these steps are omitted from this description.
Inclusion of the new geometry modelling feature is achieved in step 2.3. Prior to this step, single lift and drag curves are assigned for all elements for preliminary calculations. Following the calculation of Reynolds number across the rotor blade, unique lift and drag curves are assigned to each element. Two tables are populated prior to the start of the BEMT numerical model, one with lift curves and one with drag curves. Interpolation of these tables take place during step 2.3, which depends on the Reynolds number and geometry of each element. Precisely, the lift and drag curves that populate the tables are lift and drag coefficients against angle of attack. Representation of the interpolation tables is shown in Figure 2.6.

1. Import data
    - Synthetic flow field
    - Rotor blade geometry
2. Loop over blade elements
    1 Assume values for two induction factors: axial *(a)* and tangential *(b)*
    2 Calculate:
        - Relative velocity
        - Angle of attack
        - Reynolds number
    3 ***Assign unique lift and drag curves to each element***
    4 Calculate new values for the induction factors a and b
    5 Feed these values back in as the starting values in 2.1 and repeat the process until a converged solution is obtained
3. Induction factors a and b are read to the post processor which calculates the load for each blade element and any subsequent parameters

Re ($1x10^5$)	Blade profile (e.g % thickness/chord)					
	100	45	30	27	24	20
6	-	-	-	-	-	-
5	-	-	-	-	-	-
4	-	-	-	-	-	-
3	-	-	-	-	-	-
2	-	-	-	-	-	-
1	-	-	-	-	-	-

Figure 2.6: Representation of the interpolation table used in assigning unique lift and drag curves to each element in the BEMT numerical model.

Calculation of Reynolds number

Reynolds Number, which is necessary in assigning accurate unique lift and drag curves to each element in step 2.3 is calculated using Equation 2.57. Calculation of fluid velocity with respect to the rotor blade, Equation 2.58, is required prior to the calculation of Reynolds number. At each time step, Reynolds number for all elements is calculated, stored, and used in the assigning unique lift and drag curves.

The extent that the Reynolds Number changes between time steps across the turbine rotor blade is correlated to the turbulence intensity of the flow field. Higher turbulence flow fields result in greater Reynolds number change which will increase the scatter in the predicted performance results from the BEMT model.

$$Re = \frac{Vc}{\upsilon} \tag{2.57}$$

$$V = \sqrt{U^2 + (\Omega R)^2} \tag{2.58}$$

2.2.6 Alternative numerical models

2.2.6.1 Generalised Actuator Disk Computational Fluid Dynamics

Generalised actuator disk, and computational fluid dynamics are two numerical models which have been combined by [76]. The generalised actuator disk computational fluid dynamics (GAD-CFD) numerical model combines the advantages of both methods, the accuracy of CFD and computational efficiency of GAD (a technique similar to BEMT), without their main limitations. The GAD-CFD numerical model can model individual TSTs and their wakes, but also how these interact with other turbines, modelling the interactions of multiple turbines in farms.

CFD and the governing equations

This model combines a finite volume CFD code from OpenFOAM toolbox [77] for its implementation with additional source terms representing the rotor. The finite volume code solves the Navier-Stokes equations for momentum, incorporating an additional momentum source/sink term to characterise the interaction between the rotor and the fluid flow.
The k-epsilon RNG [78] is implemented as the turbulence model because of work done by [79] in demonstrating good fit with experimental data, and the effectiveness of the k-epsilon RNG model for use with large downstream wakes and their structures [80].

The GAD-CFD method

The properties of each hydrofoil element are determined and leads to the definition of the axial and tangential source terms, S_{a} and S_{t}, which are incorporated into the source terms S_{i} in the momentum equation. Full details of the method are presented by [80].

An extended downwash distribution method

An additional source term which represents the tip vortex induced downwash w, is computed to improve the prediction of the effective tip losses on the flow field. The force deflecting around the foil (S_{a} and S_{t}) is proportional to the downwash force w, and thus is weighted by a downwash distribution function $E(r)$.
[80] describes the use of the elliptical downwash distribution $E(r) \in [0, ..., 1]$, when the normalised distribution is 0 at the hub and 1 at the tip. However, a more robust distribution method is used in the model used in this work, which utilises the foil geometry to generate a more accurate representation of the downwash distribution. This method analytically solves a set of linear equations based on Prandtl's classical lifting line theory [81].
The axial and tangential source terms are given in Equation 2.59 and Equation 2.60. The spanwise coordinate transform is a function of θ, where b/2 is the foil radius and $0 \leq \theta \leq \pi$ and is given in Equation 2.61. $\mathrm{C_L}$ and $\mathrm{C_D}$ are the lift and drag coefficients respectively, ρ is the density, c is the chord length and v_{R} is the resultant velocity.

$$S_{\mathrm{a}} = dF_{\mathrm{A}} = 0.5\rho|v_{\mathrm{R}}|^2 c(C_{\mathrm{L}}\sin(\varphi) + C_{\mathrm{D}}\cos(\varphi)dr \tag{2.59}$$

$$S_{\mathrm{t}} = dF_{\mathrm{T}} = 0.5\rho|v_{\mathrm{R}}|^2 c(C_{\mathrm{L}}\cos(\varphi) - C_{\mathrm{D}}\sin(\varphi)dr \tag{2.60}$$

$$y = -\frac{b}{2}\cos(\theta) \tag{2.61}$$

The elliptical downwash distribution as a function of theta is given in Equation 2.62.

$$\Gamma(\theta) = \Gamma_0 \sin(\theta) \tag{2.62}$$

It can be solved using a Fourier sine series to represent the distribution along a fixed length foil. Thus, it can be presumed generally that:

$$\Gamma(\theta) = 2bv_\infty \sum_{1}^{n} A_\mathrm{n} \sin(n\theta) \tag{2.63}$$

where the quantity of N terms defines the required accuracy of the solution, and coefficients A_n (where $n = 1, ..., N$) are to be solved. However, the A_n's must agree with Prandtl's lifting line equation, Equation 2.64, where it is evaluated at a given spanwise location θ_0.

$$\alpha(\theta_0) = \frac{2b}{\pi c(\theta_0)} \sum_{1}^{N} A_\mathrm{n} \sin(n\theta) + \alpha_{\mathrm{F_L{=}0}}(\theta_0) + \sum_{1}^{N} nA_\mathrm{n} \frac{\sin(n\theta_0)}{\sin(\theta_0)} \tag{2.64}$$

Derived from the foil section geometry, b, $c(\theta_0)$, and $\alpha_{\mathrm{F_L{=}0}}(\theta_0)$ are all known values. Only the A_n's need to be determined. At a given spanwise location, specified θ_0, Equation 2.64 is one algebraic equation with N unknowns, A_1, A_2, ..., A_n. The distribution of the downwash $(\Gamma(\theta))$ can be calculated by substituting the A_n's in Equation 2.63 once the A_n coefficients are determined.

The source term S_i is appended to the momentum equation and defined thus:

$$S_\mathrm{i} = S_\mathrm{a}\hat{v}_\mathrm{ai} + S_\mathrm{t}\hat{v}_\mathrm{ti} + S_\mathrm{v}\hat{v}_\mathrm{wi} \tag{2.65}$$

as defined in Equation 2.59 and Equation 2.60, the scalar terms S_a and S_t are the magnitude of the kinetic energy per unit volume in the axial and tangential directions. S_v is the additional downwash force, $\hat{v}_\mathrm{a}$ and $\hat{v}_\mathrm{t}$ are the axial and tangential unit vectors respectively, and $\hat{v}_\mathrm{w}$ is the unit vector normal to the plane defined by $\hat{v}_\mathrm{a}$ and $\hat{v}_\mathrm{t}$.

Combining the downwash distribution function with the predicted axial and tangential forces gives the downwash term:

$$S_\mathrm{i} = S_\mathrm{a}\hat{v}_\mathrm{ai} + S_\mathrm{t}\hat{v}_\mathrm{ti} + E(r)(S_\mathrm{a}\hat{v}_\mathrm{ai} + S_\mathrm{t}\hat{v}_\mathrm{ti}) \tag{2.66}$$

which simplifies and reduces the computational cost of the implementation.
From Equation 2.66, power and thrust is determined by:

$$T = \sum_{i=0}^{N} S_{\mathrm{a}} \hat{v}_{\mathrm{ai}} Vol_{\mathrm{i}} \rho \tag{2.67}$$

$$P = \sum_{i=0}^{N} S_{\mathrm{t}} \hat{v}_{\mathrm{ti}} Vol_{\mathrm{i}} \rho r \omega \tag{2.68}$$

where $\mathrm{Vol_i}$ is the volume of cell, n is the set of cell indices, and i bounded by the flow domain associated with the rotor.
Further model refinements have been made which include tip radius treatment and radially changing foil sections, described in detail by [76].

2.2.6.2 Vortex Particle Method

One of BEMT's most significant simplifications is the use of an assumed form for the loss of momentum downstream of the turbine, as well as the assumption of no interaction between the fluid in the streamtube of the turbine and the broader flow field. This means that it is impossible to use BEMT simulations to predict details of the wake behind the TST. The vortex particle method (VPM), in contrast to BEMT, resolves the physics of the flow field and can therefore be used to simulate both TSTs and their wakes with relatively little increase in computational cost.

Vortex Particle Method

The flow field is discretised into vorticity carrying particles in the unsteady Lagrangian Vortex method [82, 83, 84]. The Navier-Stokes equations in their velocity and vorticity $(\boldsymbol{u}, \boldsymbol{\omega})$ formulations are used as the governing equations, along with the incompressibility condition.

$$\boldsymbol{\nabla . u} = \mathbf{0} \tag{2.69}$$

$$\frac{\boldsymbol{D\omega}}{\boldsymbol{Dt}} = (\boldsymbol{w . \nabla})\boldsymbol{u} + \boldsymbol{v \Delta w} \tag{2.70}$$

where $\boldsymbol{u}$ is the velocity field, $\boldsymbol{\omega} = \boldsymbol{\nabla} \wedge \boldsymbol{u}$ is the vorticity field, and $\boldsymbol{v}$ is the kinematic viscosity. The transposition of the momentum equation into the velocity-vorticity formulation is given in Equation 2.70. The first term on the right-hand side, $(\boldsymbol{\omega . \nabla})\boldsymbol{u}$, represents the stretching and the second term, $\boldsymbol{v \Delta \omega}$, the diffusion. The fluid domain is discretised into

N_p particles, with each particle, i, represented by its position $\boldsymbol{X}_i$, vortical weight $\boldsymbol{\Omega}_i$, and volume $\boldsymbol{V}_i$. Equation 2.71 is a displacement equation for the i^{th} particle, integrated using regular time stepping schemes that describes the particles' transport over time.

$$\frac{d\boldsymbol{X}_i}{dt} = \boldsymbol{u}(\boldsymbol{X}_i) = \boldsymbol{U}_i \tag{2.71}$$

The evolution of the vorticity carried by each particle $\boldsymbol{i}$, is described by the discretisation of the Navier-Stokes Equation 2.70. Treatment of the stretching term is detailed by [85], and the diffusion term by [86, 87].

$$\frac{d\boldsymbol{\Omega}_i}{dt} = \underbrace{(\boldsymbol{\Omega}_i.\boldsymbol{\nabla})\boldsymbol{U}_i}_{\text{Stretching term}} + \underbrace{\boldsymbol{v}|\boldsymbol{\Delta w}|_{X=X_i}\boldsymbol{V}_i}_{\text{Diffusion term}} \tag{2.72}$$

Helmholtz decomposition of the velocity field, Equation 2.73, is a crucial part of the Lagrangian Vortex method. There are three velocity components, rotational $\boldsymbol{u}^{\psi}$, potential $\boldsymbol{u}^{\phi}$, and upstream $\boldsymbol{u}_{\infty}$.

$$\boldsymbol{u} = \underbrace{\boldsymbol{\nabla} \wedge \boldsymbol{\psi}}_{\boldsymbol{u}^{\psi}} + \underbrace{\boldsymbol{\nabla}\boldsymbol{\phi}}_{\boldsymbol{u}^{\phi}} + \boldsymbol{u}_{\infty} \tag{2.73}$$

The rotational velocity component $\boldsymbol{u}^{\psi}$ accounts for the particle-to-particle interactions, and the component $\boldsymbol{U}^{\psi}$ is the discrete solution of the continuity equation by applying the Helmholtz decomposition (Equation 2.73) into the definition of vorticity.

$$\boldsymbol{\Delta\psi} = -\boldsymbol{w} \tag{2.74}$$

At any point M of the fluid domain, the solution of Equation 2.74 is given by the Biot-Savart Law.

$$\boldsymbol{U}^{\psi}(\boldsymbol{M}) = \frac{\mathbf{1}}{\mathbf{4\pi}} \sum_{\boldsymbol{i=1}}^{\boldsymbol{N_p}} \frac{\boldsymbol{MX}_i}{|\boldsymbol{MX}_i|^{\mathbf{3}}} \wedge \boldsymbol{\Omega}_i \tag{2.75}$$

The potential velocity component $\boldsymbol{u}^{\phi}$ accounts for the influence of a solid body: in this case, the presence of the turbine rotor blades [82]. Derived from the scalar potential ϕ, the potential velocity component must satisfy:

$$\boldsymbol{\Delta\phi} = \mathbf{0} \tag{2.76}$$

Equation 2.76 is obtained by substituting the velocity decomposition, Equation 2.73, into the continuity Equation 2.69.
The upstream velocity component, as the name suggests, represents the upstream velocity field at infinity, and is generally treated as a constant vector, although a Synthetic Eddy method is used to model the ambient turbulence in this VPM model.
The time integration scheme uses a second order Runge-Kutta implementation. The second order Runge-Kutta is preferred to the fourth order version due to the computational efficiency whilst still producing reasonable accuracy.

Vortex Line Method

Within the VPM model of the flow field, the hydrodynamic forces due to the interaction between the rotor blades and the flow are characterised using the vortex line method (VLM). This method is based on generalised lifting line theory. The method is restricted to blade geometries that are slender and have minimal curvature, showing little radial flow interactions. The flow is assumed to be incompressible as the local onset flow velocities are much smaller that the speed of sound; this is consistent with the assumptions underpinning VPM. Displacements effects are also not included in the model. The flow domain can be represented by Equation 2.77, with only the vorticity effects needing to be modelled.

$$\boldsymbol{\sigma = (\vec{\nabla}.\vec{u}) = 0} \tag{2.77}$$

Figure 2.7 shows the resulting flow model [12]. Included in the Figure are vortex lines which are part of a vortex ring as vortex tubes cannot have free ends (Kelvin's circulation theorem) [88, 12].

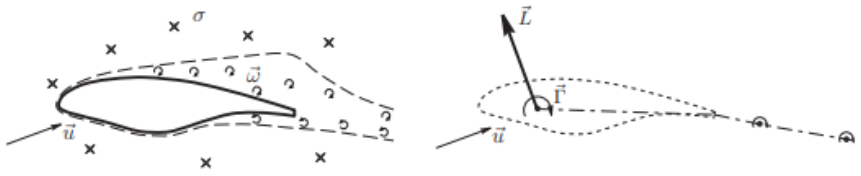

Figure 2.7: Vortex particle method; lifting line theory flow field model [12].

The total external force $\boldsymbol{F}$ exerted on a body by the fluid is given by:

$$\boldsymbol{\vec{F} = \iiint \rho(\vec{u}x\vec{\omega})dV} \tag{2.78}$$

where the fluid vorticity $\boldsymbol{\omega}$ is defined by:

$$\vec{\omega} = \vec{\nabla} x \vec{u} \tag{2.79}$$

For a vortex line element $\boldsymbol{dl}$, Equation 2.77 transforms into lift $\boldsymbol{dL}$:

$$d\vec{L} = \rho(\vec{u} x \vec{\Gamma}) dl = \rho \Gamma (\vec{u} x d\vec{l}) \tag{2.80}$$

The direction of the lumped volume vorticity distribution is used as the definition for the positive vortex line element direction.
The velocity field associated with the volume distributed vorticity is given by:

$$\vec{u}_{\mathrm{w}}(\vec{x}_{\mathrm{p}}) = \frac{1}{4\pi} \iiint \frac{\vec{w} x \vec{r}}{r^3} dV \tag{2.81}$$

where $\vec{x}_{\mathrm{p}}$ is the evaluation point, and:

$$\vec{r} = \vec{x}_{\mathrm{p}} - \vec{x} \tag{2.82}$$

$$r = \sqrt{\vec{r}.\vec{r}} = |\vec{r}| \tag{2.83}$$

The Biot-Savart law is used to compute an equivalent formula for the velocity induced by a volume of vorticity lumped into a vortex line element:

$$\vec{u}_{\Gamma}(\vec{x}_{\mathrm{p}}) = \frac{-1}{4\pi} \int \Gamma \frac{\vec{r} x d\vec{l}}{r^3} \tag{2.84}$$

2.2.6.3 Actuator line

The actuator line (AL) numerical model is an unsteady method which represents each blade as a line acting as a momentum source/sink embedded within a domain where the governing flow equations are solved using a CFD solver. As with many other tidal turbine numerical models, the AL method was originally developed for wind turbines [89]. The AL numerical model captures discrete blade effect such as tip vortices and wake structure by embedding a discrete representation of the rotor blade in the flow domain CFD solver. The rotor blades are replaced by point forces which are distributed along the span of each rotor blade. The point forces are usually computed along the centre of pressure of the blade. The flow domain is sampled at each timestep around the point forces for selection of lift and drag polars. The polars are used to compute the resulting blade loads that are

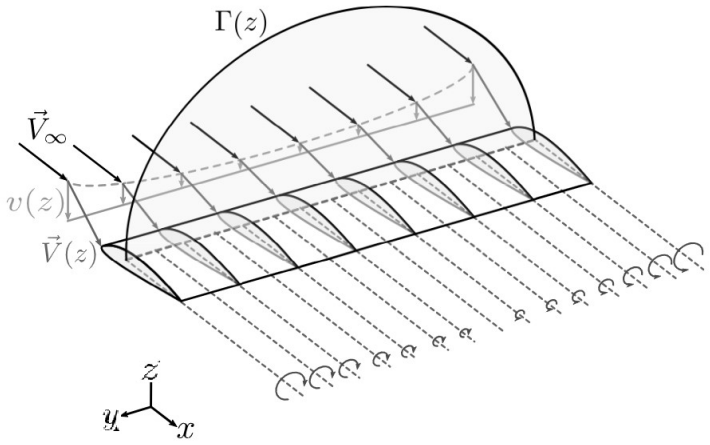

Figure 2.8: Schematic of Prantl's classical lifting line theory on an aerofoil.

then reimposed back into the flow domain. The CFD solver then updates the flow domain and proceeds to the next timestep. A numerical model rotates the rotor blades through the flow domain without resolving the physical geometry of the blades, offering substantial computational cost saving compared to blade resolved CFD numerical models.

Prandtl lifting line theory Prandtl lifting line theory is a common method used to calculate the point forces along the span of each rotor blade [90, 91, 92]. Alternatively, AL numerical models can also use a similar process to the BEMT to resolve the blade forces from the lift and drag polars.

The Prandtl's lifting line theory combines the concepts of circulation and the Kutta-Joukowski theory. The theory assumes incompressible and inviscid flow, and models the wing as a single bound vortex line located at 25% chord position. The flow over a finite, high-aspect-ratio wing is represented by a sheet of semi-infinite vortices of variable strength, originating from the locus of aerodynamic centres of the aerofoil, as shown in Figure 2.8. The circulation of the aerofoil is assumed to vary as a function of the spanwise location. The transformed coordinate of the spanwise location y is given by Equation 2.85, where y is spanwise location, and s is half the span of the wing. The spanwise lift distribution assumption is shown in Figure 2.9

$$y = s\cos(\theta) \tag{2.85}$$

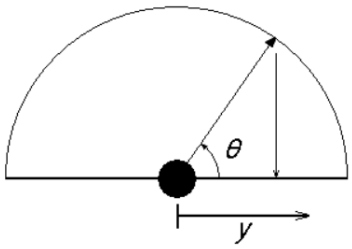

Figure 2.9: Schematic of spanwise lift distribution of Prandtl's lifting line theory.

The infinite Fourier sine series solution to Prantdl's lifting line equation is used to approximate the variation in section circulation along the span of a finite wing, $\boldsymbol{\Gamma(\theta)}$.

$$\boldsymbol{\Gamma(\theta) = 4sV_\infty \sum_{n=1}^{\infty} A_n \sin(n\theta)} \tag{2.86}$$

Based on the definition of the lift coefficient and the Kutta-Joukowski theorem, a relationship between the section circulation, $\boldsymbol{\Gamma(\theta)}$, and the section lift coefficient, $\boldsymbol{C_L(\theta)}$, is given as,

$$\boldsymbol{C_L(\theta) = \frac{2\Gamma(\theta)}{V_\infty c(\theta)}} \tag{2.87}$$

Aerofoils at small angle of attacks can be assumed to have lift that can be closely approximated as a linear function of angle of attack. The section lift coefficient, $\boldsymbol{C_L(\theta)}$, can be approximated by,

$$\boldsymbol{C_L(\theta) = C_{L,\alpha}(\alpha_e(\theta) - \alpha_{0L})} \tag{2.88}$$

where $\boldsymbol{C_{L,\alpha}}$ is the aerofoil section lift slope, $\boldsymbol{\alpha_e(\theta)}$ is the effective local angle of attack, and $\boldsymbol{\alpha_{0L}}$ is the zero lift angle of attack. Equation 2.87 and Equation 2.88 are combined to give Prandtl's lifting line equation applying on each lifting surface,

$$\boldsymbol{\frac{2\Gamma(\theta)}{V_\infty c(\theta) C_{L,\alpha}} - \alpha_e(\theta) = -\alpha_{0L}} \tag{2.89}$$

Once the effective local angle of attack, $\boldsymbol{\alpha_e(\theta)}$, is calculated, the Prandtl's lifting line equation can be solved.

2.2.6.4 Computational fluid dynamics blade resolved

Computational fluid dynamics (CFD) blade resolved (BR) numerical models are the most computationally intensive of all numerical models. It is the most detailed method to investigate unsteady aerodynamic behaviour of flow round tidal turbine rotor blades and the

generated wake [92, 93]. The BR CFD numerical model accurately describes the geometry of the rotor blades in its simulations. The rotor blades and any other physical objects, e.g. nacelle, tower, are explicitly represented in a domain that is discretised with a mesh. Turbulence is modelled by using either unsteady Reynolds average Navier-Stoke (URANS) model [94, 95], large Eddy simulations (LES) [96], or detached Eddy simulation (DES) [97], as direct numerical simulations (DNS) to analyse tidal turbines is still not feasible. Many options are available to model turbulence in BR CFD simulations, with the most appropriate option depending on the complexity of the problem, computational cost, and flow conditions. A CFD solver is used to simulate the flow through the flow domain with the physical surfaces, i.e. rotor blades, nacelle, are modelled as boundaries. Again, many CFD solvers options exist, with the best option depending on the specific simulation parameters.

Governing equations The continuity, momentum, and energy are the fundamental governing equation of fluid dynamics, describing fluid motion, which forms the foundations of CFD numerical models.
Conservation of mass;

$$\boldsymbol{\nabla \cdot u = 0} \tag{2.90}$$

Conservation of momentum, derived from Newton's second law: $\boldsymbol{F = ma}$;

$$\frac{\boldsymbol{\partial u}}{\boldsymbol{\partial t}} + \boldsymbol{\nabla \cdot (uu) = -\nabla p + \nabla \cdot (v \nabla u) + f} \tag{2.91}$$

Conservation of energy, derived from the first law of thermodynamics;

$$\frac{\boldsymbol{\partial}}{\boldsymbol{\partial t}}[\boldsymbol{\rho}(\boldsymbol{e} + \frac{\boldsymbol{v^2}}{\boldsymbol{2}})] + \boldsymbol{\nabla \cdot [\rho}(\boldsymbol{e} + \frac{\boldsymbol{v^2}}{\boldsymbol{2}})\boldsymbol{\vec{v}}] = \boldsymbol{\rho \dot{q}} - \frac{\boldsymbol{\partial (up)}}{\boldsymbol{\partial x}} - \frac{\boldsymbol{\partial (vp)}}{\boldsymbol{\partial y}} - \frac{\boldsymbol{\partial (wp)}}{\boldsymbol{\partial z}} + \boldsymbol{\rho \vec{f} \cdot \vec{V}} \tag{2.92}$$

2.3 Discussion & Conclusions

In this chapter, the BEMT numerical model used throughout this thesis has been described in detail. Firstly, a comprehensive literature review of the development and current BEMT numerical models has been presented, which includes studies of correction factors, blade hydrodynamic properties, dynamic loads, unsteady flow conditions, blockage ratio, and VATT. The underlying equations used in the steady-state BEMT are presented, which are

Table 2.2: Summary of the strengths and limitations of various numerical models used for prediction of tidal stream turbines.

Numerical model	Strengths	Limitations	Computational demands	Physical representation
BEMT	The BEMT numerical model is the most computationally efficient model which lends itself to evaluation of tidal stream turbines in the early development stages and investigation of a wide range of flow cases	Does not model physical fluid flow and thus cannot simulate tip vortices and wakes	1	4
GAD-CFD	The GAD-CFD model offers the benefits of both CFD and GAD methods, the accuracy of CFD and the computational efficiency of GAD without their main limitations. The GAD-CFD model can simulate the interactions of multiple turbines in farms	The flow domain is solved using a CFD solver which is computationally intensive especially for more complex flows with turbulence and waves	3	2
VPM	The VPM model resolves the physics of the flow field and can therefore simulate rotor blade loads and their wakes with minimal computational cost	The treatment of the boundary conditions and the distortion of particle distribution are an intrinsic limitations	2	3
AL	The AL method gives detail of tip vortices and wake structures without fully describing the rotor blades (representation with point forces) which gives substantial computational saving compared to BR CFD	The blades are not physically represented which is often a source of error in predicting rotor performance	3	2
BR CFD	The BR CFD method accurately describes the geometry of the rotor blades in its simulations, giving the most detail of the aerodynamic behaviour of flow around the rotor blades and the generated wake	It is the most computational intensive of all numerical models	4	1

Computational demands
1. Very low
2. Low
3. High
4. Very high

Physical representation
1. Very detailed
2. Detailed
3. Inaccurate
4. Very inaccurate

derived from two models; momentum theory and blade element theory. Following on from the steady-state model, a description of the transient model and the various control schemes are given. Details of the correction factors used in the BEMT numerical model in this thesis are then given, which includes hub, tip and high induction.

An important feature of the BEMT numerical model used in this thesis is its ability to assign each element an unique lift and drag curve based on its foil shape and Reynolds number. The relatively simple and computationally inexpensive procedure used to achieve this is described. Another important component of the transient BEMT numerical model is the input flow field. An accurate flow field must be used to correctly predict the performance of TSTs from the BEMT numerical model. The synthetic turbulence flow fields are produced from the Sandia method which creates flow fields that are non-physical but match statistical properties of real turbulence at low computational costs. The Airy wave theory is used to model the wave kinematics and dynamics. The wave flow field is combined with the synthetic turbulence flow field to produce a single input flow field to the BEMT numerical model which includes turbulence and waves. An important consequence of waves and turbulence on rotor blades are the acceleration "added mass" forces. Details of how the acceleration forces are accounted for in the BEMT numerical model are given.

In the last section of this chapter, four alternative numerical models which are used to model TSTs are presented; GAD-CFD, VPM, AL, and BR CFD. The strengths and limitations of each numerical model are summarised in Table 2.2. The BEMT numerical model is the focus of this section of the thesis and used as a tool for the development of the RRES in the later section due its ability to predict accurate loads and performance of a rotor blade in a very efficient manner (i.e. quickly). It is particularly advantageous in early developments of tidal stream turbines where design changes are numerous. In more mature projects when they are in the stages of developing tidal farms, other numerical models which model the fluid are needed to simulate the interactions between individual tidal stream turbines.

Chapter 3

Blade Element Momentum Theory - Case studies

The accuracy and robustness of the BEMT numerical model is validated by comparison against empirical data from physical experiments and other numerical models. Comparison is made against two scale models of prototype tidal stream turbines and three important lab-scale investigations of more general turbine geometries in a wide variety of flow conditions.

Anonymisation of data

Coefficient of power, C_P, is the ratio of output power produced from the available input power, given in Equation 3.1; where P is the hydrodynamic power produced by the rotor, A_R is the rotor swept area, and U_c is the free stream flow velocity. The specific data on power and thrust for the Magallanes ATIR and Sabella D12 (see Sections 3.1.2 and 3.1.3) turbines are commercially sensitive. To anonymise the data, therefore, all C_P values on all figures relating to these turbines are scaled against a single value, the optimum C_P, and all C_T values are scaled against C_T for the same case. Coefficients scaled in this way are denoted $C_P{}^*$ and $C_T{}^*$.

$$C_P = \frac{P}{\frac{1}{2}\rho A_R {U_c}^3} \tag{3.1}$$

$$C_{P,max} = C_P(TSR = TSR_{optimum}) \tag{3.2}$$

$$C_P{}^* = \frac{C_P}{C_{P,max}} \tag{3.3}$$

Coefficient of thrust, C_T, similar to coefficient of power, is calculated using Equation 3.4, where F_T is rotor thrust. C_T is normalised by dividing by the thrust coefficient, $C_T{}^+$ (Equation 3.5), value which corresponds to the maximum coefficient of power, $C_{P,max}$ (Equation 3.2), value used in normalising C_P.

$$C_T = \frac{F_T}{\frac{1}{2}\rho A_R U_c{}^2} \tag{3.4}$$

$$C_T{}^+ = C_T(TSR = TSR_{optimum}) \tag{3.5}$$

$$C_T{}^* = \frac{C_T}{C_T{}^+} \tag{3.6}$$

Tip speed ratio is defined as the ratio of the tangential speed at the tip of the rotor blade against the free stream flow velocity.

$$TSR = \frac{\Omega R}{U_c} \tag{3.7}$$

3.1 Turbine description

The important detail of the tidal turbines used in the BEMT numerical model case studies will be presented in this section. These details will include rotor blade profile, including their lift and drag polars.

3.1.1 Oxford

The tidal turbine Oxford blind test is being conducted and funded by the UK's EPSRC and Supergen ORE Hub [98]. Participants were invited to take part in the blind prediction exercise of a flume-scale rotor geometry, where details of the test campaign and rotor design were released, but performance data were withheld until the end of the exercise. The main objectives of the project were to improve accuracy and confidence of modelling techniques, and quantify modelling errors under different flow conditions. A large experimental test campaign of a highly instrumented tidal turbine rotor in turbulent and wave flow conditions was conducted to provide the underlying data. The first stage is concerned with steady flow conditions with low and elevated turbulence (3.1%) [99]. A second stage, concerned with unsteady flow including waves is planned but the laboratory

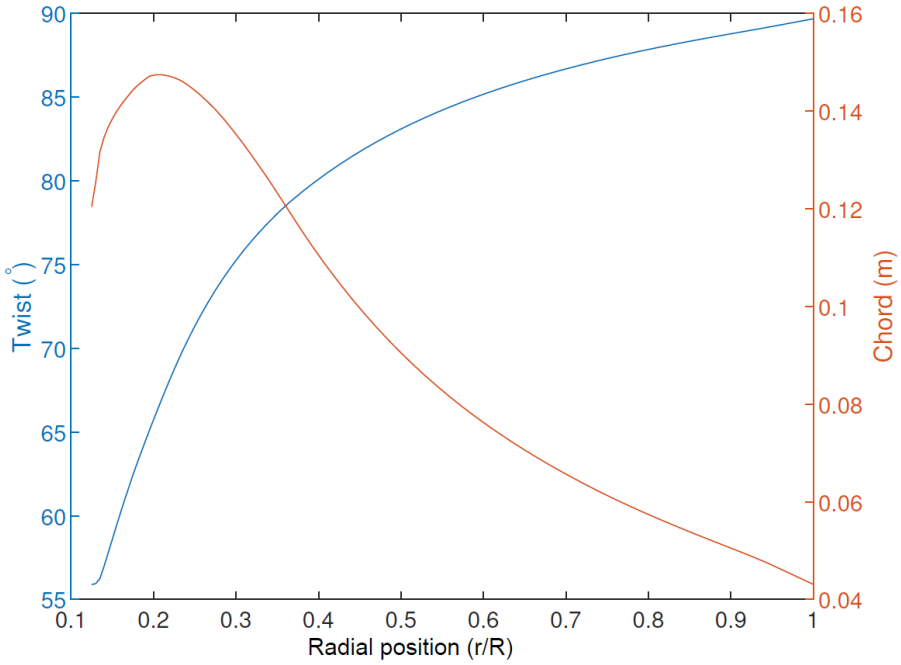

Figure 3.1: Plot of Oxford rotor blade twist and chord against radial position.

results were not complete in time to present here.

The Oxford "benchmark project" tidal turbine has three rotor blades of 1.6m diameter. The rotor blades have in-blade sensing, (strain gauges are located at six radial locations in both edgewise and flapwise direction), to measure spanwise loading distribution which is critically important to achieve Reynolds number independence. Additionally, blade root bending sensors are located on the root of each rotor blade to measure individual loads. A torque and thrust transducer is located upstream of the front bearing to measure accurate total turbine torque and thrust. The rotor angular velocity and position is measured by a rotary encoder.

A single hydrofoil, the NACA 63-415 is chosen for the rotor blade profile. Using a constant profile across the blade radius will simplify the modelling process. The twist and chord distribution along the benchmark rotor blade is visualised in Figure 3.1. A summary and complete details of twist and chord distribution for the blades are given in Table A.1 and Table A.2 respectively in Appendix A. The source data is available from [98].

Each rotor blade is represented by 176 radial elements of 0.004m length in the BEMT numerical model. The polars used were lift and drag provided by the project co-ordinators, and are given in Table A.3 in Appendix A. The lift and drag polars are plotted against

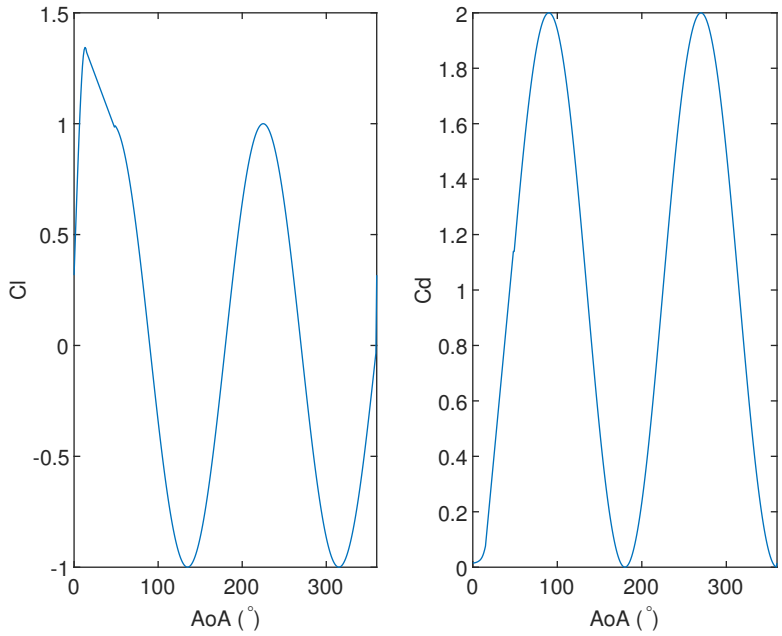

Figure 3.2: Plot of polars of the hydrofoil NACA 63-415 at Reynolds number of 288,888 and turbulence intensity of 0.01% used in for the benchmark cases.

360° angle of attack (AoA) in Figure 3.2. No interpolation of polars relative to Reynolds number or blade geometry is done (i.e. single lift and drag data is used for all elements).

3.1.2 Magallanes ATIR

The Magallanes ATIR is a commercial floating tidal stream turbine structure which at full-scale has two coaxial three-bladed turbines [100, 13]. In the laboratory and numerical model only one turbine is tested. Figure 3.3 shows a photo of the physical laboratory scale turbine used for experimental testing. The chord and twist distribution along the radial length of the Magallanes ATIR rotor blade is plotted in Figure 3.4. The chord is normalised by dividing all chord lengths by the maximum chord length. This is done to protect the commercial sensitivity of the rotor blade. Table A.4 in Appendix A gives the normalised chord and twist distribution along the radial length of the Magallanes ATIR rotor.
In the absence of laboratory lift and drag data, the XFOIL tool version 6.96 [2] and the flat plate theory [101] are used to produce the lift and drag polars. The XFOIL tool is used to produce lift and drag curves for angle of attacks between -5° and 15°, with the remainder of the 360° angle of attack being produced by the flat plate theory. The lift and drag

Figure 3.3: Photo of the physical laboratory scale Magallanes ATIR turbine used for experimental testing.

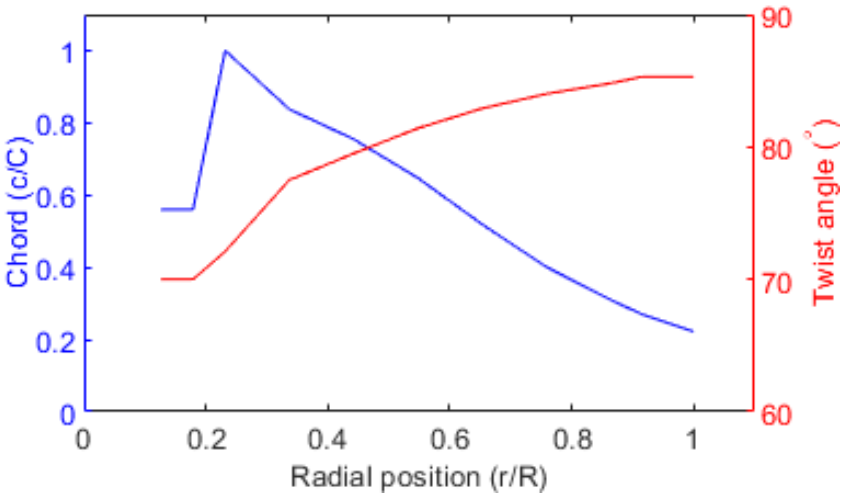

Figure 3.4: The chord and twist distribution along the radial length of the Magallanes ATIR rotor blade.

coefficients of a flat plate are calculated using Equations 3.8 and 3.9 respectively [101]. This is the procedure used for all consequent lift and drag polars that is produced in this thesis.

$$C_{\mathrm{L,FP}} = sin(2\alpha) \tag{3.8}$$

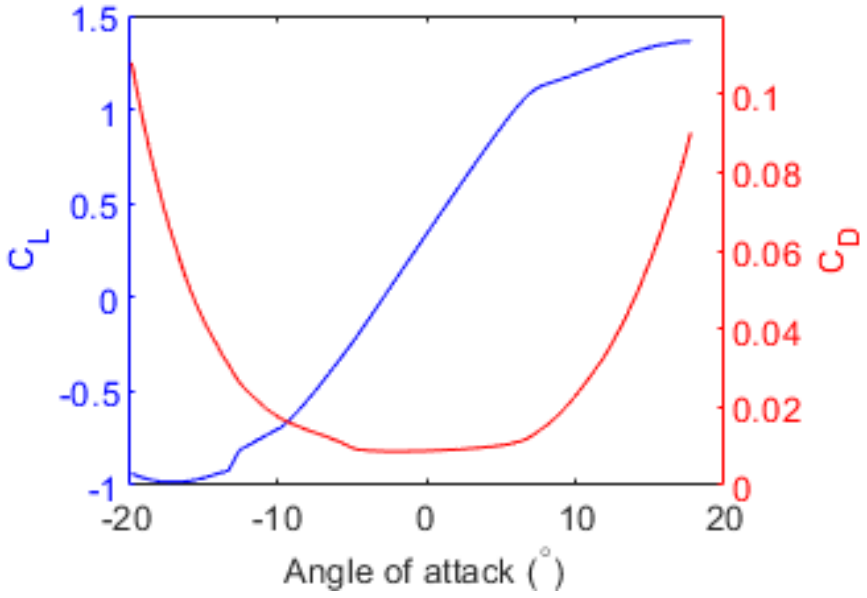

Figure 3.5: Lift and drag coefficient against angle of attack for the NACA-63(3)418 aerofoil at a Reynolds number of $\mathbf{5 \times 10^5}$ used in the numerical modelling of the Magallanes ATIR turbine, produced by the XFOIL tool [2] and flat plate theory.

$$C_{D,FP} = 2sin^2(\alpha) \tag{3.9}$$

The profile of the Magallanes ATIR rotor blades are based on the NACA-63(3)418 aerofoil. Lift and drag polars against angle of attack for the ATIR rotor blade are plotted in Figure 3.5. A Reynolds number of $\mathbf{5 \times 10^5}$ is used as it is the average value across all laboratory tests. The summary of the polars for angle of attack of 0-15° are given in Table A.5 in Appendix A. Figure 3.6 shows a selection of C_L and C_D curves used in the improved BEMT numerical model for the Magallanes ATIR case studies.

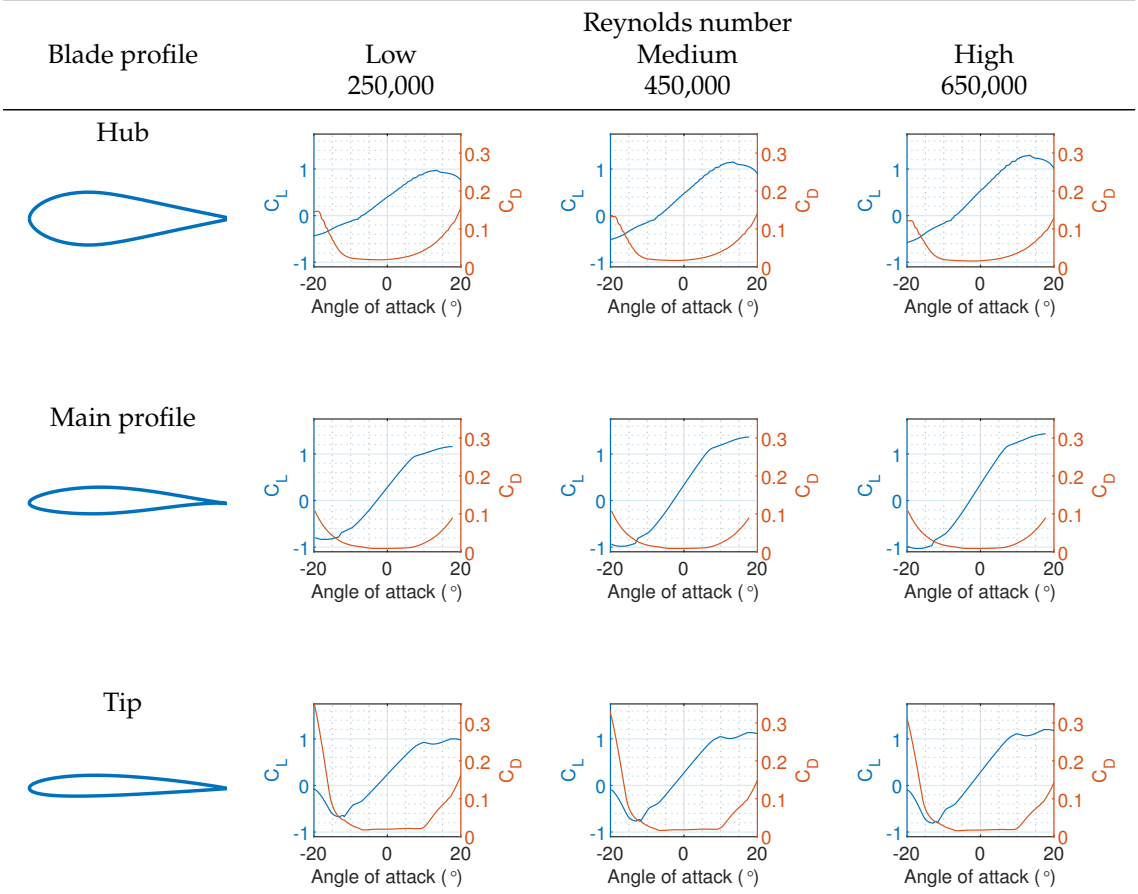

Figure 3.6: Selection of C_L and C_D curves used in the improved BEMT numerical model in the Magallanes ATIR steady-state case study.

3.1.3 Sabella D12

The Sabella D12 is a 5 bladed seabed mounted tidal stream turbine. A picture of the proposed design is shown in Figure 3.7[13]. The chord and twist distribution along the radial length of the Sabella D12 rotor blade is shown in Figure 3.8. The chord is normalised by dividing all chord lengths with the maximum chord, as was done with the Magallanes ATIR to protect the commercial sensitivity of this rotor blade. Table A.6 in Appendix A gives the normalised chord and twist distribution along the radial length of the Sabella D12 rotor.

The Sabella D12 rotor blades are based on the NACA-63(3)418 aerofoil profile. Lift and

drag data for this profile at a Reynolds number of $\mathbf{2.5 \times 10^5}$ was produced using the XFOIL tool version 6.96 [2] for angle of attacks of -17.5-17.5°, and flat plate theory for the remaining angle of attack 0-360°, and is plotted in Figure 3.9. Table A.7 in Appendix A gives the summary of the polars for angle of attacks of 0-15°.

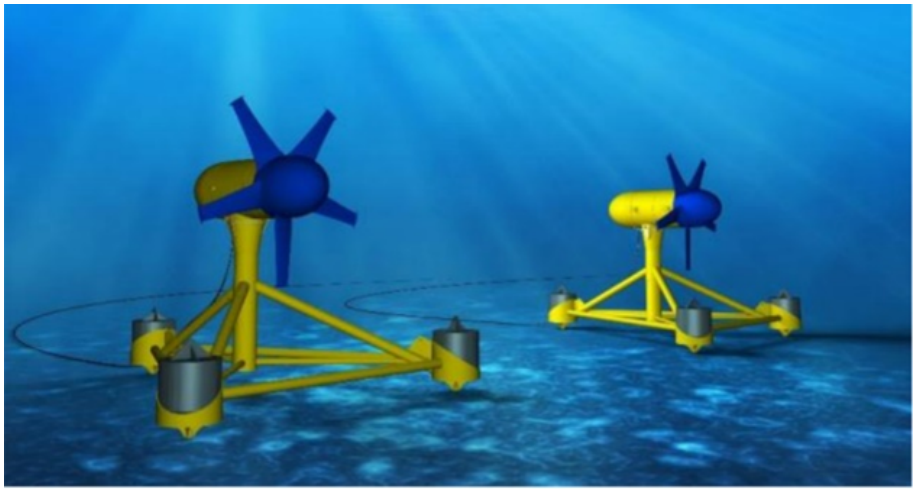

Figure 3.7: Proposed design of the Sabella D12 sea-bed mounted tidal stream turbine [13].

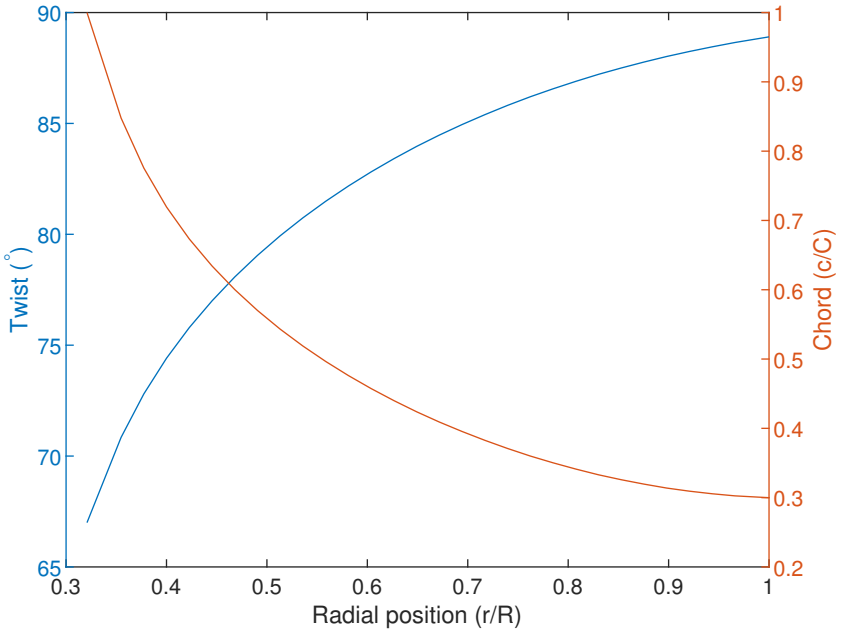

Figure 3.8: The chord and twist distribution along the radial length of the Sabella D12 rotor blade.

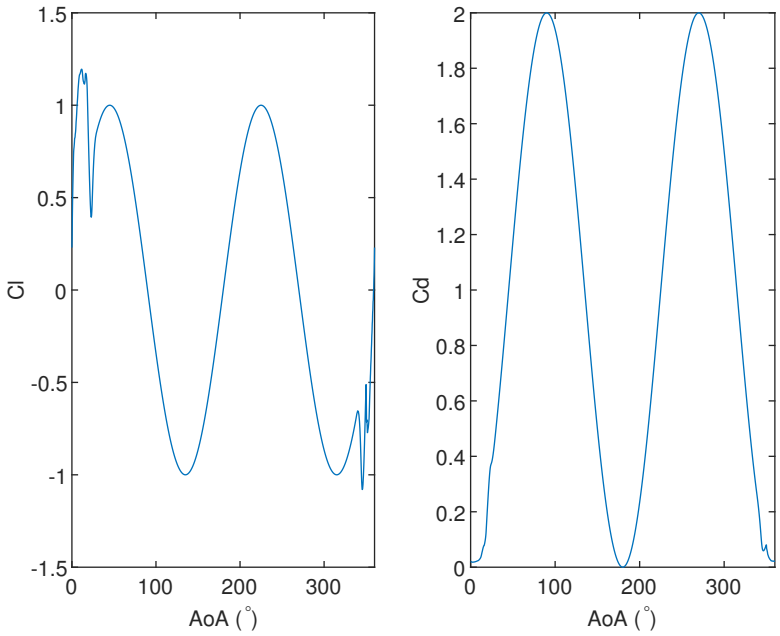

Figure 3.9: Lift and drag coefficient against angle of attack for the NACA-63(3)418 aerofoil profile at a Reynolds number of $\mathbf{2.5 \times 10^5}$ used in the numerical modelling of the Sabella D12 turbine, produced by the XFOIL tool [2] and flat plate theory.

3.1.4 Barltrop

A laboratory scale tidal stream turbine has been tested by Barltrop et al. [14, 15]. The three bladed turbine has a diameter of 400mm which has rotor blades of length 160mm with a maximum chord of 66.5mm. A picture of the laboratory scale Barltrop turbine is shown in Figure 3.10 [14, 15]. The chord and twist distribution along the radial length of the Barltrop rotor blades are shown in Figure 3.11. Table A.8 in Appendix A gives the chord and twist distribution along the radial length of the laboratory scale Barltrop rotor. The rotor blades have the NREL S814 aerofoil profile. The lift and drag polars for this profile at a Reynolds number of $\mathbf{3 \times 10^6}$ are given in Figure 3.12. The lift and drag data were produced from wind tunnel testing [14, 15]. Table A.9 in Appendix A gives the summary of the polars for angle of attacks of 0-15°.

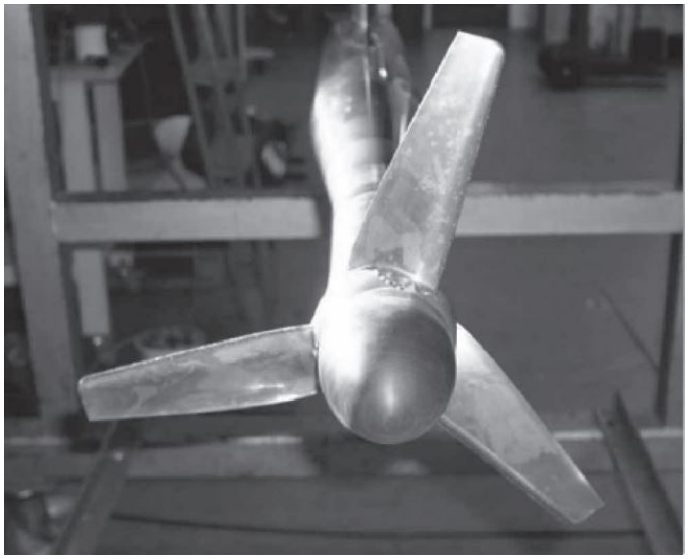

Figure 3.10: Photo of the physical laboratory scale Barltrop turbine used for experimental testing [14, 15].

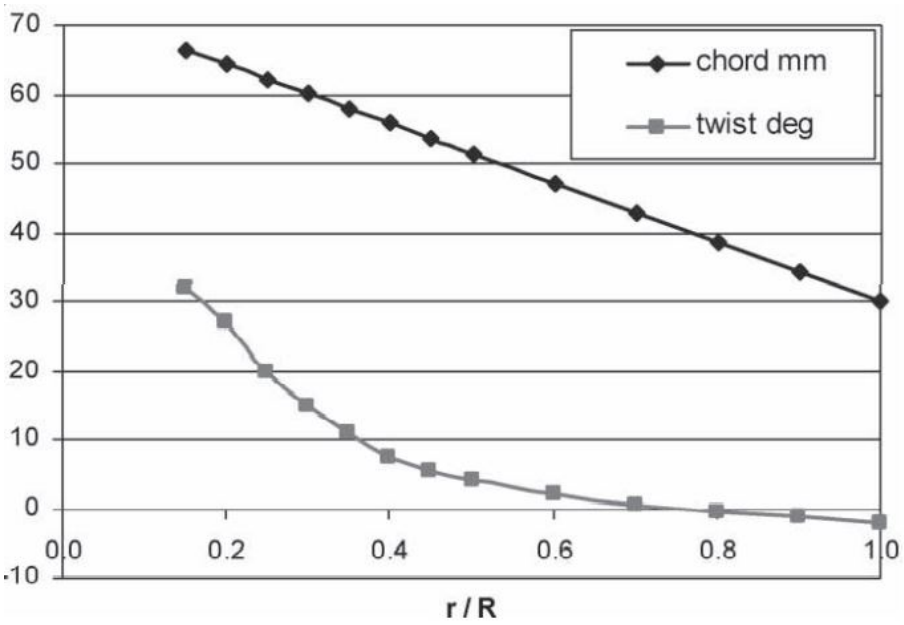

Figure 3.11: The chord and twist distribution along the radial length of the laboratory scale Barltrop rotor blade [14, 15].

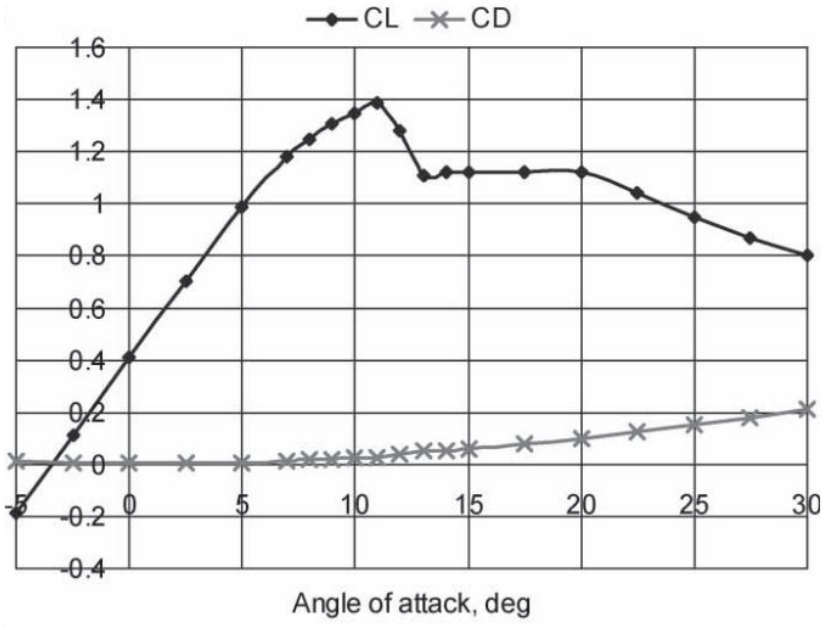

Figure 3.12: Lift and drag coefficient against angle of attack for the NREL S814 aerofoil at a Reynolds number of $\mathbf{3 \times 10^6}$ used in the numerical modelling of the laboratory scale Barltrop turbine, produced by wind tunnel experiments [14, 15].

3.1.5 IFREMER

The IFREMER tidal stream turbine has 3 rotor blades which are designed based on the NACA-63(3)418 aerofoil profile [16]. The profile of the rotor blades varies across their radius, which starts as a cylinder at the root and thins towards the tip. The turbine used in the laboratory and numerical model testing in the following work has a rotor radius of 362mm and a hub radius of 55mm. Figure 3.13 shows a photo of the IFREMER turbine used for laboratory testing [16]. The chord and twist distribution along the radial length of the IFREMER rotor blade is plotted in Figure 3.14. Table A.10 in Appendix A gives the chord and twist distribution along the radial length of the IFREMER turbine. The rotor blades are based on the NACA-63(3)418 aerofoil profile. The lift and drag polars for this profile at a Reynolds number of $\mathbf{3.5 \times 10^5}$ was produced using the XFOIL tool version 6.96 [2] for angle of attacks of -17.5-17.5°, and flat plate theory for the remaining angle of attack 0-360°, and is plotted in Figure 3.15. The summary of the polars for angle of attack of 0-15° is given in Table A.11 in Appendix A.

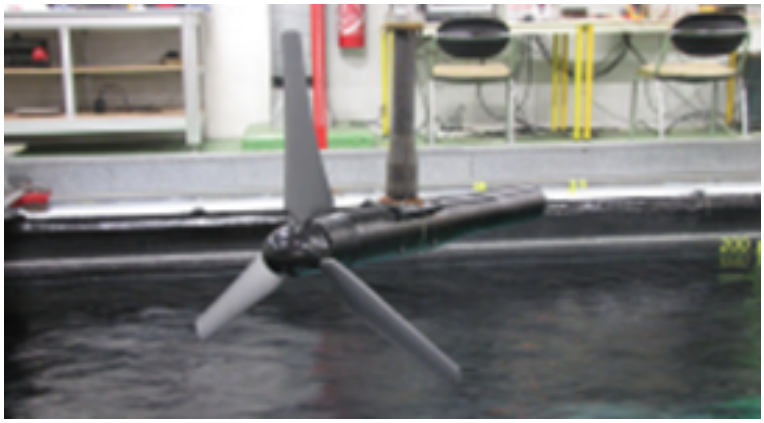

Figure 3.13: Photo of the physical laboratory scale IFREMER turbine used for experimental testing [16].

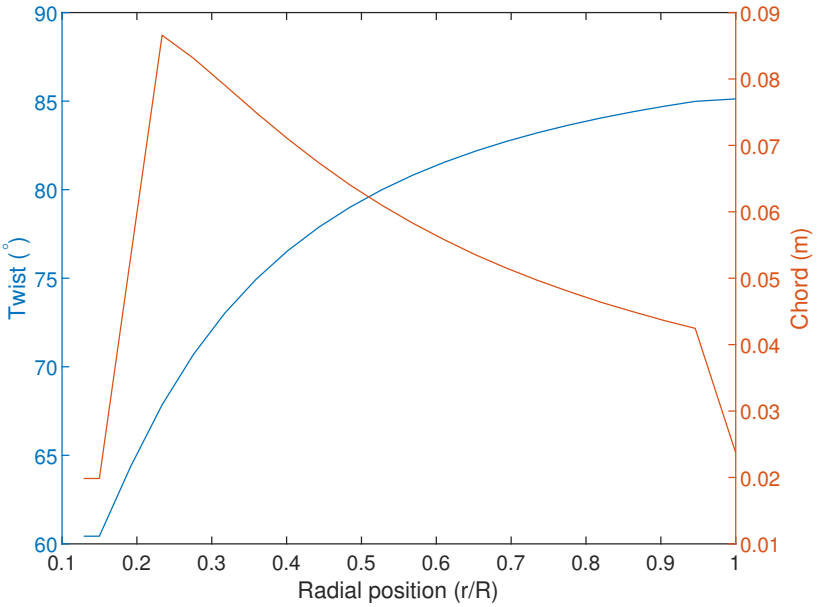

Figure 3.14: The chord and twist distribution along the radial length of the laboratory scale IFREMER rotor blade.

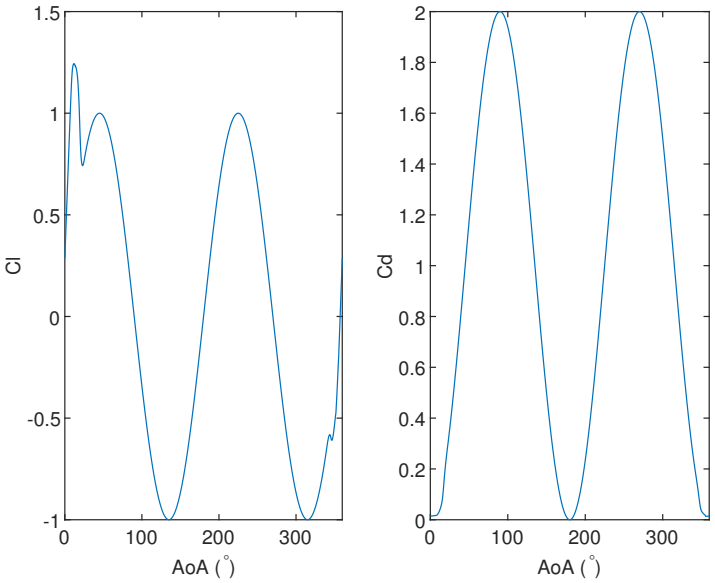

Figure 3.15: Lift and drag coefficient against angle of attack for the NACA-63(3)418 aerofoil at a Reynolds number of $\mathbf{5 \times 10^5}$ used in the numerical modelling of the IFREMER turbine, produced by the XFOIL tool [2] and flat plate theory.

3.1.6 IFREMER - modified

The IFREMER turbine has been modified to be used on the RRES. The number of rotor blades has been reduced from 3 to 2, whilst the chord has been increased by 1.5x to maintain the same solidity as the original turbine. The number of blades has been reduced from 3 to 2 to decrease the complexity of manufacture and maintenance to keep in line with the aims of the RRES.

The rotor blades profile varies across their radius, which starts as a cylinder at the root and thins towards the tip, and are based on the NACA-63(3)418 aerofoil. Two different sized IFREMER modified turbine rotor blades are used in the development of the RRES. The first has a diameter of 0.9m and a hub diameter of 0.195m, and the second has a diameter of 3.0m and a hub diameter of 0.65m. A photo of the larger rotor blades is shown in Figure 3.16. Table A.12 in Appendix A gives the twist, chord, and thickness distribution along the radial length of the 3.0m diameter IFREMER modified turbine. Similarly, Table A.13 in Appendix A gives the twist, chord, and thickness distribution along the radial length of the 0.9m diameter IFREMER modified turbine. The rotor blades polars have previously been given in Section 3.1.5, in Figure 3.15 and Table A.11.

Figure 3.16: IFREMER modified rotor blades used for 3.0 diameter remote river energy system.

3.2 Laboratory test facilities

Important details of the laboratory test facilities used to obtain empirical data against which the BEMT results are validated are presented in this section. These details include physical parameters of the test facilities and their capabilities.
Flow velocity and turbulence intensity are the important flow condition parameters that are needed to be known to replicate the laboratory test by numerical models. These parameters are measured using a laser doppler velocimeter (LDV) and an acoustic doppler velocimeter (ADV) in all test facilities.

3.2.1 IFREMER wave and current flume tank

The experimental testing of the laboratory scaled Magallanes ATIR, Sabella D12, and IFREMER turbines ware completed at IFREMER wave and current flume tank in Boulogne-Sur-Mer, France. Detailed description of the IFREMER wave and current flume tank laboratory facility can be found in previous works [102, 17, 103, 104, 16]. Figure 3.17 shows a schematic of the IFREMER wave and current flume tank used in the laboratory testing of the Magallanes ATIR turbine [17].
The torque and axial force measurements for the rotor in the IFREMER flume are directly measured on the rotation axis which eliminates nacelle or support drag in recorded data. Each blade is fitted with a five-component load-cell at their root which measures two

forces and three moments. The rotor is mounted to a motor-gearbox assembly which allows accurate control of its rotational speed.
Flow speeds in the range of 0.8m/s-1.4 m/s are reliably achievable in the IFREMER flume which equates to Reynolds number range of $\mathbf{2.7x10^5 - 5.7x10^5}$ based on chord at 70% span. The mean velocity profile in the laboratory flume is fairly uniform across the rotor span. Turbulence intensities of $\mathbf{1.5\%, 3\%}$, and $\mathbf{15\%}$ are attainable in the wave and current flume tank with combinations of different flow straightening meshes. The blockage ratio was ≈4.5% for the laboratory experiments which is deemed small enough to neglect any effects [105, 106].

3.2.2 QinetiQ towing tank

The Oxford blind test turbine was tested in the QinetiQ towing tank facility in Haslar, Portsmouth. The tow tank is 5.4m deep, 12.2m wide, and 270m long which results in low blockage ratio of 3%. Carriage speeds up to 12.25m/s and drag loads up to 5kN are achievable at QinetiQ towing tank. Different turbulence intensities can be generated by placing different flow straighteners upstream of the rotor on the towing carriage.

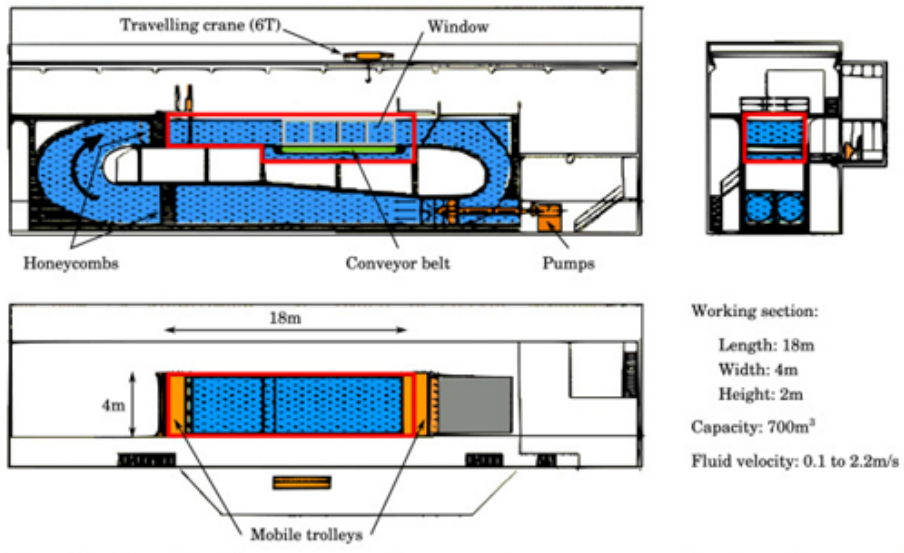

Figure 3.17: Schematic of the IFREMER wave and current flume tank used for the laboratory testing of the Magallanes ATIR turbine [17].

3.2.3 University of Glasgow and Strathclyde wave and towing tank

The laboratory experiments of the Barltrop turbine were conducted in a 2.5m deep, 4.6m wide, and 77m long wave and towing tank at the University of Glasgow and Strathclyde. The blockage ratio is 1.1% and thus no corrections are necessary [105, 106]. Carriage velocities up to 5m/s are achievable in the wave and towing tank. In a similar method to the QinetiQ tow tank, different turbulence intensities can be generated by placing different flow straighteners upstream of the rotor on the towing carriage. In the laboratory experiments of Barltrop the thrust transducer could only measure in one direction, thus axial force was only measured for positive values.

3.3 Foil shape & Reynolds number dependence

The first development of the Swansea University BEMT numeric model undertaken as part of the studies described in this thesis was an adaptation to more accurately describe the effects of turbine geometry, and in this section we examine the effect and size of this adaption.

Four BEMT numerical model versions were tested, with each successive version increasing the accuracy of the blade geometry modelling. The first BEMT numerical model (xx) used single lift and drag curves for all elements, the *"original"* model. The second version (gx) allowed unique lift and drag curves to be assigned to each element based on their geometry profile. Similarly, the third version (xr) allowed unique lift and drag curves to be assigned to each element but are based on their Reynolds Number alone. The fourth version (gr) combines the second and third versions, allowing for unique lift and drag curves to be assigned to each element based on both their geometry and Reynolds Number. Summary of the four BEMT numerical model versions used in the case study of foil shape and Reynolds number dependence are given in Table 3.1.

Table 3.1: Summary of the four BEMT numerical model versions used in the case study of foil shape and Reynolds number dependence.

Version	Geometry dependent?	Reynolds number dependent?
1. *xx*	✗	✗
2. *gx*	✓	✗
3. *xr*	✗	✓
4. *gr*	✓	✓

Results from the four BEMT versions are compared to laboratory testing of the Magallanes ATIR, Sabella D12, and IFREMER turbines only (tests on the Oxford and Barltrop rotors are described in Sections 3.4.1 and 3.4.3) to quantify any improvements in the predicted turbine performance of the BEMT numerical models. Simulation parameters for the BEMT numerical models were chosen to match the available laboratory data. Flow conditions, in particular free stream velocity and turbulence intensity have a significant impact on rotor performance. The BEMT numerical models used Sandia synthetic flow fields (see Section 2.2.4.1) which statistically match the flow fields used in the laboratory testing.

3.3.1 Magallanes ATIR

Details of the Magallanes ATIR turbine and its laboratory testing are given in Section 3.1.2 and Section 3.2.1 respectively. Slama *et.al.* have previously studied the ATIR turbine laboratory results [107]. Six different flow conditions are used for the analysis which have different combinations of two flow speeds and three turbulent intensities. Plots with results from all four BEMT versions and laboratory testing are produced for each flow case. Specifically, the diagrams plot rotor blade C_p* against TSR. Optimum rotational rate of the Magallanes ATIR turbine rotor is deduced from laboratory testing and used as the point of comparison between BEMT numerical model versions and flow cases. Details of the flow conditions for each plot is given in Table 3.2. The flow conditions used in the analysis are limited to those achievable in the laboratory testing, due to the necessity of the laboratory results to validate any improvements to the BEMT numerical model.

Table 3.2: Details of the flow conditions used in each test case for the analysis of Reynolds number and foil geometry dependence of the Magallanes ATIR turbine.

Test case	Current speed (m/s)	Turbulence intensity (%)
1	1.0	1.5
2	1.0	5.0
3	1.0	15.0
4	1.4	1.5
5	1.4	5.0
6	1.4	15.0

All results for C_p have been scaled to ensure commercial sensitivity is maintained, as described at the start of Chapter 3. Plots of scaled coefficient of power against tip speed ratio results from laboratory testing for the Magallanes ATIR turbine rotor at various flow speeds and turbulent intensities are shown in Figure 3.18. Six curves are plotted

which represent each of the test cases stated previously. Rotor performance increases significantly with flow speed whilst relatively little change is seen with different turbulent intensities. Optimum rotor performance is seen at TSR of 5.0 for flow speed of 1.0m/s and at TSR of 4.5 for flow speed of 1.4m/s.

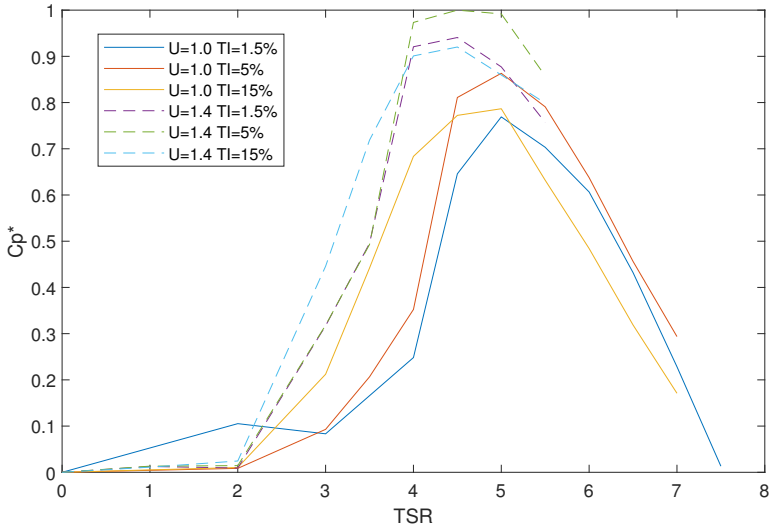

Figure 3.18: Scaled plot of coefficient of power against tip speed ratio for laboratory results for the Magallanes ATIR turbine rotor at various flow speeds and turbulent intensities.

Reynolds Number across the Magallanes ATIR turbine rotor blade has been calculated for flow speeds of 1.0m/s and 1.4m/s at TSR of 4.75. A plot of Reynolds Number against rotor blade radial distance is shown in Figure 3.19. There is very little difference in Reynolds Number variance across rotor blade radius at different turbulence intensities and thus this is not included in the diagram. As expected, the Reynolds Number distribution across the rotor blade has the same shape at different flow speeds and differs only in magnitude. The Reynolds Number distribution for the Magallanes ATIR turbine rotor blade increases from its minimum at the blade root to its maximum around the mid rotor radius length, element 7, and then decreases towards the rotor tip. Minimum Reynolds Number is approximately 40% of the maximum value, seen at the rotor hub, and the Reynolds Number at the rotor tip is approximately 60% of the maximum value.

C_p* against TSR results for each of the tested flow cases from BEMT versions 1-4 and laboratory results are shown in Figure 3.20. Summary and comparison of the maximum C_p* results can be found in Table 3.3. As previously stated, each test case represents

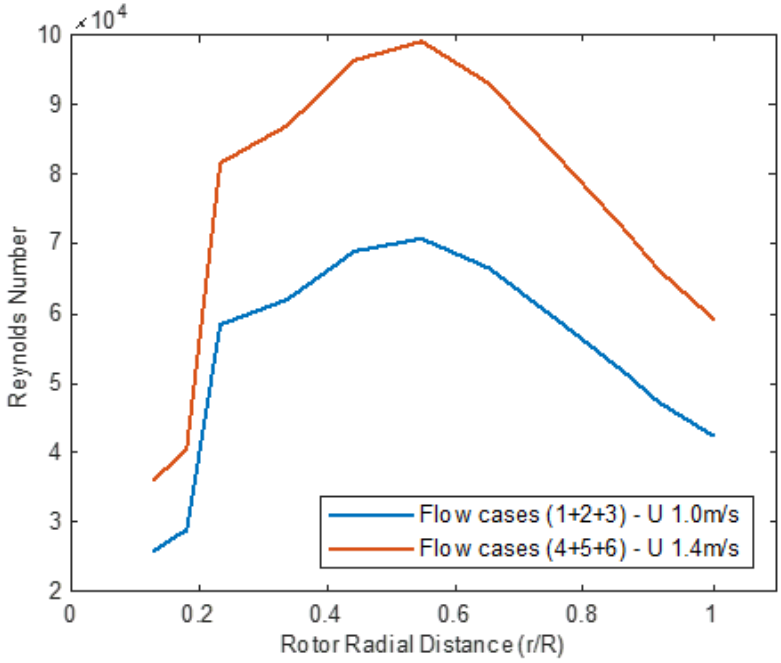

Figure 3.19: Reynolds number against rotor radial distance for the Magallanes ATIR rotor blade at current speeds of 1.0m/s and 1.4m/s at TSR of 4.75.

different flow conditions which differ by current velocity and turbulence intensity. Results for all test cases follow the same trend and have similar curves with the only major difference being maximum C_P, which varies up to 10% between low and high current velocities.

All BEMT versions over-predict the performance of the turbine. BEMT version 1.xx is the most inaccurate in matching the laboratory results followed closely by version 3.xr, with the difference exaggerated in the overspeed operating range (TSR > 4.75). Considerable improvement in matching laboratory results over the whole range of tested TSR is seen by BEMT versions 2.gx and 4.gr, with version 4 always being the best match. Prediction of optimum TSR from the BEMT numerical model is in good agreement with the empirical laboratory data, although difficult to fully compute due to the low resolution of the empirical laboratory data.

Test case 6 in Figure 3.20 shows an inflection in BEMT version 3 at the overspeed region at TSR of 8. This is due to the axial induction factor >0.4 which has caused the high induction correction factor to be used as described in Section 2.2.3.3.

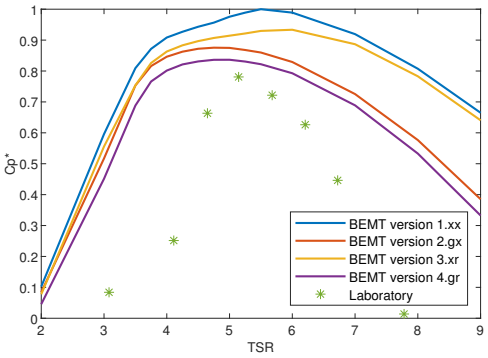

(a) Flow case 1

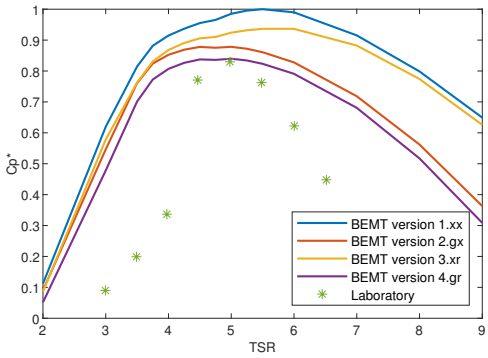

(b) Flow case 2

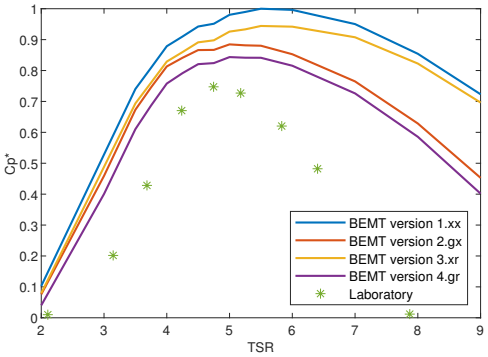

(c) Flow case 3

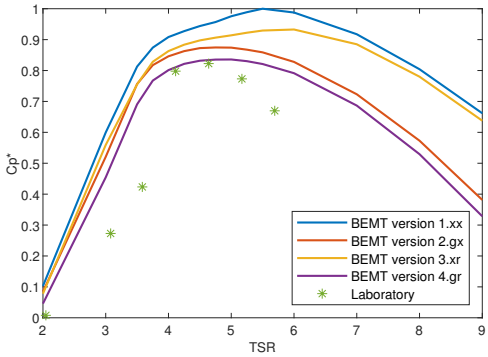

(d) Flow case 4

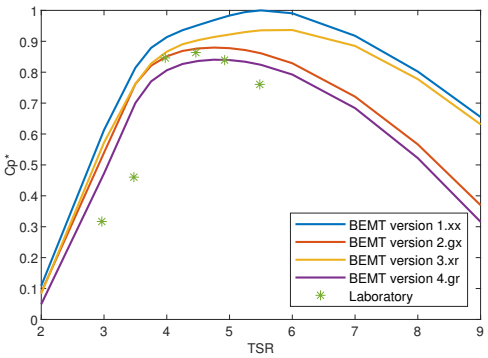

(e) Flow case 5

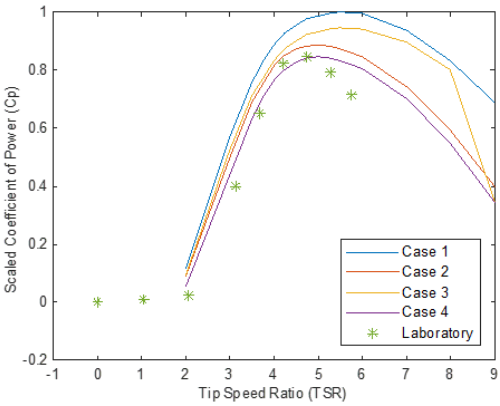

(f) Flow case 6

Figure 3.20: Reynolds number and foil geometry dependency study; scaled plot of coefficient of power against tip speed ratio from BEMT versions 1, 2, 3, and 4, and laboratory testing in various flow conditions for the Magallanes ATIR turbine.

Table 3.3: Reynolds number and foil dependency testing of the Magallanes ATIR turbine; summary of maximum scaled coefficient of power results from BEMT versions 1, 2, 3, and 4, and laboratory testing across 6 flow cases.

Flow cases	Maximum scaled coefficient of power					Difference in maximum coefficient of power to laboratory (%)			
	BEMT version				Laboratory	BEMT version			
	1.xx	2.gx	3.xr	4.gr		1.xx	2.gx	3.xr	4.gr
1	1.000	0.873	0.934	0.834	0.780	+28.2	+12.0	+19.7	+6.9
2	1.000	0.880	0.937	0.842	0.832	+20.2	+5.7	+12.5	+1.1
3	1.000	0.887	0.946	0.844	0.748	+33.7	+18.6	+26.5	+12.9
4	1.000	0.874	0.933	0.835	0.822	+21.6	+6.3	+13.5	+1.6
5	1.000	0.881	0.936	0.841	0.796	+25.7	+10.7	+17.7	+5.7
6	1.000	0.886	0.944	0.843	0.846	+18.2	+4.7	+11.6	-0.3

3.3.2 Sabella D12

Details of the Sabella D12 turbine and its laboratory testing are given in Section 3.1.3 and Section 3.2.1 respectively. Slama *et.al.* have previously studied the D12 turbine laboratory results [107]. The Sabella D12 rotor blades have a constant profile which means that there is no scope to introduce varying foil geometry in the BEMT numerical model. As such, improvements to the BEMT numerical model are based solely on the inclusion of the Reynolds number dependency for the D12. Only BEMT versions 1.xx and 3.xr are tested. Six different flow conditions are used for analysis which have different combinations of three flow speeds and two turbulence intensities. Plots with results from the BEMT version 1.xx and 3.xr, and laboratory testing are produced for each of the flow conditions. Specifically, the diagrams plot torque, T, against TSR. Optimum rotation rate of the D12 turbine is deduced from laboratory testing and is used as the point of comparison between cases. Detail of the flow conditions for each plot is tabulated in Table 3.4.

Table 3.4: Details of the flow conditions used in each test case for the analysis of Reynolds number and foil geometry dependence of the Sabella D12 turbine.

Test case	Current speed (m/s)	Turbulence intensity (%)
1	0.8	1.5
2	0.8	15.0
3	1.0	1.5
4	1.0	15.0
5	1.4	1.5
6	1.4	15.0

All results of torque have been scaled to ensure commercial sensitivity is maintained. This is done exclusively for each set of results visualised by dividing all torque values by the maximum torque value in each individual plot. Plot of scaled torque (T*) against TSR for laboratory results of the Sabella D12 turbine rotor at various flow speeds and turbulent intensities are shown in Figure 3.21. Six curves are plotted which are for each of the flow conditions stated previously. Both flow speed and turbulent intensity influence the rotor performance. Higher flow speed results in increased rotor performance whilst an increase in turbulent intensity decreases the rotor performance. Optimum rotor performance is seen at TSR of 3.8 for all flow conditions. Torque is used for the analysis of the Sabella D12 turbine rotor blade rather than power, as used for the Magallanes ATIR turbine, due to the available laboratory data. Limited rotational rate data is available due to recording issues.

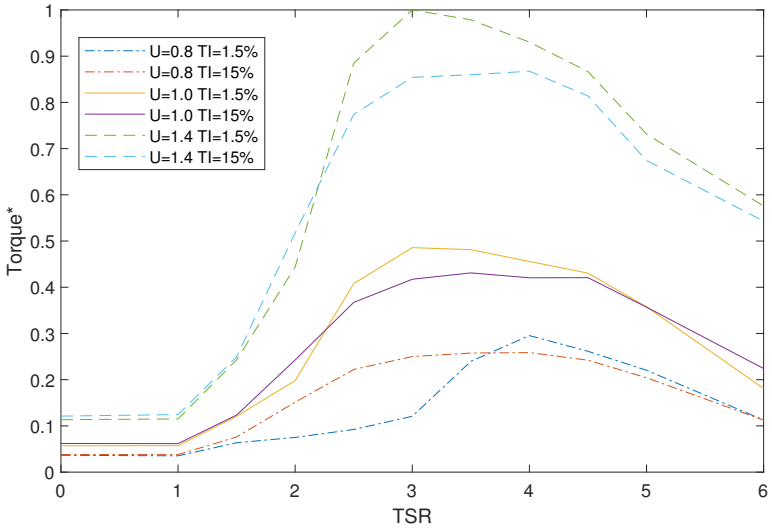

Figure 3.21: Plot of scaled torque of coefficient of power against tip speed ratio for laboratory results for the Sabella D12 turbine rotor at various flow speeds and turbulent intensities.

Figure 3.22 shows the Reynolds Number against rotor blade radial distance for the Sabella D12 tidal stream turbine at three flow speeds of 0.8m.s^{-1}, 1.0m.s^{-1}, and 1.4m.s^{-1} at TSR of 3.8. Plots with the same flow velocities are combined as turbulence intensity has little effect on the Reynolds Number. The Reynolds Number distribution across the rotor blade has the same shape at different flow speeds and differs only in magnitude. Maximum Reynolds Number is seen at the blade root. It decreases to its minimum value, which is 70% of the maximum, at 80% of the rotor blade radius, and then increases to 75% of the maximum value at the rotor blade tip. The Reynolds Number across the Sabella D12 turbine rotor blade varies by 30%, which is a comparably small range and is likely to result in minimal improvements in the BEMT model rotor performance predictions vs. the conventional BEMT version 1.xx without variable Reynolds number.

Scaled torque against TSR for each tested flow conditions for BEMT versions 1.xx and 3.xr and laboratory results are shown in Figure 3.23. Summary of the maximum scaled torque results can be found in Table 3.5. As previously stated, each plot represents different flow conditions which differ by free stream flow velocity and turbulence intensity.
Results for all plots follow the same trend and have similar curves with the only major difference being maximum torque, which varies up to 12% between low and high current velocities. The BEMT version 1.xx and BEMT version 3.xr have similar results due to

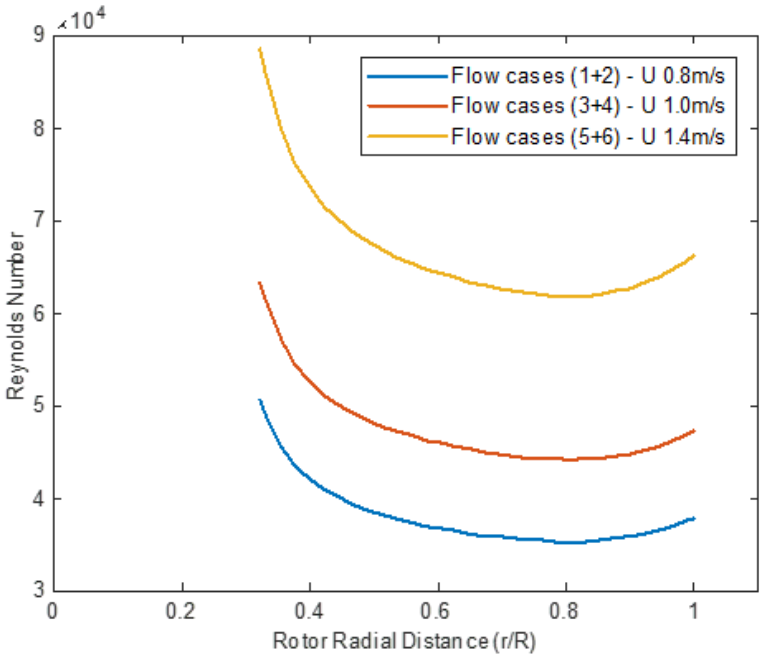

Figure 3.22: Reynolds number against rotor radial distance for the Sabella D12 rotor blade at current speeds of 0.8m/s, 1.0m/s, and 1.4m/s at TSR of 3.8.

the relatively small Reynolds Number variance across the rotor blade. Prior to optimum rotor operating speed, BEMT version 1.xx predicts slightly higher torque values than BEMT version 3.xr, whilst after optimum rotor operating speed BEMT version 3.xr predicts higher torque than BEMT version 1.xx. At optimum rotor operating speed, both BEMT versions predict higher torque values than recorded in the laboratory testing. In every tested flow condition BEMT version 1.xx predicts higher maximum torque values than BEMT version 3.xr. Another observation from Figure 3.23 is that test cases 2, 4, and 6 have higher optimum TSR values compared to test cases 1, 3, and 5. Test cases 2, 4, and 6 also have a less abrupt fall in C_p in the stall region, hypothesised to be a result of a delay to the boundary layer reversal leading to stall in higher turbulent flows. The higher turbulence intensity test cases, (e.g. 2, 4, and 6), are more energetic and thus explains the higher optimum TSR.

Turbulence intensity of the flow field has a significant impact on the difference between maximum torque predicted by the BEMT versions and what is recorded from laboratory testing. In low and medium flow speeds test cases (1-4), the difference in maximum torque values of the BEMT and laboratory results are significantly larger than in the

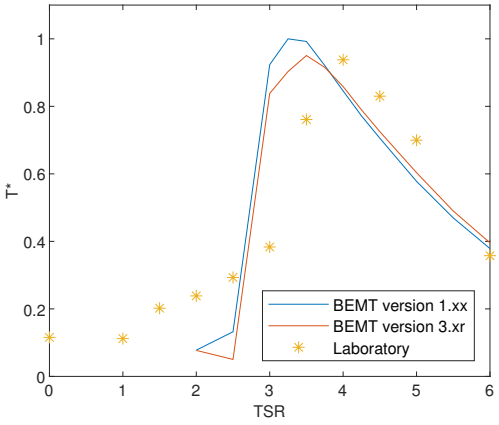

(a) Test case 1

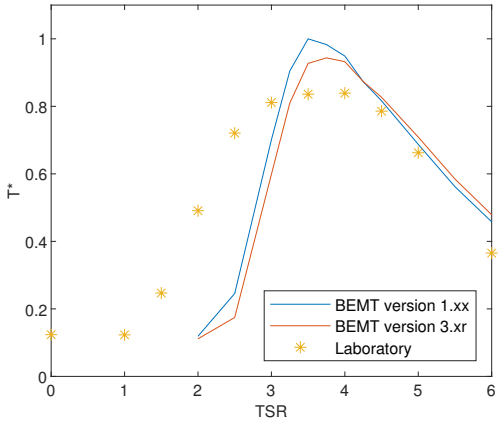

(b) Test case 2

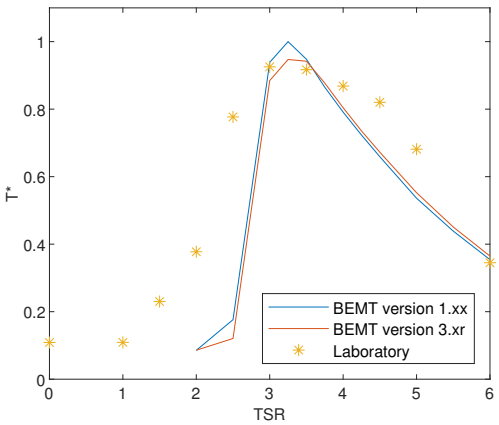

(c) Test case 3

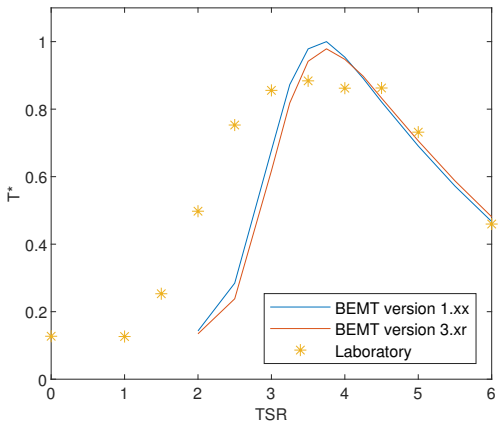

(d) Test case 4

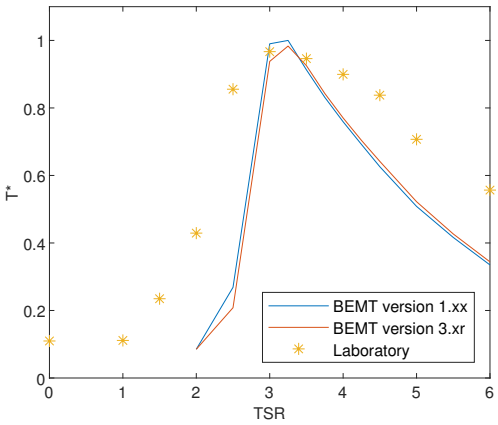

(e) Test case 5

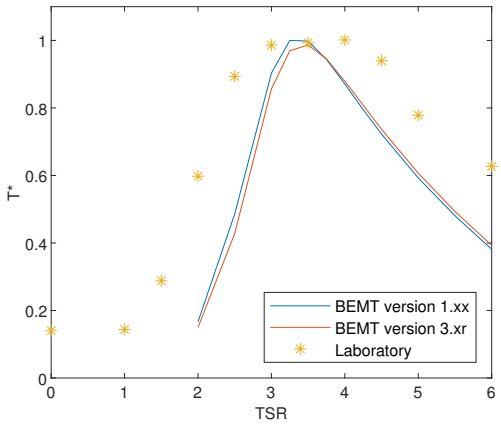

(f) Test case 6

Figure 3.23: Reynolds number and foil geometry dependency study; plot of scaled torque against tip speed ratio from BEMT versions 1.xx, and 3.xr, and laboratory testing in various flow conditions for the Sabella D12 turbine.

higher flow speeds test cases (5-6). In the high flow speed cases (5-6), the difference in maximum torque values of the BEMT versions and the laboratory results decrease slightly with higher turbulent intensity.

Table 3.5: Reynolds number and foil dependency testing of the Sabella D12 turbine; summary of maximum scaled coefficient of power results from BEMT versions 1.xx, and 3.xr, and laboratory testing.

Flow cases	Maximum scaled torque			Difference in maximum torque to laboratory (%)	
	BEMT version		Laboratory	BEMT version	
	1.xx	3.xr		1.xx	3.xr
1	1.000	0.951	0.938	+6.6	+1.4
2	1.000	0.942	0.839	+19.2	+12.4
3	1.000	0.947	0.925	+5.6	+2.4
4	1.000	0.978	0.884	+13.1	+10.6
5	1.000	0.984	0.967	+3.4	+1.8
6	0.996	0.981	1.000	-0.6	-1.9

3.3.3 IFREMER

Details of the IFREMER turbine and its laboratory testing are given in Section 3.1.5 and Section 3.2.1 respectively. Slama *et.al.* have previously studied the IFREMER turbine laboratory results [107]. Four different flow conditions were used for analysis which have different combination of two flow speeds and two turbulent intensities. A plot with results from all four BEMT versions and laboratory testing are produced for each of the flow conditions. Specifically, the diagrams plot rotor C_p against TSR. Note that unlike the Magallanes ATIR and Sabella D12 cases discussed in the previous two sections, the performance of the IFREMER turbine is not commercially sensitive and the performance data is therefore not scaled as was done in those cases. Optimum rotation rate of the IFREMER turbine is deduced from laboratory testing and is used as the point of comparison between cases. Detail of the flow conditions for each plot are given in Table 3.6.

Table 3.6: Details of the flow conditions used in each test case for the analysis of Reynolds number and foil geometry dependence of the IFREMER turbine.

Test case	Current speed (m/s)	Turbulence intensity (%)
1	0.6	3.0
2	0.6	15.0
3	1.0	3.0
4	1.0	15.0

Plots of C_p against TSR for laboratory results of the IFREMER turbine at various flow speeds and turbulent intensities are shown in Figure 3.24. Four curves are plotted which represent each of the flow conditions stated previously. As with other turbines, both flow speed and turbulent intensity influence the rotor performance. Generally, increase in flow speed increases the rotor performance whilst an increase in turbulent intensity decreases the rotor performance. Optimum rotor performance is seen approximately at TSR of 4.0 and 4.5 for flow conditions with speeds of 0.6m/s and 1.0m/s respectively. Comparison of turbine performance from the BEMT and laboratory cases will be made at TSR of 4.25.

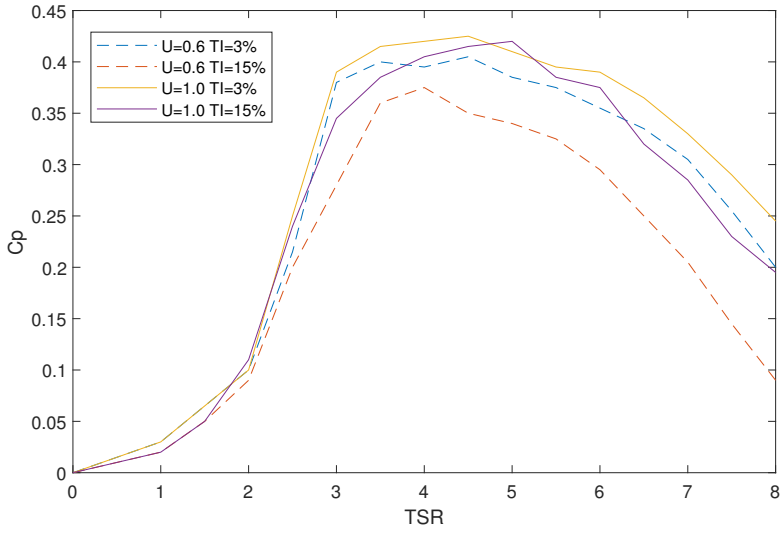

Figure 3.24: Plot of scaled coefficient of power against tip speed ratio for laboratory results for the IFREMER turbine rotor at various flow speeds and turbulent intensities.

Reynolds Number across the IFREMER turbine rotor blade has been calculated for flow speeds of 0.6m/s and 1.0m/s at TSR of 4.25. A plot of Reynolds Number against rotor blade radial distance is shown in Figure 3.25. There is very little difference in Reynolds Number variance across rotor blade radius at different turbulence intensities and thus these are not included in the diagram.

The Reynolds Number distribution across the rotor blade is the same at different flow speeds and differs only in magnitude as is seen in the other rotor blades. The Reynolds Number distribution for the IFREMER turbine rotor blade increases from its minimum at the hub to its maximum just prior to the tip. A significant drop in Reynolds Number is seen at the tip element due to a rapid change in rotor blade geometry. Minimum

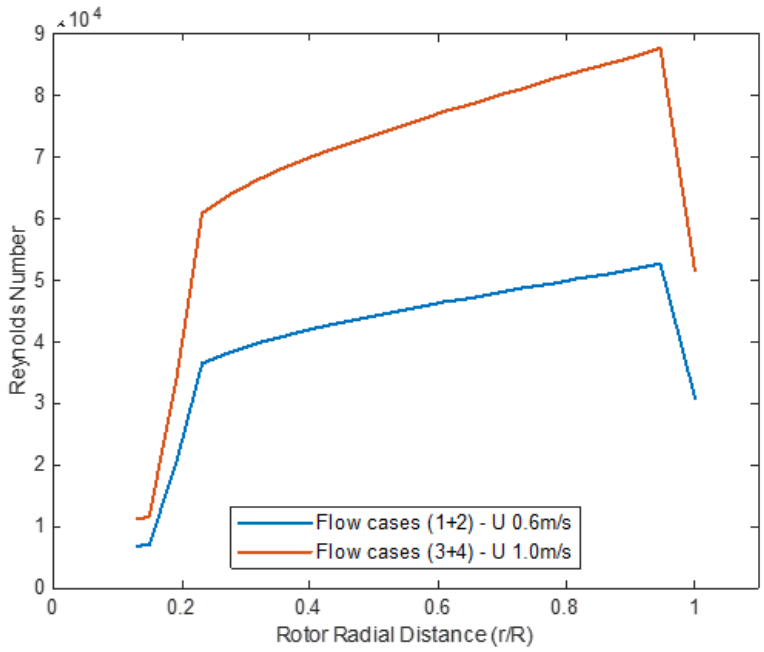

Figure 3.25: Reynolds number against rotor radial distance for the IFREMER rotor blade at current speeds of 0.6m/s and 1.0m/s at TSR of 4.25.

Reynolds Number is 13% of the maximum value, which gives a large range that will provide significant scope for BEMT improvements.

C_p against TSR for each tested flow conditions for BEMT versions 1-4 and laboratory results are shown in Figure 3.26. Summary and comparison of the maximum C_p results can be found in Table 3.7. Results for the BEMT versions follow the same trend across the different flow conditions. Prediction of rotor performance is always highest in BEMT version 1.xx, followed by version 3.xr, version 2.gx, and finally version 4.gr. There is very little difference between rotor performance prediction results from BEMT version 2.gx version 4.gr, i.e., correcting for Reynolds number effects does not have a strong influence on BEMT numerical model predictions that already account for radially-varying foil geometry. Generally, the BEMT versions under-predict the rotor performance when compared to laboratory results: exceptions to this are in the overspeed region, and for a broad range of TSR values in flow case 2. The best correlation between the BEMT versions and laboratory results is seen at the higher turbulence intensity flow conditions. An anomaly in the results has occurred in test case 2 for BEMT versions 1.xx, 2.gx, and 3.xr between TSR 3.5-4.5 where a dip in C_P is seen. This is due to non linear stall of the rotor due to the

high turbulence and low mean flow speed of the flow field. This is not seen in BEMT version 4.gr due to the assignment of different lift and drag polars.

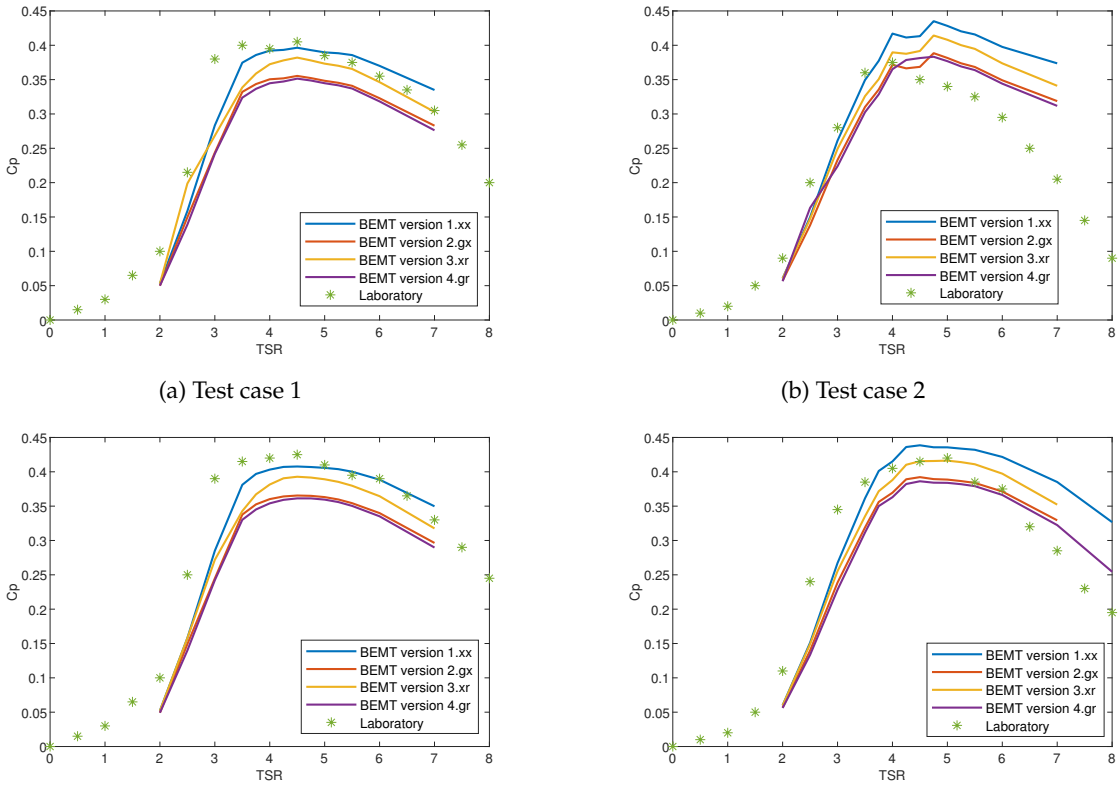

(a) Test case 1

(b) Test case 2

(c) Test case 3

(d) Test case 4

Figure 3.26: Reynolds number and foil geometry dependency study; plot of scaled coefficient of power against tip speed ratio from BEMT versions 1.xx, 2.gx, 3.xr and 4.gr, and laboratory testing in various flow conditions for the IFREMER turbine.

Table 3.7: Reynolds number and foil dependency testing of the IFREMER turbine; summary of maximum scaled coefficient of power results from BEMT versions 1, 2, 3, and 4, and laboratory testing.

Flow cases	Maximum coefficient of power					Difference in maximum coefficient of power to laboratory (%)			
	BEMT version				Laboratory	BEMT version			
	1.xx	2.gx	3.xr	4.gr		1.xx	2.gx	3.xr	4.gr
1	0.396	0.355	0.382	0.351	0.405	-2.2	-12.3	-5.7	-13.3
2	0.435	0.389	0.414	0.383	0.375	+16.0	+3.7	+10.4	+2.1
3	0.408	0.366	0.393	0.361	0.425	-4.0	-13.9	-7.5	-15.1
4	0.439	0.392	0.416	0.386	0.420	+4.6	-6.7	-1.0	-8.1

3.3.4 Discussion & Conclusions

In the classical BEMT model, the rotor blades are modelled using single lift and drag curves for all elements in version 1.xx whilst in version 4.gr each element is assigned unique lift and drag curves based on their foil geometry and Reynolds Number. Using unique lift and drag curves for each element is a more accurate representation on the rotor blades and should improve the performance prediction of the BEMT model. Due to the constant geometry profile of the Sabella D12 turbine rotor blades, it was only possible to use BEMT versions 1.xx and 3.xr in its analysis, the inclusion of Reynolds Number dependency. Full analysis has been undertaken on the Magallanes ATIR and IFREMER turbine rotor blades, made possible due to their varying blade geometry.
As is seen in all results, BEMT version 4.gr always predicts lower turbine rotor performance compared to BEMT version 1.xx. This can be explained by the geometry of the rotor blades which has been previously described in detail. In BEMT version 1.xx all elements are assumed to have the same lift and drag characteristic which is inaccurate. Both the ATIR and IFREMER rotor blades have circular profile at their roots which gradually thins to their main profile. Accurately portraying the lift and drag characteristics of all elements across the rotor blades, as is achieved in BEMT version 4.gr, decreases the predicted performance of the turbine rotor which is mainly due to the lower performance of the inner most elements which were previously being represented as having performance closer to the outboard elements with better hydrodynamic characteristics. This particularly lowers C_p at high TSR values, where most of the effective torque is generated from the inboard sections of the rotor blades.
The best match to the laboratory results is always seen with the most accurate BEMT version 4.gr for the Magallanes ATIR and Sabella D12 turbine rotors. The IFREMER turbine rotor results are not as straightforward, with the best match to laboratory results seen with different BEMT versions depending on the flow conditions. The closest match to the laboratory results is seen with BEMT version 4.gr for the high turbulence (15%) flow conditions and BEMT version 1.xx for the low turbulence (3%) flow conditions. A possible explanation for this observation is that the flow fields with 3% turbulence intensity in the laboratory experiments are not accurate. It is difficult to achieve accurate low turbulence in a flume and is most probably below 3%.
There is only one flow condition that was common across all rotors whose laboratory tests are summarised in this section: 1.0m/s free stream velocity and 15% turbulence intensity.

A plot of C_p* against TSR for all rotor blades is shown in Figure 3.27. BEMT version 1.xx, BEMT version 4.gr, and laboratory results are included for the Magallanes ATIR and IFREMER turbine rotors and BEMT version 1.xx, BEMT version 3.xr, and laboratory results for the Sabella D12 turbine rotor. As discussed above, BEMT version 4.gr predicts lower rotor performance compared to BEMT version 1.xx for the ATIR and IFREMER turbines. There is very little difference between BEMT versions for the D12 turbine due to the constant geometry of its rotor blade and minimal Reynolds number change. An improvement of 20% in predicting laboratory maximum rotor performance results is seen for the ATIR turbine rotor from BEMT version 1.xx to BEMT version 4.gr, whereas the same change in BEMT model decreases the accuracy of the predicted performance result for the IFREMER rotor by 3%. Although the accuracy in predicting maximum rotor performance decreases between BEMT version 1.xx and 4.gr for the IFREMER rotor, the accuracy of predicted power output across the broader range of TSR values (i.e., between TSR 3 & 7) has improved by 5%.

As previously discussed, a classical BEMT model (version 1.xx) assignes each blade element with the same lift and drag polars which causes inaccuracies in predicting the performance of a TST. Improvements have been made to the BEMT model by assigning unique lift and drag polars to each blade element in the work presented in this thesis. Additionally, further improvements could be made to the classical BEMT model by studying the behaviour and effects of the correction factors. In the work presented in this thesis, the improvements were achieved by accurate assignment of lift and drag polars to the hub elements, which were previously over prediciting their hydrodynamic performance. A future study should look at the possibility of achieving the same improvements by using the correction factors.

Conclusions

Rotor blade geometry modelling in the BEMT model is, in general, improved by introducing the ability to assign unique lift and drag curves to each element based on their foil geometry and Reynolds number. Comparison of BEMT rotor performance prediction with and without the improved blade geometry modelling has been made against laboratory results. In the majority of cases, the BEMT model with the advanced blade geometry modelling reproduce closer results to those of the laboratory testing when looking at optimum C_p only; in cases where prediction of optimum C_p is not specifically improved, results across a broader range of TSR values nonetheless tend to be better than in the classical BEMT model.

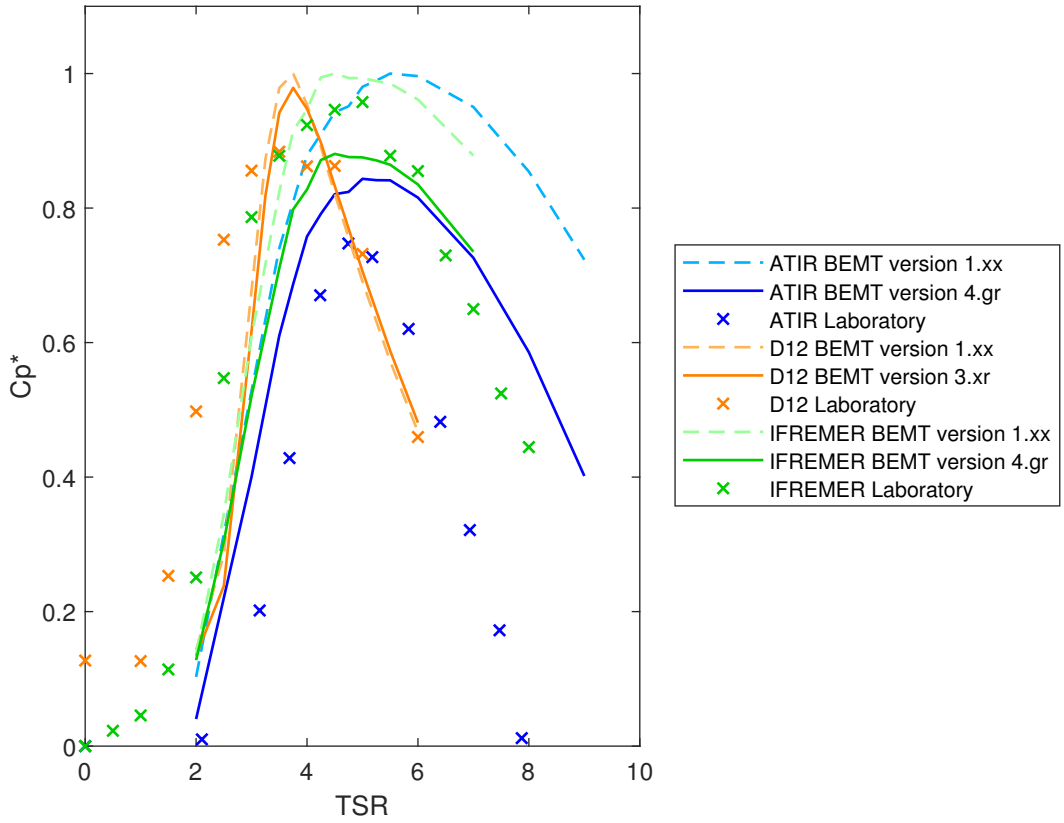

Figure 3.27: Plot of scaled coefficient of power against tip speed ratio in flow condition of free stream velocity of 1.0m/s and turbulence intensity of 15% for BEMT version 1.xx, BEMT version 4.gr, and laboratory results for the Magallanes ATIR and IFREMER turbine rotor blades and BEMT version 1.xx, BEMT version 3.xr, and laboratory results for the Sabella D12 turbine rotor blade. For each turbine, the C_P value used to scale the results is taken as the optimum C_P in the BEMT version 1.xx simulation.

BEMT model prediction of maximum rotor performance to laboratory results has improved by an average of 20.0% and 4.6% respectively for the Magallanes ATIR and Sabella D12 turbine rotor blades whilst it has decreased by 3.0% for the IFREMER turbine rotor with the inclusion of the improved blade geometry modelling.

Comparing BEMT versions 2.gx and 3.xr, it is clear that including geometry dependence has significantly greater impact on the BEMT model than that of Reynolds Number dependence. Including geometry dependence compared to Reynolds Number dependence has an average of 40% greater improvement in BEMT rotor performance prediction to

laboratory as discussed in Section 3.3.4. This is unsurprising as there is a more significant change in geometry than Reynolds Number across the rotor blades.
In every tested case, the BEMT versions which include the improved blade geometry modelling predict reduced rotor performance. This is due to accurate assignment of lift and drag curves to each BEMT element. BEMT elements in the original model, particular ones towards the blade hub, were assigned lift curves which were inappropriate and over-predicted their performance. This had a particularly strong effect at high TSR, where near-hub sections have a proportionally greater effect on the turbine torque and power.
The flow conditions have significant impact on the BEMT results. Rotor performance is positively correlated to free stream velocity whilst turbulence intensity can change the operating region of the turbine. It is possible that different synthetic flow field methods could significantly influence the BEMT prediction of turbine performance of turbine performance, but that is beyond the scope of the study presented here.
Introducing the improved blade geometry modelling to the BEMT model has increased the computational time by approximately 10%. This is an acceptable increase in computational time in respect to added accuracy of the blade geometry modelling and the BEMT model prediction of rotor performance.
Increasing the accuracy of the BEMT model in predicting tidal stream turbine rotor performance will result in improved rotor blade design and reliability. This will in turn reduce the cost associated with tidal stream turbines, increasing their adoption as generators of low carbon energy.

3.4 Uniform flow with turbulence

In this section three rotor blades (Barltrop, ATIR, Oxford) are studied in flow field with constant mean current flow velocity with varying levels of turbulence. The Barltrop rotor is studied first where the BEMT numerical model is compared to laboratory results and another BEMT model. Secondly, the ATIR turbine is studied where the BEMT numerical model is compared to laboratory and GAD-CFD results. The last study is of the Oxford turbine, where the BEMT numerical model is compared against laboratory results and a number of different numerical models. This section aims to highlight the capabilities and limitations of the BEMT numerical model. The alternative numerical models which are compared against the BEMT model in these case studies are dictated by the available data.

3.4.1 Preliminary test

Barltrop: Details

The first steady-state case study is performed on the Barltrop rotor blade. Details of the Barltrop turbine and its laboratory testing are given in Section 3.1.4 and Section 3.2.3 respectively. The turbulence intensity of the flow is negligible, as the test was carried out in a still-water towing tank, and is presumed to be 0 in the synthetic flow fields used in the numerical model input. This uniform flow case study is included as a precursour to the Barltrop wave cases, with the aim to show good agreement between the BEMT model and laboratory prior to including waves. 16 individual flow fields (plug flows) are used as inputs for the numerical model, each with different flow velocity. Details of the steady-state flow field are given in Table 3.8. The rotor has a constant rotational speed of 200rpm and the current velocity is varied between 0-1.6m/s. Rotor performance predictions from the numerical model are compared to laboratory experiments and Barltrop BEMT numerical model [14, 15].

Table 3.8: Details of the parameters for the steady-state flow fields for the testing of the laboratory scale Barltrop turbine. The turbulence intensity is ≈0% and the rotor rotational speed is 200rpm for all cases.

No.	Current speed (m/s)	Tip speed ratio
1	0.1	41.88
2	0.2	20.94
3	0.3	13.96
4	0.4	10.47
5	0.5	8.38
6	0.6	6.98
7	0.7	5.98
8	0.8	5.24
9	0.9	4.65
10	1.0	4.19
11	1.1	3.81
12	1.2	3.49
13	1.3	3.22
14	1.4	2.99
15	1.5	2.79
16	1.6	2.62

Barltrop: Results & Discussion

Figure 3.28 shows torque and axial force results against current speed from the BEMT numerical model, Barltrop simulation, and Barltrop experiments. The Barltrop numerical

results are from a BEMT model. The Swansea BEMT numerical model matches the torque and axial force results from Barltrop experiments and simulations very well up to current speed of 1.3m/s, which equates to a TSR of 3.2. At current speeds higher than 1.3m/s, (i.e. in stall, TSR below 3), the Swansea BEMT model drastically under predicts both torque and axial force compared to Barltrop. The drop in torque and axial force in the Swansea BEMT model is due to the tip correction which is overly aggressive for the Barltrop rotor.

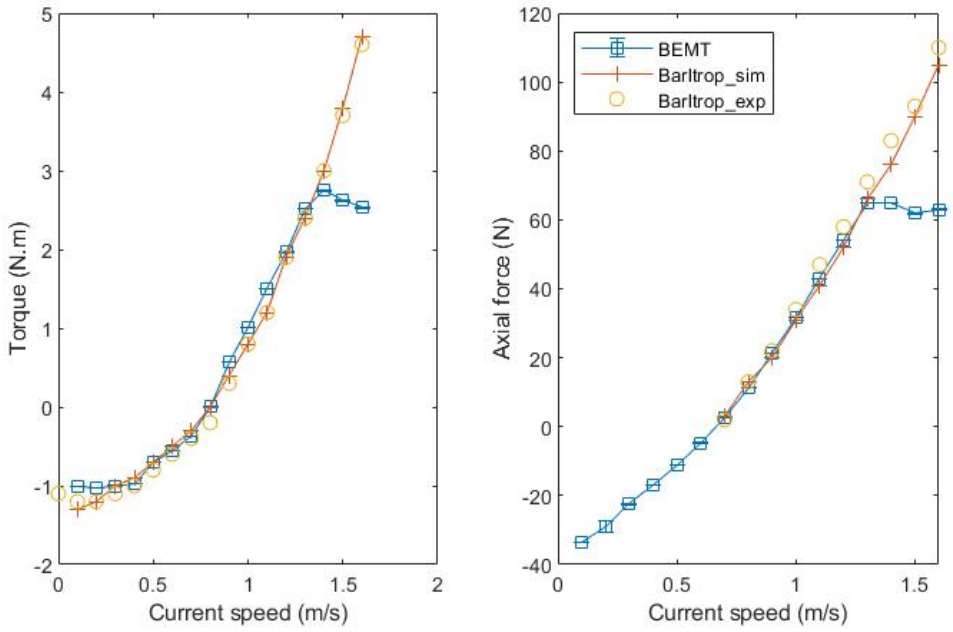

Figure 3.28: Torque and axial force results against current speed from the BEMT numerical model, Barltrop simulations, and Barltrop experiments.

3.4.2 BEMT vs GAD-CFD

Magallanes ATIR: Details

The second steady-state case study is performed on the Magallanes ATIR rotor blade and is intended to show the difference between the BEMT and GAD-CFD numerical models. The GAD-CFD numerical model is described in Section 2.2.6.1. All results from the GAD-CFD numerical model have been produced by C. Badoe. Detail of the Magallanes ATIR turbine and its laboratory testing are given in Section 3.1.2 and Section 3.2.1 respectively. This case study is in steady-state flow fields, i.e. uniform mean flow and turbulence without waves.

Details of the steady-state flow fields are given in Table 3.9. Flow fields with two different current speeds, each with three different turbulence intensities, are studied.

Table 3.9: Details of the parameters for the steady-state flow fields for the testing of the Magallanes ATIR.

No.	Current speed (m/s)	Turbulence intensity (%)
1	1.0	1.5
2	1.0	3.0
3	1.0	15.0
4	1.4	1.5
5	1.4	3.0
6	1.4	15.0

Unlike the Barltrop case described above, different TSR are achieved by changing the rotation rate of the rotor blades. The C_p and C_T results are averages of a time series of length 30s performed at each TSR.

Each test case has results from four sources; 1) original BEMT version 1.xx, 2) improved BEMT version 4.gr, 3) GAD-CFD, and 4) laboratory experiments. The BEMT version 1.xx (1) and GAD-CFD (3) numerical models assigns each rotor blade element with the same lift and drag characteristics, Figure 3.5, while the BEMT version 4.gr (2) assigns each rotor blade element with unique lift and drag characteristics based on their foil geometry and Reynolds number, Figure 3.6, as detailed in Section 3.3. Analysis of the original version 1.xx vs improved version 4.gr BEMT numerical models has already been done in Section 3.3, but due to the GAD-CFD using a single lift and drag polars (same as the BEMT version 1.xx), the BEMT version 1.xx is thus also included in this study for further comparison.

Magallanes ATIR: Results & Discussions

Figure 3.29 is a plot of C_P* and C_T* against TSR for the laboratory scale ATIR turbine from both the versions 1.xx and 4.gr BEMT numerical models, GAD-CFD model, and laboratory experiments in flow fields with current speed of 1.0m/s and turbulence intensities of (a) 1.5%, (b) 3%, and (c) 15%. Similarly, Figure 3.30 is for current speed of 1.4m/s. Standard deviation is shown as a shaded band around the mean value for the BEMT models and laboratory results, but this data was was not available from the GAD-CFD model due to difficulty running the model long enough to achieve statisticlly stability, and limitations with data storage. Good agreement in standard deviation is seen between the BEMT models and laboratory results across all cases which indicate that the performance variability due to the effects of turbulence is being correctly modelled in the BEMT. The

BEMT version 4.gr is the most accurate at predicting the optimum operating TSR in flow with uniform mean flow with turbulence.

The BEMT version 1.xx tends to predict optimum at 1 TSR higher than the laboratory results. This suggests a higher lift:drag ratio at low angle of attacks in the numerical model than in reality. This could be due to surface finish of rotor blades, twist and profile errors in the manufacturing of the blades, or poor estimation of drag. XFOIL is used to generate the lift and drag data which tends to underestimate the drag, especially at low Reynolds number. Another possible reason could be the simplification of the geometry in the BEMT version 1.xx numerical model. As the rotor rotates faster, the centre of productive torque action on the blade moves inwards. On the real blades, this is where the section becomes more like a cylinder, i.e., it is worse-performing hydrodynamically; but in the BEMT version 1.xx numerical model this stays as NACA-63418. In the BEMT version 4.gr, the portions of the blade with less hydrodynamically-effective sections are represented more accurately and therefore their contribution to rotor torque and power is reduced, which reduced the optimum TSR.
The prediction of the maximum $C_P{}^*$ is most accurately achieved by the BEMT models whilst the GAD-CFD model over-predicts by an average of $\sim$7%, which has also been observed in previous studies [76]. Implementation of GAD-CFD models tend to fall short of accurately determining tip losses, which are a function of the hydrofoil geometry. It is important to note that the prediction of maximum $C_P{}^*$ by the GAD-CFD is significantly different between the two mean flows; GAD-CFD over-predicts by $\sim$15% in the 1m/s flow fields but by only $\sim$7% in the 1.4m/s flow fields which we hypothesise to be related to Reynolds number effects meaning that sectional lift and drag coefficients are more accurate in the 1.4m/s flow cases. The maximum $C_P{}^*$ from the BEMT version 4.gr is always lower than that of the BEMT version 1.xx. This is due to the uniquely assigned lift characteristics of the rotor elements, which on average have a worse hydrodynamic performance. Generally, the laboratory experiments show that rotor performance decreases sharply in overspeed region which the BEMT version 1.xx and GAD-CFD numerical models fail to capture, but the BEMT version 4.gr replicates better. In the overspeed region, we have low and negative angle of attacks for outboard sections of the blades; an explanation of the failure of the models in capturing the sharp decrease in rotor performance could be due to poor estimations of drag and negative lift at negative angle of attacks. On the contrary, the rotor

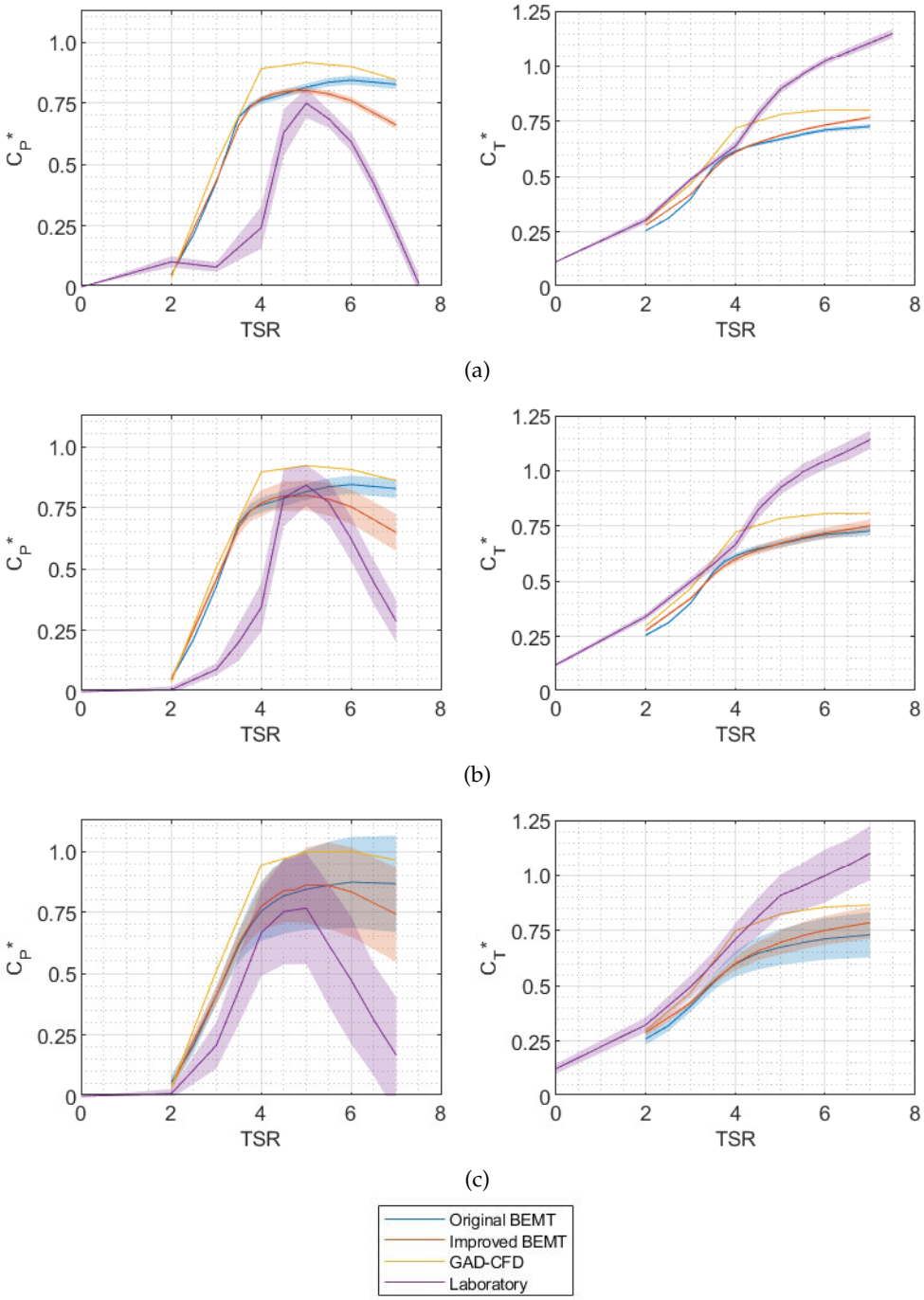

Figure 3.29: Plot of C_P* and C_T*, with errorbands representing standard deviation, against TSR for the laboratory scale ATIR turbine from both the original and improved (versions 1.xx and 4.gr) BEMT models, steady state GAD-CFD model, and laboratory experiments in flow fields with current speed of 1.0m/s and turbulence intensities of (a) 1.5%, (b) 3%, and (c) 15%.

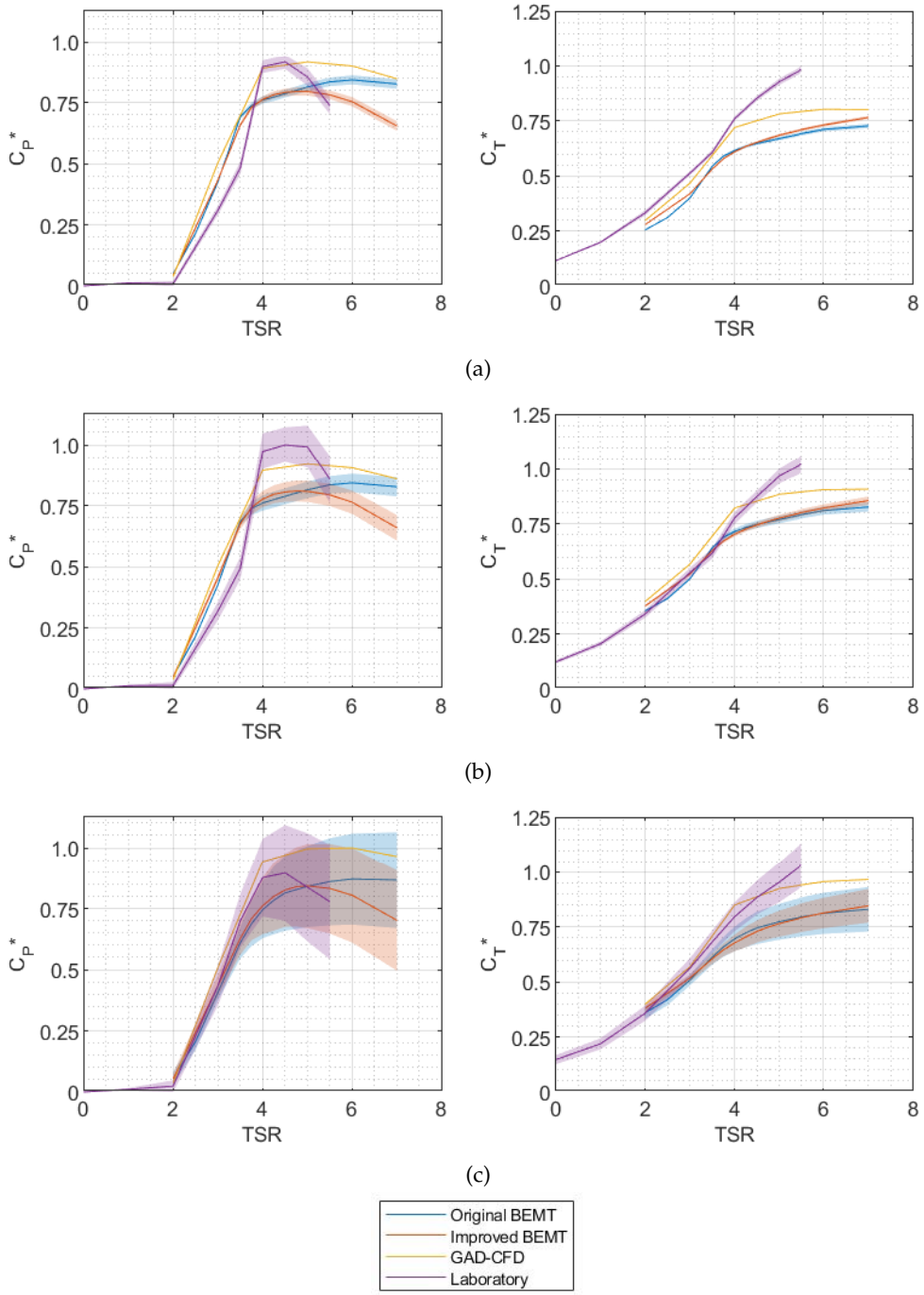

Figure 3.30: Plot of C_P* and C_T*, with errorbarband representing standard deviation, against TSR for the laboratory scale ATIR turbine from both the original and improved (versions 1.xx and 4,gr) BEMT models, steady state GAD-CFD model, and laboratory experiments in flow fields with current speed of 1.4m/s and turbulence intensities of (a) 1.5%, (b) 3%, and (c) 15%.

performance in the stall region is well matched by all the numerical models, particularly as the turbulence intensity increases.

C_T* plots for all flow cases follow the same trend. Up to a TSR of 4 the numerical models are in good agreement with the laboratory experiments, with the GAD-CFD model always predicting higher values than the BEMT models. Above a TSR of 4, the numerical models predict that the C_T* flattens whilst the laboratory experiments have C_T* continuing to increase. This could be due to high-induction effects which are accounted for in the BEMT model with the high induction and tip loss correction factors. Further research is needed to evaluate the effects of these correction factors which is outside the scope of the work presented in this thesis. The gap between the models can be explained by physically modelled high induction from the GAD-CFD vs. semi-empirical correction in the BEMT. Another possible cause for the difference between the BEMT and GAD-CFD models is the blockage caused by the interaction of the flow field in the GAD-CFD with the boundary conditions. There is no interaction between the flow field and the boundaries in the BEMT. Incorporating rotor element foil geometry and Reynolds number dependency in BEMT has very little impact on the C_T* predictions.

Increasing the flow field current speed has negligible effect on mean C_P* prediction from the numerical models, although a decrease of $\sim$5% in maximum C_P* is seen with increasing turbulence. A decrease of $\sim$4% in C_P is also seen in the laboratory experiments with increasing turbulence intensity, but contrary to the numerical models, laboratory experiments C_P* increases by $\sim$6% with current speed. Increasing the turbulence intensity has negligible effect on the C_T* predicted from the numerical models, but C_T* from the numerical models does increase by $\sim$12.5% with an increase in current speed from 1.0m/s to 1.4m/s. The measured C_T* from the laboratory experiments does not significantly change with either current speed or turbulence intensity.

The summary of the results are detailed in Table 3.10. The results are averaged across all cases in each study, i.e. the optimum TSR for the BEMT version 1.xx for study 1 is the average of the optimum TSR for the BEMT version 1.xx across all six cases presented. In the first study, uniform mean flow with turbulence, the best numerical model at predicting optimum TSR was the BEMT version 4.gr, whilst the GAD-CFD and the BEMT version 4.gr numerical models are equally as good at predicting C_P* between TSR 3-6 and its maximum. The GAD-CFD model tends to over-predict by $\sim$5% whilst the BEMT version 4.gr tends to under-predict by $\sim$5%.

Table 3.10: ATIR steady-state case study; summary of the results (averaged across all cases) from original and improved (versions 1.xx and 4.gr) BEMT numerical models, GAD-CFD numerical model, and laboratory experiments.

Source	Optimum TSR (average of 6 cases)	C_P* (average of 6 cases) Maximum	% to laboratory (TSR 3-6)
Original BEMT version 1.xx	5.25	0.88	79
Improved BEMT version 4.gr	4.50	0.85	84
GAD-CFD	5.00	0.95	85
Laboratory	4.50	0.90	100

Magallanes ATIR: Conclusions

An original and improved (versions 1.xx and 4.gr) BEMT, and GAD-CFD numerical models have been used to predict the performance of the Magallanes ATIR tidal stream turbine. Comparison of the results from the numerical models have been made to laboratory experiments. The performance of the ATIR turbine in flow fields with uniform mean flow with turbulence was well captured by both the original and improved BEMT and GAD-CFD models in stall and optimum regions, with accuracy ∼95%. In the overspeed region the BEMT version 1.xx and GAD-CFD numerical models fail to capture the sharp drop off in performance seen from the laboratory experiments. The BEMT version 4.gr is ∼7% better at predicting the the rotor performance in the overspeed region due to the assignment of unique lift and drag characteristics to each rotor element based on their geometry and Reynolds number.

3.4.3 BEMT vs alternative numerical models

Oxford blind test: Stage I - steady flow blind predictions: Detail

Detail of the Oxford blind test turbine and its laboratory testing are given in Section 3.1.1 and Section 3.2.2 respectively. Stage 1 comprised of 13 clean (TI 0%) and 11 grid (TI 3.1%) cases. The parameters of these cases are shown in Tables 3.11 & 3.12 respectively. All clean cases have flow velocity of 1m/s, whilst all grid cases have flow velocity of 0.9207m/s, turbulence intensity of 3.1%, and integral lengthscale of 0.037m. The experimental parameters are summarised in Table 3.13.

The BEMT numerical model is used to predict the force and moment distributions in x, y, and z directions along the rotor blade radius. Subsequently, total rotor forces, moments, and power and thrust coefficients are calculated. The coordinate system used for the forces and moments is shown in Figure 3.31.

Table 3.11: Parameters for the benchmark clean cases. All cases have flow velocity is 1m/s.

Case	RPM	TSR
Clean 1	48	4.02
Clean 2	54	4.52
Clean 3	60	5.03
Clean 4	64	5.36
Clean 5	66	5.53
Clean 6	69	5.78
Clean 7	72	6.03
Clean 8	78	6.53
Clean 9	80	6.70
Clean 10	84	7.04
Clean 11	86	7.20
Clean 12	90	7.54
Clean 13	94	7.87

Table 3.12: Parameters for the benchmark grid cases. All cases have flow velocity of 0.9207m/s, turbulence intensity of 3.1%, and integral lengthscale of 0.037m.

Case	RPM	TSR
Grid 1	43	3.91
Grid 2	49	4.46
Grid 3	54	4.91
Grid 4	59	5.37
Grid 5	62	5.64
Grid 6	64	5.82
Grid 7	68	6.19
Grid 8	70	6.37
Grid 9	76	6.92
Grid 10	81	7.37
Grid 11	85	7.73

Table 3.13: Summary of the benchmark experimental parameters.

Parameter	Units	Value
Turbine Geometry		
Turbine Diameter	m	1.6
Nacelle Diameter	m	0.2
Tip Clearance	m	0.354
Tow Tank Geometry		
Tow Tank Width	m	12.2
Tow Tank Depth	m	5.4
Global Blockage Ratio	%	3.05
Water Properties		
Water Temperature	°	12.97
Water Density	kg/m^3	999.4
Water Dynamic Viscosity	Pa.s	1.2160E-03

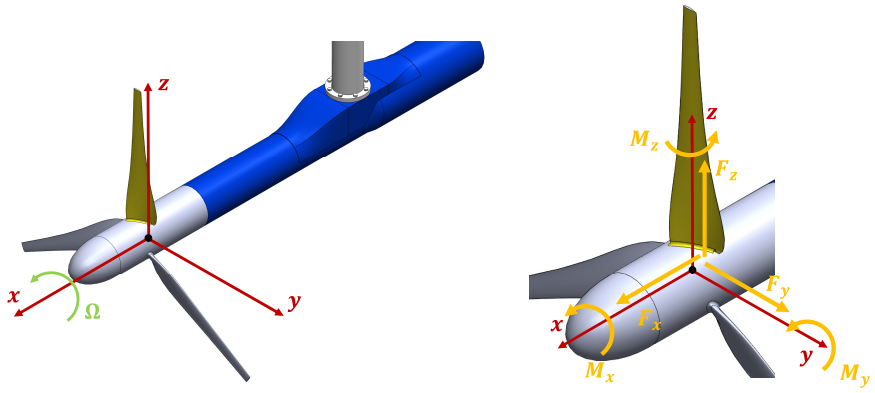

Figure 3.31: Forces and moments coordinates system for the benchmark cases.

Oxford blind test: Stage I - steady flow blind predictions: Results & Discussion

Plots of the distribution of thrust and torque per element length along the length of the benchmark rotor blade for the clean and grid cases from the BEMT numerical model are shown in Figures 3.32 & 3.33 respectively.

As expected, increasing TSR increases thrust whilst decreasing torque for both clean and grid cases. The current flow velocities are slightly different for the clean and grid case, 1.0m/s and 0.9207m/s respectively, which accounts for the slight difference in magnitude of thrust and torque between both clean and grid cases. It is also clear to see the consequence of the tip correction factor in Figures 3.32 & 3.33. The sudden change in thrust and torque towards the tip (r/R >0.8) is due to the tip correction factor. As the TSR increases, so does the number of elements affected by the implementation of the tip correction factor, with the span affected increasing inwards towards the hub.

BEMT numerical prediction for the whole rotor forces, moments, and power and thrust coefficients for the benchmark clean and grid cases are given in Tables 3.14 & 3.15. No values for the Fz force and Mz moment are given as they are not computable with the BEMT numerical model. Figures 3.34 & 3.35 show plots of Cp and Ct against TSR from various BEM model submissions to the benchmark project for the clean and grid cases respectively.

The BEMT numerical model best matches the experimental results for thrust. The majority of BEMT thrust predictions are within 2.5% of experimental results. The only major

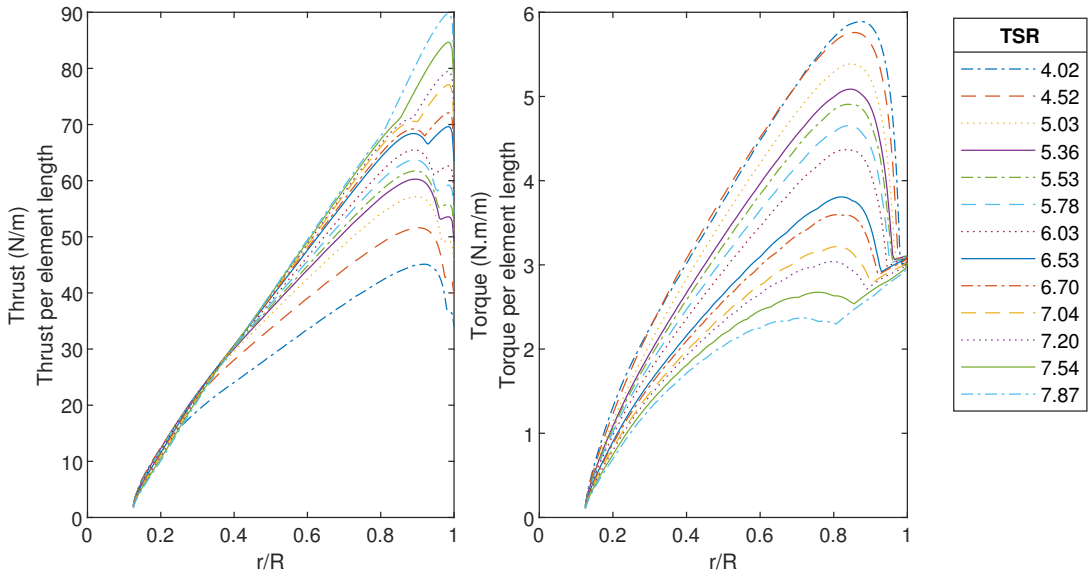

Figure 3.32: Plot of thrust and torque distribution along the length of the benchmark rotor blade for the clean cases.

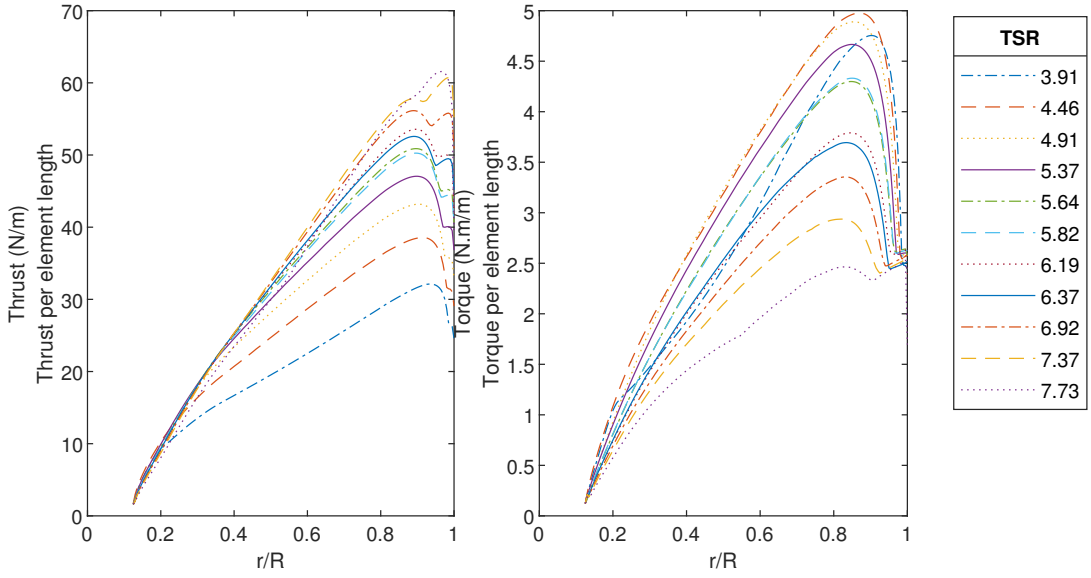

Figure 3.33: Plot of thrust and torque distribution along the length of the benchmark rotor blade for the grid cases.

Table 3.14: BEMT results for whole rotor forces, moments, and power and thrust coefficients for the benchmark clean cases.

Case	Fx [N]	Fy [N]	Mx (N.m)	My (N.m)	Ct	Cp
Clean 1	633.15	179.92	80.27	332.53	0.62	0.39
Clean 2	727.24	178.03	79.33	383.03	0.71	0.44
Clean 3	789.08	165.28	73.72	419.39	0.77	0.45
Clean 4	820.33	155.99	69.51	438.69	0.80	0.45
Clean 5	834.57	151.15	67.28	447.69	0.81	0.45
Clean 6	853.64	144.04	63.99	460.01	0.83	0.45
Clean 7	870.92	137.07	60.74	471.41	0.85	0.45
Clean 8	901.37	123.66	54.47	492.26	0.88	0.43
Clean 9	910.75	119.28	52.42	498.91	0.89	0.43
Clean 10	928.73	110.85	48.49	512.01	0.91	0.42
Clean 11	937.09	107.06	46.74	518.22	0.91	0.41
Clean 12	955.43	99.49	43.31	532.12	0.93	0.40
Clean 13	975.16	92.92	40.46	547.17	0.95	0.39

deviation from the BEMT and experiment results for thrust is seen at the overspeed region for the grid cases where the BEMT underpredicts thrust by 12% in comparison to the experimental results over the TSR range 6.5-8. The optimum C_p is seen at TSR of 6 for the experimental clean and grid cases. The BEMT numerical model predicts optimum C_p at TSR of 5.5 for the clean case and TSR 5.75 for the grid cases. The BEMT model under predicts C_p by $\sim$10% for the clean cases and over predicts C_p by $\sim$10% for the grid cases. The BEMT numerical model used in this thesis, i.e. Swansea University BEM, is compared against other BEM submissions for the benchmark project, plotted in Figures 3.34 & 3.35. It shows that Swansea University BEM numerical model is better than most other BEM models in predicting the torque and thrust of clean and grid cases. The differences in BEM models are due to several components, such as implementation of correction factors, lift and drag polars, modelling of the flow field, and the minimisation routine to find the induction factors from the blade element and momentum theory.

Table 3.15: BEMT results for whole rotor forces, moments, and power and thrust coefficients for the benchmark grid cases.

Case	Fx [N]	Fy [N]	Mx (N.m)	My (N.m)	Ct	Cp
Grid 1	439.75	129.34	59.19	231.01	0.51	0.30
Grid 2	542.12	151.91	67.86	284.72	0.62	0.40
Grid 3	605.68	148.09	66.74	319.91	0.70	0.43
Grid 4	650.47	140.85	63.39	345.78	0.75	0.44
Grid 5	687.88	129.09	58.29	369.29	0.79	0.45
Grid 6	679.97	129.38	58.47	364.82	0.78	0.44
Grid 7	708.48	115.22	51.83	383.74	0.82	0.43
Grid 8	706.21	115.36	51.51	381.44	0.81	0.43
Grid 9	738.50	105.10	46.96	403.30	0.84	0.42
Grid 10	756.96	96.05	42.65	416.42	0.86	0.40
Grid 11	729.51	81.64	36.27	405.11	0.83	0.36

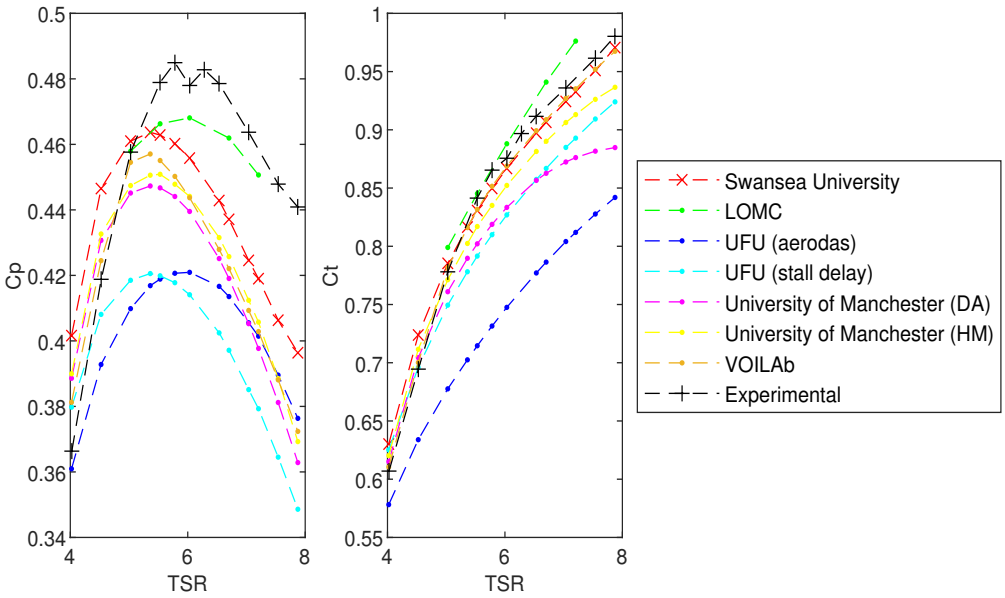

Figure 3.34: Plot of Cp and Ct against TSR for various BEM submissions to the benchmark project for the clean cases.

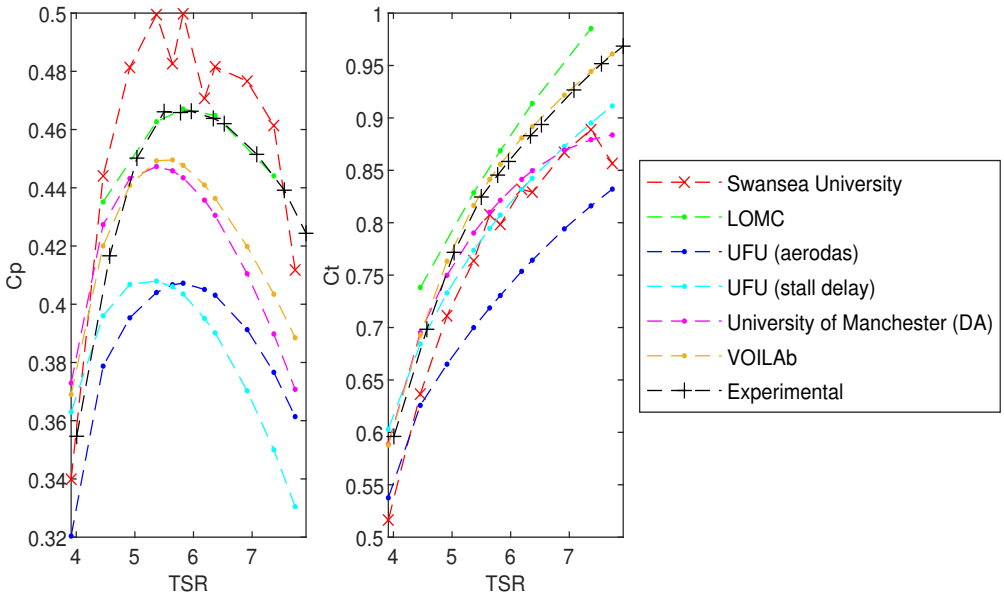

Figure 3.35: Plot of Cp and Ct against TSR from various BEM submissions to the benchmark project for the grid cases.

3.4.4 Discussion & Conclusions

The twist and chord distribution along the radial length of the five tested rotor blades, (Magallanes ATIR, Sabella D12, IFREMER, Oxford, and Barltrop), are plotted collectively in Figure 3.36. The difference in the twist and chord distribution between rotor blades are clear to see in Figure 3.36. Although each rotor blade has different distributions of twist and chord, all have chord reducing and twist increasing towards the tip.

Plots of C_p against TSR from the BEMT numerical model and laboratory experiments for the five tested rotor blades are shown in Figure 3.37. Similarly, plots of C_t against TSR for the same cases are shown in Figure 3.38. To maintain the anonymity of the commercially sensitive rotor blades, the exact plotted cases are not stated and the C_p and C_t ticks have been removed from the y-axis. All cases are from the uniform mean flow with turbulence study and have small turbulence intensity levels. Summary of optimum performance from the BEMT numerical model and laboratory experiments are give in Table 3.17.

C_p results from the BEMT model are very close to experimental testing for all rotor blades, with the exception of the IFREMER turbine. Although the BEMT model underpredicts the C_p of the IFREMER turbine, it does accurately predict the TSR of optimum C_p. This

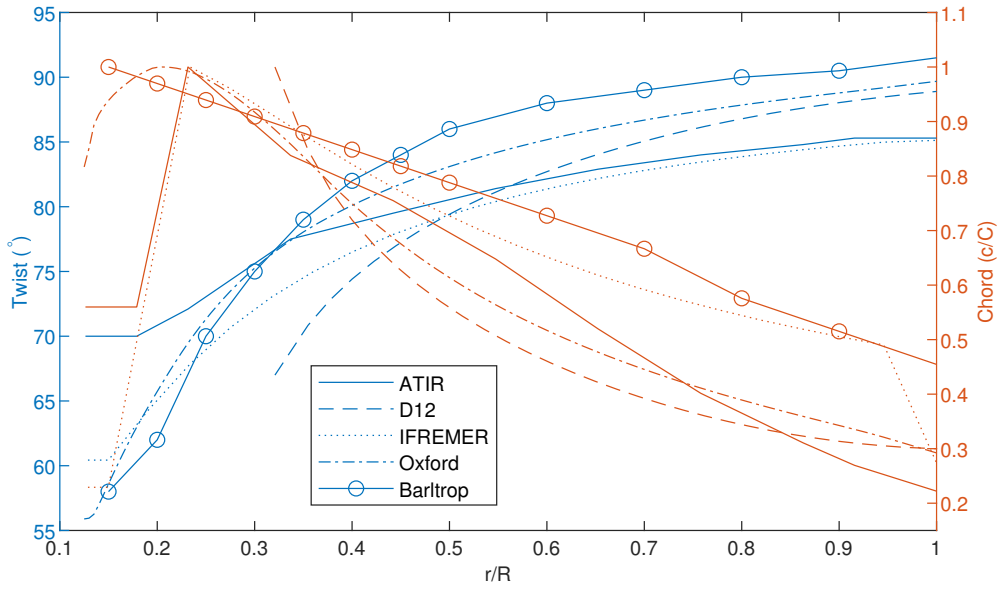

Figure 3.36: Plot of twist and chord distribution along the radial length of five rotor blades; Magallanes ATIR, Sabella D12, IFREMER, Oxford, and Barltrop.

indicates that it is likely inaccurate lift and drag polars which are giving lower C_p values. The TSR of optimum performance is correlated to the twist along the rotor blade. Table 3.16 compares the optimum TSR against maximum twist of the rotor blades. A trend of decreasing optimum TSR with increasing maximum twist is seen with the rotor blades, with the exception of the Oxford rotor blade. The ATIR, D12, IFREMER, and Barltrop rotor blades all have very similar hydrofoil profile, but the Oxford rotor blade is significantly different, causing the difference seen in optimum TSR and twist correlation. If the maximum twist of the Oxford rotor blade was increased (i.e. pitching up of rotor blade), then the optimum TSR would decrease. This would be true for any rotor blade beacause for a more twisted blade, outboard sections will approach low/zero angle of attack at comparatively lower TSR values. This would result in their hydrodynamic lift (and therefore their primary contribution to overall rotor torque/power) decreases more rapidly with TSR than for a blade with less twist.

Another observation of the power curves from Figure 3.37 is that the maximum C_p increases with higher optimum TSR. The more the rotor blades are pitched downwards (i.e. less twist), the greater the power coefficient. A disadvantage of pitching down a rotor blade to gain greater power coefficient is the need for higher rotor rotational speed

Table 3.16: Comparison of rotor blades optimum TSR against maximum twist.

Rotor blade	Optimum TSR	Maximum twist (deg)
Barltrop	3.5	91.5
Sabella D12	4.0	88.9
IFREMER	4.5	85.1
Magallanes ATIR	5.0	85.1
Oxford	5.8	89.7

Table 3.17: Summary of optimum performance from BEMT numerical model and laboratory experiments for the five studied rotor blades.

Rotor blade	Optimum TSR		Difference in maximum C_p between BEMT numerical model and laboratory experiments (%)
	BEMT numerical model	Laboratory experiment	
Magallanes ATIR	5.00	5.0	6.4
Sabella D12	4.00	4.0	3.5
IFREMER	4.50	4.5	15.0
Oxford	5.40	5.8	4.4
Barltrop	3.25	3.5	4.2

(requiring a gearbox instead of a direct drive system), greater forces on rotor components, and a need for a more energetic site.

The C_t curves are all very similar with good comparison from the BEMT numerical model to laboratory experiments across the whole TSR for the majority of rotor blades. A notable exception to this general result is the significant difference in C_t from the BEMT numerical model and the laboratory experiments in the overspeed region of for the Magallanes ATIR rotor blade. Many factors could be responsible for this discrepancy in the BEMT numerical model (e.g. inaccurate lift and drag polars, correction factors, or flow field representation). The discrepancies could also be due to limitations of the laboratory experiments (e.g. inaccurate measurement of flow conditions or manufacture of rotor blades). There is suspicion that the Magallanes ATIR rotor blades used in the laboratory experiments were not manufactured accurately and had differing twist and chord distributions to the design. This would be an obvious source of inaccuracy between the BEMT numerical model and the laboratory experiments.

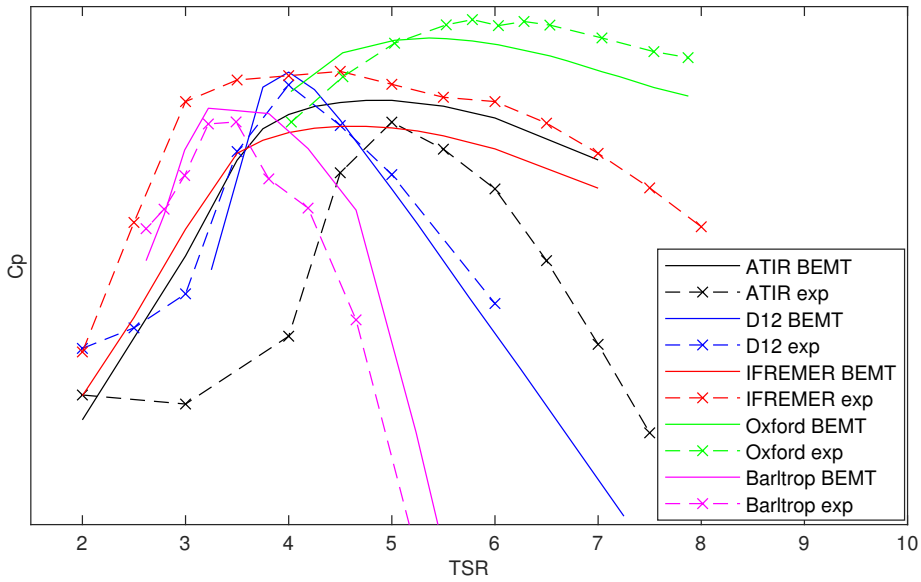

Figure 3.37: Plot of Cp against TSR from BEMT numerical model and laboratory experiments for five tested rotor blades; Magallanes ATIR, Sabella D12, IFREMER, Oxford, Barltrop.

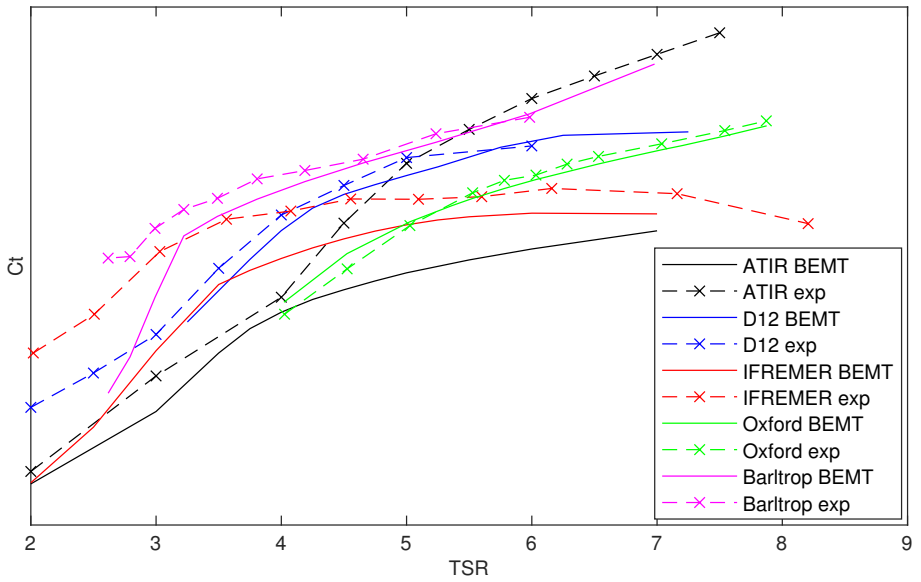

Figure 3.38: Plot of Ct against TSR from BEMT numerical model and laboratory experiments for five tested rotor blades; Magallanes ATIR, Sabella D12, IFREMER, Oxford, Barltrop.

3.5 Transient

In this section four rotor blades (IFREMER, Barltrop, ATIR, and D12) are studied in flow fields with constant mean flow with turbulence and waves. The first study looks at quantifying the effect of including added mass effects in the BEMT numerical model on its predictions of performance and loads of the IFREMER turbine. The second study looks at the Barltrop turbine where the BEMT numerical model predictions are compared to Barltrop BEMT simulations and Barltrop laboratory experiments. In this study, the BEMT flow fields have waves but no turbulence to improve the readability and validation of its predictions of turbine performance in waves. The third study looks at the ATIR turbine, where predictions from the BEMT and GAD-CFD numerical models are compared to laboratory experiments. Lastly, the D12 turbine is studied, where predictions from the BEMT numerical model is again compared to laboratory results. This section aims to highlight the capabilities and limitations of the BEMT numerical model in predicting turbine loads and performance in flow fields with turbulence and waves.

3.5.1 Sensitivity of IFREMER turbine to added mass

In this study we quantify the contribution of the inertia term to the overall turbine torque and thrust predictions from the BEMT numerical model in transient flow fields with turbulence and waves, as described in Section 2.2.4.2. The control scheme employed for the BEMT numerical model for this study is a constant rotational rate. The acceleration of the flow field is calculated by taking the difference in velocity between the current and previous time step. The acceleration of the flow field is used to compute the inertia "added mass" forces. The laboratory scale IFREMER-LOMC turbine, rotor radius of 0.343m, is used as the rotor for this study as it is well tested and studied. Description of the IFREMER-LOMC turbine is given in Section 3.1.5.

The preliminary test case has a generic BEMT input flow field which has a current speed of 1.0m/s, turbulence intensity of 2.5%, and a monochromatic wave height and period of 0.10m and 1.2s respectively. The rotational rate of the rotor is kept at a constant 11rad/s which is the equivalent to its optimum TSR in steady flow field with current speed of 1m/s. Shown in Figure 3.39 are time series of predicted torque and thrust from the BEMT numerical model. Plotted on each diagram are the contributions from the hydrodynamic and added mass terms respectively, and the combined total output.
The results show us that the added mass contribution to the rotor torque is negligible. The

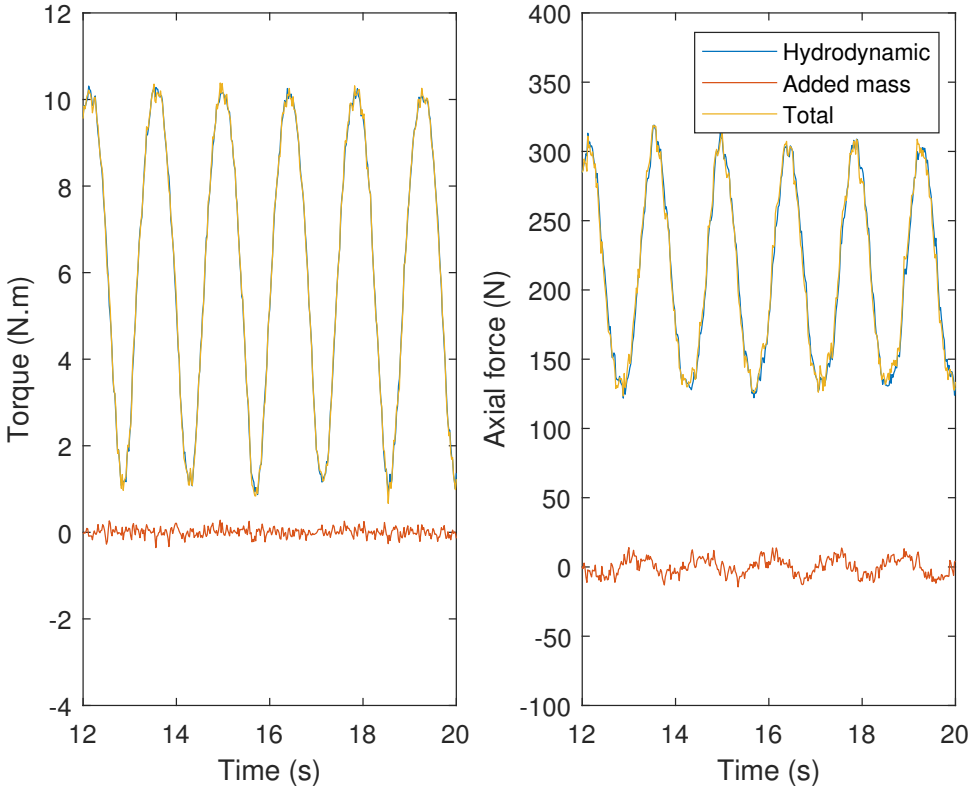

Figure 3.39: Time series plot of BEMT numerical model results for torque and thrust of the IFREMER-LOMC laboratory scale turbine in a flow field with 2.5% turbulent intensity and a monochromatic wave of height and period of 0.1m and 1.2 respectively.

maximum torque of the added mass is 2% of the hydrodynamic term. This is expected as waves are co-linear to the current direction, travelling at a perpendicular direction to the rotor rotation plane, resulting in fluid particle acceleration in the rotor plane due to waves to be small in comparison to rotor speed.

The contribution from the added mass to the rotor axial force is greater. As previously described, this is expected due to the waves travelling perpendicular to the rotor rotation plane. The peak value for the added mass and hydrodynamic axial force are 15.8N and 322.7N respectively. This equates to the maximum axial force added mass term being 4.9% of that of the hydrodynamic term.

It is also seen in the thrust loads that the hydrodynamic and added mass terms are 90° out of phase. The added mass terms are dependent on the fluid acceleration whilst the hydrodynamic terms are dependent on the fluid velocity, thus a 90° out of phase is expected.

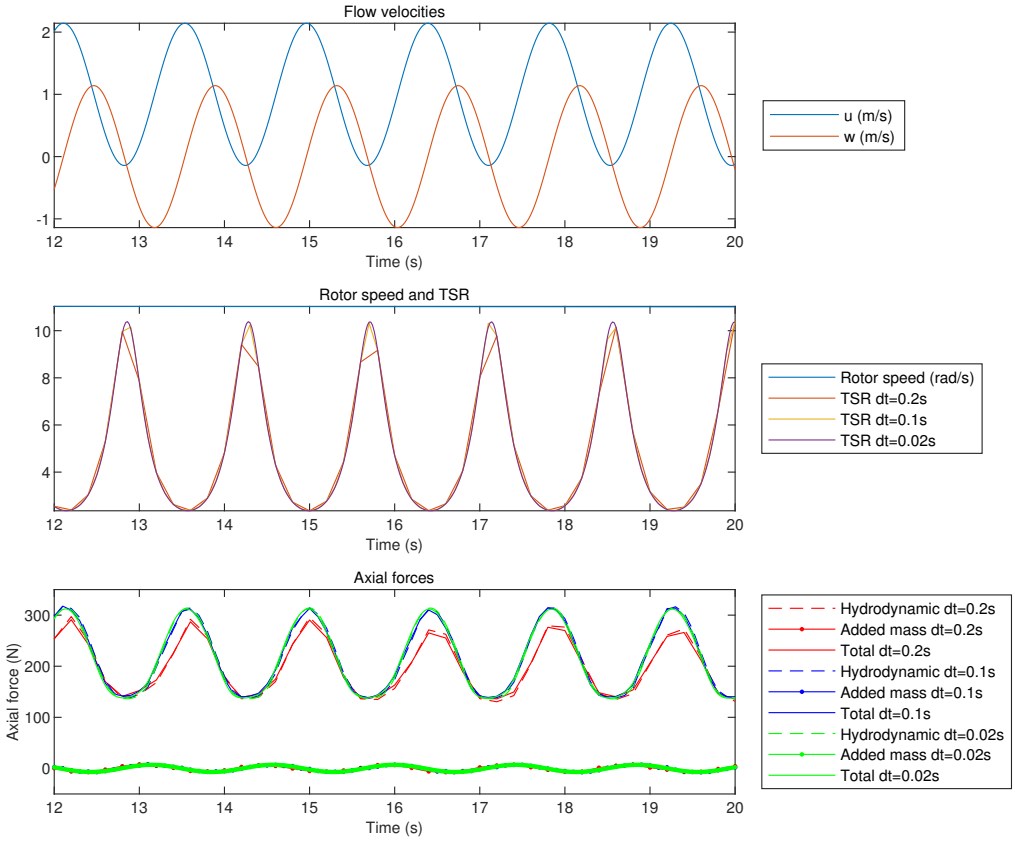

Figure 3.40: IFREMER BEMT added mass study: time series plots of a) vertical and horizontal flow velocities, b) rotor rotational speed and TSR, and c) axial forces results with varying time steps.

The added mass contribution results in the maxima and minima of total rotor axial force to be smaller than that seen from the hydrodynamic term. Due to the added mass term having a mean of zero, the average axial force for the total and hydrodynamic terms are the same.

Time step sensitivity

A time step sensitivity study was undertaken to find the most appropriate time step for the BEMT numerical model. The cases where for the IFREMER-LOMC turbine in flow condition with current speed of 1.0m/s, wave of 0.1m height and 1.2s period, with no turbulence. Flow fields with no turbulence are used in this time step sensitivity study to improve the interpretation of the results. Three different time steps are tested in the BEMT numerical model; 0.2s, 0.1s, and 0.02s. 0.02s is the resolution of the flow fields thus

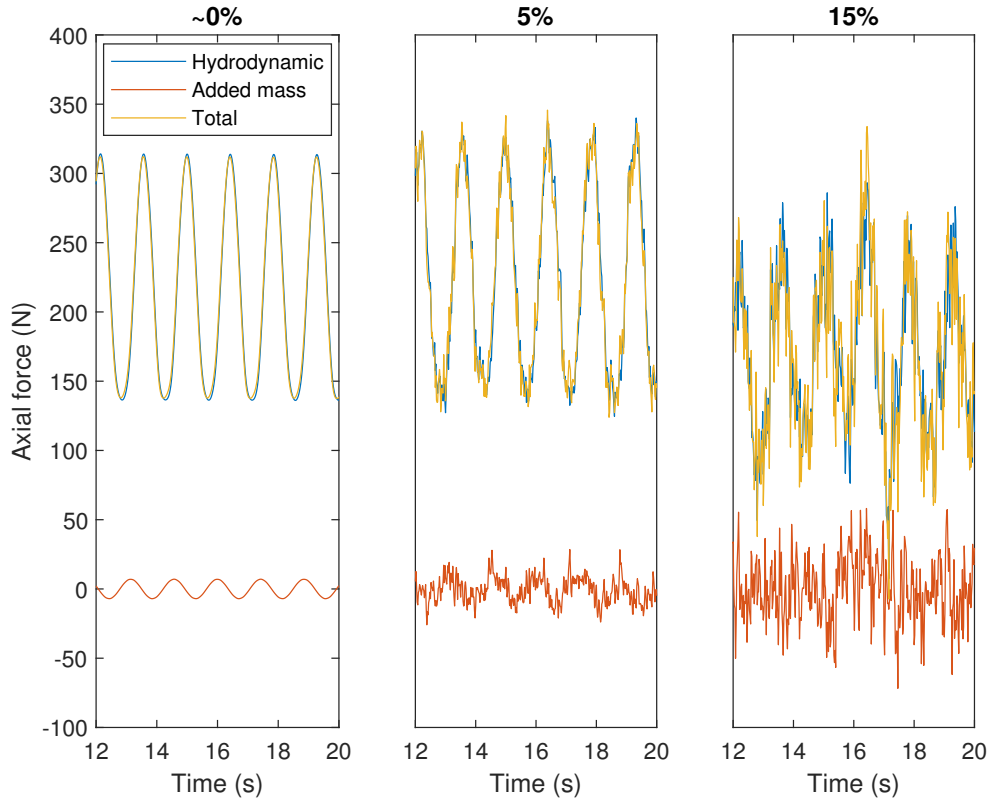

Figure 3.41: Added mass and hydrodynamic axial force results from the BEMT numerical model in flow fields with turbulence levels of 0%, 5%, and 15%.

testing a smaller time step in the BEMT numerical model would result in interpolation of the flow field and not improving the accuracy of capturing the flow field dynamics. BEMT numerical model time series plots of a) vertical and horizontal flow velocities, b) rotor rotational speed and TSR, and c) axial forces results with varying time steps for the IFREMER rotor blade are shown in Figure 3.40. When using a time step of 0.2s, the BEMT numerical model fails to capture the complete dynamic load effect. It captures the period of the wave but fails in most wave cycles to attain the maximum and minimum values. On the other hand, when using a time step of 0.02s, the same resolution as the flow field, the BEMT numerical model computes identical results for each wave cycle.

Turbulence sensitivity

The BEMT numerical model was run using flow fields with varying turbulence intensities of between 0% and 15%, to deduce the influence of turbulence on the added mass terms.

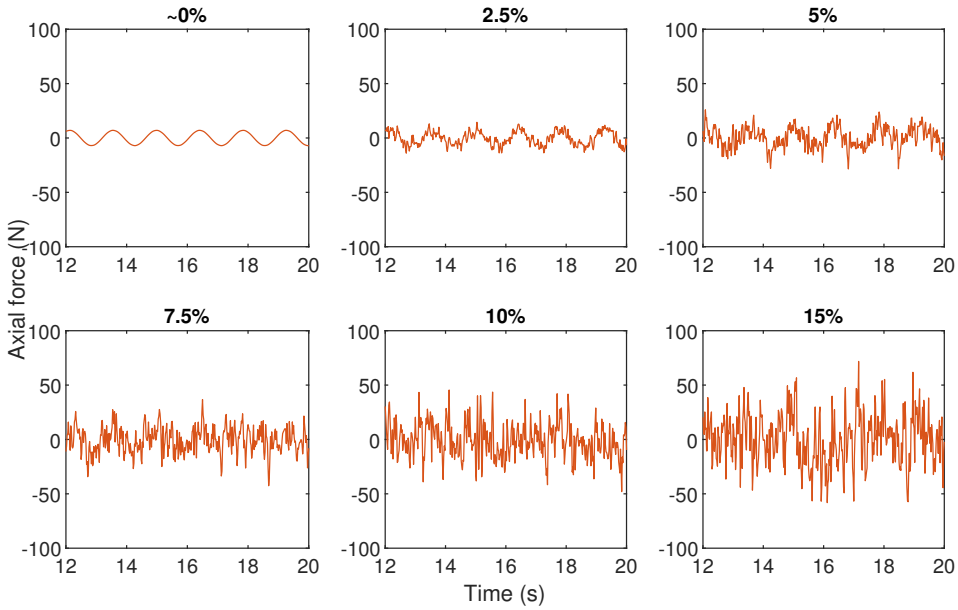

Figure 3.42: Added mass axial force results from the BEMT numerical model in flow fields with turbulence levels of 0%, 2.5%, 5%, 7.5%, 10%, and 15%.

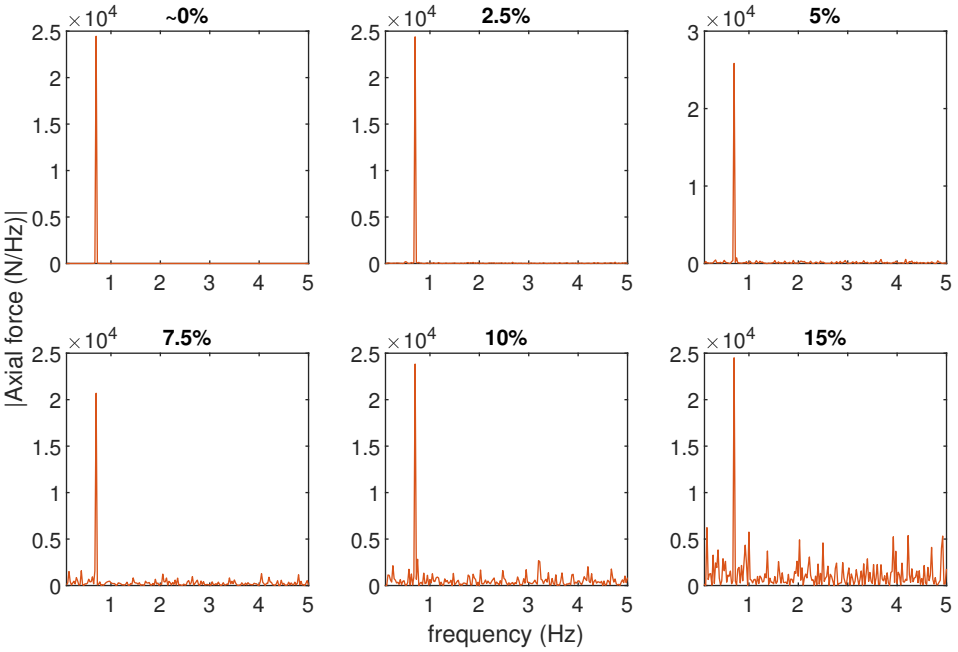

Figure 3.43: Added mass axial force results in the frequency domain from the BEMT numerical model in flow fields with turbulence levels of 0%, 2.5%, 5%, 7.5%, 10%, and 15%.

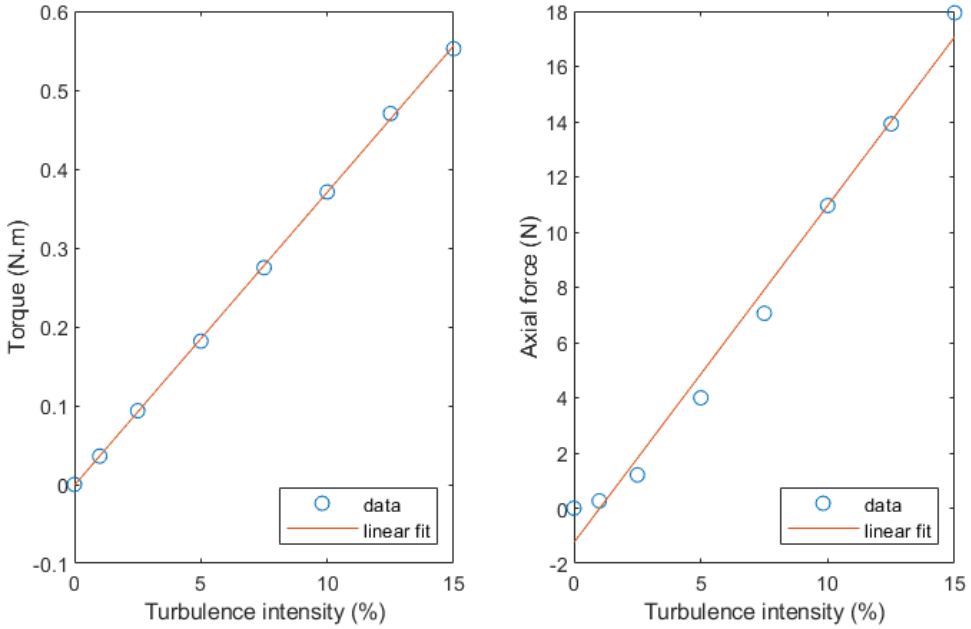

Figure 3.44: Standard deviation of added mass torque and axial force from BEMT numerical model results in flow fields with varying turbulence intensities.

The wave properties are kept constant across the flow fields and are the same as previously described. Figure 3.41 shows added mass and hydrodynamic axial force results from the BEMT numerical model in flow fields with turbulence levels of 0%, 5%, and 15%. Increasing the turbulence intensity of the flow field increases the magnitude of the added mass axial force. The mean total axial force are 214.48N, 224.03N, and 166.29N respectively for the 0%, 5%, and 15% cases. The mean axial force for the 15% case is significantly lower than the 0% and 5% cases, which is due to rotor TSR moving from optimum to overspeed region, decreasing its performance. In flow fields with higher TI, the fluctuations in rotor TSR are higher upwards than downwards.

Figure 3.42 shows the added mass axial force results from the BEMT numerical model in flow fields with turbulence levels of 0%, 2.5%, 5%, 7.5%, 10%, and 15%. The flow fields have a mean current velocity of 1m/s and waves with frequency and height of 0.83Hz and 0.1m respectively. The mean value is unchanged from zero for all cases but the standard deviation increases with turbulence intensity. This can also be seen in Figure 3.43 which is Figure 3.42 plotted in the frequency domain. A clear peak is seen at 0.83Hz, which corresponds to the frequency of the wave. As the turbulence intensity increases we see

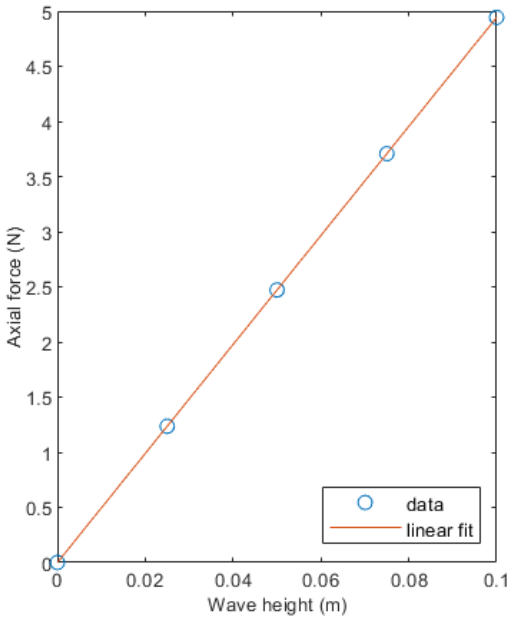

Figure 3.45: Added mass axial force standard deviation in flow fields with varying wave heights.

larger magnitude fluctuations in force across the whole frequency range. The standard deviation of the added mass torque and axial force results are plotted against turbulence intensities in Figure 3.44. Included in the plot is a linear fit which clearly shows that there is a linear correlation between turbulence intensity of the flow field and the standard deviation of the added mass torque and axial force.

Wave height sensitivity

Flow fields with varying wave heights were used in the BEMT numerical model to deduce its effect on the added mass terms. Unsurprisingly, there was a perfect linear correlation (+1 coefficient) between wave height and the added mass terms. This is due to the added mass term being proportional to the velocity of the flow particle, as is shown in Equation 2.54 and Equation 2.53. Figure 3.45 shows added mass axial force standard deviation in flow fields with varying wave heights.

Conclusions

A case study to establish the sensitivity of the IFREMER rotor blade to added mass (i.e. acceleration forces) in the BEMT numerical model has been conducted and has shown that;

- The added mass has negligible contribution to the rotor torque, with the torque from the added mass being 2% of the hydrodynamic term.
- The contribution of the added mass on the rotor thrust is greater as the waves travel perpendicular to the rotor rotation plane. The thrust from the added mass is 4.9% of the hydrodynamic term.
- The hydrodynamic and added mass terms are 90° out of phase. The added mass terms are dependent on the fluid acceleration and the hydrodynamic terms are dependent on the fluid velocity.
- As a result, the maximum and minima of total rotor thrust is smaller with the inclusion of added mass terms, but the average rotor thrust is unchanged as the added mass term has a average of zero.
- Time step sensitivity study has shown that a time step of 0.02s is necessary to fully capture the flow field dynamics which has a 1.2s period wave; in particular, a coarser timestep leads to significant underestimation of peak rotor thrust loads.
- There is a linear correlation between added mass thrust and both turbulence and wave height of the flow field.

3.5.2 Barltrop

Barltrop: Details

Details of the Barltrop rotor blade and the laboratory test facility are given in Section 3.1.4 and Section 3.2.3 respectively. The first wave comparison is for a constant 150rpm rotor rotational speed study, where the current velocity was incrementally changed between 0.2-1.3m/s. The waves in the flow fields were 150mm high with a 0.50Hz frequency. 12 individual flow fields are used as inputs into the numerical model, each with different current velocity.

The second transient study of Barltrop turbine was with time series results for a constant rotor rotation speed of 90rpm. Four wave heights were tested, 0, 35, 84, and 126mm, all with frequency of 0.833Hz in current velocity of 0.7m/s. Details of the transient flow fields for the different studies are given in Table 3.18. The first transient study will be compared to both Barltrop experimental and simulation results, whilst the second transient study will only be compared to Barltrop experimental results due to absence of Barltrop

simulation results. The flow fields of the BEMT numerical model in both studies will have a turbulence intensity of 0% to improve the readability of the results, helping to validate to models ability to predict turbine performance in flow fields with waves.

Table 3.18: Details of the parameters for the transient flow fields for the testing of the laboratory scale Barltrop turbine.

No.	Current speed (m/s)	Turbulence intensity (%)	Rotational speed (RPM)	Tip speed ratio	Wave height (m)	Wave frequency (Hz)
1.1	0.2	≈5	150	15.71	0.15	0.50
1.2	0.3	≈5	150	10.47	0.15	0.50
1.3	0.4	≈5	150	7.86	0.15	0.50
1.4	0.5	≈5	150	6.28	0.15	0.50
1.5	0.6	≈5	150	5.24	0.15	0.50
1.6	0.7	≈5	150	4.49	0.15	0.50
1.7	0.8	≈5	150	3.93	0.15	0.50
1.8	0.9	≈5	150	3.49	0.15	0.50
1.9	1.0	≈5	150	3.14	0.15	0.50
1.10	1.1	≈5	150	2.86	0.15	0.50
1.11	1.2	≈5	150	2.62	0.15	0.50
1.12	1.3	≈5	150	2.42	0.15	0.50
2.1	0.7	≈5	90	2.69	0	0
2.2	0.7	≈5	90	2.69	0.035	0.83
2.3	0.7	≈5	90	2.69	0.084	0.83
2.4	0.7	≈5	90	2.69	0.126	0.83

Barltrop: Results & Discussion

Torque and axial force results for the BEMT numerical model, Barltrop simulation, and Barltrop experiments for the first wave study (constant rotational rate of 150rpm and varying current flow velocities are plotted against current speed) are shown in Figure 3.46. The BEMT numerical model torque and axial force results match Barltrop well up to current speed of 1.1m/s, TSR 2.9, following a similar trend to the still water case. Above current speed of 1.1m/s, below TSR 2.9, the BEMT numerical model underpredicts in comparison to Barltrop. Errorbars are included for the BEMT numerical model results which tend to decrease for both torque and axial force with increasing current speeds.

In the second wave study, a comparison is made to Barltrop et al. time series results. Due to experiment instrument limitations Barltrop et al. could only measure positive axial force. Torque and axial force results for three wave cycles from the BEMT numerical model and Barltrop laboratory experiments are plotted in Figure 3.47. The solid line are results from the BEMT numerical model and the dashed line is Barltrop laboratory results. As expected, torque and axial force variability from both the BEMT numerical model and Barltrop laboratory experiments increase with wave height. Every wave cycle is exactly

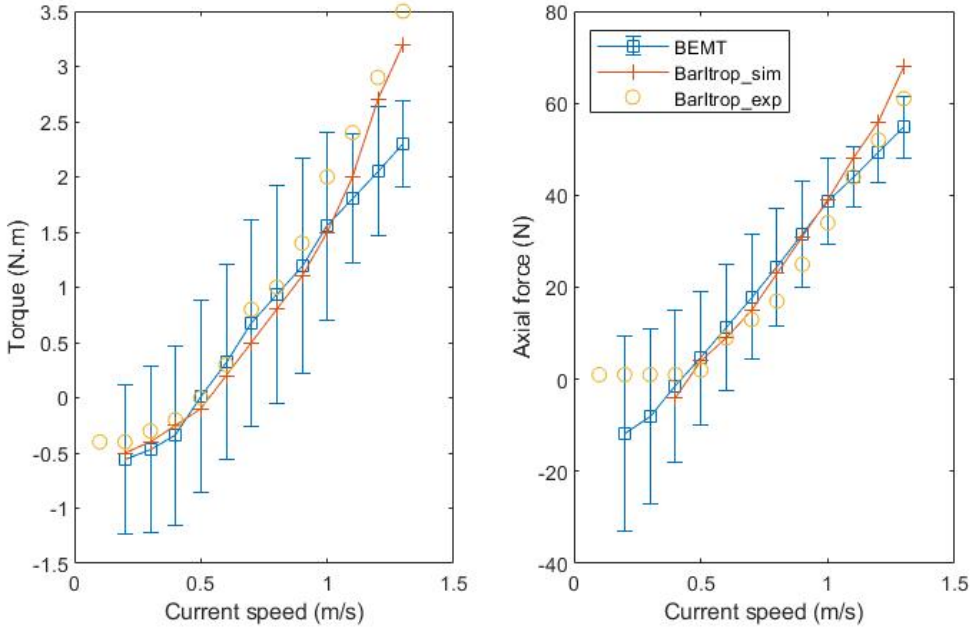

Figure 3.46: Torque and axial force results against current speed from the BEMT numerical model (+ errorbars), Barltrop simulations, and Barltrop experiments in wave conditions with height of 150mm and frequency of 0.5Hz at constant rotor rotation speed of 150r/min.

the same from the BEMT numerical model which is notably different to the variability in Barltrop laboratory results. The shape of the wave cycle along with the peak values differ significantly from one cycle to the other in Barltrop laboratory results which makes comparison between results difficult. However, the BEMT always underpredicts the rotor torque whilst always overpredicting the axial force compared to the Barltrop results. A comparison against more reliable laboratory data is necessary for validation of the BEMT.

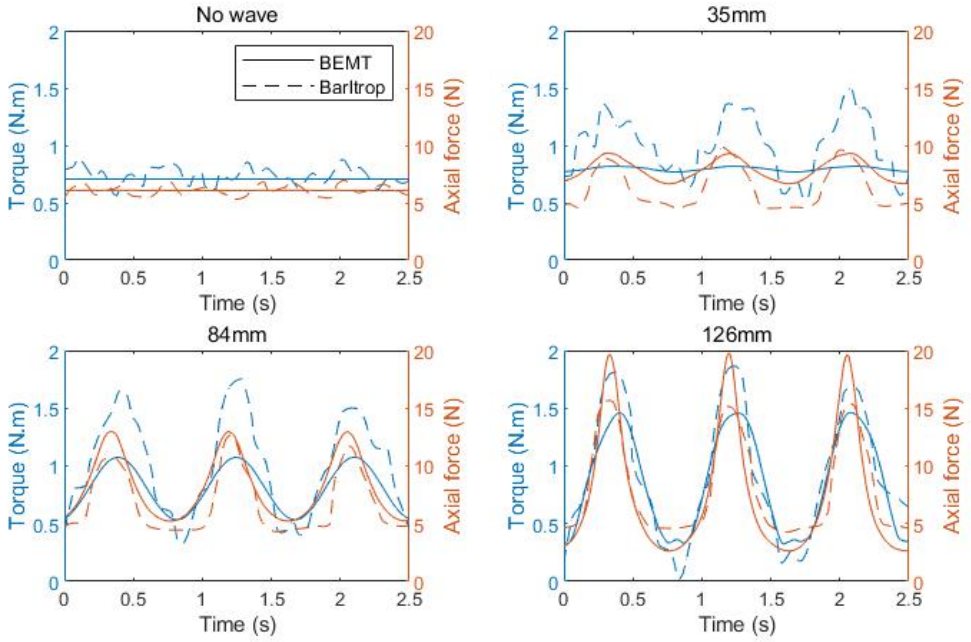

Figure 3.47: Barltrop rotor torque and axial force time series in different wave heights from BEMT numerical model and Barltrop laboratory experiments.

3.5.3 Magallanes ATIR

Magallanes ATIR: Details

Details of the Magallanes ATIR rotor blade and its laboratory testing are given in Section 3.1.2 and Section 3.2.1 respectively. The second study of the Magallanes ATIR turbine is in transient flow fields, i.e. flow field with waves. The added mass effects are included in the BEMT transient model in the following studies. Details of the transient flow fields are given inTable 3.19. Two cases are studied to match the available laboratory results. The current speed and turbulence intensity of the flow fields are 1.0m/s and 1.5% for both wave cases. The waves have different wave height and frequency of 1) 0.190m and 0.5Hz, and 2) 0.280m and 0.7Hz respectively.

The available statistical details of the flow field in the laboratory experiments are average values for current speed, turbulence intensity, and wave height and frequency. Time series of flow velocity across wave flume height are not available and thus the synthetic flow fields used in the numerical model will not replicate the exact feature to feature details of the laboratory flow field, but they will match the main statistics of the flow fields. Therefore, the time plots of the numerical models will not show the small features which

will be present in the laboratory experiments.
Likewise to the steady-state ATIR cases, the specific data on power and thrust are anonymised to protect the commercial sensitivity of the data. It is achieved in the same manner by scaling against a single value, the optimum C_P seen in case no.5 from Section 3.4.2, and all C_T values are scaled against C_T for the same case. Coefficients scaled in this way are denoted C_P* and C_T*, Equations 3.3 and 3.6.

Table 3.19: Details of the parameters for the transient flow fields for the testing of the Magallanes ATIR.

No.	Current speed (m/s)	Turbulence intensity (%)	Wave height (m)	Wave frequency (Hz)
1	1.0	1.5	0.19	0.5
2	1.0	1.5	0.28	0.7

Matching the steady-state ATIR case study, each test cases will have results from four sources; 1) original BEMT version 1.xx, 2) improved BEMT version 4.gr, 3) GAD-CFD, and 4) laboratory experiments. The original BEMT version 1.xx (1) and GAD-CFD (3) numerical models assigns each rotor blade element with the same lift and drag characteristics, Figure 3.5, while the improved BEMT version 4.gr (2) assigns each rotor blade element with unique lift and drag characteristics based on their foil geometry and Reynolds number, Figure 3.6, as detailed in Section 3.3.

Magallanes ATIR: Results & Discussions

Time series of C_P* at a TSR of 5 are plotted in Figure 3.48 for the BEMT versions 1.xx and 4.gr, GAD-CFD model, and laboratory experiments in flow fields with current speed of 1.0m/s and turbulence intensity of 1.5% and waves of height and frequency of (a) 0.095m and 0.5Hz, and (b) 0.140m and 0.7Hz. Included in the plot are results from the BEMT version 4.gr in high turbulence (15%) flow fields. The higher TI BEMT results are included because the noise from the laboratory experiments was much greater than the numerical models. It is hypothesised that the TI in the laboratory experiments was significantly higher than the 1.5% target. The turbulence generated by the presence of the wavemaker in the flume has been measured to be approximately 10%; measured when idle in the water, thus creating no waves [108]. Further turbulence is also expected due to reflective waves in the flume. As expected, increasing the TI in the BEMT model increases the noise of the result. In the high TI BEMT case the noise is comparable to that of the laboratory. This is better visualized in Figure 3.49, which plots Figure 3.48 in the frequency domain. It

shows that all results have the same main peak, which corresponds to the frequency of the wave. Figure 3.50 and Figure 3.51 are similar plots to Figure 3.48 and Figure 3.49; plots of time and frequency for C_T* which indicate that the same results are visible in the thrust measurements as well as the power measurements.

As seen in Figure 3.48, the C_P* cycle from both BEMT and GAD-CFD numerical models have the same period as the laboratory results which confirms that key features of the wave cycle are being correctly interpreted in the models. The mean and range of C_P* are very similar between the BEMT model and laboratory results, whereas the GAD-CFD has similar mean C_P* but much smaller range and fails to capture the full effect of the wave. The failure of the GAD-CFD in capturing the complete wave dynamics is due to flow domain error and not fundamental issues with the model, due to the difficulty of modelling a transient wave structure with a RANS formulation. Specifically, lower wave-induced velocity fluctuations are seen at the rotor in the GAD-CFD model due to the attenuation of the wave as it travelled from the flow domain inlet to the rotor. The peak velocity at the rotor is approximately 30% smaller in the GAD-CFD model compared to the BEMT model. Theoretically, this would result in peak power to be approximately 35% of the BEMT, which is realized in the results, as plotted in Figure 3.52.

Figure 3.52 shows a plot of C_P* and C_T*, with errorbars, against TSR for the laboratory scale ATIR turbine for the wave cases from both the original and improved BEMT models, GAD-CFD model, and laboratory experiments in flow fields with the same conditions as described in Figure 3.48. As previously described, only a single TSR value is investigated for the GAD-CFD model for the wave cases due to the high computational cost of pre-computing the wave cases for the URANS implementation. This is shown in the figure as a single point with an errorbar. The value and TSR of the maximum C_P* predicted by the BEMT models in both wave cases are within $\sim$95% of laboratory results. Similar to the uniform mean flow with turbulence cases shown in the results of Figure 3.29 and Figure 3.30, the improved BEMT model captures the sharp drop off in rotor performance seen in overspeed region much better than the original version. The standard deviation of C_P* and C_T* for the BEMT models and laboratory experiments, as visualised with the errorbars in Figure 3.52, are >95% similar between TSR 2-7. This gives confidence that the BEMT models are correctly capturing the magnitude of the effects from the waves.

It is clear that waves are dominant compared to the turbulence in the numerical models (i.e. the main frequency response of rotor power is the same as the wave frequency),

which is not as obvious in the laboratory data. The distinction is harder to make for the laboratory experiments, due to the reflective waves in the flume increasing the TI as previously explained in this section.

The results are summarised in Table 3.20, averaged across both cases, i.e. the optimum TSR for the original BEMT version 1.xx is the average of the optimum TSR for the original BEMT version 1.xx across both presented cases. A similar trend is observed to the steady-state case study in Section 3.4.2. The improved BEMT version 4.gr is the best numerical model at predicting optimum TSR, matching laboratory data, whilst the others have optimum at higher TSR. The best prediction of C_P* between TSR 3-6 and its maximum is achieved by the improved BEMT version 4.gr. It predicts the exact maximum C_P* value, has a 88% match to laboratory between TSR 3-6, and has standard deviation within 5% to the laboratory data.

Table 3.20: ATIR transient case study; summary of the results (averaged across all cases) from original and improved BEMT numerical model, GAD-CFD numerical model, and laboratory experiments.

Source	Optimum TSR (average of 2 cases)	C_P* (average of 2 cases)		
		Maximum	Average standard deviation	% to laboratory (TSR 3-6)
Original BEMT	5.0	0.97	0.27	76
Improved BEMT - Low TI	4.5	0.96	0.23	88
Improved BEMT - High TI	4.5	0.95	0.24	87
GAD-CFD	5.0	0.74	0.04	62
Laboratory	4.5	0.96	0.25	100

Magallanes ATIR: Conclusions

An original version 1.xx and improved version 4.gr BEMT, and GAD-CFD numerical models have been used to predict the performance of the Magallanes ATIR tidal stream turbine. Comparison of the results from the numerical models have been made to laboratory experiments. The performance predictions of the ATIR turbine in flow fields with waves from the BEMT numerical models are very good. The BEMT models predicts the performance of the turbine well in the stall and optimum region, but still overestimate the rotor performance in overspeed region. Once again, the BEMT version 4.gr model is best at predicting the turbine performance in the overspeed region. The standard deviation from the BEMT models and laboratory experiments are very similar. This is clearly seen with the time series plots where the BEMT C_P* cycles have the same range and mean as the laboratory experiments. The GAD-CFD model predicts mean C_P* well for the wave cases but fails to capture the full effect of the wave, resulting in significantly

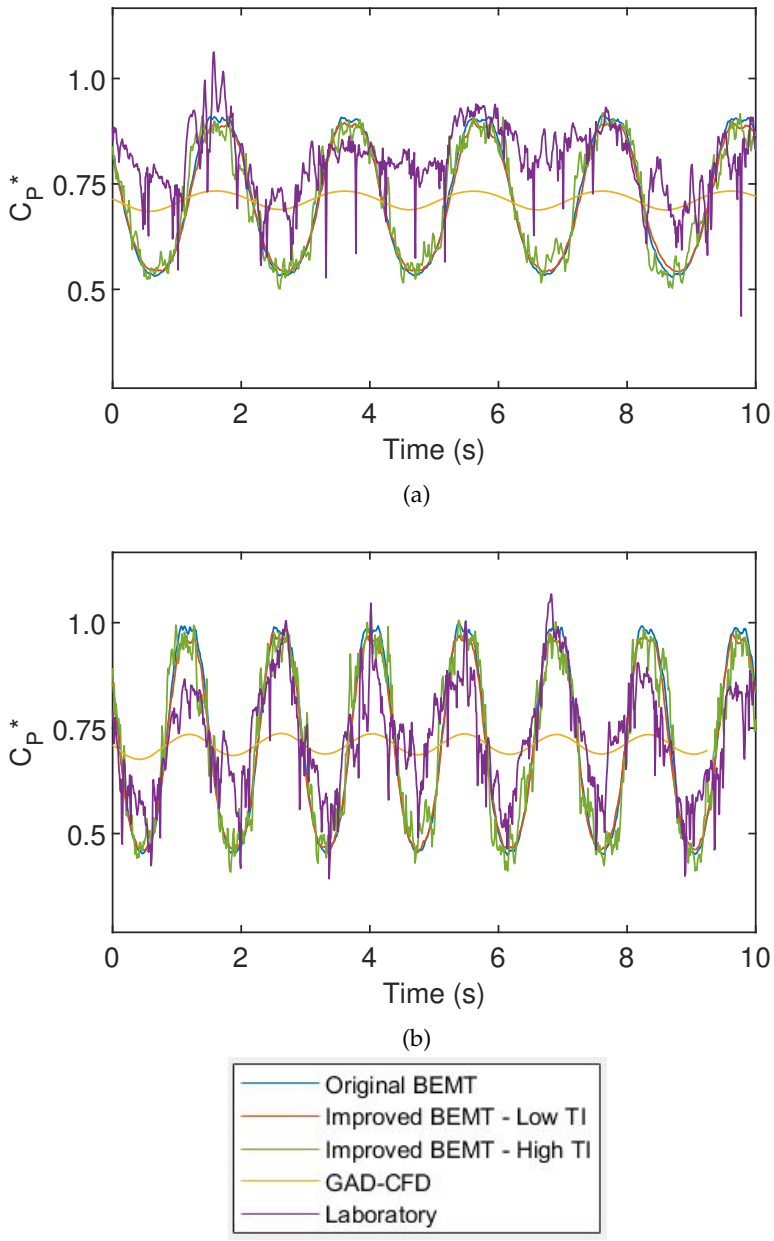

Figure 3.48: Time series of C_P* for the laboratory scale ATIR turbine at TSR 5 from both the original and improved BEMT models, GAD-CFD model, and laboratory experiments in flow fields with current speed of 1.0m/s and turbulence intensity of 1.5% and waves of height and frequency of (a) 0.095m and 0.5Hz, and (b) 0.140m and 0.7Hz.

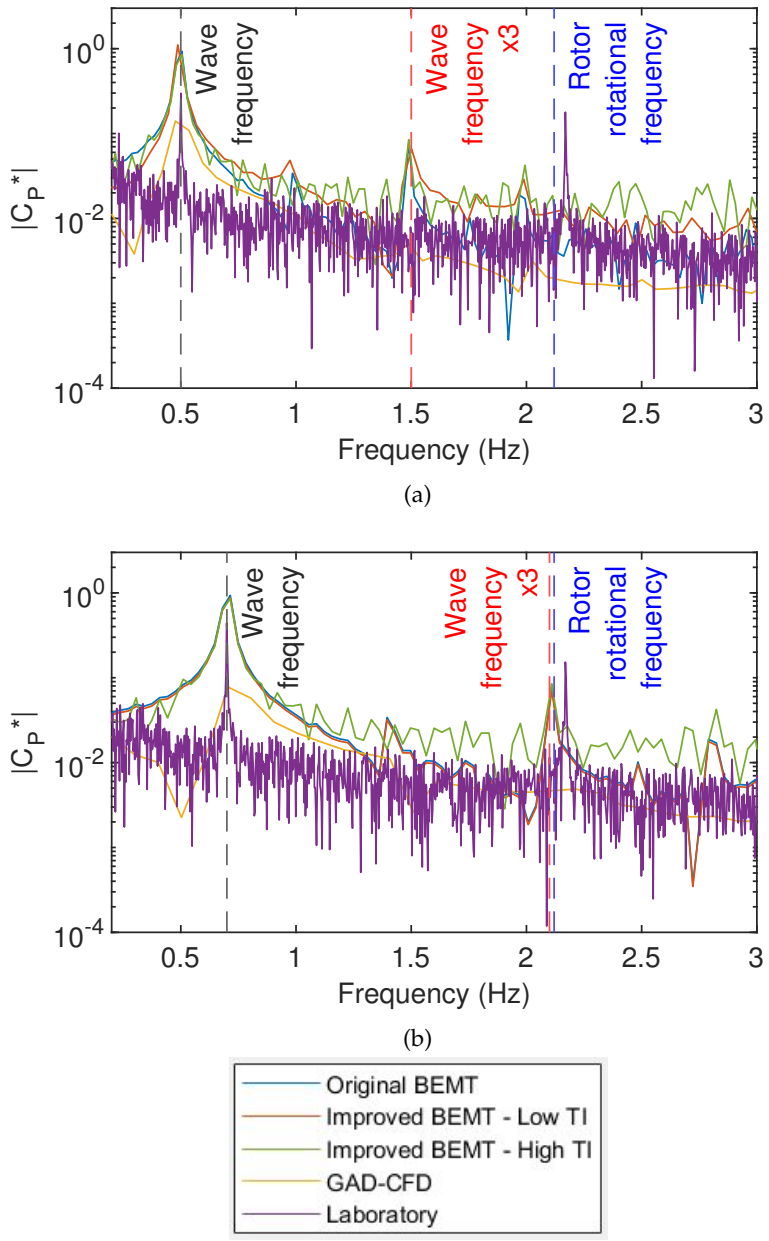

Figure 3.49: Frequency domain plot of C_P^* for the laboratory scale ATIR turbine at TSR 5 from both the original and improved BEMT models, GAD-CFD model, and laboratory experiments in flow fields with current speed of 1.0m/s and turbulence intensity of 1.5% and waves of height and frequency of (a) 0.095m and 0.5Hz, and (b) 0.140m and 0.7Hz.

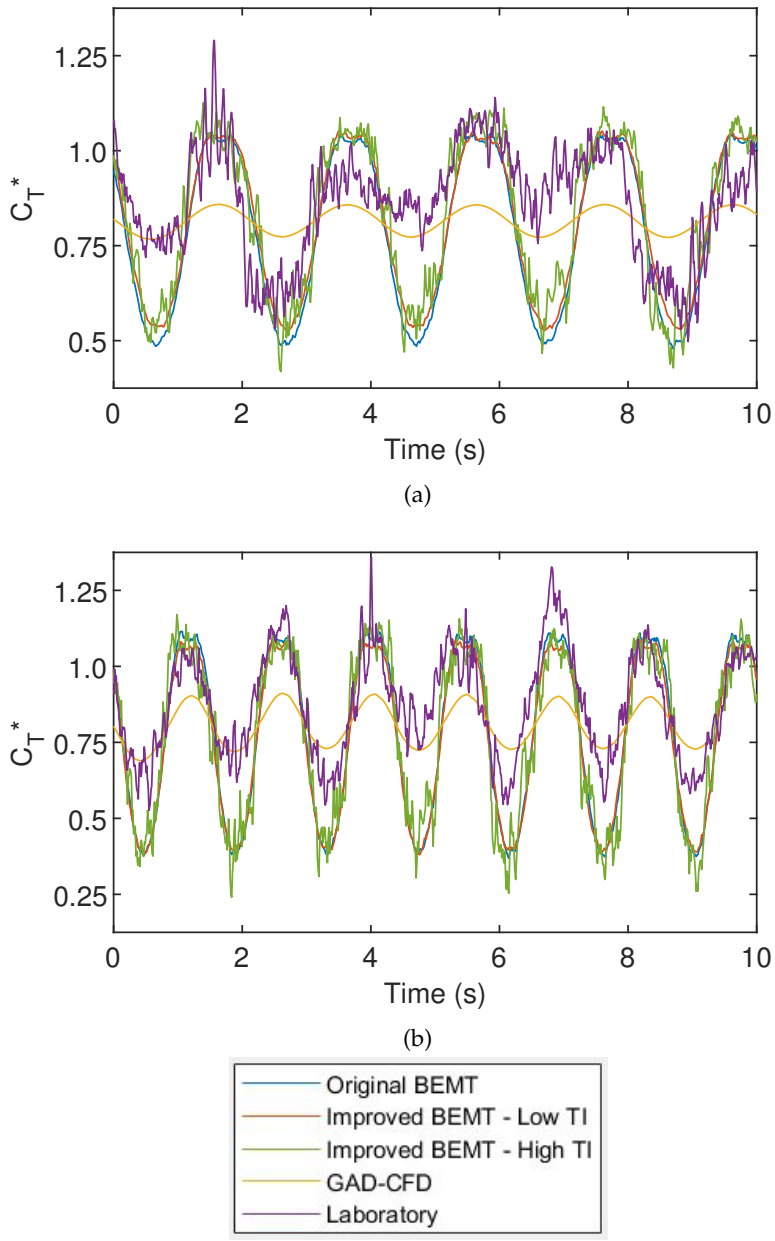

Figure 3.50: Time series of C_T* for the laboratory scale ATIR turbine at TSR 5 from both the original and improved BEMT models, GAD-CFD model, and laboratory experiments in flow fields with current speed of 1.0m/s and turbulence intensity of 1.5% and waves of height and frequency of (a) 0.095m and 0.5Hz, and (b) 0.140m and 0.7Hz.

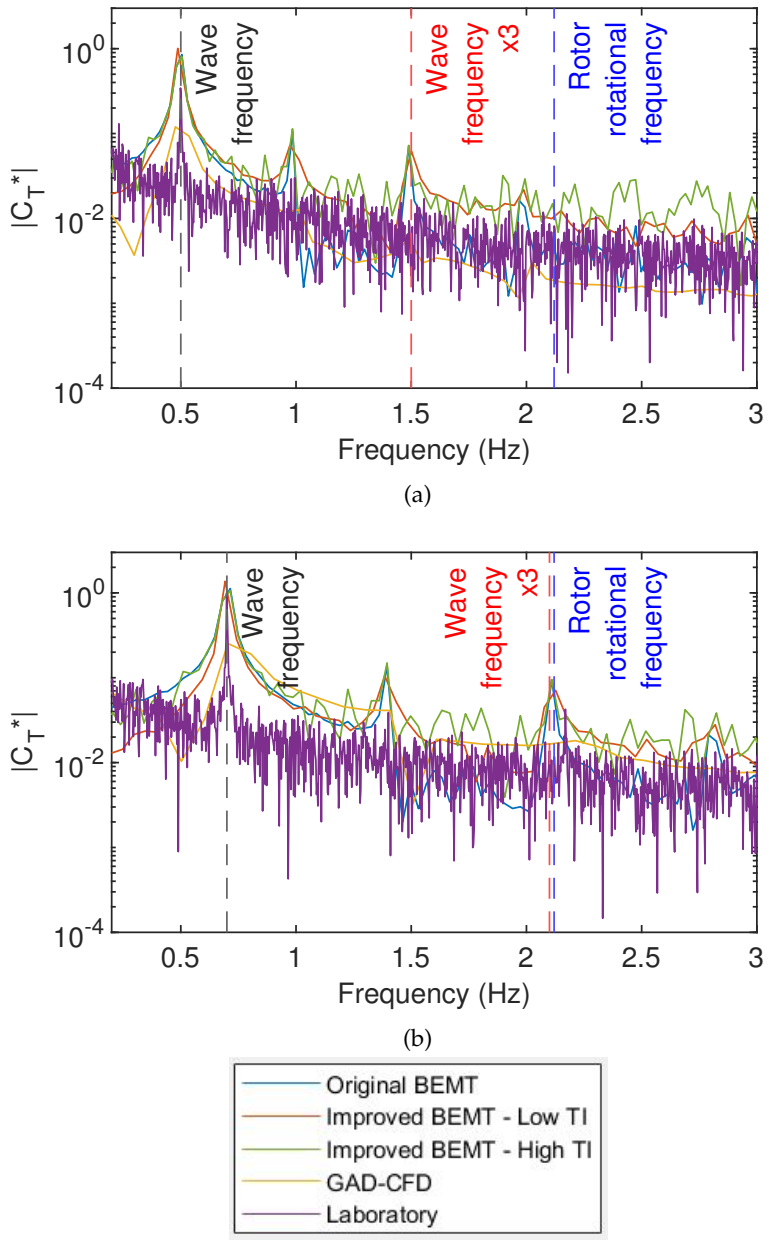

Figure 3.51: Frequency domain plot of C_T* for the laboratory scale ATIR turbine at TSR 5 from both the original and improved BEMT models, GAD-CFD model, and laboratory experiments in flow fields with current speed of 1.0m/s and turbulence intensity of 1.5% and waves of height and frequency of (a) 0.095m and 0.5Hz, and (b) 0.140m and 0.7Hz.

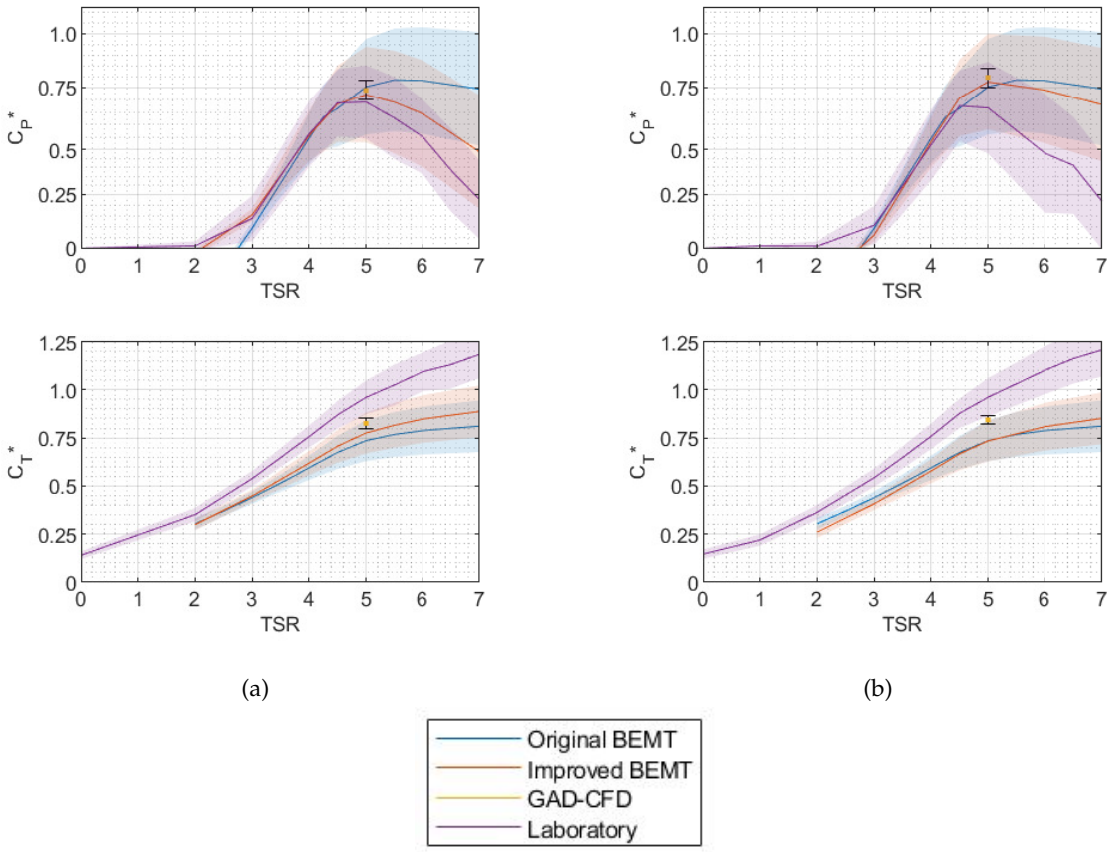

Figure 3.52: Plot of C_P* and C_T*, with errorbands representing standard deviation, against TSR for the laboratory scale ATIR turbine from both the original and improved BEMT models, GAD-CFD model, and laboratory experiments in flow fields with current speed of 1.0m/s and turbulence intensity of 1.5% and waves of height and frequency of (a) 0.095m and 0.5Hz, and (b) 0.140m and 0.7Hz.

underestimating the range of C_P*. This is due to the attenuation of the wave from flow domain inlet to rotor in the GAD-CFD model.

The GAD-CFD model can predict mean values of rotor performance well but fails to predict their variability. This is a considerable limitation when analysing rotor performance in flow conditions with significant waves and turbulence. It is therefore better to use the less computationally demanding BEMT model to predict rotor performance in these conditions. The BEMT is a very quick numerical model with acceptable accuracy, as proven with comparison to laboratory experiments. It cannot model turbine arrays or its wake which is often necessary towards the end of the design process. It best lends

itself to the beginning of the design stage for initial design iterations. The GAD-CFD model can accurately predict the performance of turbines in quasi-steady conditions as well as their wakes and interactions with other turbines, but its computational demands are much greater than the BEMT model. It is therefore best used towards the end of the design stage where more detail is required to refine the design.

3.5.4 Sabella D12

Sabella D12: Details

Details of the Sabella D12 rotor blade and the laboratory test facility are given in Section 3.1.3 and Section 3.2.1 respectively. The second study of the Sabella D12 turbine is in transient flow fields, i.e. flow field with waves. Details of the transient flow fields are given in Table 3.21. Three cases are studied to match the available laboratory results. The current speed and turbulence intensity of the flow fields are 0.8m/s and 1.5% for all wave cases. The waves have different wave height and frequency of 1) 0.190m and 0.5Hz, 2) 0.260m and 0.7Hz, and 3) 0.310m and 0.6Hz respectively.
The available statistical details of the flow field in the laboratory experiments are average values for current speed, turbulence intensity, and wave height and frequency. Time series of flow velocity across wave flume height are not available and thus the synthetic flow fields used in the numerical model will not replicate the exact feature to feature details of the laboratory flow field. They will match the main statistics of the flow fields, therefore, the time plots of the numerical models will not show the small features which will be present in the laboratory experiments.
Similarly to the steady-state cases, the specific data on power and thrust are anonymised to protect the commercial sensitivity of the data. It is achieved in the same manner by scaling against a single value, the optimum C_P seen in case no.3, and all C_T values are scaled against C_T for the same case. Coefficients scaled in this way are denoted $C_P{}^*$ and $C_T{}^*$.

Table 3.21: Details of the parameters for the transient flow fields for the testing of the laboratory scale Sabella D12 turbine.

No.	Current speed (m/s)	Turbulence intensity (%)	Wave height (m)	Wave frequency (Hz)
1	0.8	1.5	0.19	0.5
2	0.8	1.5	0.26	0.7
3	0.8	1.5	0.31	0.6

Sabella D12: Results & Discussion

Figure 3.53a shows C_P* and C_T* against TSR in flow field with current speed of 0.8m/s, turbulence intensity of 1.5%, and wave of 0.19m height and frequency of 0.5Hz for the BEMT numerical model and laboratory experiments. A time series at TSR of 4 from Figure 3.53a is shown in Figure 3.53b. Similarly, Figures 3.54 and 3.55 are for flow conditions with waves of 0.26m height and 0.7Hz frequency, and 0.31m height and 0.6Hz frequency respectively.

Overall, the BEMT numerical model is in good agreement with the laboratory experiments results for all three wave cases. Laboratory and BEMT peak rotor performance occurs within 0.25 TSR across all cases. The mean axial force is very similar between laboratory and BEMT up to a TSR of 4.5. Above a TSR of 4.5, the BEMT code underpredicts the axial force in comparison to the laboratory experiments. The standard deviation of the BEMT numerical model is generally larger than the laboratory experiments which can also be seen from the time series plots. The fluctuations at the wave frequency are much more dominant in the BEMT numerical model than in the laboratory experiments. A possible explanation is that the turbulence intensity of the laboratory experiments is hard to maintain constant. This would explain the greater noise in the laboratory time series plots.

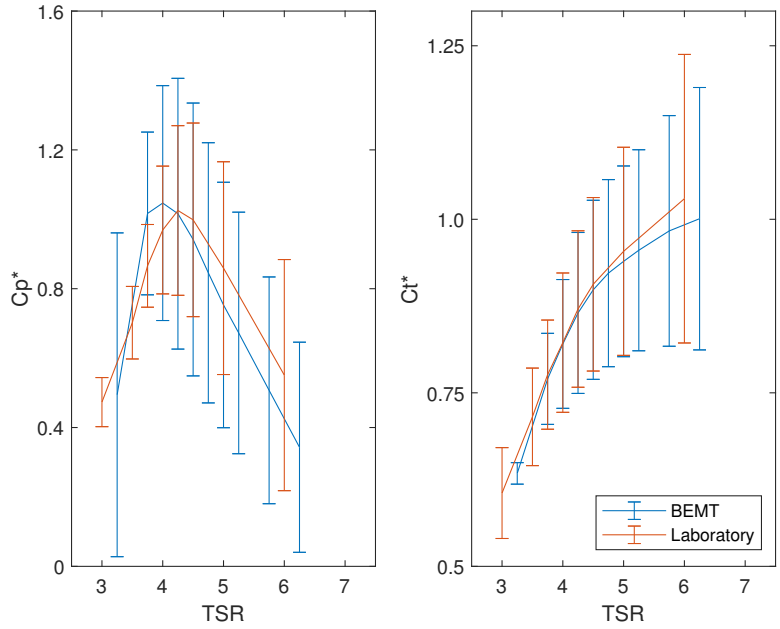

(a) Plot of C_P* and C_T* against TSR.

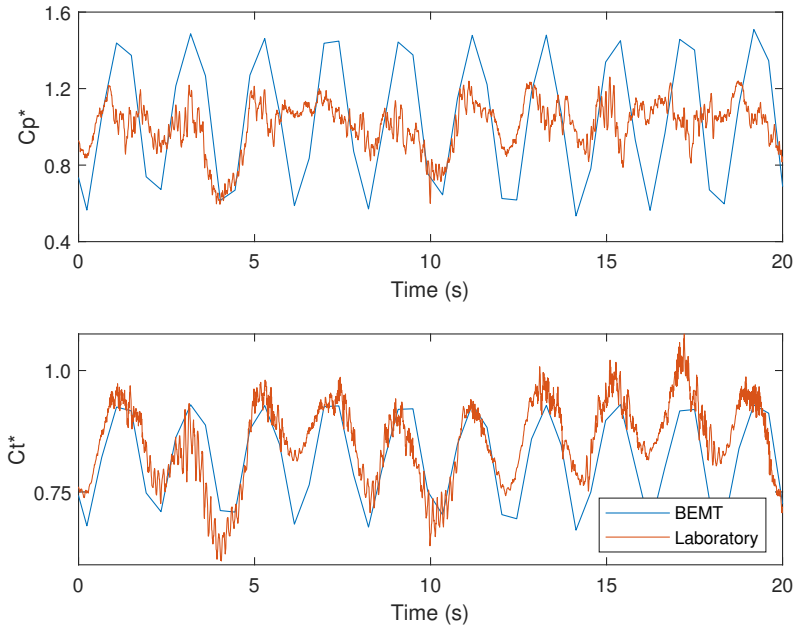

(b) Time series of C_P* and C_T* at TSR of 4.

Figure 3.53: C_P* and C_T* results for the Sabella D12 turbine from the BEMT numerical model and laboratory experiments in flow conditions with current speed of 0.8m/s and turbulence intensity of 1.5% with waves of 0.095m amplitude and 0.5Hz frequency.

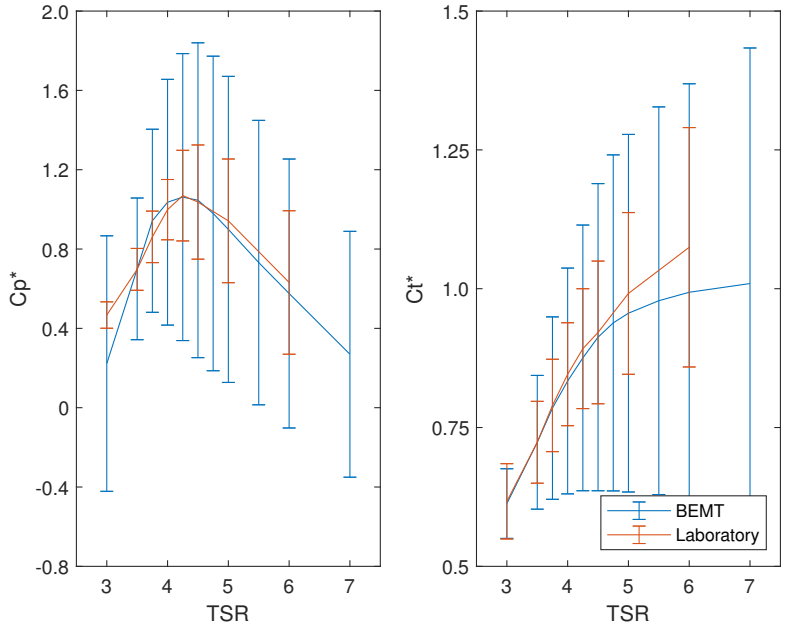

(a) Plot of C_P* and C_T* against TSR.

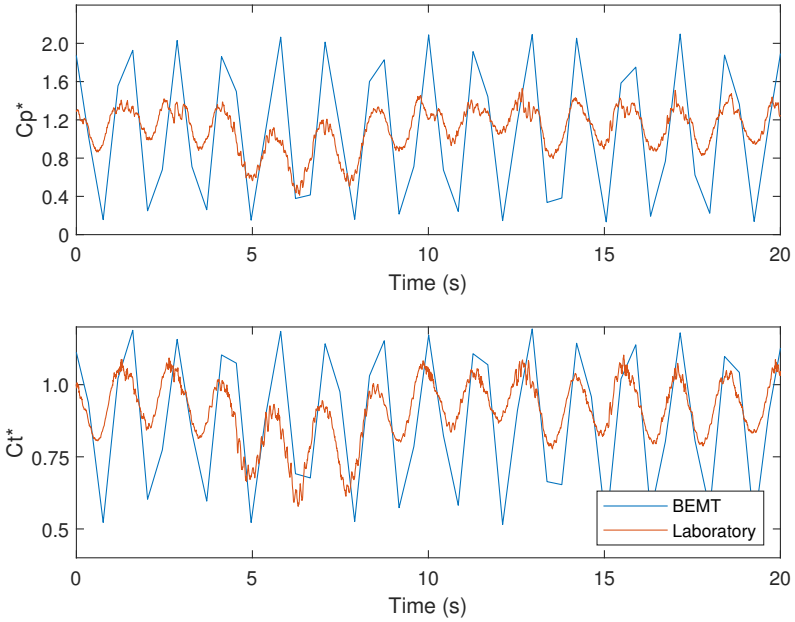

(b) Time series of C_P* and C_T* at TSR of 4.25.

Figure 3.54: C_P* and C_T* results for the Sabella D12 turbine from the BEMT numerical model and laboratory experiments in flow conditions with current speed of 0.8m/s and turbulence intensity of 1.5% with waves of 0.13m amplitue and 0.7Hz frequency.

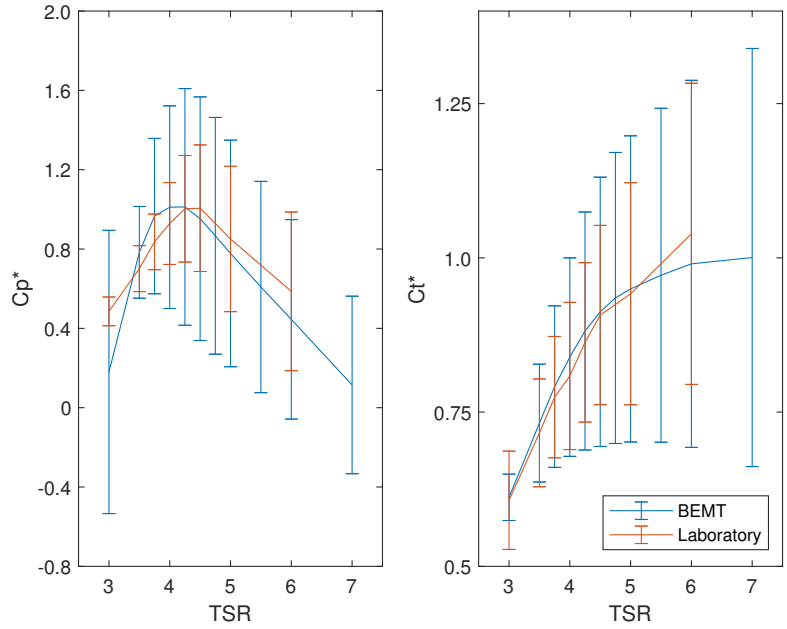

(a) Plot ofC_P* and C_T* against TSR.

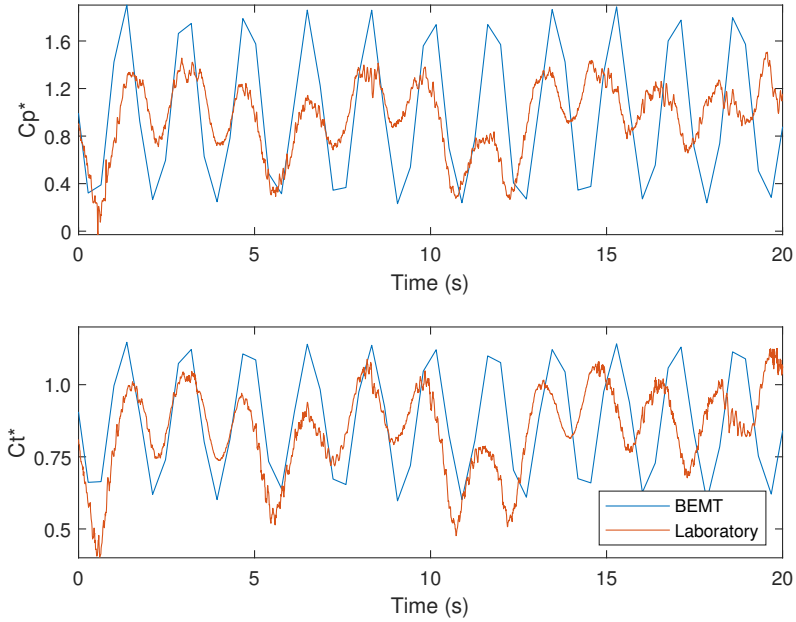

(b) Time series of C_P* and C_T* at TSR of 4.25.

Figure 3.55: C_P* and C_T* results for the Sabella D12 turbine from the BEMT numerical model and laboratory experiments in flow conditions with current speed of 0.8m/s and turbulence intensity of 1.5% with waves of 0.155m amplitue and 0.6Hz frequency.

3.6 Discussion & Conclusions

Validation of the BEMT numerical model has been achieved by carrying out case studies of five different rotor blades. Each rotor blade has been extensively tested in laboratory scaled experiments which provided empirical data for validation of the BEMT numerical model. The rotor blades have different hydrofoil profiles, and twist and chord distribution which tests the limits of the BEMT numerical model.

Foil shape & Reynolds number dependence

A study has been conducted which looked at the effect of assigning each element across the rotor blades with individual lift and drag polars based on their hydrofoil shape and Reynolds number.

- The classical BEMT numerical model uses a single lift and drag polar for the whole rotor blade. This leads to inaccuracies in rotor performance predictions due to varying hydrofoil shape and Reynolds number across the rotor blades.
- Rotor blade geometry modelling in the BEMT model has been improved by introducing the ability to assign unique lift and drag curves to each element based on their foil geometry and Reynolds number.
  - Comparison of BEMT rotor performance prediction with and without the improved blade geometry modelling has been made against laboratory results.
  - In the majority of cases, the BEMT model with the advanced blade geometry modelling reproduce closer results to those of the empirical laboratory results.
- BEMT model prediction of maximum rotor performance to laboratory results has improved by an average of 20.0% and 4.6% respectively for the Magallanes ATIR and Sabella D12 turbine rotor blades whilst it has decreased by 3.0% for the IFREMER turbine rotor with the inclusion of the improved blade geometry modelling.
- Comparing BEMT versions 2 and 3, it is clear that including geometry dependence has significantly greater impact on the BEMT model than that of Reynolds Number dependence.
  - Including geometry dependence compared to Reynolds Number dependence has an average of 40% greater improvement in BEMT rotor performance

prediction to laboratory. This is unsurprising as there is a more significant change in geometry compared to Reynolds Number across the rotor blades.

- In every tested case the BEMT models which include the improved blade geometry modelling predict reduced rotor performance.
  - BEMT elements in the original model, particularly ones towards the blade hub, were assigned lift curves which were inappropriate and over-predicted their performance.
- Introducing the improved blade geometry modelling to the BEMT model has increased the computational time by approximately 10%. This is an acceptable increase in computational time in respect to added accuracy of the blade geometry modelling and the BEMT model prediction of rotor performance.

Uniform flow with turbulence

Five steady-state case studies have been carried out, where the performance of five rotor blades (Oxford, ATIR, D12, IFREMER, and Barltrop) were predicted by the BEMT numerical model in flow field with constant mean current flow velocity with varying levels of turbulence.

- BEMT numerical model is best at predicting rotor blade performance in stall and optimum operating region, with larger deviation in the overspeed operating region.
- The five tested rotor blades have different twist and chord distribution along their radial length, but all have decreasing chord and twist towards the tip.
- The location of optimum performance TSR is generally correlated to the twist along the rotor blade. A trend of decreasing optimum TSR with increasing maximum twist is seen with the rotor blades, with the exception of the Oxford rotor blade. The ATIR, D12, IFREMER, and Barltrop rotor blades all have very similar hydrofoil profile, but the Oxford rotor blade is sufficiently different, causing the difference seen in optimum TSR and twist correlation. If the maximum twist of the Oxford rotor blade was increased (i.e. pitching up of rotor blade), then the optimum TSR would decrease. This would be true for any rotor blade.

- Another observation of the power curves is that the maximum C_P increases with higher optimum TSR. The more the rotor blades are pitched downwards (i.e. less twist), the greater the power coefficient. A disadvantage of pitching down a rotor blade to gain greater power coefficient is the need for higher rotor rotational speed, greater forces on rotor components, and a need for a more energetic site.

- The C_T curves are all very similar with good comparison from the BEMT numerical model to laboratory experiments across the whole TSR for the majority of rotor blades.

- There is a significant difference in C_T from the BEMT numerical model and the laboratory experiments in the overspeed region for the Magallanes ATIR rotor blade. Many factors could be responsible for this discrepancy in the BEMT numerical model (e.g. inaccurate lift and drag polars, correction factors, or flow field representation). The discrepancies could also be due to limitations of the laboratory experiments (e.g. inaccurate measurement of flow conditions or manufacture of rotor blades). There is suspicion that the Magallanes ATIR rotor blades used in the laboratory experiments were not manufactured accurately and had differing twist and chord distributions to the design. This would be an obvious source of inaccuracy between the BEMT numerical model and the laboratory experiments.

Transient

A case study to establish the sensitivity of the IFREMER rotor blade to added mass (i.e. acceleration forces) in the BEMT numerical model has been conducted and has shown that;

- The added mass has negligible contribution to the rotor torque, with the torque from the added mass being 2% of the hydrodynamic term.

- The contribution of the added mass on the rotor thrust is greater as the waves travel perpendicular to the rotor rotation plane. The thrust from the added mass is 4.9% of the hydrodynamic term.

- The hydrodynamic and added mass terms are 90° out of phase. The added mass terms are dependent on the fluid acceleration and the hydrodynamic terms are dependent on the fluid velocity.

- The maximum and minima of total rotor thrust is smaller with the inclusion of added mass terms, but the average rotor thrust is unchanged as the added mass term has a average of zero.
- The time step sensitivity study has shown that 60 timesteps per wave period is necessary to fully capture the flow field dynamics.
- There is a linear correlation between added mass thrust to both turbulence and wave height of the flow field.

Transient case studies of four rotor blades (ATIR, D12, IFREMER, and Barltrop) have been completed. The flow fields of the transient case studies included waves and turbulence. The BEMT numerical model successfully captures the key parameters of the wave cycle of the flow fields.

- Similar to the steady-state cases, the BEMT numerical model is best at predicting rotor blade performance in stall and optimum operating region, with larger deviation in the overspeed operating region.
- The standard deviation of power and thrust of the BEMT numerical model predicition is within an average of >95% across all cases to laboratory experiments, verifying that the BEMT is accurately accounting for the waves in the flow fields.
- The flow conditions and their representation in the synthetic flow fields have significant impact on the BEMT results.
- The rotor performance has a strong positive correlation to free stream velocity but has no correlation to turbulence intensity.
- Using representative synthetic flow fields that match statistical properties of real flows in the BEMT numerical model is crucial in ensuring useful prediction of rotor performance.

Chapter 4

Remote river energy system: Design

In the following chapter, the design process for the RRES is given which proceeds from the initial RRES small-concept testing, completed in previous work [35]. Firstly, the specification and stages of development for the RRES are given followed by a description of the test site. The BEMT numerical model is used to predict the performance of the RRES, providing loads which govern its design. The laboratory rig is introduced and described which is used to test key components of the RRES prior to deployment at sea. Finally, the deployment of RRES is summarised. The development of the RRES is based around two different scaled versions, a 0.9m and 3.0m versions. The 0.9m and 3.0m represents the diameter of the rotor which is used on the version. The 0.9m version is used for the preliminary testing of the concepts intended for the 3.0m "full scale" version.

4.1 Specification

4.1.1 Device overview

The Remote River Energy System (RRES) is a floating platform which has a two bladed turbine suspended in the flow of the river and is held in situ by four submerged mooring lines. The test site is within a river tidal range and thus requires mooring in both the upstream and downstream directions. However, the rotor will only be under test in one direction. Sketches of (a) the general configuration of the RRES and (b) pontoon arrangement are shown in Figure 4.1, credit D. Glasby.

The platform will be assembled from two modular pontoon hulls, which individually measure 0.7m deep, 1.4m wide, and 10.0m long. The turbine is installed with a pivot assembly which hinges at the back of the pontoon. A boat will be used to tow the RRES to

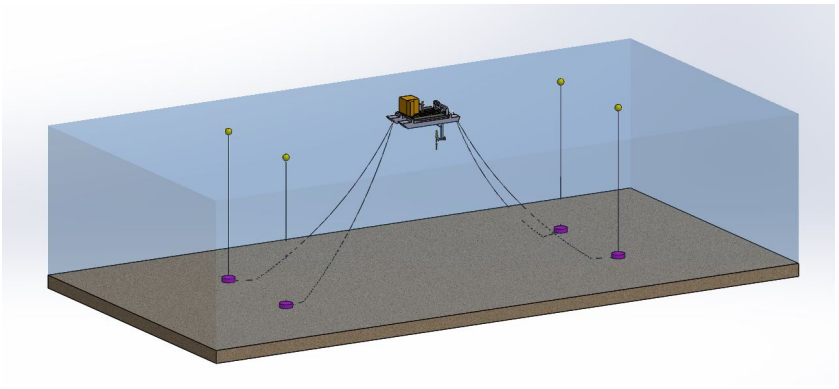

(a)

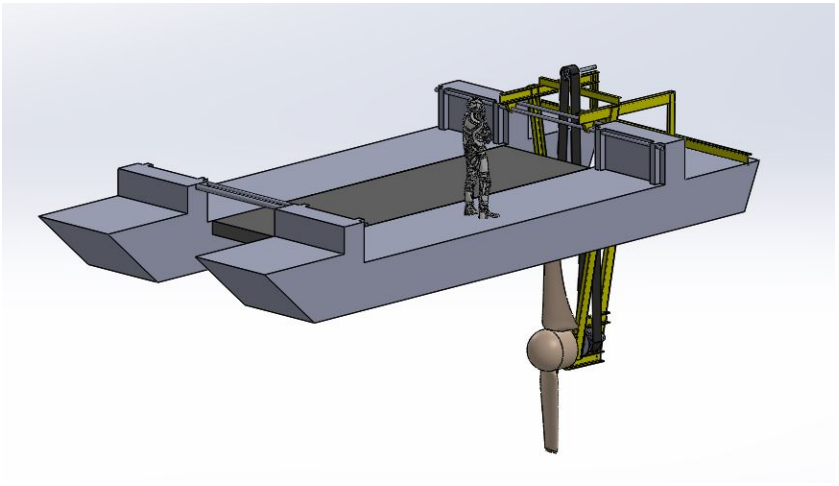

(b)

Figure 4.1: Sketch of the remote river energy system (RRES), (a) general configuration and (b) pontoon arrangement. Credit D. Glasby.

position and fixed in position using the four mooring lines. Note that Figure 4.1b shows a planned future deployment of the full scale 3.0m device; the 0.9m version uses the same pontoon and support structure.
A design overview of the RRES is listed below:

- The goal of an easy to repair, robust system was formalised into the design specification shown in Table 4.1.

- The 0.9m device is to test the concepts which are proposed for the 3.0m "full scale" RRES. The main components which are of particular importance are: power take off, valves, chassis, safety braking, rotor blades, mooring, and sensors.
- Offshore, the RRES is a stationary floating platform which suspends a two blade turbine in the flow of the river.
- The platform is held in situ by four submerged mooring lines which can be used to angle the turbine directly into the flow.
  - The 3.0m device is proposed to have four mooring lines.
  - The test site is within a tidal range and thus requires mooring in both the upstream and downstream directions.
- The platform is constructed from two modular pontoons connected at both ends by steel beams.
- The rotor has a diameter of 0.9m (3m for full scale).
- The rotor blades will be manufactured using fused deposition modelling additive layer manufacture technique for the 0.9m device and manufactured from glass fibre reinforced polymer (GFRP) for the 3.0m device.
  - Quick and relatively inexpensive manufacturing technique.
  - The fused deposition modelling will use ABS material.
  - The GFRP will comprise of e-glass woven roving reinforcement along with polyester resin.
  - The rotor blades must have neutral buoyancy.
- The depth and pitch of the rotor blades will be controlled by a submersible arm which is controlled by a hydraulic arm. The submersible arm will pivot at the rear of the pontoon and will be able to completely raise the rotor blades out of the water for maintenance and transportation.
- Energy is harnessed by transferring the rotational power of the rotor blades through a geared system to actuate the PTO system, comprising a dual action piston pump and one way valves.
- The PTO system will pump pressurised water to an onshore hydro-electric generator in the full scale device.
  - To minimise complexity for 0.9m and first iteration of the 3.0m devices, no water will be pumped to shore with everything housed on the chassis. The hydro-electric generator will be replaced by an orifice plate.
- A closed loop control system is used to operate a throttling valve which regulates the flow of water in the pipes. It will be used to stops the blades if the river flow exceeds 1.8m/s.

- All components have been designed with minimal complexity so that they can be manufactured from readily available components and generic materials using basic manufacturing techniques.
- Whilst there are specialist components used in this design, many could be purchased off-the-shelf or constructed and supplied separately.

4.1.2 Device specification

The specification for the 0.9m and 3.0m RRES devices are very similar and are given in Table 4.1. Any differing specification for the 0.9m and 3.0m devices are denoted .a and .b respectively.

4.2 Stages of development

The development of the RRES follows guidance of IEC TS 62600-202:2022. It gives best practices and recommends procedures for the early stage development of tidal energy converters.

There will be four stages for the development of the RRES, which are briefly described in Table 4.2. The first stage is small-scale concept testing, which has previously been achieved [35]. In this thesis the development of the RRES commences at the second stage, which is a laboratory test rig that will be used to primarily test the PTO and control system. The third stage is a deployment of the 0.9m diameter RRES at test site which will test the performance, PTO, and control system of the RRES. The last stage is a deployment of the 3m diameter RRES at the test site which aims to demonstrate operability, maintainability, access, and health and safety.

Each stage is intended to evaluate the design of the RRES and progress its technology readiness level (TRL). The number of iterations of the RRES design concerning performance, reliability, safety, and economics is expected to decrease significantly as the stages increase, with the majority occurring in stages 1 and 2. Experimental trials will be conducted at each stage to evaluate whether the RRES meets the required objectives. Advancement to the next stage will only occur if the RRES meets all the criteria of the previous stage.

4.3 Test site

Design of the RRES is dictated by conditions at the chosen test site, which is at the marine energy test area (META) in Warrior Way, Pembroke Dock. Location of the test site is shown in Figure 4.4. The test area is a tidal estuary, with mean depth at high water of 20m and a maximum tidal range of 10m. The current flow velocities commonly range from 0-1.8m/s,

Table 4.1: Remote river energy system specification.

1. Mechanical	
1.1	Support own weight in transit and installation
1.2	Weight limit of 5000kg to minimise size of crane
1.3	Neutrally buoyant blades and shaft
1.4	Designed to operational load cases
1.5.a	Rotor diameter 0.9m
1.5.b	Rotor diameter 3.0m
1.6	Hub diameter <20% of rotor diameter
1.7	Blade tip speed <10.5m/s
1.8	Adjustable blade pitch angle
1.9	Pump, orifice valve, and electrical box on deck
2. Operating conditions	
2.1	Function at river velocities between 1-1.8m/s
2.2	Rated speed design at 1.3m/s
2.3	Shut down at 1.8m/s
2.4	Temperatures between 5 - 34 °C
2.5	Tidal estuary
3. Manufacture	
3.1	Minimise use of novel materials
3.2	Minimise use of advanced manufacturing methods
3.3	Must be designed for low cost repair
3.4	Must be designed without seals underwater
3.5.a	0.9m rotor blades are to be 3D printed
3.5.b	3.0m rotor blades are to be manufactured from fibre glass
3.6	Resist corrosion
4. Maintenance	
4.1	Will not require service as deployment will be less that 3 months
4.2	Must be safe to approach and transfer from a boat
4.3	Must be able to be lifted by a crane
4.4	All seals must be accessible in wet service
5. Health and safety	
5.1	Design must follow guidance of IEC TS 62600-202:2022
5.2	Manufacture must adhere to local legislation
5.3	Maintenance must observe local safe working practices
5.4	All components will use a safety factor (SF) of 2 unless stated otherwise
5.5	Platform to include deck and handrails
5.6	Turbine must automatically brake the rotor in the event of power failure

with 1.3m/s as the highest reliable speed within a tidal cycle. Under a severe weather event, it is hypothesised that the current flow velocity could reach 2.2m/s from historic records.

Table 4.2: Description of the development stages for the RRES.

Stage	Model test description	TRL	Typical range of scales	Test objectives	Go/No-go analysis. Stage gate success thresholds
1	Concept model (i.e. Small scale concept testing)	2-3	1:15-100	Concept verification: 1. Turbine rotor: Demonstrate power energy conversion. 2. Platform: Test initial design choices and select most favorable design configuration. 3. Characterize design loads and motions for operational reliability and survival.	Rotor power conversion demonstrated. Loads characterized for normal operating and extreme conditions. A favourable design configuration is found.
2	Design model (i.e. 0.9m diameter laboratory test rig)	4	1:3-10	Design verification: 1. Demonstrate power performance and survival in simulated tidal flow environment at a physical scale that minimizes scale effects. 2. Demonstrate component PTO. 3. Demonstrate other component or subsystem, e.g., controls.	Power performance equals or exceeds target based on numerical model. Loads characterized for normal operating and extreme conditions. PTO operates as designed and at expected efficiency. Control or other subsystem operated as designed.
3	Sub-systems model (i.e At sea deployment of 0.9m diameter RRES)	5-6	1:1-5	Sub-system model verification: 1. Assess energy production in real tide-ways. 2. Demonstrate subsystem integration. 3. Fully operational TEC tideway trials.	Power performance equals or exceeds target based on numerical model. Loads characterized for normal operating conditions. PTO operates as designed and at expected efficiency. Control or other subsystem operates as designed. Deployment operations have all worked as expected; mooring, towing, etc.
4	Solo-device providing near to full scale testing of prototype device (i.e At sea deployment of full scale RRES)	7-8	1:1-2	Technical / Operational evaluation of near-full size to full size power plant deployment. Advance pre-production to pre-commercial unit.	Operations analysis; demonstrate operability, maintainability, access, health and safety.

An example of direction and speed plots for the whole water column at Warrior Way are given in Figures 4.2 and 4.3. The data was recorded on a bottom mounted Nortek Signature 500 ADCP, sampling at 4Hz for twenty minutes every half hour for 14 days

with 0.5m bins. All plots are based off the avergae of each sample period (i.e. each data point represents the average over twenty minutes).

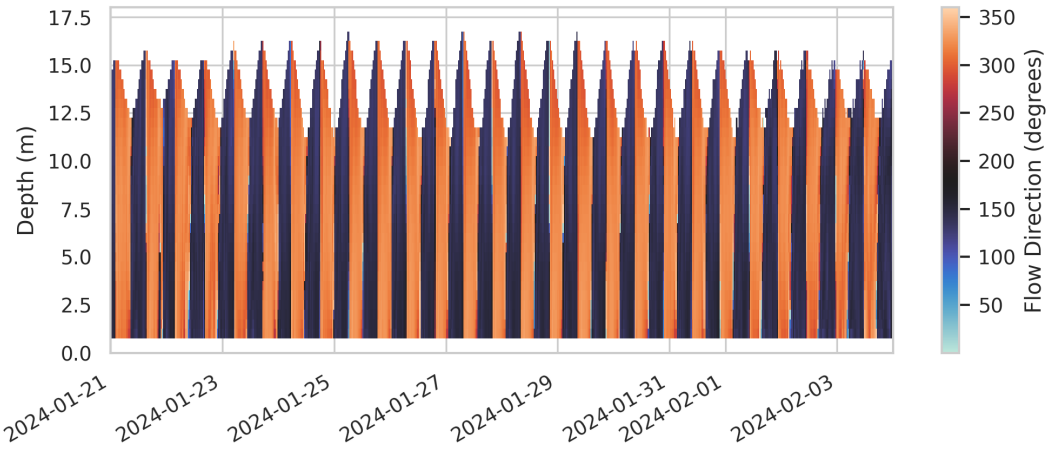

Figure 4.2: Plot of flow direction at META Warrior Way over a 14 day period.

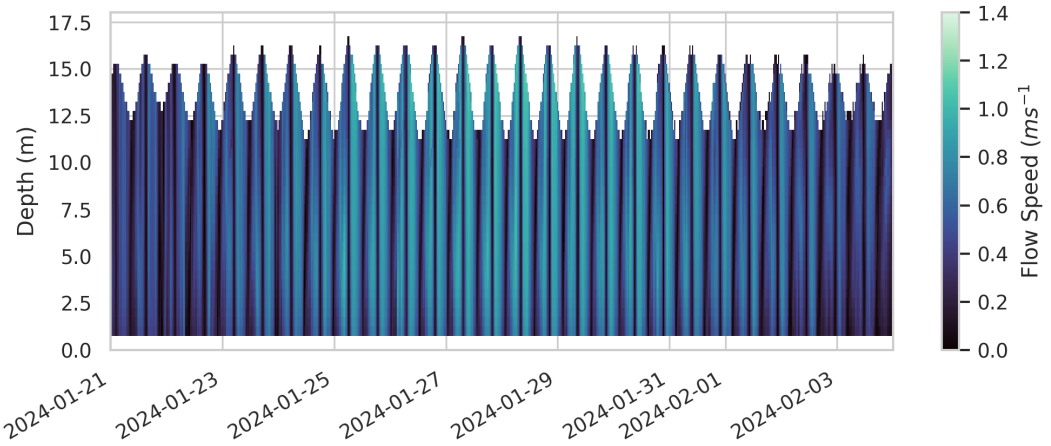

Figure 4.3: Plot of flow speed at META Warrior Way over a 14 day period.

Backscatter data of the general area of the META test site at Warrior Way is shown in Figure 4.5. Also included in Figure 4.5 are the general area of the RRES mooring. The backscatter shows minimal bedforms at the location of RRES mooring which is beneficial for gravity anchoring. Figure 4.6 shows a map of the predicted habitats at Warrior Way, which are a mixture of rock and sediment [18].

The proposed deployment location of the RRES floating device and seabed infrastructure

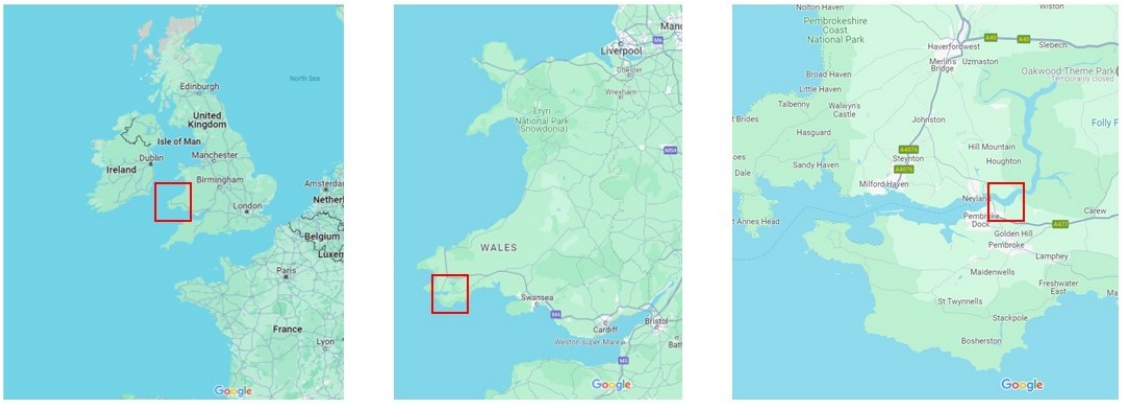

Figure 4.4: Location of the Warrior Way META test site.

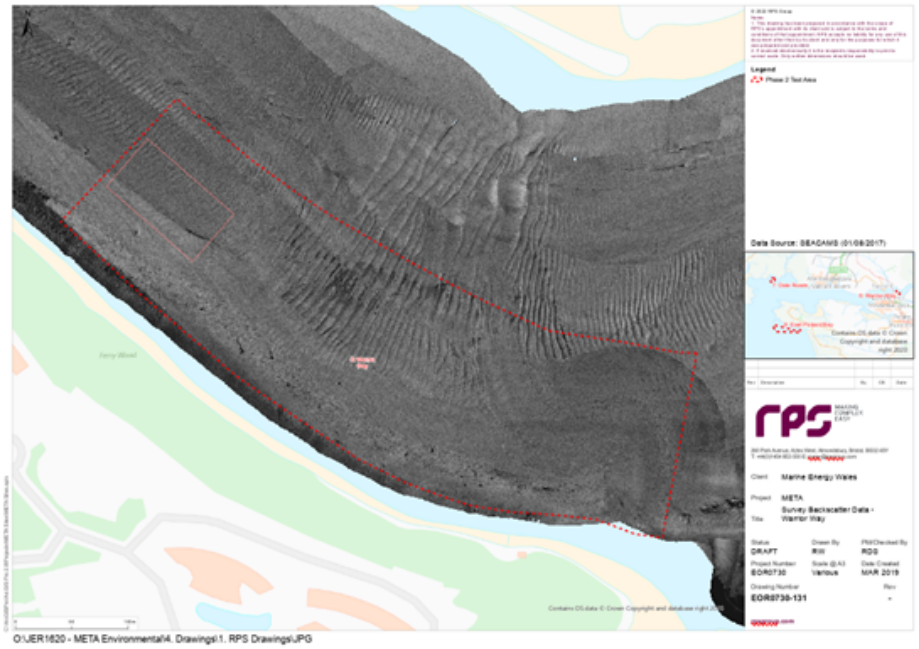

Figure 4.5: Backscatter data for the META test site at Warrior Way.

within the predicted habitat model is shown in Figure 4.7. It shows that the sea-bed habitat for the planned mooring area is sediment. Two sediment profile imagery (SPI) sample points (A & B) within the predicted habitat model are shown in Figure 4.8 [19]. Figure 4.8a shows the location of the SPI points within the predicted habitat model whilst Figure 4.8b and Figure 4.8c shows the SPI at locations A and B respectively. The sediment profile of location A and B are similar; sandy sendiment with small stones (<10cm).

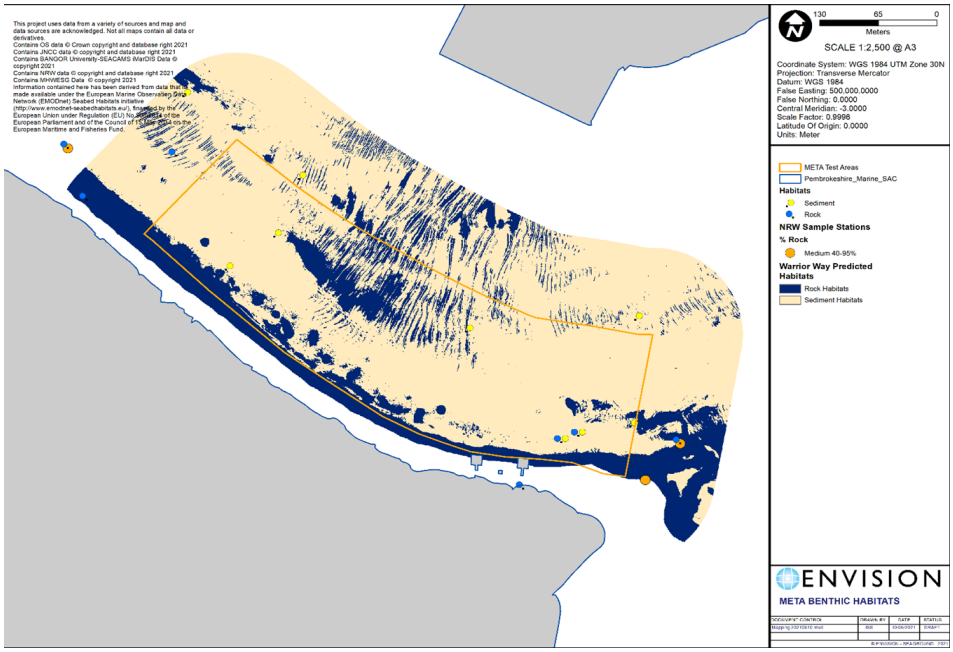

Figure 4.6: Predicted habitats at the META test site at Warrior Way [18].

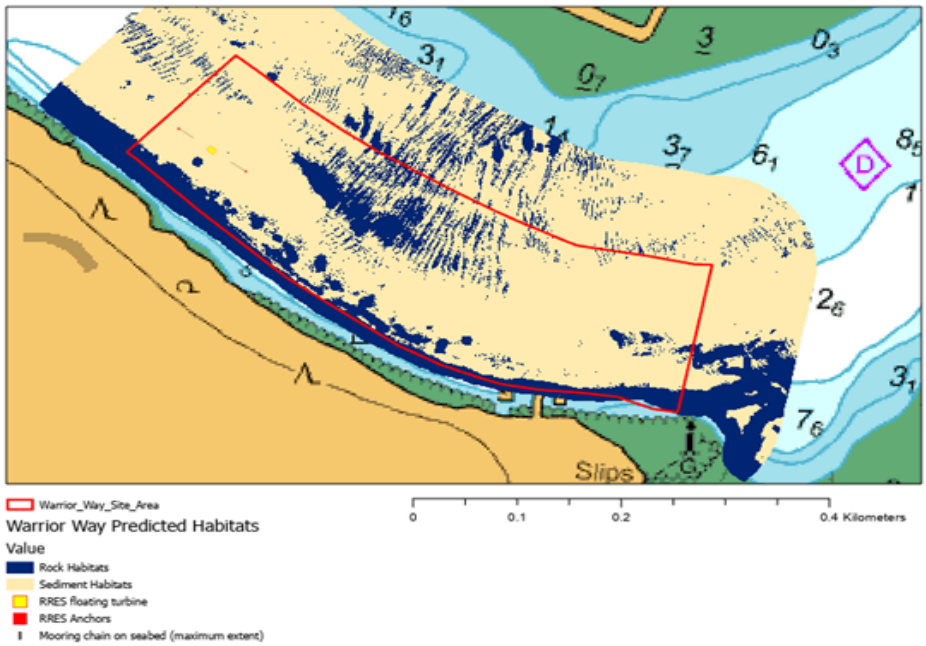

Figure 4.7: Proposed deployment location of the RRES floating device and seabed infrastructure within the predicted habitat model.

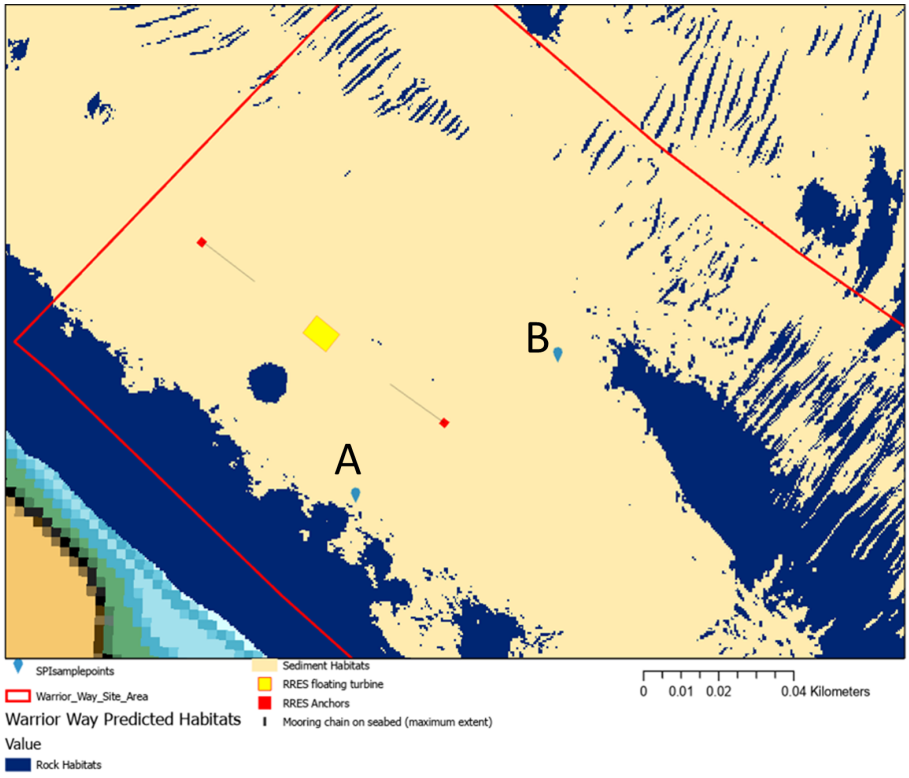

(a)

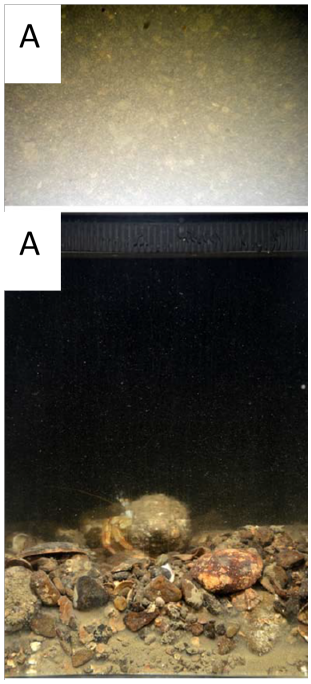

(b)

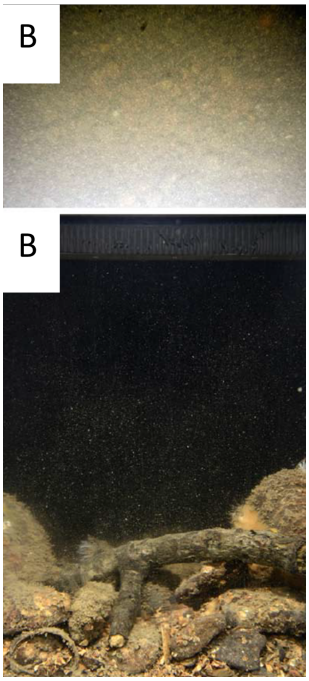

(c)

Figure 4.8: Sediment profile imagery of two sample points (A & B) within the predicted habitat model at Warrior Way [19].

4.4 Remote river energy system performance predictions

4.4.1 Rotor blade options

The rotor blades for the RRES are designed based on the IFREMER rotor blade, described in Section 3.1.6. Choosing the best rotor blade configuration for the RRES is achieved by comparing C_P and C_T curves at optimum operating conditions (flow speed of 1.3m/s). Three main configuration options are considered:

1. 2 blades with original chord
2. 3 blades with original chord
3. 2 blades with chord x1.5

C_P and C_T were calculated using the BEMT numerical model for a range of TSR from 0 to 15 for each blade option and are shown in Figure 4.9. Results shown in Figure 4.9 are calculated with no correction factors enabled in the BEMT numerical model. This was done to improve the readability of the results and make comparison easier.
As expected, options 2 and 3 have the same C_P and C_T results as they have the same total chord length. Option 1, two blade with original chord, has significantly lower C_T compared to the other two options, but has only slightly lower C_P. Importantly, its optimum TSR is at 5.3 which is significantly higher compared to 4 for the other two options. This means that the required startup torque will be higher, which could be an issue in low flow speed sites. For this reason, blade configuration option 1 is not chosen.
Blade configuration 3, 2 blades with chord x1.5, is chosen as the preferred option. It has the same solidity as option 2, but with one fewer blade. This reduces the complexity of the RRES whilst still maintaining its performance.
Figure 4.10 is the same plot as Figure 4.9 but with the tip, hub, and high induction corrections included in the BEMT. C_P and C_T results from Figure 4.10 will be used in the following calculations. The most important C_P and C_T results for the chosen option, 2 blades with chord x1.5, are included in Table 4.3.

Table 4.3: Highlight C_P and C_T results from the BEMT numerical model for the chosen blade configuration, option 3, 2 blades with chord x1.5.

Case	TSR	C_P	C_T
Optimum performance	4.5	0.395	0.706
Runaway maximum rotational rate	12.2	0	0.556

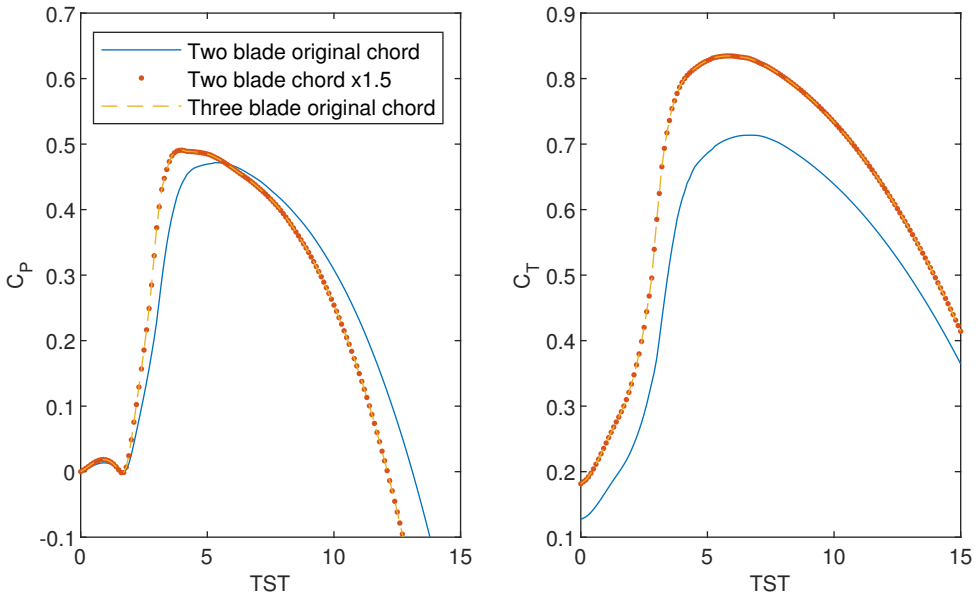

Figure 4.9: BEMT numerical model (without tip and hub ,corrections not applied) results for C_P and C_T against TSR for three different rotor blade configuration options for the RRES.

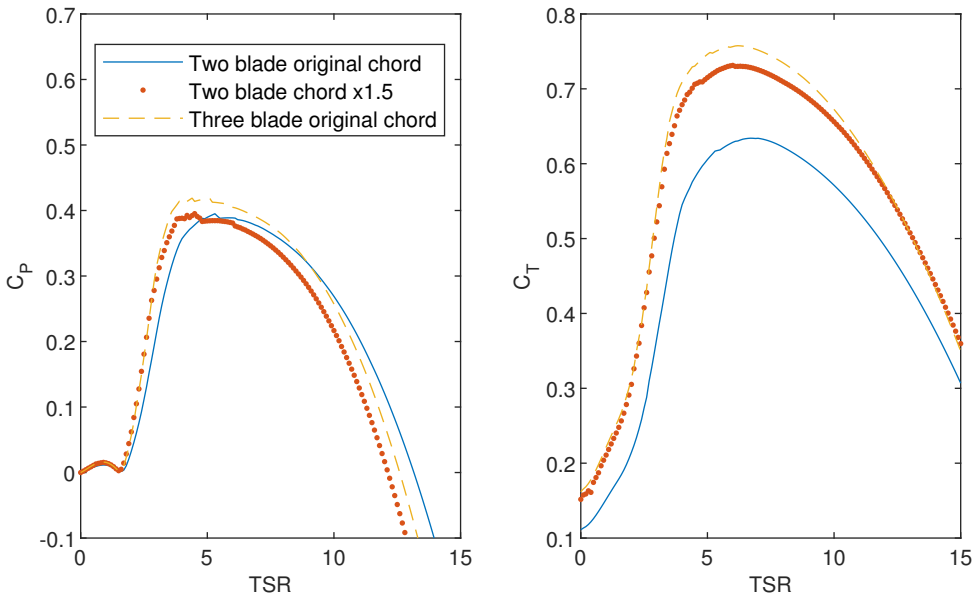

Figure 4.10: BEMT numerical model results with tip, hub, and high induction corrections for C_P and C_T against TSR for three different blade options for the RRES.

4.4.2 Design cases

Highlighted below are six cases which represent the extremities of the operating conditions that the RRES could theoretically be subjected to. The BEMT numerical model is used to calculate the loads and performance of the rotor blades in these operating conditions which will be used to guide its design.

1. Rated speed design
   - Rotor loads and performance will be calculated at optimum operating conditions, which is at TSR of 4.5, in current flow velocity of 1.3m/s.
   - This case is to determine the rated performance of the rotor.
2. Peak power before controlled shutdown
   - Controlled shut down will initiate at current flow velocity above 1.8m/s.
   - The rotor rotational rate will be kept the same as the rated speed design.
   - This case is to determine the peak power of the rotor prior to shutdown.
3. Controlled shutdown - Rotor blades parked
   - The rotor blades are stationary "parked" in this case and thus have a TSR of 0.
   - The river flow velocity is 3m/s, which is the maximum hypothesised velocity that could occur under severe weather events.
   - Due to the rotor blades being stationary, the thrust (drag) is based on plan area, not the swept area.
4. Runaway
   - A mechanical failure has taken place in this case, e.g shearing of shaft, snapping of timing belt, stripping of gears, etc.
   - This would result in the rotor spinning at run away.
   - The river flow velocity is again 3m/s.
   - This case will represent the highest thrust and rotational speed of the rotor blades.
5. Peak torque before controlled shutdown
   - River flow velocity range from 1-1.8m/s.
   - Rotor rotational rate $<$ rotor rotational rate of rated speed design case.
   - This case is used to create a specification for the test rig motor which requires the peak torque and corresponding rotational rate.

6. Start-up torque

   - Torque required to start rotor rotation.
   - Aim for rotor to start at river flow velocity of 1m/s.
   - Rotor torque at velocity of 1m/s $>$ total torque of RRES drive-train.

Table 4.4 summarizes the most important rotor loads and performance results of the 0.9m and 3.0m RRES device for each design case. The rated power of the 0.9m diameter RRES is 276W with rotor rotational rate of 2.07Hz in flow velocity of 1.3m/s. The 3.0 diameter RRES rated power is 3,070W with rotor rotational rate of 0.62Hz in flow velocity of 1.3m/s. A control system which uses a throttling valve will regulate the flow rate in the piping system and thus the rotational rate of the rotor. Peak rotor power of 629W and 6,980W for the 0.9m and 3.0m versions respectively, would occur at maximum allowable operating flow velocity and rotor rotational rate. At very similar operating conditions, peak torque of 47.6Nm and 1,760Nm respectively would occur. The maximum thrust and rotational rate values are seen in case 4, runaway, where the values are 1590N and 12.9Hz for the 0.9m device and 17,680N and 3.88Hz for the 3.0m device. These values would only be seen if a major mechanical failure were to occur, but the rotor blades will still be designed to survive such events. To ensure rotor start-up at flow velocity of 1m/s the torque in the drive train would have to be smaller than 2.6Nm for the 0.9m device and smaller than 100Nm for the 3.0m device. This will be tested during turbine commissioning, and if unachievable, the blades will be pitched to increase the rotor torque at flow speed of 1m/s.

Table 4.4: Summary of key rotor loads and performance results for 0.9m and 3.0m RRES version for all design cases from BEMT numerical model predictions with tip, hub, and high induction corrections.

Case	Torque (Nm)	Power (W)	Thrust (N)	Rotational rate (Hz)	TSR	Tip velocity (m/s)	Flow velocity (m/s)
0.9m version							
1. Rated speed design	21.2	276	380	2.07	4.5	5.85	1.3
2. Peak power before controlled shutdown	47.6	629	611	2.07	3.3	5.85	1.8
3. Controlled shutdown - Rotor blades parked	23.2	0	362	0	0	0	3.0
4. Runaway	0	0	1590	12.91	12.2	36.60	3.0
5.Peak torque before controlled shutdown	47.6	609	587	2.03	3.2	5.74	1.8
6. Start-up torque	2.6	0	40	0	0	0	1.0
3.0m version							
1. Rate speed design	790	3,070	4,220	0.62	4.5	5.85	1.3
2. Peak power before controlled shutdown	1,760	6,980	6,790	0.62	3.3	5.85	1.8
3. Controlled shutdown	860	0	4,020	0	0	0	3.0
4. Runaway	0	0	17,680	3.88	12.2	36.60	3.0
5. Peak torque before controlled shutdown	1,760	6,770	6,520	0.61	3.2	5.75	1.8
6. Start-up torque	100	0	450	0	0	0	1.0

4.5 Laboratory test rig design

4.5.1 Overview

The drivetrain test rig is installed in the ESRI Coastal Lab (ESRI 008) at Swansea University and has been designed to allow the testing and development of a hydraulic power take off mechanism that will later be use in field trials of the RRES device.

The full power take off system is designed to operate as a closed loop of clean water being pumped by the action of the rotating turbine, utilising a rotating crank mechanism to drive a double-action piston to pump water via non-return valves to a hydraulic generator. A controllable ball valve (throttling valve) is used to regulate water flow through the system, which will in turn provide resistance to rotor rotation and allow rotor speed to be controlled. The lab version of this mechanism functions in a similar manner, but uses a motor to provide input energy in a controllable manner and an open loop hydraulic circuit drawing water from a barrel that can be replenished from the lab supply if required. An orifice plate is used near to the outlet of the hydraulic loop to simulate the pressure drop

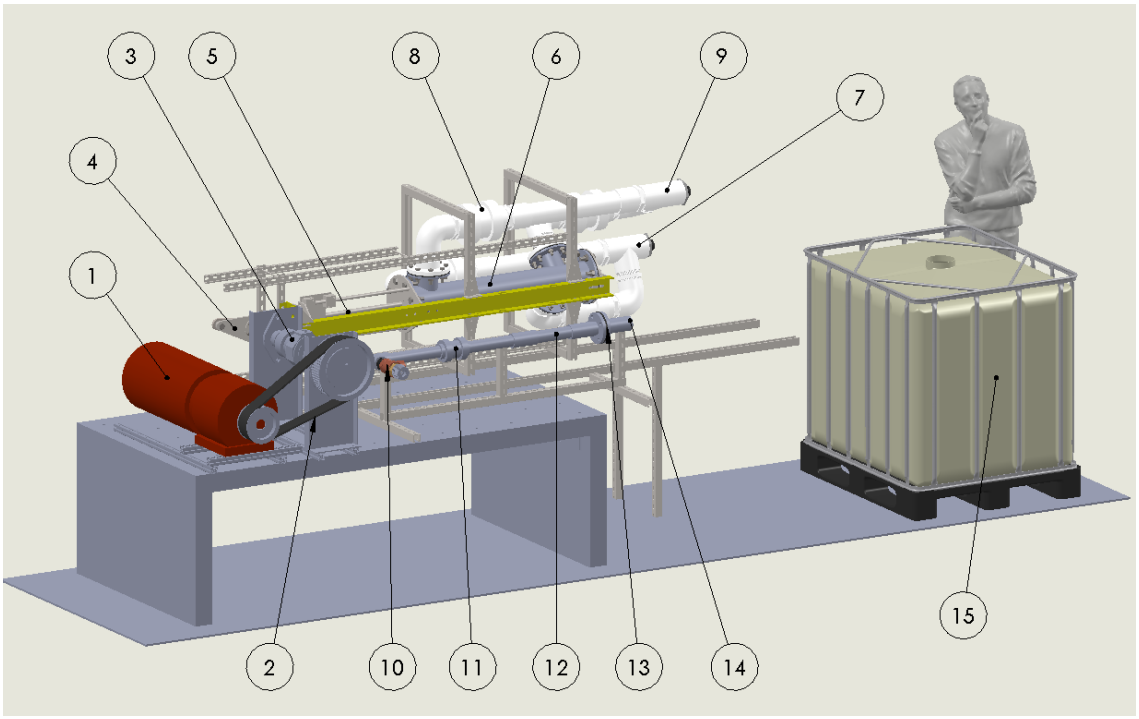

1. Motor
2. Belt pulley
3. Torque sensor
4. Crank arm
5. Piston rod
6. Pump manifold
7. Inlet pipe
8. One way “check” valve
9. Outlet pipe
10. Flow rate sensor
11. Pressure relief valve
12. Throttle valve
13. Orifice reduction plate
14. Pressure sensor
15. Water bath

Figure 4.11: CAD render of the laboratory test rig of the RRES with key components / sub-assemblies labelled.

across a hydraulic generator.

Control and data recording of the test system is provided via electronics housed in two IP67 rated enclosures. One enclosure is permanently wired to the motor and houses the motor drive unit, while the second enclosure includes the control and recording computer and sensor interfaces. CAD render of the RRES laboratory test rig which includes labels to

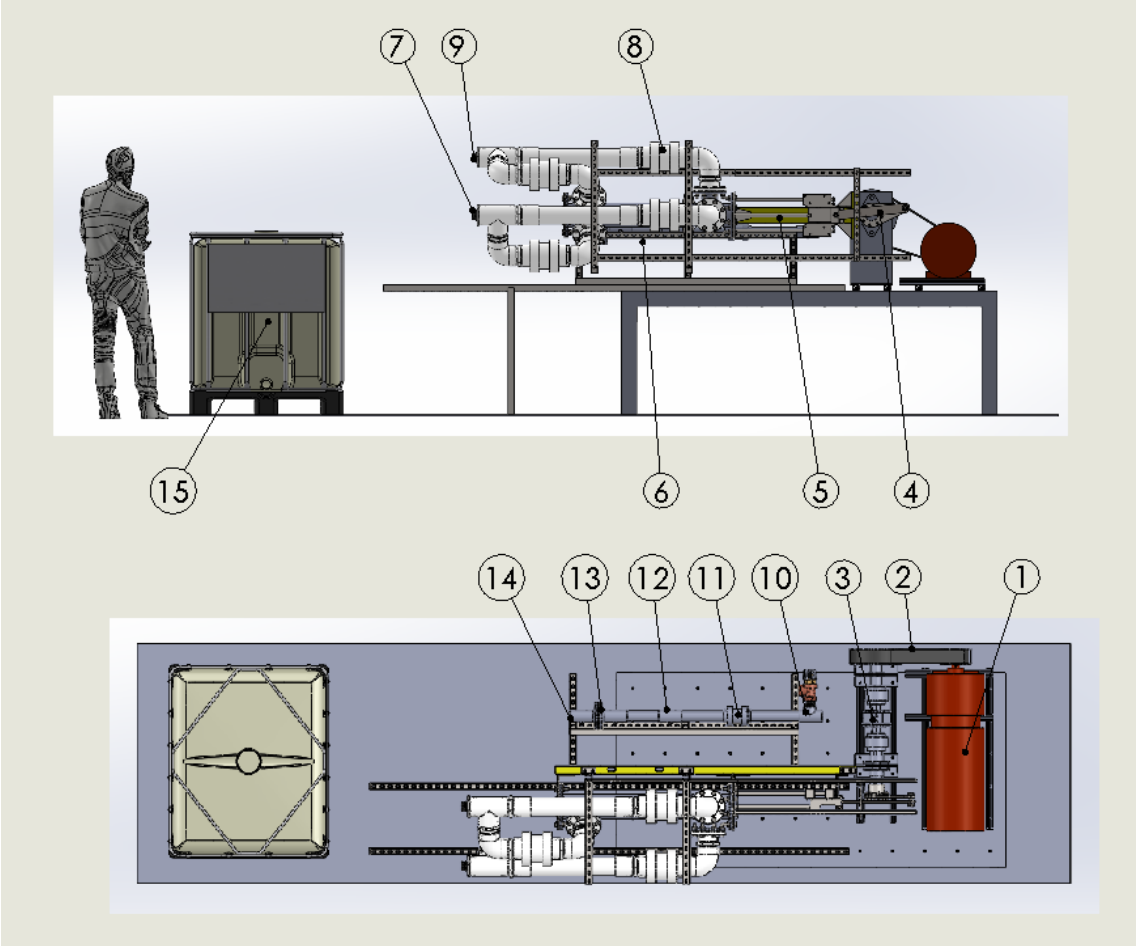

Figure 4.12: CAD render of the laboratory test rig of the RRES with key components / sub-assemblies labelled (corresponding to Figure 4.11).

identify key components / sub-assemblies is shown in Figure 4.11.

The overall layout of the test rig equipment is shown in Figure 4.12, with the motor and hydraulic circuit mounted to the test bench, water supply reservoir in the barrel on the left, and the two electronics enclosures on the right. Various photos of the RRES laboratory test rig are given in Figure 4.13. The labels on Figures 4.12 and 4.13 correspond to Figure 4.11.

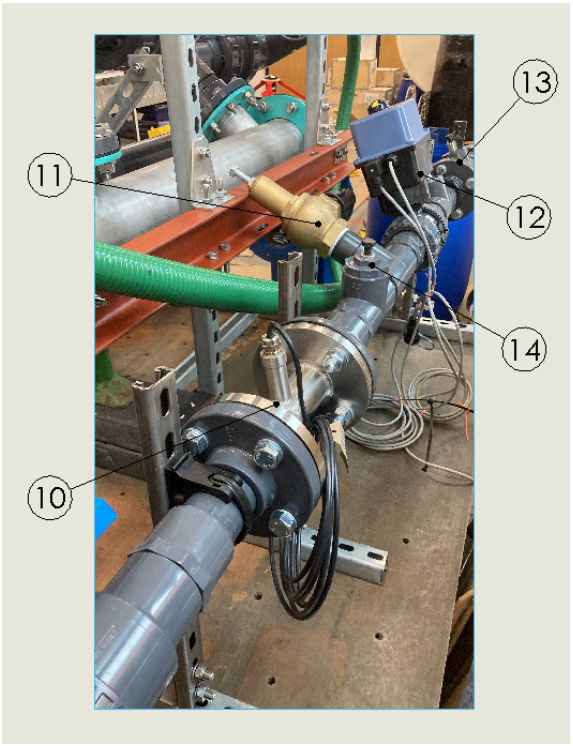

(a) Picture of the control system and sensor section of the RRES laboratory test rig.

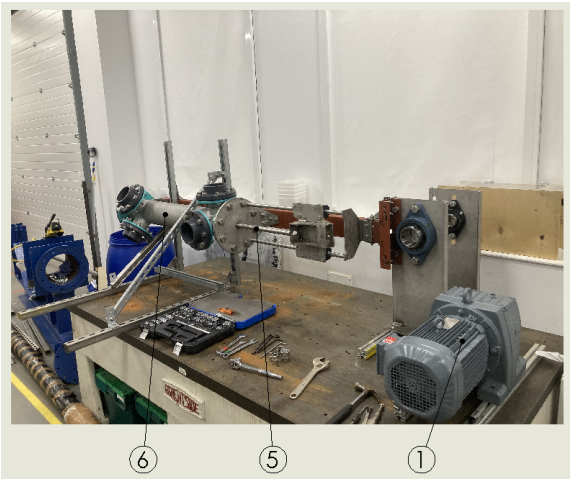

(b) Picture of early stages of construction of the RRES laboratory test rig.

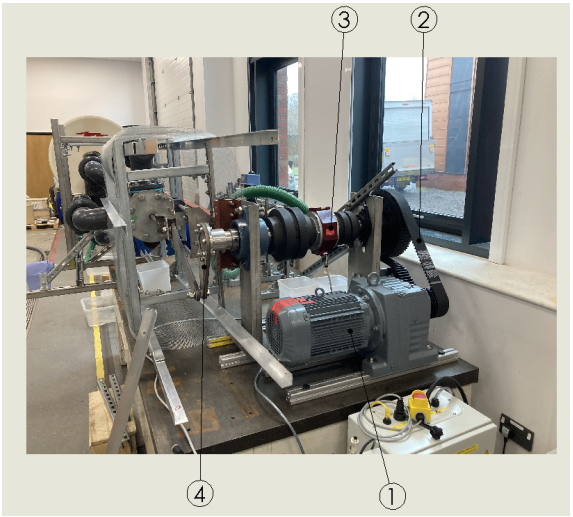

(c) Picture of completed construction of RRES laboratory test rig.

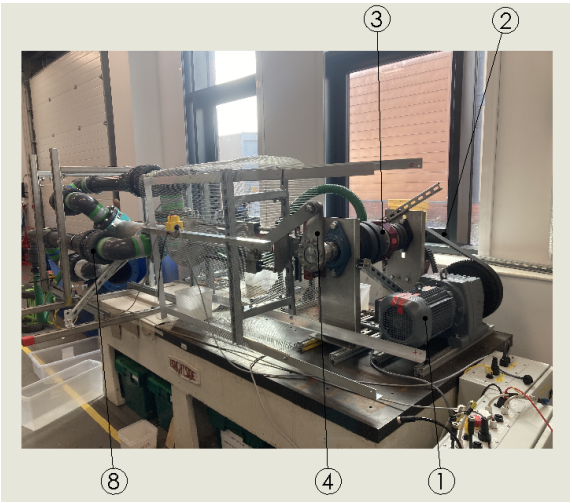

(d) Picture of completed construction RRES laboratory test rig.

Figure 4.13: Pictures of the RRES laboratory test rig with key components / sub-assemblies labelled (corresponding to Figure 4.11).

4.5.2 Design

The following equations are used to design and estimate the performance of the laboratory test rig. The same procedure is used for both 0.9m and 3.0m RRES devices, with the following presented example specifically for the 3.0m RRES laboratory test rig. Some of the key design parameters which need to be calculated are;

- Gear ratio
- Pump dimensions
- Pipe system dimension and components
- Sensors

4.5.2.1 Gear ratio

A timing belt is used to transfer power from the rotor shaft to the crankarm. A dual stroke piston system is chosen as the pump as it achieves constant flow with minimal components. It is decided for this type of pump that the maximum RPM should be kept below 130. The rotor rotational rate for the 3.0m RRES device at rated speed design is 0.62Hz as described in Section 4.4.2. Using commonly available gear ratio, η_{gear}, and ensuring that the maximum RPM of the pump stays below 130, a gear ratio of 1:3 is chosen.

4.5.2.2 Pump

The power that is delivered to the pump from the rotor is dependent on the efficiency of the drive train, η_{dt}, which is estimated to be 0.75.

$$\boldsymbol{P}_{\text{pump}} = \eta_{\text{dt}} \boldsymbol{P}_{\text{rotor}} \tag{4.1}$$

The pump rotational rate, ω_{pump}, and crank torque, $\boldsymbol{T}_{\text{crank}}$, are both dependent on the gear ratio, η_{gear}.

$$\omega_{\text{pump}} = \frac{\omega_{\text{rotor}}}{\eta_{\text{gear}}} \tag{4.2}$$

$$\boldsymbol{T}_{\text{crank}} = \eta_{\text{gear}} \eta_{\text{dt}} \boldsymbol{T}_{\text{rotor}} \tag{4.3}$$

Operating at rated speed design, the rotor will produce 790Nm of torque, $\boldsymbol{T}_{\text{rotor}}$, 3,070W of power, $\boldsymbol{P}_{\text{rotor}}$, at a rotational speed, ω_{rotor}, of 0.62Hz. Similarly, operating at peak power

case prior to shutdown, the rotor will produce 1,760Nm of torque, 6,980W of power, at a rotational speed of 0.62Hz. Table 4.5 shows the corresponding pump values for these cases.

Table 4.5: Torque, power, and rotational speed for the 3.0m RRES rotor and pump at rated speed design and peak power cases.

Case	Torque (kN.m)		Power (kW)		Rotational rate (Hz)	
	Rotor	Crank	Rotor	Pump	Rotor	Pump
1. Rated speed design	0.79	0.20	3.07	2.30	0.62	1.86
2. Peak power	1.76	0.44	6.98	5.24	0.62	1.86

As previously mentioned, the pump will be a dual stroke piston system. Crankarm length, $\boldsymbol{L}_{\text{crank}}$, and piston head area, $\boldsymbol{A}_{\text{piston}}$, are the two dimensions which dictate the pump volume, $\boldsymbol{V}_{\text{pump}}$. The volumetric flow rate of the pump, $\dot{\boldsymbol{V}}_{\text{pump}}$, is calculated by multiplying the pump volume by twice its rotational rate.

$$\boldsymbol{V}_{\text{pump}} = \boldsymbol{2L}_{\text{crank}}\boldsymbol{A}_{\text{piston}} \tag{4.4}$$

$$\dot{\boldsymbol{V}}_{\text{pump}} = \boldsymbol{2V}_{\text{pump}}\boldsymbol{\omega}_{\text{pump}} \tag{4.5}$$

The diameter of the piston head is chosen to be 101.6mm (4") (x2 of 0.9m device), as this is the diameter of the PVC flexible hose available for the piping system. Maintaining a standard diameter wherever possible will reduce complexity. A flow rate of $0.01\text{m}^3/\text{s}$ (600l/min) is the target whilst operating at rated speed design (x4 of 0.9m device). This value is within the specified working range of the majority of sensors which are intended to be used. Using the flow rate and piston head diameter, the remaining pump parameters are calculated, detailed in Table 4.6.

Table 4.6: Dimensions of the 3.0m RRES pump.

Detail	Symbol	Value	Unit
Piston diameter	$\boldsymbol{D}_{\text{piston}}$	0.1016	m
Piston area	$\boldsymbol{A}_{\text{piston}}$	0.00812	m^2
Crank length	$\boldsymbol{L}_{\text{crank}}$	0.166	m
Stroke length	$\boldsymbol{L}_{\text{stroke}}$	0.332	m
Pump volume	$\boldsymbol{V}_{\text{pump}}$	0.00269	m^3

The maximum force in the pump, $\boldsymbol{F}_{\text{pump}_{\text{max}}}$, is calculated by taking the maximum crank torque and dividing by its length, whilst the maximum pump pressure, $\boldsymbol{p}_{\text{pump}_{\text{max}}}$, is

calculated by dividing the maximum pump force by the piston area head. The maximum pump force and pressure will occur during design case 5, peak rotor torque, and are 2,660N and 0.328MPa respectively.

$$\boldsymbol{F}_{\text{pump}_{\text{max}}} = \frac{\boldsymbol{T}_{\text{crank}_{\text{max}}}}{\boldsymbol{L}_{\text{crank}}} \tag{4.6}$$

$$\boldsymbol{p}_{\text{pump}_{\text{max}}} = \frac{\boldsymbol{F}_{\text{pump}_{\text{max}}}}{\boldsymbol{A}_{\text{piston}}} \tag{4.7}$$

The piston rod is a critical component of the pump and must withstand the maximum force of 2,660N without buckling. The piston rod is chosen to be 12mm diameter made from stainless steel grade 316. Euler column formula is used to calculate the critical load for the piston rod;

$$\boldsymbol{F}_{\text{crit}} = \frac{\boldsymbol{n}\boldsymbol{\Pi}^{\mathbf{2}}\boldsymbol{E}\boldsymbol{I}}{\boldsymbol{L}^{\mathbf{2}}} \tag{4.8}$$

where $\boldsymbol{n}$ is the factor accounting for the end conditions, $\boldsymbol{E}$ is the modulus of elasticity, $\boldsymbol{I}$ is the cross-sectional moment of inertia, and $\boldsymbol{L}$ length of rod.
One end of the rod will be fixed to the crank arm whilst the other will be supported at the piston head, and thus an end condition factor of 2 is chosen. The maximum length of the rod will be equal to the stroke, and is 0.332m. The modulus of elasticity of 316 SS is 193GPa. The moment of inertia is calculated using Equation 4.9 and is 2.011x10^{-10}m^4.

$$\boldsymbol{I} = \frac{\boldsymbol{\Pi}\boldsymbol{d}^{\mathbf{4}}}{\mathbf{64}} \tag{4.9}$$

The critical load, $\boldsymbol{F}_{\text{crit}}$ for the piston rod is 35kN which is 13x larger than the predicted maximum force. Although over engineered the rod diameter will be kept at 12mm, as reducing the rod size further would result in difficulties in assembly.
A simple numerical model is coded in MATLAB which is used to predict the operating parameters of the laboratory test rig. Figure 4.14 shows one complete pump cycle for (a) force, (b) pressure, and (c) volumetric flow rate at rated speed design case. As can be seen in Figure 4.14c, water is pumped in both stroke direction as the pump is a dual stroke piston system. There is no difference in pump force and pressure in either stroke direction and the negative values only indicate opposite direction to the positive.
Pump head, $\boldsymbol{h}_{\text{pump}}$, indicates the height to which the pump can raise a fluid. It is an important parameter which indicates how much energy will be in the system. It is

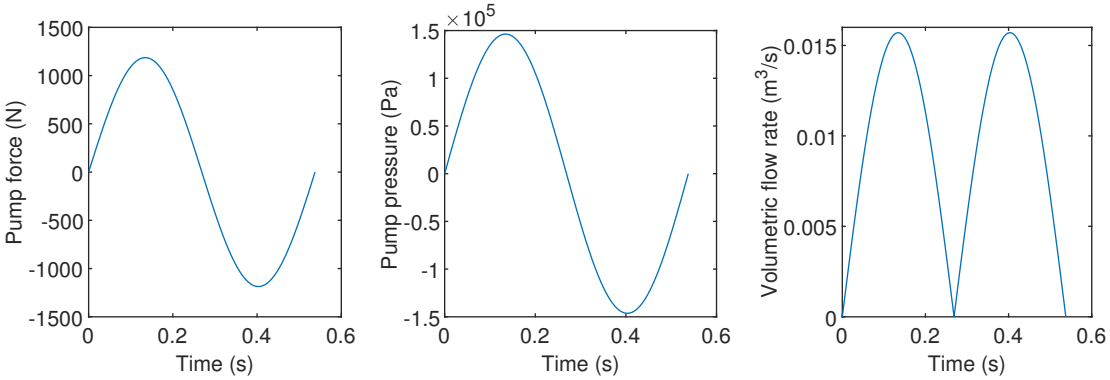

(a) (b) (c)

Figure 4.14: One complete pump cycle for (a) force, (b) pressure, and (c) volumetric flow rate at rated speed design case for the 3.0m RRES.

calculated using Equation 4.10, which is derived from Bernoulli's equation. η_{pump} is the pump efficiency, and is estimated to be 0.7. $\boldsymbol{P}_{\text{pump}}$ and $\dot{\boldsymbol{V}}_{\text{pump}}$ are pump power and volumetric flow rate respectively.

$$\boldsymbol{h}_{\text{pump}} = \frac{\boldsymbol{P}_{\text{pump}} * \boldsymbol{\eta}_{\text{pump}}}{\dot{\boldsymbol{V}}_{\text{pump}} * \boldsymbol{g} * \boldsymbol{\rho}} \tag{4.10}$$

Figure 4.15 is a surface plot of pump head against current flow velocity and rotor rotational rate for the 3.0m RRES. 36.22m is the maximum pump head which is seen at maximum rotor rotational rate and current speed of 0.62Hz and 1.8m/s respectively.

4.5.2.3 Pipe system

The pressure in various locations in the piping system are important to know to ensure appropriate fittings and sensors are used. Figure 4.16 is a diagram of the piping system indicating locations of pressure calculations using Bernoulli's equation 4.11.

$$\frac{\boldsymbol{p}_1}{\boldsymbol{\rho g}} + \frac{\boldsymbol{U}_1{}^{\boldsymbol{2}}}{\boldsymbol{2g}} + \boldsymbol{z}_1 + \boldsymbol{h}_{\text{pump}} = \frac{\boldsymbol{p}_2}{\boldsymbol{\rho g}} + \frac{\boldsymbol{U}_2{}^{\boldsymbol{2}}}{\boldsymbol{2g}} + \boldsymbol{z}_2 + \boldsymbol{h}_{\text{L}} \tag{4.11}$$

It is assumed that the water in the pipe system is an incompressible ideal fluid. The pipe diameter is constant throughout the system and thus fluid velocity, $\boldsymbol{U}_1$ and $\boldsymbol{U}_2$, will always be equal. Additionally, the whole pipe system is approximately at the same height and thus the height terms, z_1 and z_2 , will also always be equal. Equation 4.11 can thus be simplified to Equation 4.12.

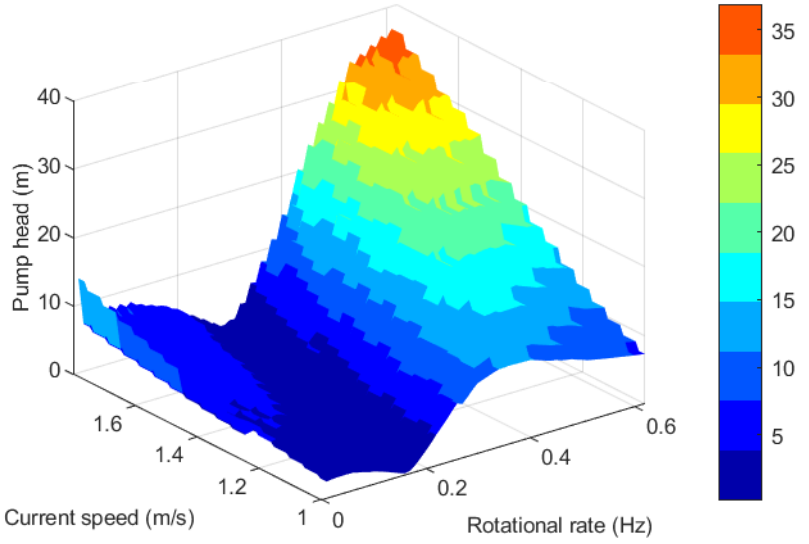

Figure 4.15: Surface plot of pump head against current flow velocity and rotor rotational rate for the 3.0m RRES.

$$\frac{p_1}{\rho g} + h_{\text{pump}} = \frac{p_2}{\rho g} + h_{\text{L}} \tag{4.12}$$

h_{L} is the head losses in the system due to fluid friction which occur at the pipe wall, valves, fitting, and sensors. Empirical values are available to estimate these losses. Darcy's equation can be used to calculate the frictional head loss from the pipe wall.

$$h_{\text{L}} = f\frac{L}{D}\frac{U^2}{2g} \tag{4.13}$$

where f is the friction factor, L length of pipe, D diameter of pipe, U mean velocity, and g gravitational acceleration. The friction factor is selected from the Moody diagram which relates the friction factor to the Reynolds number and relative roughness of the pipe, ϵ/D. The friction factor will be approximately 0.02 in our medium density polyethylene (MDPE) piping.

In addition to losses from the pipe wall, we also have minor losses from components and fittings in our system. These are calculated using Equation 4.14, where K_{L} is the loss coefficient. Common values for K_{L} are included in Table 4.7.

$$h_{\text{L}} = K_{\text{L}}\frac{U^2}{2g} \tag{4.14}$$

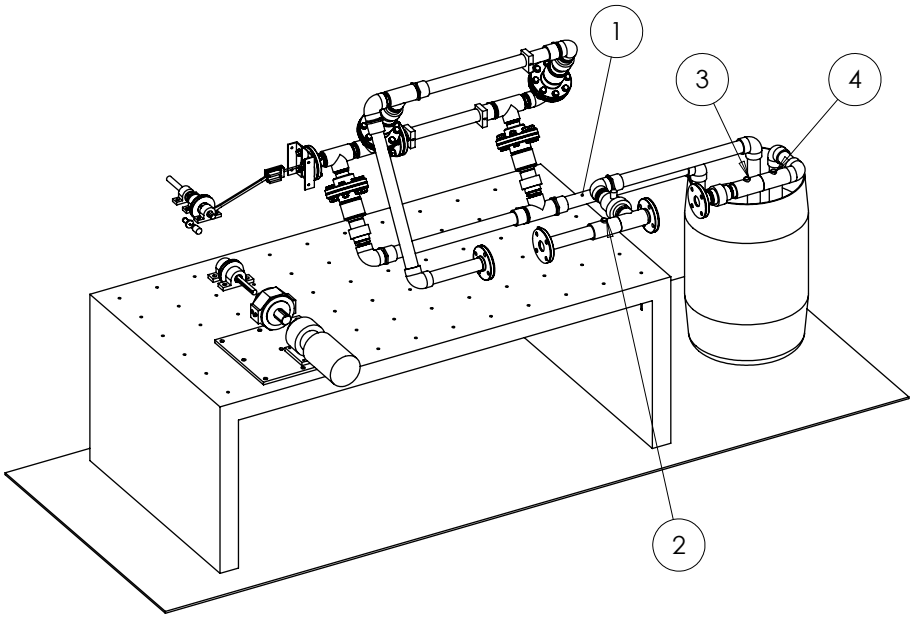

NO.	LOCATION
1	Inlet pipe to pump
2	Outlet pipe from pump
3	Downstream of throttling valve and upstream of orifice plate
4	Downstream of orifice plate

Figure 4.16: Diagram of the RRES laboratory test rig piping system indicating location of pressure calculations.

Table 4.7: Values of common loss coefficient of pipe system components.

Component	$\boldsymbol{K}_{\mathrm{L}}$ Value
Elbow join	0.70
Tee join	0.90
Check valve	2.00
Ball valve, fully open	0.05
Flow rate sensor	0.10

The head loss in the whole piping system of the full scale RRES device for various pipe sizes against volumetric flow rate is shown in Figure 4.17. The head loss for pipe size of 4″ and above are relatively similar thus it is decided based on minimising pipe cost and material that a 4″ pipe will be used.

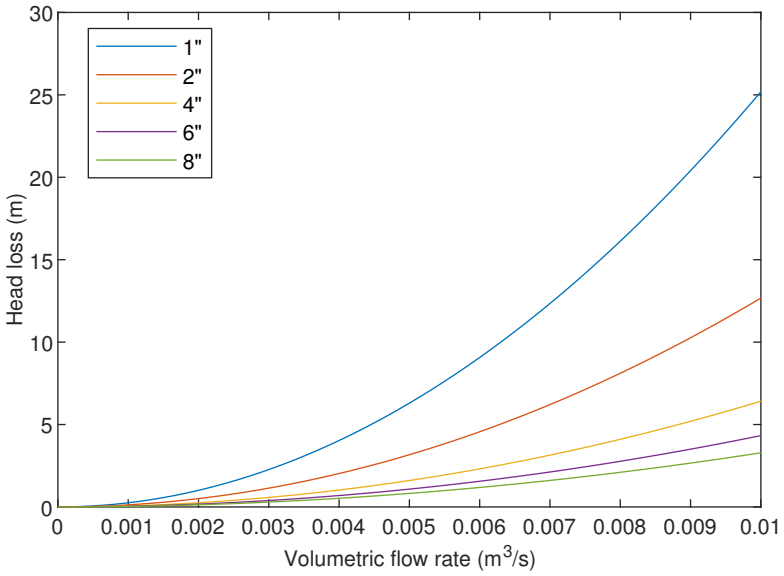

Figure 4.17: Plot of total head loss in the whole piping system of the 3.0m RRES laboratory rig for various pipe sizes against volumetric flow rates.

The pressure in the inlet pipe, p_1, is assumed to be approximately 101kPa (1 atm). Using Equation 4.12, we can now calculate the pressure in the outlet pipe, p_2. A plot of outlet absolute pressure is shown in Figure 4.18 where the maximum pressure will be 3.97 atm.

$$p_2 = p_1 + h_{\text{pump}}\rho g - h_{\text{L}}\rho g \tag{4.15}$$

A restriction orifice plate will be located in the piping system between the throttling valve and the discharge to the water bath to reduce the water pressure in the RRES laboratory rig. The pressure drop across a restriction orifice is calculated using Equation 4.16, where β is the ratio of orifice to pipe diameter, Q is the volumetric flow rate, C_{d} is the orifice discharge coefficient, and A_{o} is the area of the orifice.

$$\Delta p_{\text{orifice}} = \frac{1}{2}\rho(1-\beta^4)\left(\frac{Q}{C_{\text{d}}A_{\text{o}}}\right)^2 \tag{4.16}$$

A significant pressure drop is not required and thus a relatively high β of 0.5 is chosen. As the pipe has a diameter of 101.6mm (4″), the area of the orifice, A_{o}, will be 2.027x10^{-3}m^2. The orifice discharge coefficient, C_{d}, is dependent on β and the Reynolds number of the flow. In this case it is approximately 0.60. A plot of pressure drop across the restriction

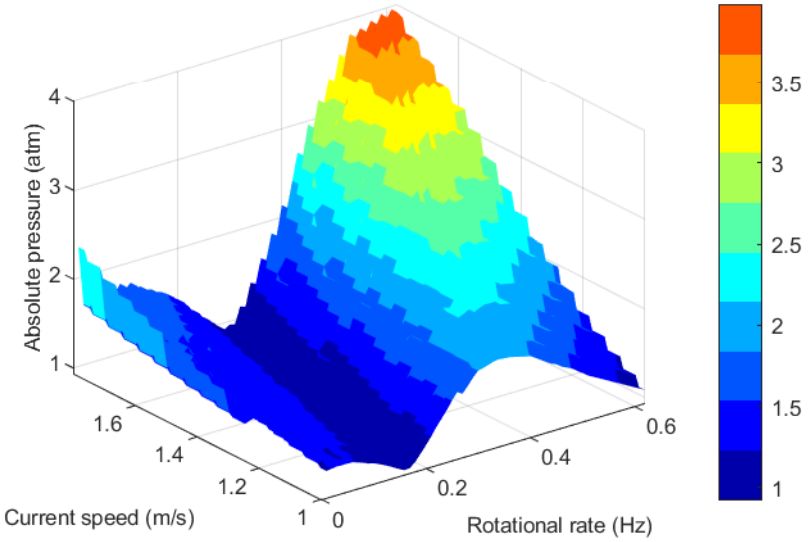

Figure 4.18: Surface plot of absolute pressure in the outlet pipe of the piping system of the 3.0m RRES laboratory rig against current flow velocity and rotor rotational rate.

orifice against flow rate is shown in Figure 4.19. A maximum pressure drop of 1.04 atm occurs at the maximum allowable flow rate of $0.01\mathrm{m}^3/\mathrm{s}$.

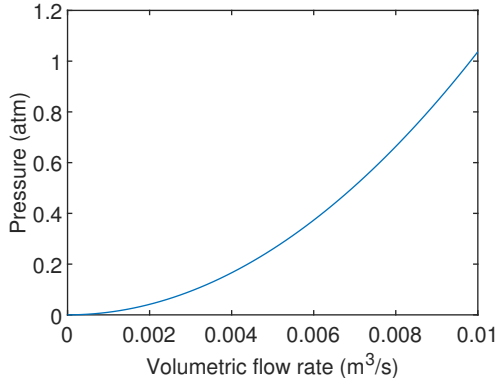

Figure 4.19: Pressure drop across the restriction orifice plate in the 3.0m RRES laboratory test rig piping system.

The throttling valve will be used to control the flow rate in the piping system. Calculation of the energy extracted by the throttling valve will be made by measuring the downstream pressure, at location 3, and comparing to the upstream pressure, at location 2. Pressure in

the piping system downstream of the restriction orifice, location 4, will be the pressure of the discharge water into the water bath and is calculated using Equation 4.17.

$$p_4 = p_2 - \Delta p_{\text{orifice}} - \Delta p_{\text{valve}} \tag{4.17}$$

Shown in Figure 4.20 is the absolute pressure downstream of the restriction orifice for the whole operating range of the 3.0m RRES. The results in this plot assumes a fully open throttling valve with no pressure loss across it.

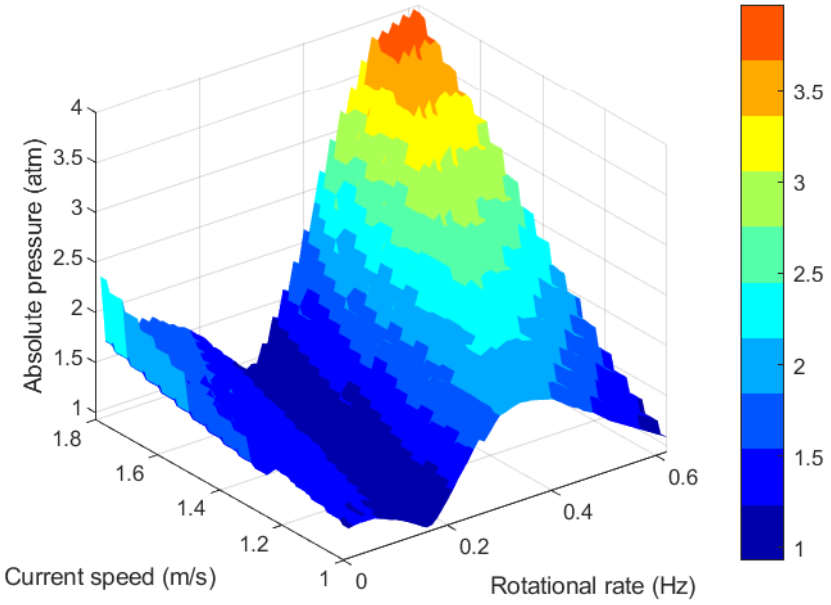

Figure 4.20: Absolute pressure downstream of the restriction orifice for the whole operating range of the 3.0m RRES laboratory test rig.

The pressure drop across an orifice restriction plate is proportional to flow rate. As seen in Figure 4.15, the pressure varies significantly at same rotational rate (flow rate). At rotational rate of 0.62Hz the pressure varies from 1.1-4.0 atm. To mitigate against misuse of laboratory test rig where the pressure is significantly higher than designed, a pressure relief valve is located upstream of the throttle valve which will discharge if the pressure reaches 5 atm.

4.5.2.4 Motor

An electric motor is used in the laboratory test rig to replicate the rotational torque generated by the rotor blades at sea. The torque and power requirements for the motor

across the whole operating range, for both 0.9m and 3.0m devices are shown in Figure 4.21 and Figure 4.22 respectively.

Due to the very low required rotational rates, an inline helical gear motor coupled with an AC inverter is chosen as the most appropriate set-up.

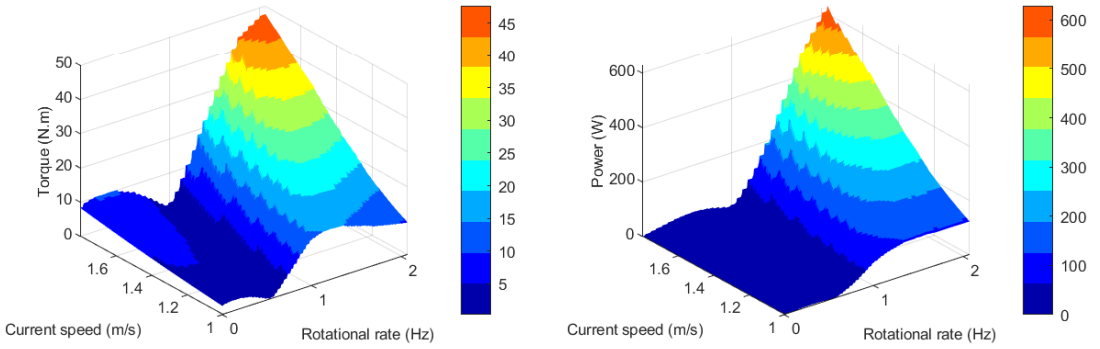

(a) (b)

Figure 4.21: Motor (a) torque and (b) power requirements for the 0.9m RRES device across the entire operating range.

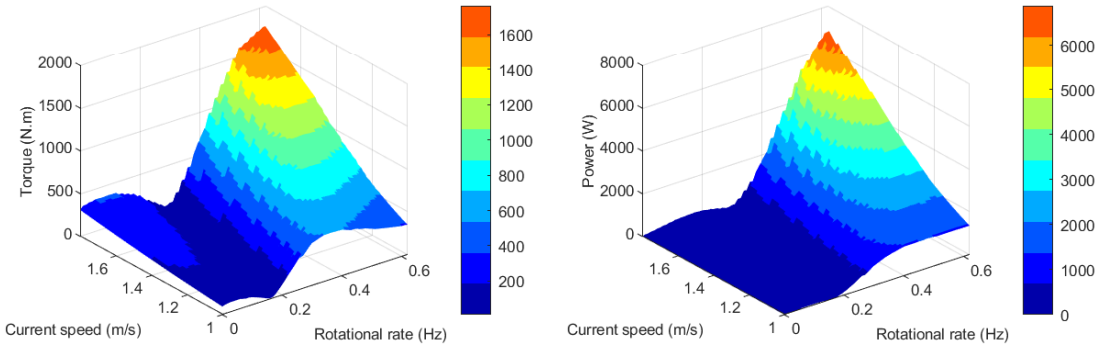

(a) (b)

Figure 4.22: Motor (a) torque and (b) power requirements for the 3.0m RRES device across the entire operating range

4.5.3 Failure mode effect analysis

This section details identified mechanical failure modes and subsequent effects of failure modes for the RRES laboratory test rig designed and being manufactured as part of the MEECE project for eventual deployment at the marine energy test site in Warrior Way. This is a design level failure mode effect analysis (FMEA), and includes mitigations considered

at the design stage as well as steps to be followed during manufacture and operation of the laboratory test rig.
Only mechanical failures are considered, **M**echanical, and assigned an ID of the form Constituent/System/Number (e.g. M/P/1 is the first failure mode of the mechanical pump). Each failure is also rated in terms of severity, with 1 being total and unrecoverable failure, 2 being loss of function, and 3 being partial loss of function.
These failures are summarised in Table 4.8 at the end of the section.

4.5.3.1 Mechanical Failures

The laboratory test rig consists of several mechanical sub-assemblies whose failures will have both primary and secondary consequences.

Motor

The inline helical gear motor is used as low speed, high torque is required. It is the most important mechanical system, supplying torque to the test rig. A total failure of the motor would fall under severity 1 - total and unrecoverable failure.

- **M/M/1 - Mechanical break.**
  Severity 1 - permanent loss of function

  In the event of a mechanical break which renders the motor unusable, the laboratory test rig will cease to be operable. Following the manufactures guidance and ensuring it is operated within its designed range should prevent such break occurring.

- **M/M/2 - Overheating.**
  Severity 2 - temporary loss of function

  The motor will temporarily cease to work in the event of overheating, rendering the whole test rig unusable. The motor will be located in an appropriate location which follows manufactures guidance on ventilation procedures.

- **M/M/3 - Slipping.**
  Severity 3 - reduced torque input to test rig

  In the event of the motor connection slipping, torque transfer to the test rig will be significantly reduced. This will reduce the range of tests which can be performed

and limit the usefulness of the test rig. The use of industry standard coupling of motor to test rig should ensure reliable torque transfer.

Power take off

The PTO sub-assembly transfers the rotational power of the motor to the linear power of the pump. Failure to transfer the power would result in a loss of function of the test rig, severity 2.

- **M/PTO/1 - belt pulley slipping.**
  Severity 3 - reduced power transfer to pump

  In the event of the belt pulley slipping power transfer to the pump is greatly reduced. This will reduce the range of tests which can be performed and limit the usefulness of the test rig. Correct standard belt pulley tensioner will be used to minimise the chance of belt slipping.

- **M/PTO/2 - belt pulley snapping.**
  Severity 2 - loss of power transfer to pump

  In the event of the belt pulley snapping from overheating due to excessive loads or speed, power transfer to the pump is lost and the test rig has lost its function. Ensuring the belt pulley is rated to the predicted loads and speeds, as well as following correct operating guidance will minimise the likelihood of any failures.

- **M/PTO/3 - crankarm assembly misalignment.**
  Severity 3 - reduced efficiency and increased risk of more severe failures

  In the event that there is misalignment in the crank assembly, efficiency of the test rig will be reduced along with increased loads on components which will increase the risk of more severe failures. Incorporating bearings in appropriate locations as well as following best practice for assembly, misalignment of parts can be kept to a minimum.

- **M/PTO/4 - crankarm assembly failure.**
  Severity 2 - loss of power transfer to pump

In the event of the crank arm assembly failure from excessive loads, speeds, or misalignment, power transfer to the pump is lost and the test rig has lost its function. Ensuring the crank arm assembly is correctly assembled, minimising misalignment, is rated to the predicted loads and speeds, will minimise the likelihood of any failures.

- **M/PTO/5 - bearing failure.**
  Severity 3 - reduced efficiency

  In the event of bearing failure, the efficiency of the test rig will be significantly reduced. Bearing failure could occur due to incorrect bearing choice, defects, or misalignment. Choosing appropriate bearings, rated to the loads and speeds, as well as following best practices during assembly will minimise the chances of any failures.

Pump

The pump is a dual stroke piston system, chosen as it achieves constant flow with minimal components. It is used to pump water around the closed loop piping system, which consists of valves and sensors. If it fails to pump water around the piping system, then the whole test rig is rendered useless, severity 2.

- **M/P/1 - pump rod buckling.**
  Severity 2 - loss of pump function

  In the event of the pump rod buckling due to excessive force, the pump will cease to operate and no water will be pumped around the piping system. Designing the pump rod to a high SF of 3 and ensuring motor output loads are limited will minimise the likelihood of any buckling.

- **M/P/2 - pump head tolerance.**
  Severity 2 - loss of pump function

  In the event of inappropriate pump head tolerance with the pump cylinder, pump efficiency or function will be negatively impacted. If the tolerances are to small, additional friction loads will be placed on the pump rod, potentially leading to

buckling and loss of function. On the contrary, if the tolerances are to big, the pump will be very inefficient and be limited to the amount of water it can pump, resulting in loss of function. Using best practice tolerances and manufacturing technique will maximise the chances of correct pump manufacture and minimise any likelihood of the failures associated with incorrect tolerances.

- **M/P/3 - surface finish of components.**
  Severity 3 - reduced efficiency

  In the event of the pump cylinder and/or pump head having poor surface finishes due to poor manufacturing choices, pump efficiency will be negatively effected. Poor surface finish will increase the wear on components as well as reducing the systems efficiency, increasing the risk of a more severe failure. Choosing the most appropriate manufacturing and surface finishing techniques will minimise the chance of failure due to poor surface finish of parts.

Piping system

The piping system is an assembly of pipes, joins, valves, and sensors which creates a closed loop system which has water flowing throughout. Water is sucked out of a reservoir by the pump before passing though one way ball valves, flow sensor, throttling valve, and an orifice plate. The water then exits the piping system back into the reservoir. Any failures within the piping system would cease experimental testing and recording of any meaningful data, severity 2.

- **M/PS/1 - severe leakage (burst).**
  Severity 2 - loss of pressure and water leakage

  In the event of severe leakage from a component due to excessive pressure in the system, recording of meaningful data from the test rig will stop. A pressure relief valve is included upstream of the throttling valve which will allow the discharge of water in the event of excessive pressure in the system, ensuring no damage in inflicted on any components.

- **M/PS/2 - debris in water.**
  Severity 1 - permanent damage to sensors

In the event of debris being sucked into the piping system and flowing through the pressure and flow rate sensors, irretrievable damage could be caused to these sensors. Ensuring the water reservoir is debris free is fairly easy in a laboratory setting, but including a filter in the inlet pipe would reduce the chances of debris entering the piping system to a minimum.

- **M/PS/3 - one way ball valve failure.**
  Severity 2 - loss of pump function

  In the event of the one way ball valves not working as designed (creating a seal) due to incorrect application, the pump will not supply a flow of water in the piping system. Ensuring the appropriate valves are used, and assembled as designed will limit the likelihood of any failure.

- **M/PS/4 - small leaks in joins.**
  Severity 3 - dripping of water on components

  In the event of joint leakage due to inadequate joining method, water will seep out and drop on components beneath. A small leak is tolerated in most cases as it has negligible impact. But in the case of leakage onto an electrical component, this could cause a more serious failure. Ensuring best practice joining techniques are used during assembly will minimise the chances of any leaks occurring.

- **M/PS/5 - air in system.**
  Severity 3 - reduced water flow and pressure

  In the event of air being trapped in the piping system, water flow will be reduced as well as pressure. Also, pressure readings from the sensors could be obscured. Incorporating air valves and ensuring system is primed with water will minimise any air trapped in the piping system.

4.5.3.2 Summary Table

Table 4.8: Summary table of mechanical failure mode effect analysis of the remote river energy system laboratory test rig.

ID	System	Component	Failure	Failure Cause	Failure Effect	Severity	Mitigation/Fallback
M/M/1	Mechanical	Motor	Mechanical break	Mechanical defect	Permanent loss of function	1	Operating within its designed range
M/M/2	Mechanical	Motor	Overheating	Inadequate ventilation	Temporary loss of function	2	Locate motor in appropriate location with sufficient ventilation as per manufactures guidance
M/M/3	Mechanical	Motor	Slipping	Inadequate coupling	Reduced torque input to test rig	3	Use appropriate mechanical technique to couple motor to test rig
M/PTO/1	Mechanical	Power take off	Belt pulley slipping	Lack of tension in belt	Reduced power transfer to pump	3	Use belt tensioner to maintain appropriate tension in belt
M/PTO/2	Mechanical	Power take off	Belt pulley snapping	Excessive loads or speeds	Loss of power transfer to pump	2	Ensure belt is rated to expected loads and speeds and follow operating guidance
M/PTO/3	Mechanical	Power take off	Crank arm assembly misalignment	Inappropriate assembly techniques	Reduced efficiency and increased risk of more severe failures	3	Incorporating bearings in appropriate locations as well as following best practices for assembly
M/PTO/4	Mechanical	Power take off	Crank arm assembly failure	Excessive loads, speeds, or misalignment	Loss of power transfer to pump	2	Ensure correct assembly and rated to predicted loads and speeds

M/PTO/5	Mechanical	Power take off	Bearing failure	Inadequate, defective, or misaligned bearing	Reduced efficiency	3	Choosing appropriate bearings, rated to predicted loads and speeds, and assembled using best practices
M/P/1	Mechanical	Pump	Pump rod buckling	Excessive loads	Loss of pump function	2	Limiting motor outputs and design rod to SF of 3
M/P/2	Mechanical	Pump	Pump head tolerance	Inappropriate pump head tolerances - too small a tolerance will increase friction and loads, too big a tolerance will reduce pump efficiency	Loss of pump function	2	Using best practice tolerances and manufacturing techniques
M/P/3	Mechanical	Pump	Reduced efficiency	Surface finish of components	Efficiency of pump is negatively effected by poor surface finishes if pump cylinder and head	3	Using most appropriate manufacturing and surface finish techniques
M/PS/1	Mechanical	Piping system	Sever leakage (burst)	Excessive pressure in system	Loss of pressure and water leakage	2	Including a pressure relief valve upstream of the throttling valve will allow the discharge of water in the event of excess pressure

M/PS/2	Mechanical	Piping system	Debris in water	Debris being sucked into the piping system	Permanent damage to sensors and pump	1	Including a filter in the inlet pipe
M/PS/3	Mechanical	Piping system	One way ball valve failure	Incorrect application or assembly	Loss of pump function	2	Ensuring appropriate valves are used and assembled as designed
M/PS/4	Mechanical	Piping system	Small leaks in joins	Inadequate joining methods	Dripping of water on components	3	Ensuring best practice joining techniques are used during assembly
M/PS/5	Mechanical	Piping system	Air in system	Inadequate priming or assembly	Reduced water flow and pressure	3	Incorporating air valves and ensuring system is primed

4.6 Full scale deployment

4.6.1 Assembly

Figures 4.23 and 4.24 shows a CAD render of the RRES with key components / sub-assemblies labelled. Figure 4.24 is a detailed view A from Figure 4.23.
The RRES is held in position by 4 mooring lines which all have (1) gravity anchor, (2) weighted chain, (3) tug rope. A buoy line (4) raises from each gravity anchor which is attached to a marker buoy (5) on the water surface to warn other vessels of the foot-print of the RRES. Detailed description of the mooring is given later in Section 4.6.6.

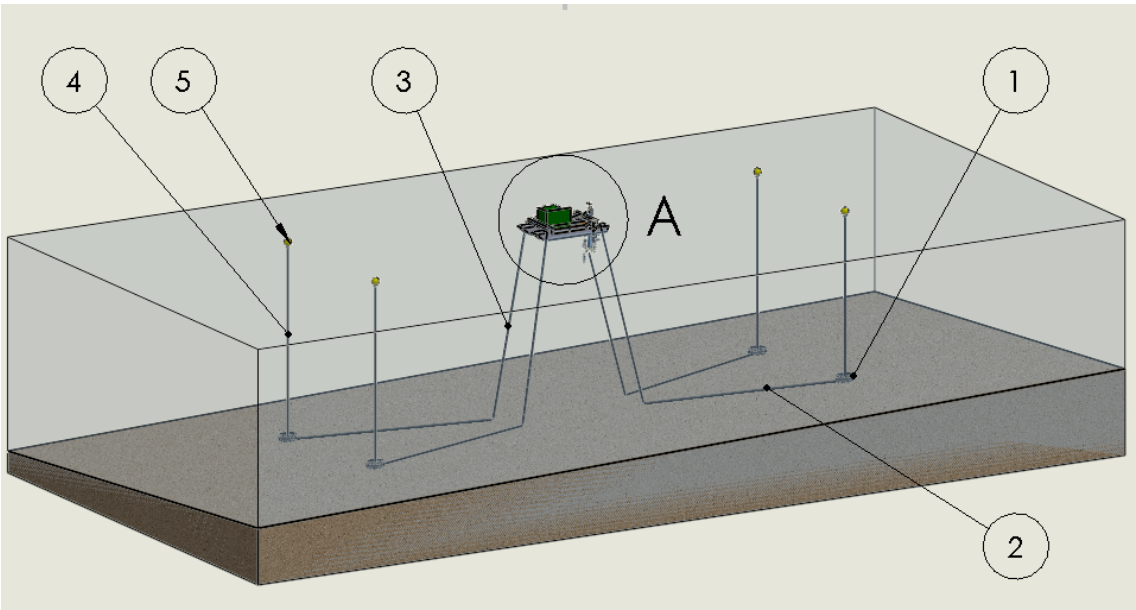

1. Gravity anchor
2. Weighted chain
3. Tug rope
4. Buoy line
5.Marker buoy

Figure 4.23: CAD render of the whole RRES assembly with key mooring components labelled.

Two modular pontoons (6) form the main structure of the floating test platform which are connected by steel beams at both ends. At the rear of the platform a submersible arm (8) pivots on the steel beam which is raised and lowered by a hydraulic arm (9). The PTO (10) assembly is located at the bottom of the submersible arm and is directly driven by

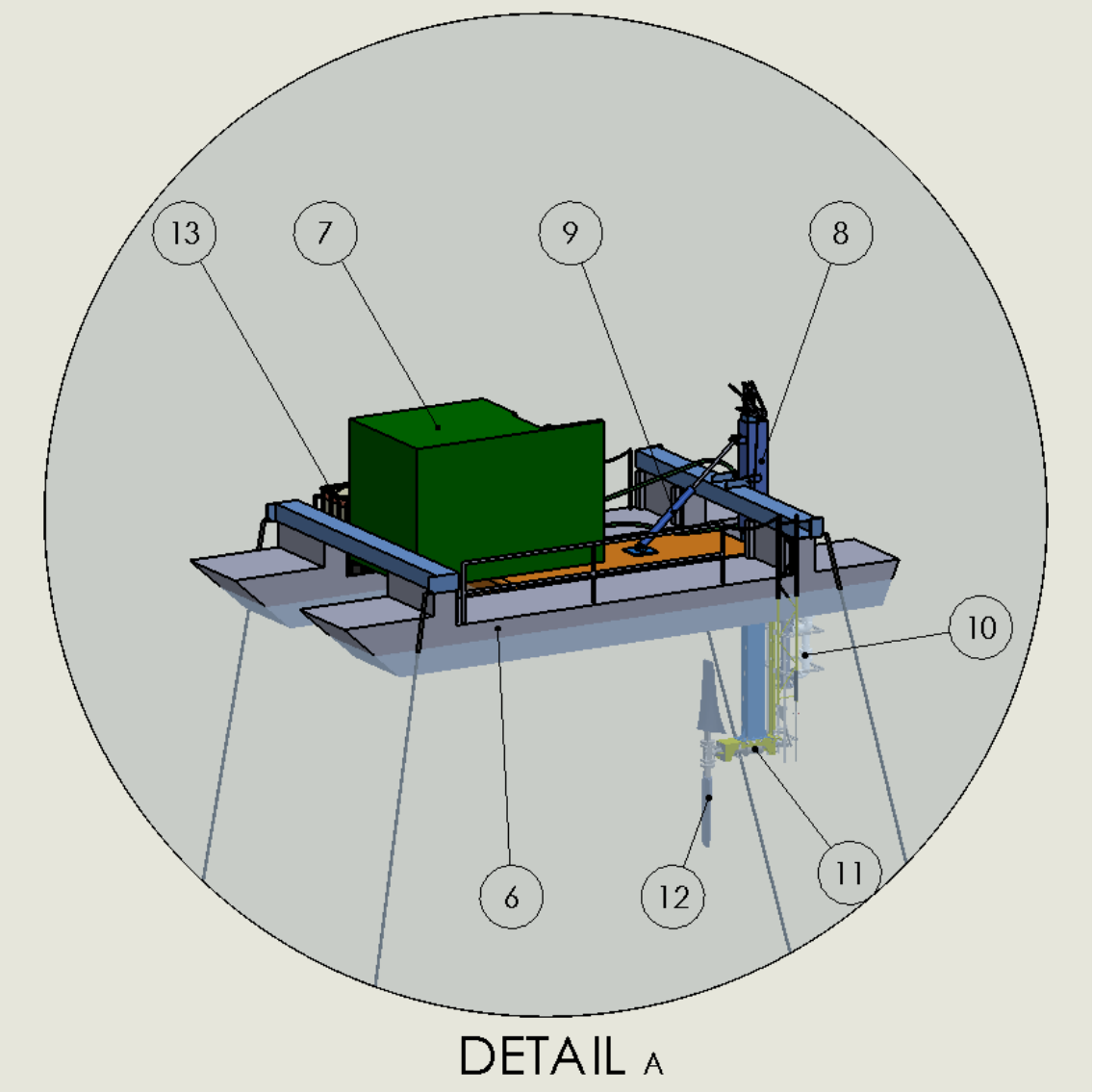

6. Modular pontoon
7. Cabin
8. Submersible arm
9. Hydraulic arm
10. Power take off
11. Drive train
12. Rotor blades
13. Water tank

Figure 4.24: CAD render (detail view A from Figure 4.23) of the RRES floating platform assembly with key components / sub-assemblies labelled.

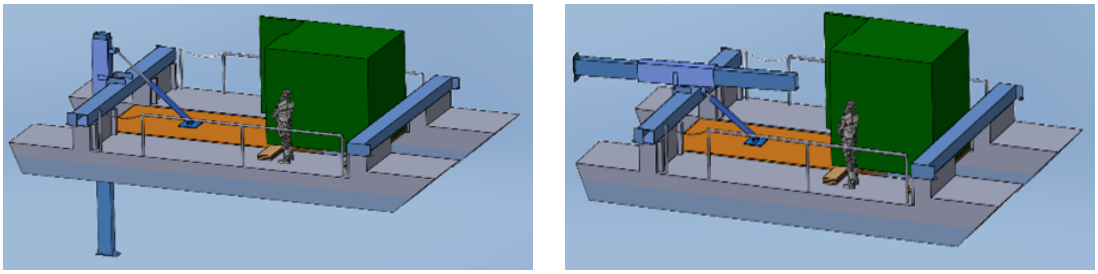

a b

Figure 4.25: Schematic of the RRES submersible arm movement; a. submerged and b. raised.

the rotor drive train (11). This eliminates the need to transfer the rotational power from the rotor drive train to the platform surface by the means of mechanical systems, which has reduced the complexity and cost of the RRES. Two bladed rotor blade (12) turbine is located at a hub depth of 3.0m. As the META at Warrior Way is exposed to bad weather, a cabin (7) is included on the platform to protect operators and sensitive electrical systems from the weather.

A key design feature of the RRES is a submersible arm which is controlled by a hydraulic arm, giving control over the depth and pitch of rotor blades. It pivots at the rear of the RRES and can raise the rotor blades completely out of the water for transportation and maintenance. A schematic of the RRES with the arm a. submerged and b. raised is given in Figure 4.25.

4.6.2 Rotor blades

4.6.2.1 Design

Details of the geometry of the RRES rotor blades are given in Section 3.1.6. A drawing of the rotor blade and spar assembly which includes key dimensions is given in Figure 4.26. The spar end plate has a number of holes as shown in Figure 4.27. The numbers refer to the offset in angle of attack in degrees which is achieved when using the combination of holes. This allows the RRES rotor blades to be pitched from -5° to 15° at intervals of 2.5°.

Choosing the most appropriate material and manufacturing technique for the rotor blades requires knowing of the total loads and their distribution. The BEMT numerical model is used to predict the total load (Table 4.10) and the distribution of that load along the rotor blades (Table 4.11).

The rotor blades are manufactured using GFRP, comprising of e-glass woven roving reinforcement along with polyester resin. Each composite ply should have a thickness of

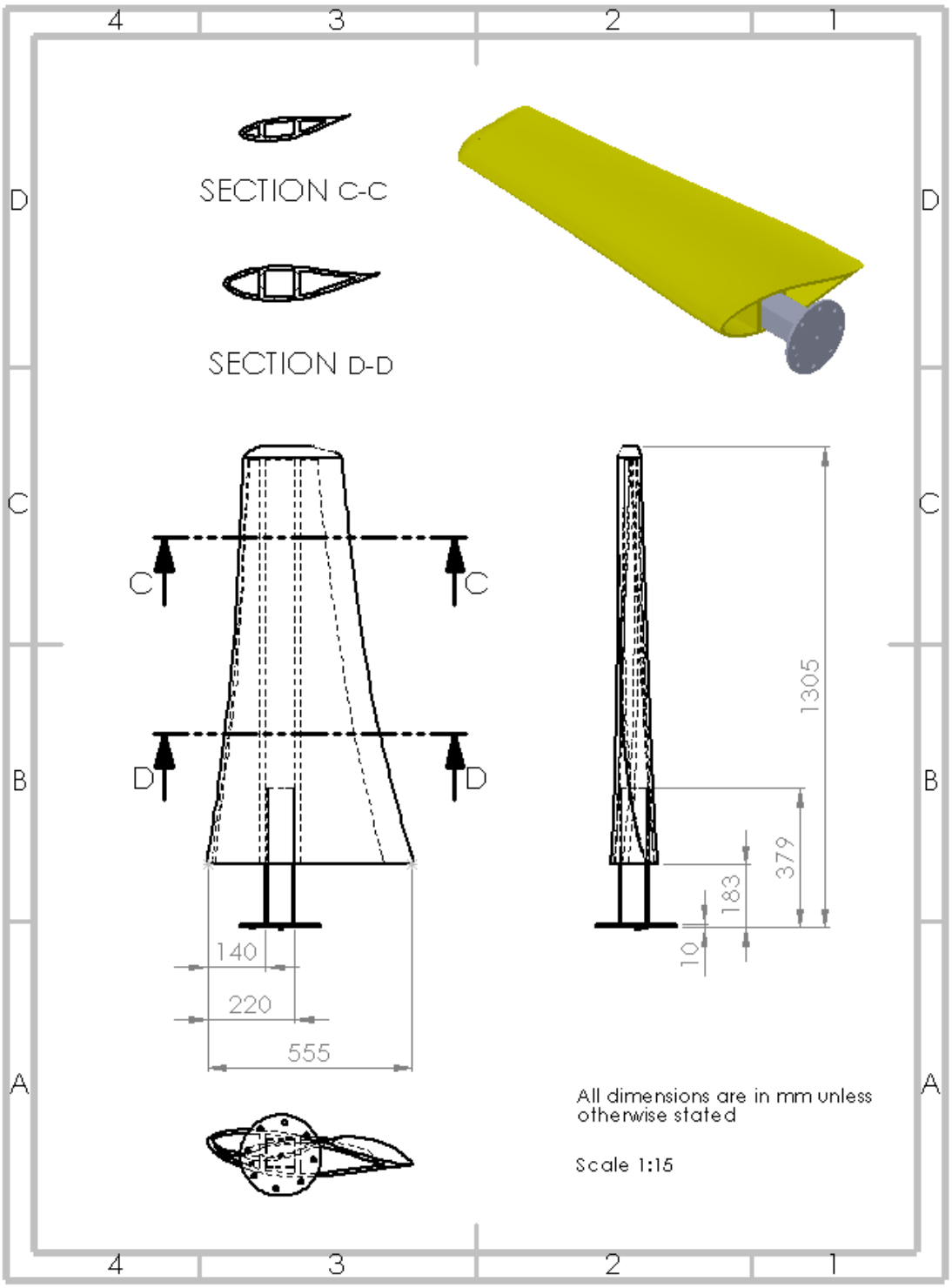

Figure 4.26: Drawing of the 3.0m RRES rotor blade and spar assembly.

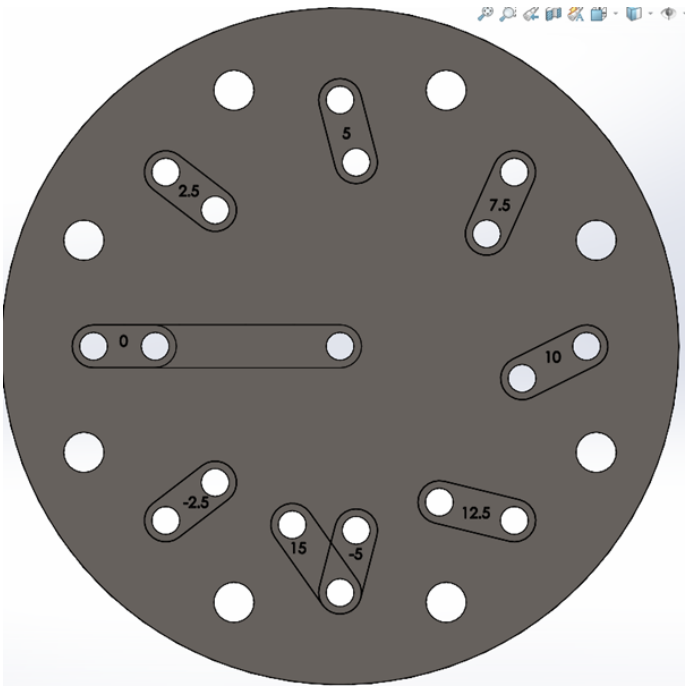

Figure 4.27: Schematic of the end plate of the spar for the 3.0m RRES used to pitch blades.

Table 4.9: Material properties of glass fibre reinforced polymer used for manufacture of 3.0m RRES rotor blades.

Properties	Value	Units
Tensile strength	228	MPa
Compressive strength	129	MPa
Tensile modulus	15.2	GPa
Compressive modulus	10.9	GPa
Failure strain	2.8	%

Table 4.10: Total rotor blade loads of the 3.0m RRES predicted from the BEMT numerical model.

Total (Contribution from both blades)	Value	Units
Max thrust	6,790	N
Max torque	1,760	Nm
Max power	6,980	W

Table 4.11: Radial distribution of maximum thrust and torque per blade of the 3.0m RRES predicted from the BEMT numerical model.

Radius (m)	Thrust (N)	Torque (N.m)
0.363	77.195	17.504
0.428	86.014	20.915
0.492	97.470	24.901
0.558	109.593	28.946
0.623	123.053	33.380
0.687	136.657	38.026
0.753	152.531	43.652
0.818	164.131	49.055
0.882	175.217	54.862
0.948	194.096	62.043
1.013	222.312	71.991
1.077	246.959	72.306
1.143	254.132	73.374
1.208	258.162	72.845
1.272	257.886	70.065
1.338	250.543	63.985
1.403	231.823	53.879
1.467	201.204	43.036
1.500	105.246	32.384

≈1mm, and the percentage of fibre volume should be ≈36%. The mechanical properties of the GFRP material are given in Table 4.9.

4.6.2.2 Cavitation

Cavitation is the term used to describe the formation of vapour filled cavities in a fluid when its static pressure falls below its vapour pressure. This can arise for a tidal stream turbine which is undesirable as it increases the environmental impact and blade damage. A compatible cavitation detection model has been introduced to a BEMT numerical model to indicate any cavitating blade elements by Buckland *et.al.* [109]. The cavitation number is calculated by;

$$\sigma = \frac{p - p_v}{0.5\rho V_R^2} \tag{4.18}$$

where p is the static pressure, p_v is the vapour pressure, and V_R is the rotor velocity. The rotor velocity is calculated by;

$$V_R = \sqrt{U_c^2 + (\Omega R)^2} \tag{4.19}$$

where U_c is the current flow velocity, Ω is the rotor rotational speed, and R is the rotor radius. The vaporisation pressure (p_v) of water at 15°C is 1.614kPa (0.0159 atm). Deriving from Bernoulli's equation, the static pressure is calculated by;

$$p = \rho g d_w + p_{atm} + \frac{1}{2}\rho(U_c^2 - V_R^2) \tag{4.20}$$

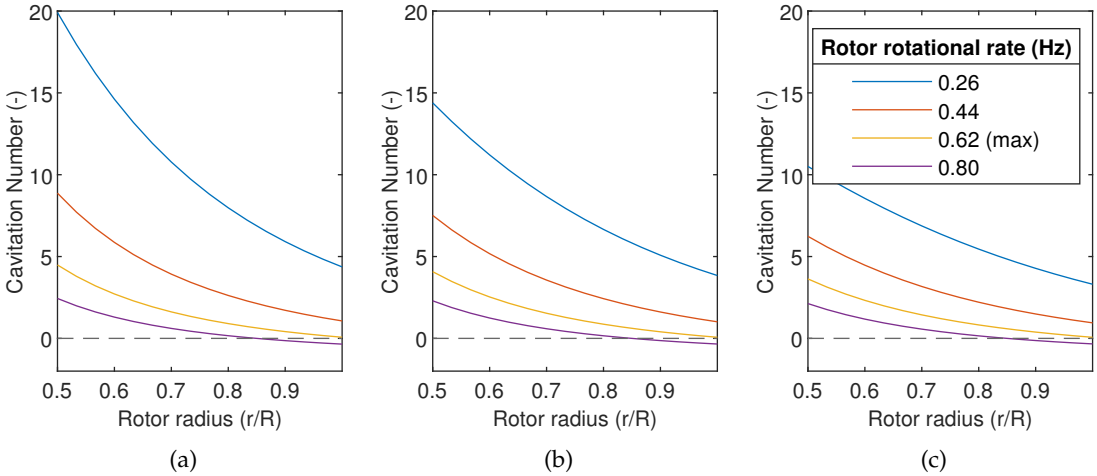

Figure 4.28: Plot of cavitation number against rotor blade radius at various rotor rotational rates in current flow velocities of a) 1m/s, b) 1.4m/s, and c) 1.8m/s for the 3.0m RRES.

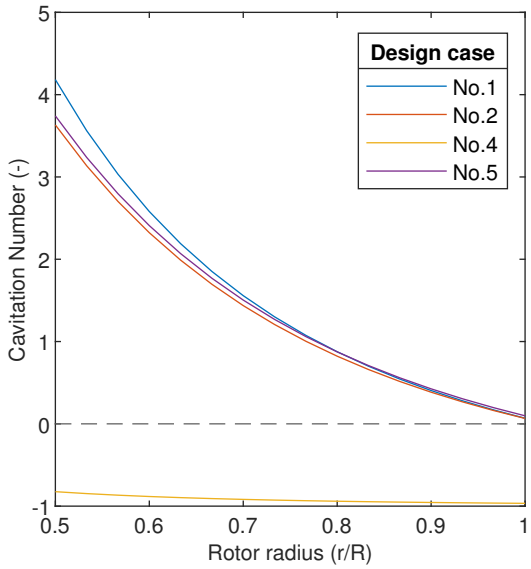

Figure 4.29: Plot of cavitation number against rotor blade radius for design cases 1, 2, 4, and 5 for the 3.0m RRES.

where d_w is the depth of water.

Hub depth for both RRES devices is 3.0m. At this depth, cavitation will not occur for either scaled devices at any planned operating condition (Current flow velocity 1-1.8m/s and rotor rotational rate (0-2.07Hz 0.9m device)(0-0.62Hz 3.0m device). Figure 4.28 shows plots of cavitation number against rotor blade radius for different rotor rotational rates in current flow velocities of a) 1m/s, b) 1.4m/s, and c) 1.8m/s for the 3.0m RRES device. Similarly, Figure 4.29 is a plot of cavitation number against rotor blade radius for design cases 1, 2, 4, and 5 for the 3.0m RRES device. A negative cavitation number would indicate that cavitation would occur. This is not seen at any point within our operating range and thus we would not expect to experience any cavitation. However, we can not be totally assured that no cavitation would occur as accurately predicting the process is difficult as it depends on several parameters, such as local static and vapour pressures, and the time required for the cavitation nuclei to grow to a sufficient size.

4.6.3 Blade root bending moment sensor

Torque and thrust are two important parameters which are used to evaluate the performance of the RRES. The torque is the moment in the plane of rotor rotation whilst thrust is the force perpendicular to the rotor rotation direction. The most accurate location to measure

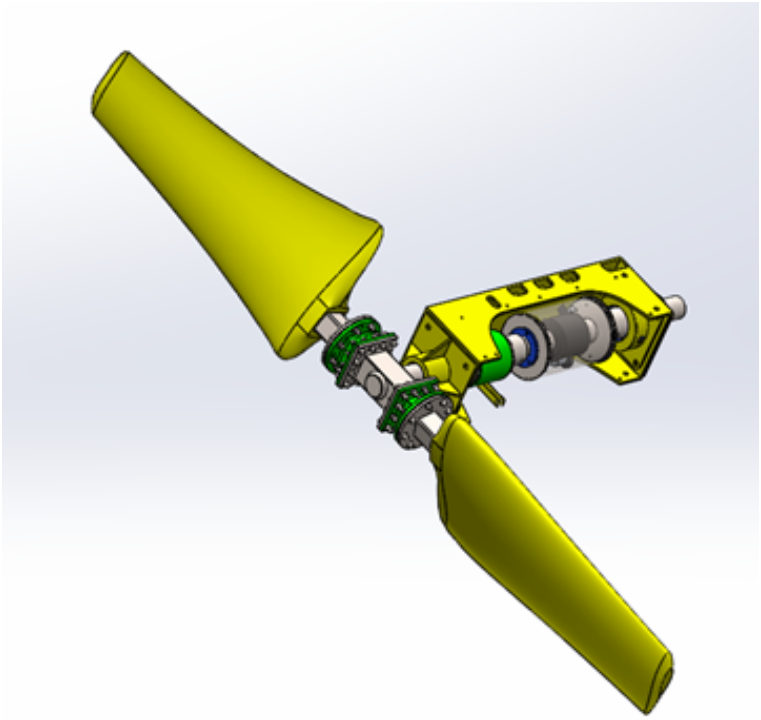

Figure 4.30: Isometric view of the RRES blade and hub assembly with the blade root strain housing coloured green.

these loads is at the root of the rotor blades, which eliminates inaccurate measurements due to losses which occur downstream of bearings and drive-trains.
Each rotor blade root will have four strain gauges, two in each axial and tangential direction. CAD renders of the blade and hub assembly are shown in Figures 4.30 and 4.31 which has the blade root bending moment sensor housing coloured green. Drawing of the blade and hub assembly with key dimensions (mm) is shown in Figure 4.32.

The strain gauges are located in the blade root bending moment housing, which is shown in Figure 4.33. Half Wheatstone bridge circuit is used to make the blade root bending moment sensors. Figure 4.34 shows a schematic of the half Wheatstone circuit used, which includes two strain gauges and two 350Ω resistors. The strain gauges are linear type with one measurement grid per strain gauge. The nominal resistance of the gauges are 350Ω and are 18mm long and 8mm wide. The bonding surfaces are prepared using standard cleaning products and the strain gauges are bonded using a cold cure adhesive. Cold cure adhesive is chosen for its ease of use.

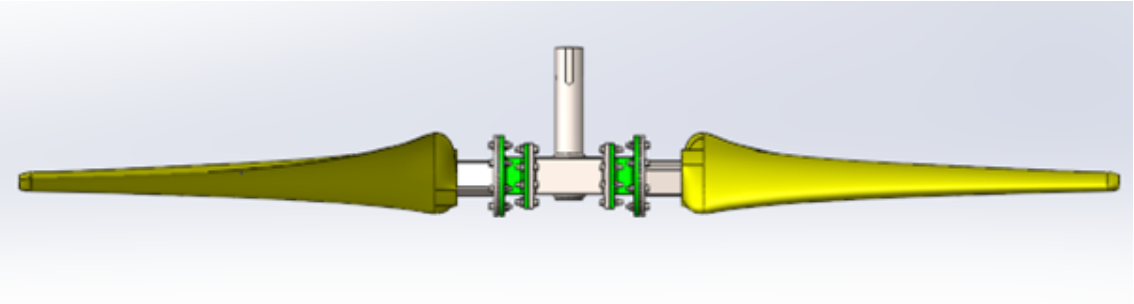

Figure 4.31: Top view of the RRES blade and hub assembly with the blade root strain housing coloured green.

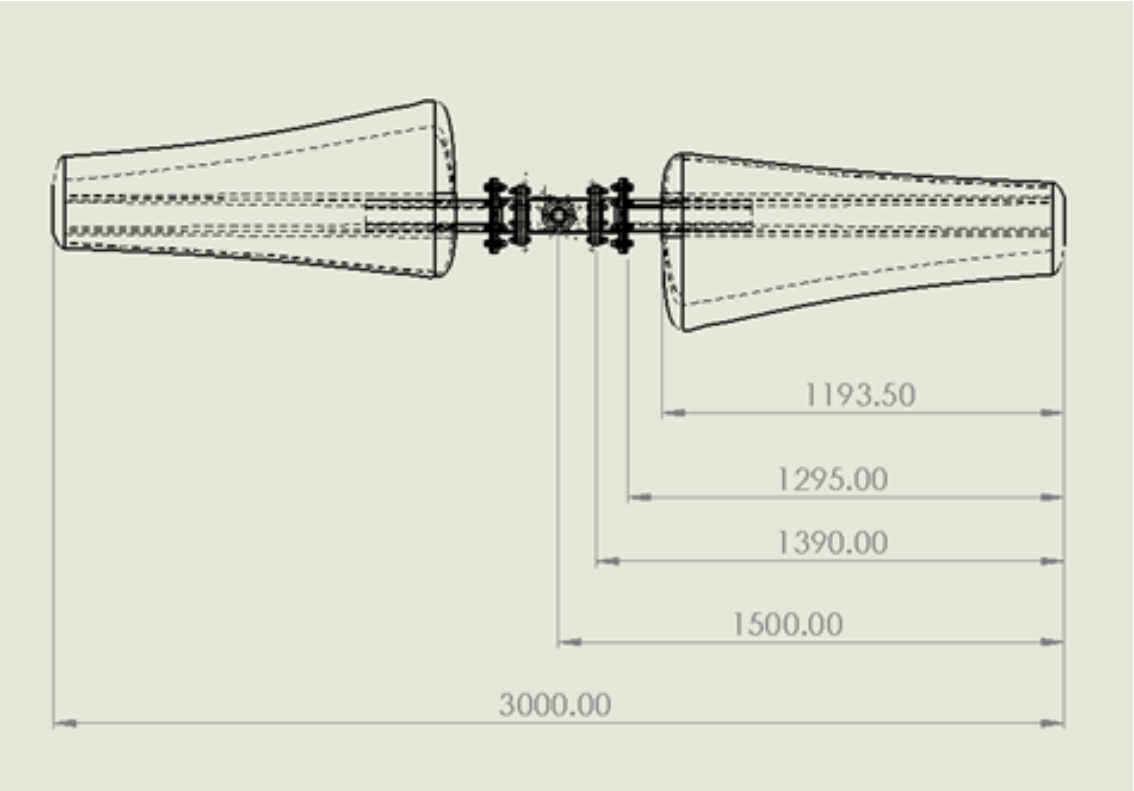

Figure 4.32: Drawing of the RRES blade and hub assembly with key dimensions (mm).

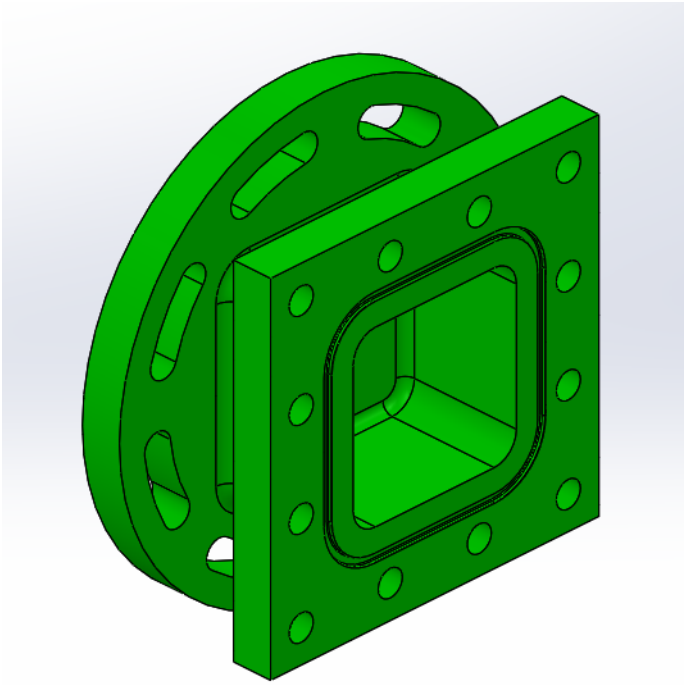

Figure 4.33: CAD render of the RRES blade root bending moment sensor housing.

The housing must have IP68 rating as it will be submerged in salty water. This is achieved by ensuring surface finish of 0.8μm on mating surfaces along with using gaskets. The electrical cables are layed inside the shaft to a slip ring, where electrical cables run to the surface at the platform deck.

A bending beam rig is used to calibrate the blade root bending moment sensor [110]. The sensor is fixed at one end and a force applied at the other. The force is applied in a perpendicular direction to the fixed surface and is accurately measured using a load cell. The orientation on the blade root bending moment sensor is changed to calibrate each direction (torque and thrust).

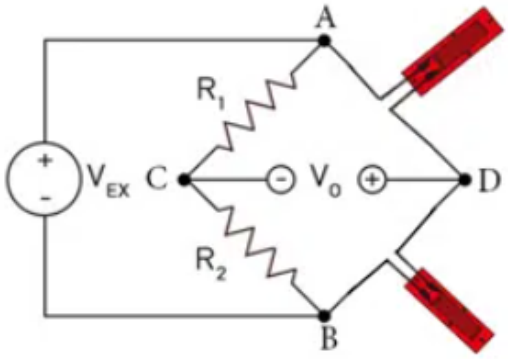

Figure 4.34: Schematic of the half Wheatstone bridge circuit used for the blade root bending moment sensors for the RRES.

4.6.4 Bearings

Journal and thrust bearings are required on the drive train of the RRES to provide contact from the rotating shaft to the stationary support frame. The locations of the journal and thrust bearings along the drive train of the RRES are highlighted in a drawing shown in Figure 4.35. The journal and thrust bearings are highlighted yellow and blue respectively. The journal bearings are manufactured from a engineered thermoplastic whilst the thrust bearings are manufactured from brass.

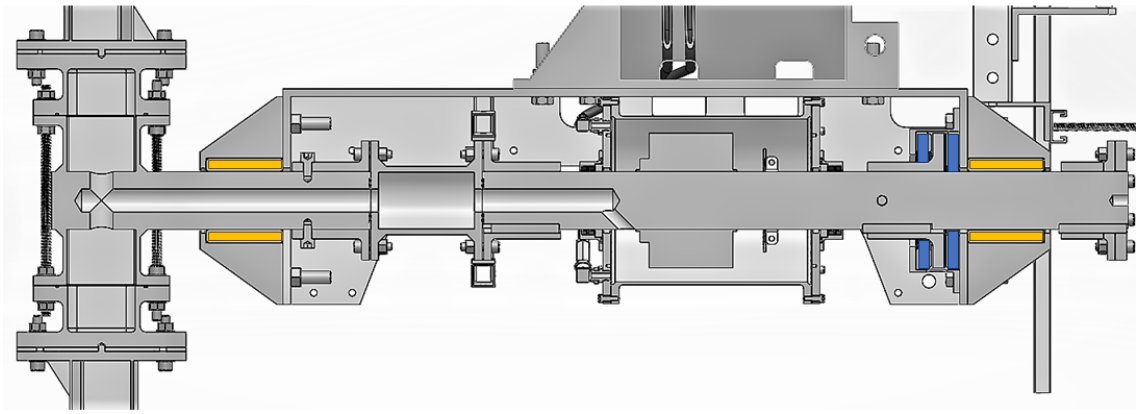

Figure 4.35: CAD drawing of the RRES drive train with location of journal (yellow) and thrust (blue) bearings highlighted.

The following equations are used to design the journal and thrust bearings.

- D_2 = outer bearing diameter (m)

- D_1 = inner bearing diameter (m) (i.e. same as diameter of rotating shaft)
- W_{th} = Max thrust load (N)
- W_{jo} = Load on journal bearing (N)
- k_g = Pad / circumference ratio (usually 0.8)
- p_{th} = Pressure bearing capacity (Pa) (Parallel surface load <517kPa)
- p_{jo} = Bearing pressure (Pa)
- L_{jo} = Length of journal bearing (m)
- a = Radial pad width (m)
- B = Pitch line circumference (m)
- i = Number of bearing pads
- b = length of bearing pad (m)

Journal bearing

$$\boldsymbol{p}_{\text{jo}} = \frac{\boldsymbol{W}_{\text{jo}}}{\boldsymbol{L}_{\text{jo}}\boldsymbol{D}_1} < \mathbf{0.5}\text{MPa} \tag{4.21}$$

$$\text{typical}\frac{\boldsymbol{L}_{\text{jo}}}{\boldsymbol{D}_1} = \mathbf{2.5} \tag{4.22}$$

Thrust bearing

$$\boldsymbol{D}_2 = (\frac{\mathbf{4}\boldsymbol{W}_{\text{th}}}{\boldsymbol{\pi}\boldsymbol{k}_{\text{g}}\boldsymbol{p}_{\text{th}}} + \boldsymbol{D}_1{}^{\mathbf{2}})^{\frac{\mathbf{1}}{\mathbf{2}}} \tag{4.23}$$

$$\boldsymbol{a} = \frac{\boldsymbol{D}_2 - \boldsymbol{D}_1}{\mathbf{2}} \tag{4.24}$$

$$\boldsymbol{B} = \frac{\boldsymbol{\pi}(\boldsymbol{D}_2 + \boldsymbol{D}_1)}{\mathbf{2}} \tag{4.25}$$

$$\boldsymbol{i} = \frac{\boldsymbol{B}\boldsymbol{k}_{\text{g}}}{\boldsymbol{a}}(\text{closest whole number}) \tag{4.26}$$

$$\boldsymbol{b} = \frac{\boldsymbol{B}\boldsymbol{k}_{\text{g}}}{\boldsymbol{i}} \tag{4.27}$$

Standard bearing wall thickness of both journal and thrust bearings is ≈20% of D_1.
The 3.0m RRES device has the following parameters;

- D_1 = 0.075m
- W_{th} = 6,790N
- W_{jo} = 3,000N
- k_g = 0.8
- p_{th} = 517kPa

Parameters of the journal and thrust bearings of the 3.0m RRES are given in Table 4.12.
CAD renders of the journal and thrust bearings for the 3.0m RRES are shown in Figure 4.36.

Table 4.12: Summary of the parameters of journal and thrust bearings of the 3.0m RRES.

Bearing	Parameters	Value
Journal	ID (D_1) (m)	0.0750
	OD (D_2) (m)	0.1200
	Length (L_{jo}) (m)	0.1500
	Thickness (m)	0.0225
Thrust	ID (D_1) (m)	0.0750
	OD (D_2) (m)	0.1630
	Thickness (m)	0.0225
	Number of pads (i)	7
	Length of bearing pad (b)	0.0427

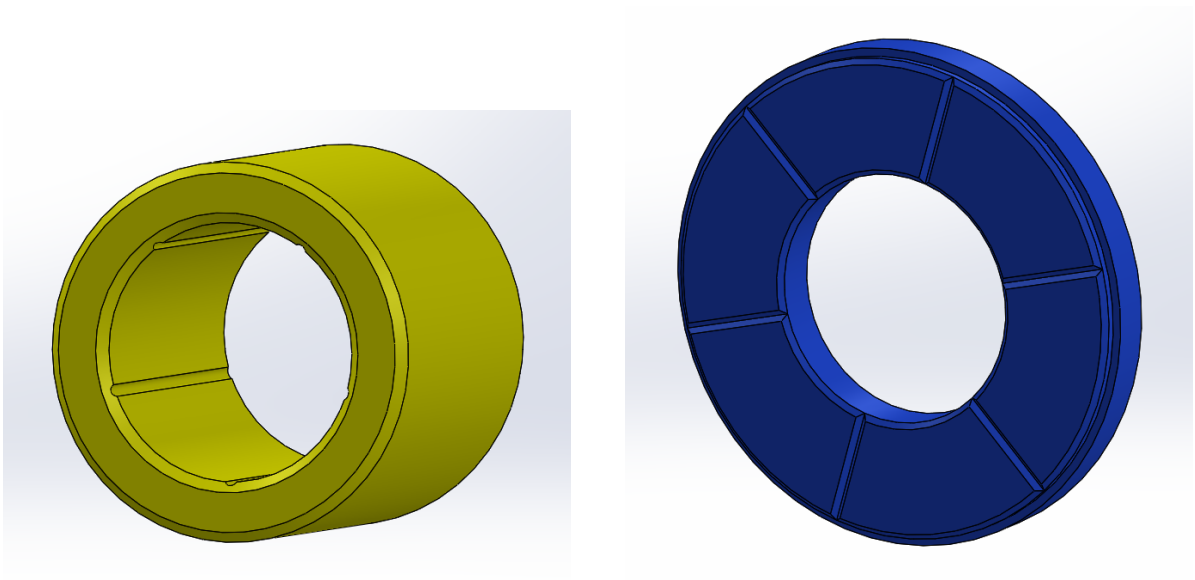

(a) (b)

Figure 4.36: CAD renders of a. journal bearing and b. thrust bearing of the 3.0m RRES.

4.6.5 Control system

The control system is designed to allow monitoring and recording of the different sensors, as well as control of the throttling valve and (in the laboratory tests) motor drive parameters. The system is also responsible for ensuring parameters remain within safe limits and shutting down the device if limits are exceeded - either by allowing the brake to apply on field deployments or triggering the motor emergency stop in the laboratory.
The control system is built around a low cost commodity computer and hardware expansion boards, using OpenPLC to expose the various sensor inputs and hardware controls, and provide runtime supervision of the control software. OpenPLC also allows access to these inputs and controls by external software over Modbus, which is used to provide a suitable graphical interface for testing and operation.
During the laboratory testing, the control software enforces safety limits but allows other parameters to be adjusted manually as required to meet the various test criteria. For the field deployments of the RRES device, the control software will additionally be responsible for adjusting the throttling valve based on the upstream flow speeds in order to maximise the rotor performance. This will be based on the volumetric flow rate of fluid through the piping system and the upstream flow velocity reported by an

ADV, with the rotor speed controlled indirectly by varying the throttling valve and the resulting flow through the piping system. Schematic of the control system employed on the RRES field deployment is shown in Figure 4.37.

Figure 4.37: Schematic of the control system employed on the RRES field deployment.

4.6.6 Mooring

The mooring design will follow the standards and guidance of DNVGL-ST-N001. Two quasi-static design cases are considered; 1. Intact condition, and 2. redundancy check. Intact condition is the mooring system operating as designed, whereas the redundancy check is for a complete redundancy of one mooring leg (i.e. loads are all imposed on one anchor).

The duration of deployment will be approximately 3 months, categorising the design as mobile mooring. Safety factors for axial and lateral directions are 1.2 and 1.0 respectively for the redundancy check case, and 1.5 and 1.2 for the intact condition case (Table 17.6 DNVGL-ST-N001). Current and wind loads are considered in the following calculations. Wave loadings and line drag are not explicitly accounted for in the design, but as it is considered to be mobile mooring, the wave loadings and line drag are sufficiently accounted for in the redundancy case.

4.6.6.1 Overview

Details of the META test site at Warrior Way are given in Section 4.3. To minimise cost and logistical challenges, the same mooring system will be used for both 0.9m and 3.0m RRES devices. The greatest requirements of the mooring system will be for the largest 3.0m RRES device, and thus the following mooring calculations are based on the 3.0m RRES device.

At the META test site in Warrior Way, pile anchoring is prohibited, and thus the only viable option is gravity anchoring. The test site is a tidal estuary and thus mooring must be provided in both ebb and flood directions. To minimise cost and environmental impact

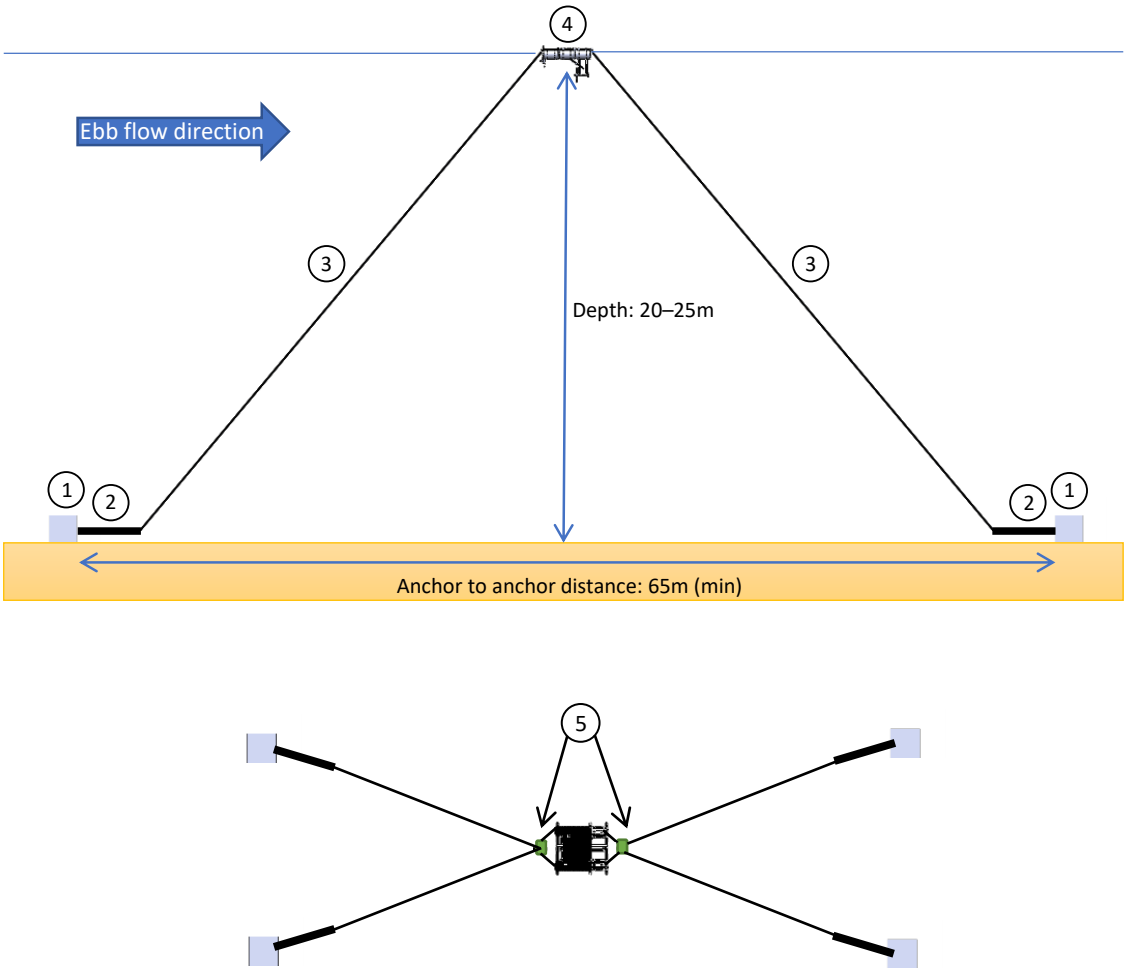

1. Gravity anchor
2. Weighted chain
3. Mooring line
4. Floating river turbine (Barge)
5. Load cell shackle

Figure 4.38: A schematic of the mooring layout for the RRES.

on the river bed, the number of gravity anchors is kept to a maximum of 4. Tension is maintained in the mooring line with a slack weighted chain which links the mooring line and the gravity anchor. A schematic of the mooring layout, including estimated distances, is shown in Figure 4.38. Load cell shackles will be located at the join of the mooring lines and device and used to monitor the mooring loads.

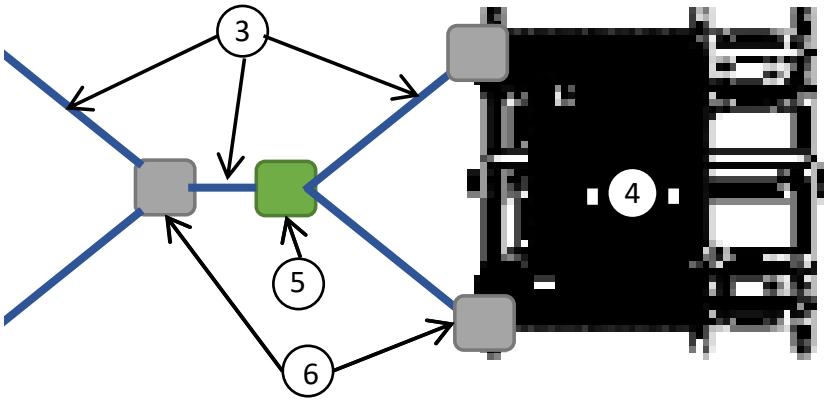

3. Bridle (tug) rope
4. Barge
5. Load cell shackle
6. Shackle

Figure 4.39: A detailed schematic of the mooring line connection to the barge for the RRES mooring system.

Detail schematic of the connection of mooring lines to barge is shown in Figure 4.39. Bridle (tug) rope is used as the mooring line. Two mooring lines join at a shackle before a short piece of bridle rope joins to a load cell shackle. Two mooring line leave the load cell shackle joining to the barge at each corner with a shackle. The same arrangement is used at the other side of the barge.

4.6.6.2 Equipment list

- 1,700kg steel blocks (gravity anchor) x4
- 2" steel chain length 24m x4
- 28mm diameter nylon tug rope length 20m rated to a safe working load of 10,000kg (mooring line) x4
- 6 shackles rated to safe working load of 3,000kg
- 2 load cell shackles rated to safe working load of 3,000kg

4.6.6.3 Calculations

A free body diagram (FBD) of the forces on the mooring is shown in Figure 4.40. The necessary weight of the gravity anchors is dependent on the drag force and rotor thrust. The rotor will be functional between current flow velocities of 1-1.8m/s. Above current flow velocities of 1.8m/s the rotor blades will be parked.

There are two possible scenarios for maximum mooring loads;

1. At maximum current flow velocity which would occur during a severe weather event. The rotor blades would be parked during this scenario and thus the mooring loads would come from the barge and rotor drag alone.
2. At maximum rotor thrust, where the load on the mooring would be a combination of rotor thrust and barge drag.

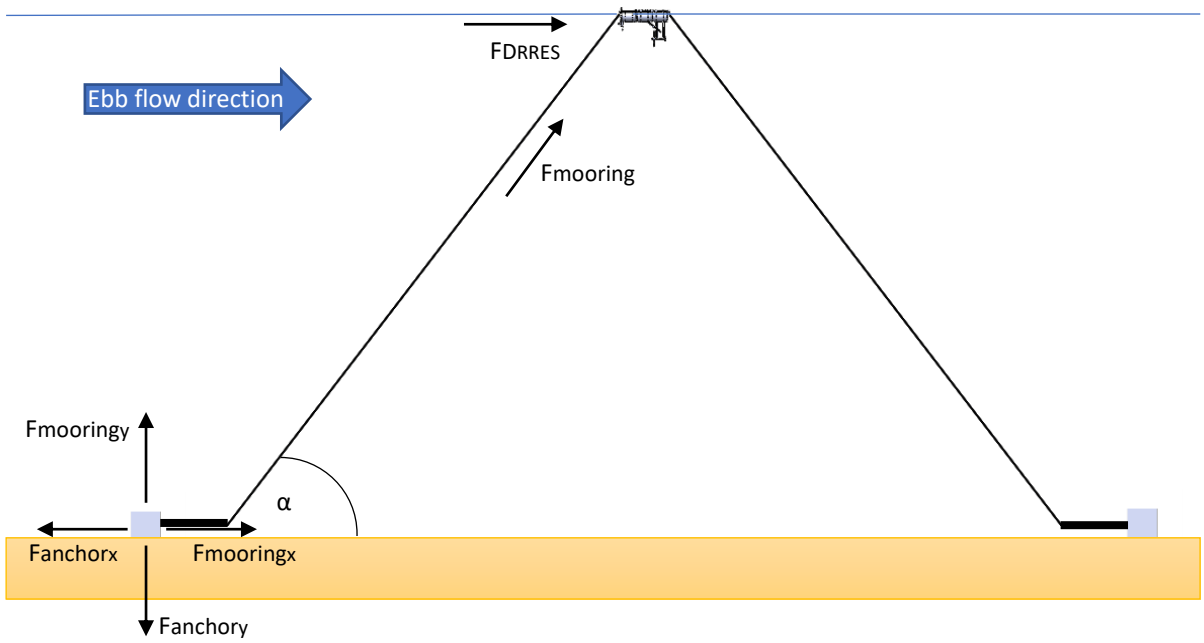

Figure 4.40: Free body diagram of the RRES mooring system.

Drag loads

Scenario 1 The drag force, $\boldsymbol{F}_{D_{RRES}}$, exerted on the RRES by the flow of the water and wind is calculated using Equation 4.30. Under severe weather events, the maximum hypothesised

current flow and wind speed are 2.2m/s and 30m/s respectively, and are used in the following calculations.

The frontal area of the RRES device that will be submerged is estimated at 1.34m^2. 0.84m^2 of that area is sloped at 45° to the current flow and 0.5m^2 is perpendicular to the flow. An of overall drag coefficient is extimated to be 0.75.

In addition to drag created by the frontal area perpendicular to the current flow direction, there will also be drag created by the surfaces parallel to the current flow direction (side and bottom). The total parallel area which is exposed to the current flow is 24m^2 and the length of the pontoon is 10m. Calculating the parallel drag coefficient is done using Equation 4.29, which is dependent on the Reynolds number. The Reynolds number is calculated using Equation 4.28.

The rotor blades are parked (stationary) in this case and thus the drag force is based on its plan area, which is 1.02m^2. The drag coefficient is estimated to be 1.75.

In addition to current drag on the barge, wind will also produce significant drag force, $\boldsymbol{F}_{\mathrm{D_{wind}}}$, on large areas above the water. A cabin is the only significant item which will be exposed to winds on barge, and has a the dimensions of of 8" x 6". Wind speed of 60 knots are used for the worst case scenario. This results in a wind drag force of 2,800N.

$$\begin{aligned} \boldsymbol{Re} &= \frac{\boldsymbol{U L}_{\mathrm{pontoon}}}{\boldsymbol{\nu}} \\ &= \frac{\mathbf{2.2 \times 10}}{\mathbf{0.00122}} \\ &= \mathbf{18,033} \end{aligned} \tag{4.28}$$

$$\begin{aligned} \boldsymbol{c}_{\mathrm{d}} &= \mathbf{0.664}\boldsymbol{Re}^{-\frac{1}{2}} \\ &= \mathbf{0.664 \times 18,033}^{-\frac{1}{2}} \\ &= \mathbf{0.00494} \end{aligned} \tag{4.29}$$

$$\begin{aligned} \boldsymbol{F}_{\mathrm{D_{RRES}}} &= \frac{\mathbf{1}}{\mathbf{2}}\boldsymbol{\rho u}^{\mathbf{2}}(\underset{\boldsymbol{perpendicular}}{\boldsymbol{A c}_{\mathrm{d}}} + \underset{\boldsymbol{parallel}}{\boldsymbol{A c}_{\mathrm{d}}} + \underset{\boldsymbol{rotor}}{\boldsymbol{A c}_{\mathrm{d}}}) + \boldsymbol{F}_{\mathrm{D_{wind}}} \\ &= \frac{\mathbf{1}}{\mathbf{2}} \times \mathbf{1000} \times \mathbf{2.2}^{\mathbf{2}} \times ((\mathbf{1.34 \times 0.75}) + (\mathbf{24 \times 0.00494}) + (\mathbf{1.02 \times 1.75})) + \mathbf{2,800} \\ &= \mathbf{2,432 + 267 + 4,320 + 2,800} \\ &= \mathbf{9,819}\boldsymbol{N} \end{aligned} \tag{4.30}$$

Scenario 2 The rotor produces maximum thrust of 6.79kN in current flow velocity of 1.8m/s. The values of the submerged perpendicular and parallel areas of the RRES are the same as in scenario 1. In current flow velocity of 1.8m/s, the current drag force of the RRES is calculated to be 1,841N. The rotor blades will not operate in winds >20 knots (10m/s), thus for this scenario where the rotor is operational, wind speed of 10m/s is used to calculate the wind drag force, which is 300N. The $\boldsymbol{F}_{\mathrm{D_{RRES}}}$ will be the total of the RRES drag and rotor thrust, which is 8,931N.

$$\boldsymbol{Re} = \frac{\boldsymbol{u}\boldsymbol{L}_{\mathrm{pontoon}}}{\boldsymbol{\nu}} = \frac{\mathbf{1.8 \times 10}}{\mathbf{0.00122}} = \mathbf{14,754} \tag{4.31}$$

$$\boldsymbol{c}_{\mathrm{d}} = \mathbf{0.664}\boldsymbol{Re}^{-\frac{\mathbf{1}}{\mathbf{2}}} = \mathbf{0.664 \times 14,754}^{-\frac{\mathbf{1}}{\mathbf{2}}} = \mathbf{0.00547} \tag{4.32}$$

$$\begin{aligned}
\boldsymbol{F}_{\mathrm{D_{RRES}}} &= \frac{\mathbf{1}}{\mathbf{2}}\boldsymbol{\rho}\boldsymbol{u}^{\mathbf{2}}(\underset{\boldsymbol{perpendicular}}{\boldsymbol{A}\boldsymbol{c}_{\mathrm{d}}} + \underset{\boldsymbol{parallel}}{\boldsymbol{A}\boldsymbol{c}_{\mathrm{d}}}) + \boldsymbol{Rotor}_{\mathrm{Thrust}} + \boldsymbol{F}_{\mathrm{D_{wind}}} \\
&= \frac{\mathbf{1}}{\mathbf{2}} \times \mathbf{1000} \times \mathbf{1.8}^{\mathbf{2}} \times ((\mathbf{1.34} \times \mathbf{0.75}) + (\mathbf{24} \times \mathbf{0.00547})) + \mathbf{6,790} + \mathbf{300} \\
&= \mathbf{1,628} + \mathbf{213} + \mathbf{6,790} + \mathbf{300} \\
&= \mathbf{8,931}\boldsymbol{N}
\end{aligned} \tag{4.33}$$

Summary The maximum drag force exerted on the RRES, $\boldsymbol{F}_{\mathrm{D_{RRES}}}$, is 9,819N and would occur in scenario 1, where the rotor blades are parked and the RRES is subjected to severe weather conditions.
Summary of the drag loads of the RRES from both scenarios are given in Table 4.13.

Table 4.13: Summary of RRES drag loads

Scenario	Drag load	Value (N)
1	Current	2,699
	Wind	2,800
	Rotor (Drag)	4,320
	Total	9,819
2	Current	1,841
	Wind	300
	Rotor (Thrust)	6,790
	Total	8,931

Mooring leg loads

Two analysis conditions are considered; 1. Intact, and 2. Redundancy check. Case 1, intact condition, is when the mooring system is working as designed, whereas case 2, redundancy check condition, is when one of the mooring legs has failed and all of the mooring load is subjected on one anchor. As previously mentioned, the DNVGL-ST-N001 standards and guidance is used to design the mooring system. Table 4.14 gives the safety factors used for both design cases for the line tension, Table 17-3 in DNVGL-ST-N001.

Table 4.14: Line tension limits and design safety factors for offshore moorings. Table 17-3 from DNVGL-ST-N001.

Analysis Condition	Analysis Method	Line Tension Limit (percent of MBL)	Design Safety Factor
Intact	Quasi-Static	50%	2.00
Redundancy check	Quasi-Static	70%	1.43

Case 1. Intact condition The force in the mooring line, $\boldsymbol{F}_{\text{mooring}}$, is calculated using Equation 4.34. $\boldsymbol{F}_{\text{D}_{\text{RRES}}}$ is divided by 2 as the load is shared between two mooring lines. It is assumed that the load will be shared equally between both mooring lines.

$$\boldsymbol{F}_{\text{mooring}} = \frac{\boldsymbol{F}_{\text{D}_{\text{RRES}}}}{\boldsymbol{2cos(\alpha)}} \tag{4.34}$$

$\boldsymbol{\alpha}$ is the angle between the mooring line and the direction of the drag force and is calculated by Equation 4.35, where D_{anchor} is the depth of the anchor and $\text{L}_{\text{mooringline}}$ is the length of the mooring line. The maximum load on the anchors will be at highest tide, corresponding

to the largest $\boldsymbol{\alpha}$ value. Maximum anchor depth is approximately 22m and the length of the mooring line will be 35m. This equates to a maximum force of 6,308N in each mooring line.

$$\boldsymbol{\alpha} = \mathbf{sin^{-1}}(\frac{\boldsymbol{D}_{\text{anchor}}}{\boldsymbol{L}_{\text{mooringline}}}) \tag{4.35}$$

$F_{mooringx}$ and $F_{mooringy}$ are calculated using Equation 4.36 and 4.37 respectively.

$$\begin{aligned} \boldsymbol{F}_{\text{mooringx}} &= \frac{\boldsymbol{F}_{\text{D}_{\text{RRES}}}}{\mathbf{2}} \\ &= \mathbf{4,910}\boldsymbol{N} \end{aligned} \tag{4.36}$$

$$\begin{aligned} \boldsymbol{F}_{\text{mooringy}} &= \boldsymbol{F}_{\text{mooring}} \mathbf{sin}\,\boldsymbol{\alpha} \\ &= \mathbf{3,961}\boldsymbol{N} \end{aligned} \tag{4.37}$$

Including the safety factor (2.00), Table 4.14, the axial and lateral loads on the mooring lines for case 1 are;
$\boldsymbol{F}_{\text{mooringx}}$ = 9,820N
$\boldsymbol{F}_{\text{mooringy}}$ = 7,922N

Case 2. Redundancy check In this case the $\boldsymbol{F}_{\text{D}_{\text{RRES}}}$ load is applied to a single mooring leg as one has failed. Using the same equations as for case 1, the axial and lateral forces are calculated to be;
$\boldsymbol{F}_{\text{mooringx}}$ = 9,819N
$\boldsymbol{F}_{\text{mooringy}}$ = 7,923N

Including the safety factor (1.43), Table 4.14, the axial and lateral loads on the mooring line for case 2 are;
$\boldsymbol{F}_{\text{mooringx}}$ = 14,041N
$\boldsymbol{F}_{\text{mooringy}}$ = 11,330N

Summary of mooring loads Summary of the loads per mooring leg are shown in Table 4.15. The loads include the relevant safety factors. Case 2 has the critical loads and thus will be used in subsequent mooring design calculations.

Table 4.15: Summary of mooring loads per leg from design cases 1 and 2.

Case	Axial (N)	Lateral (N)
1	9,819	7,923
2	14,041	11,330

4.6.6.4 Mooring leg design

It is essential to have ground chain on the seabed at all times to achieve catenary, providing a spring effect which increases the mooring stiffness as load increases (reducing snatch loads). There must also be no uplift on anchor block in quasi-static conditions.
2" steel chain (6x3.6D) will be used, which has a mass per unit length of 56kg/m, corresponding to a wet mass per unit length of 49kg/m. The tug rope has a mass per unit length of approximately 0.5kg/m. To ensure no uplift on anchor the total weight of the mooring leg must be greater than 11,330N (maximum lateral force in mooring leg).
A mooring leg consisting of 24m length of 2" chain, and 11m length of tug rope has sufficient weight to ensure no uplift on anchor block and anchor on seabed in all quasi-static design cases. The weight of the mooring leg, $\boldsymbol{W}_{\text{m}}$, is given by Equation 4.38.

$$\begin{aligned}\boldsymbol{W}_{\text{m}} =& [(\boldsymbol{m}_{2\text{" chain}} \times \boldsymbol{L}_{2\text{" chain}}) + (\boldsymbol{m}_{\text{tug rope}} \times \boldsymbol{L}_{\text{tug rope}})] \times \boldsymbol{g} \\ =& [(\mathbf{49} \times \mathbf{24}) + (\mathbf{0.5} \times \mathbf{11})] \times \mathbf{9.81} \\ =& \mathbf{11,591}\boldsymbol{N}\end{aligned} \tag{4.38}$$

The majority of chain is suspended in the current configuration which means that the pre-tension in each riser are significant (1.2 te). The pre-tension in the risers will be reduced by increasing the length of the nylon tug rope from 11m to 20m. This will reduce the lateral load on the barge as well as making connection of mooring legs to barge simpler for the vessel contractor.

Anchor block weight

The weight of the mooring leg will ensure no uplift on the anchor block, thus its weight is dictated by the axial load only. Table 4.16 gives the holding capacity safety factors of mobile mooring of gravity anchors, Table 17-4 in DNVGL-ST-N001.
The maximum axial load is 14,041N, seen in design case 2, redundancy check. Applying the holding capacity safety factor (1.2), gives mooring axial load, $\boldsymbol{F}_{\text{anchorx}}$, of 16,849N.
The frictional force from the anchor block and mooring leg must be great than the axial force to avoid anchor movement, given in Equation 4.39. Rearranging Equation 4.39 gives

an equation for the necessary mass of the anchor block, M_{anchor}, given in Equation 4.40. The river-bed is composed of loose sediment, mud, and clay which is estimated to have a static friction coefficient, c_{f}, of 0.8. The mooring leg will only have a small proportion in contact with the sea bed, and this is accounted for in its friction coefficient, $c_{\text{f}_{\text{leg}}}$.

Table 4.16: Gravity anchor - Holding capacity design safety factor of mobile mooring. Table 17-4 from DNVGL-ST-N001.

Case	Axial	Lateral
Intact condition	1.5	1.2
Redundancy check	1.2	1.0

$$F_{\text{anchorx}} = c_{\text{f}_{\text{anchor}}} M_{\text{anchor}} g + c_{\text{f}_{\text{leg}}} M_{\text{leg}} g \tag{4.39}$$

$$\begin{aligned} M_{\text{anchor}} &= \frac{F_{\text{anchorx}}}{c_{\text{f}_{\text{anchor}}} g} - \frac{c_{\text{f}_{\text{leg}}} M_{\text{leg}}}{c_{\text{f}_{\text{anchor}}}} \\ &= \frac{16,849}{0.8 \times 9.81} - \frac{0.45 \times 1,182}{0.8} \\ &= 1,482kg \end{aligned} \tag{4.40}$$

Calculation of the necessary dry weight of the anchor block is calculated using Equation 4.41, which is dependent on the density of the anchor material.

$$M_{\text{anchor}} = \frac{M_{\text{anchorx}}}{1 - \frac{\rho_{\text{water}}}{\rho_{\text{anchor material}}}} \tag{4.41}$$

Steel is chosen as the anchor material, requiring each anchor to have a dry weight of 1,700kg.

Chapter 5

Remote river energy system: Testing

5.1 Introduction

Testing of the RRES laboratory test rig is completed prior to deployment of the RRES at sea to test critical components / sub-assemblies. Detailed description of the laboratory test rig is given in Section 4.5. In the laboratory test rig the rotational power of rotor blades is replaced by an electric motor. The motor will aim to replicate the expected rotational power generated at the test site across all feasible conditions. The first aim of the testing is to validate the mechanical integrity of components / sub-assemblies such as the PTO, pump, sensors, etc. The second aim of the testing is to evaluate the efficiency of the components / sub-assemblies, ensuring that they are working as designed. Once all components / sub-assemblies have been scrutinised and measured data show that they work to a satisfactory standard, the RRES can progress to field testing.

Field testing of the RRES is conducted at a tidal estuary META site in Warrior Way, Pembrokeshire. Detail description of the field testing RRES design is given in 4.6. Testing of the RRES at a real tidal site is designed to give invaluable information on how well the RRES can capture energy from a tidal site. It shows how the performance of the RRES at a META site compares to numerical models. In addition to performance predictions of the turbine, a great deal of useful information has been gained on the logistics of deploying a tidal energy device.

5.2 Laboratory test rig

5.2.1 Test procedure

A robust test programme is necessary to ensure the threshold for all objectives for the development stages are meet. Additionally, the test programme must also provide enough data to accurately calculate the rotor performance during sea deployment. Details of the required data measurements from various instruments are given in Table 5.1. The sensors and instruments of the scaled laboratory rig are labelled in a CAD render shown in Figure 5.1.

The laboratory rig is tested across a range of motor input rotational speeds and torque. Each test takes 180s, split into three stages. The first 30s is used to reach the target motor rotational speed and pressure target, 30-60s is used to reach a steady state operation, and the final stage, 60-180s, is used to record data. The frequency of data recording is at 10Hz, which is the best compromise between experimental detail and data storage allocation. This means that for each operating point, there is 1,200 points of data from each sensor. The only divergence is for the flow rate data recording, which is at 1Hz due to instrument output signal.

The test plan for the scaled RRES laboratory rig is shown in Table 5.2. Motor drive target frequency and maximum pressure at location 3 are the two target parameters for the tests. The pressure target is measured at location 3 as it provides the most accurate indication of

Table 5.1: Detail of the sensors data measurement requirements for the laboratory rig test programme.

Instrument		Data measurement requirement
Name	No.	
Torque sensor	1	Torque and rotational speed of main shaft from motor ($\boldsymbol{T}$)
Flow rate sensor	2	Volumetric flow rate in piping system after the join of the outlet pipes ($\boldsymbol{Q}$)
Pressure sensor 1	4.1	Pressure prior to one way ball valve in outlet pipe ($\boldsymbol{p1}$)
Pressure sensor 2	4.2	Pressure downstream of one way ball valve in outlet pipe ($\boldsymbol{p2}$)
Throttle valve	3	Control and measure valve position ($\boldsymbol{TVP}$)
Pressure sensor 3	4.3	Pressure in piping system after the join of the outlet pipes and prior to throttling valve ($\boldsymbol{p3}$)
Pressure sensor 4	4.4	Pressure downstream of throttling valve prior to restriction orifice ($\boldsymbol{p4}$)
Pressure sensor 5	4.5	Pressure downstream of restriction orifice ($\boldsymbol{p5}$)
Temperature probe	5	Temperature at inlet pipe ($\boldsymbol{Temp}$)

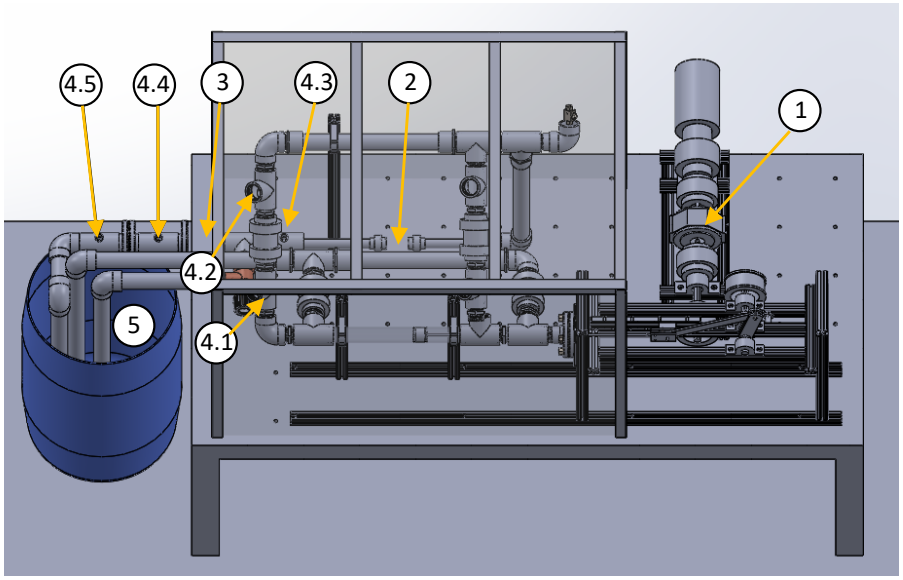

Figure 5.1: CAD render labelling the sensors and instruments of the laboratory rig.

the system, as it is located after the join of the outlet pipes and prior to throttling valve. The pressure target is the maximum value of the last 30s and is achieved by controlling the position of the throttling valve.

Table 5.2: Generic test plan for the RRES laboratory rig.

Test No.	Shaft speed (RPM)	Motor Drive Target Frequency (Hz)	Max p3 (bar)
___	[min:max]	[min:max]	[min:max]

The relationship between the motor drive target frequency and output shaft speed is given in Equation 5.1. η_{motor} is the gear ratio of the motor, which is 11.80 for the scaled motor and 52.82 for the full scale motor. 50 is the applied electrical frequency, and 1440 is a constant based on the number of motor poles.

$$\text{Motor Drive Target Frequency} = \frac{\text{Output RPM} \times \eta_{\text{motor}}}{\mathbf{1440} \times \mathbf{50}} \tag{5.1}$$

It is hypothesised that not all test cases are attainable; e.g. high shaft speed and low pressure, or low shaft speed and high pressure. Once testing had begun, it became clear

which cases could be reached. The attainable shaft speed and torque is also restricted due to the limitations of the motor.
The pressure sensors are used to calculate the pressure drop (energy loss) across three components: one way ball valve, throttling valve, and restriction orifice. The pressure drop across each component is calculated by;

$$\Delta p_{\text{Ball valve}} = p_1 - p_2 \tag{5.2}$$

$$\Delta p_{\text{Throttling valve}} = p_3 - p_4 \tag{5.3}$$

$$\Delta p_{\text{Orifice}} = p_4 - p_5 \tag{5.4}$$

The efficiency of the PTO and pump is estimated by comparing the power of the fluid at location 3, P_3, and the power of the the motor. It approximates the losses from the coupling shaft joins, belt pulley, crank assembly, and pump losses. P_3 can be calculated using Equation 5.5, which has been derived from Bernoulli's Equation. Q is the volumetric flow rate. The input power, P_{Input}, is calculated at the torque sensor using Equation 5.6, where T is torque, and ω is rotational speed.

$$P_3 = p_3 Q \tag{5.5}$$

$$P_{\text{Input}} = T\omega \tag{5.6}$$

An orifice plate is included in the outlet pipe of the laboratory rig to replicate a generator which is used in later versions of the RRES, as described in Section 4.5. Equation 5.7 is used for empirical calculation of pressure drop across a restriction orifice plate, where β is the ratio of orifice to pipe diameter, C_{d} is the orifice discharge coefficient, and A_{o} is the area of the orifice.

$$\Delta p_{\text{orifice}} = \frac{1}{2}\rho(1-\beta^4)\left(\frac{Q}{C_{\text{d}}A_{\text{o}}}\right)^2 \tag{5.7}$$

These calculations allows us to demonstrate whether the objectives success thresholds for rotor power conversion, numerically predicted power performance, and PTO operation and efficiency are met.

5.2.2 Scaled laboratory rig: Results & Discussion

5.2.2.1 Individual cases

Each laboratory rig test case was performed over 180s; 30s start-up followed by 30s of settling time, before 120s of steady-state. Data used for analysis and presented her on in are from the 120s steady-state. An example of the time series data recording from the various sensors (i.e. pressure, torque, flow rate, and rotational rate), from two test cases are given in Figure 5.2. Test case 1 has low rotational rate whilst test case 2 has high rotational rate. Both test cases have the throttle valve fully open (i.e. 100%). Summary of the plotted data in Figure 5.2 are given in Table 5.3. The figures are mean values over 120s.

It is hard to make meaningful conclusions on the performance of the laboratory rig from only the time series data due to the significant noise, and thus the data is analysed in the frequency domain. Included in the frequency domain plots are two vertical dashed lines which represent the rotor rotational frequency and rotor rotational frequency x2. The Welch overlapped segment averaging estimator function is used to estimate the PSD. It reduces noise in the estimated PSD but also the frequency resolution. The PSD plots using Welch's estimate for torque, pressure 1, 3, and 4 from test no.1 are given in Figure 5.3. As expected, there are 2 main peaks present in all PSD plots at a frequency equal to the rotational rate and rotational rate x2. During a single rotation, the crank arms pushes and pulls on the piston which results in two maximum force peaks at a frequency of x2 of rotation rate. The PSD plots in Figure 5.3 thus shows that the sensors are correcly capturing the dynamics of the system.

Table 5.3: Summary of small scale pump system data plotted in Figure 5.2. All figures are mean values over 120s.

Test No.	Torque (N.m)	Pressure 1 (Bar)	Pressure 2 (Bar)	Pressure 3 (Bar)	Pressure 4 (Bar)	Pressure 5 (Bar)	Flow rate (l/s)	Rotational rate (RPM)	Throttle valve position (%)
1	5.57	0.09	0.04	0.05	0.04	0.05	40.45	40.61	100
2	7.48	0.21	0.11	0.09	0.11	0.11	8.97	124.65	100

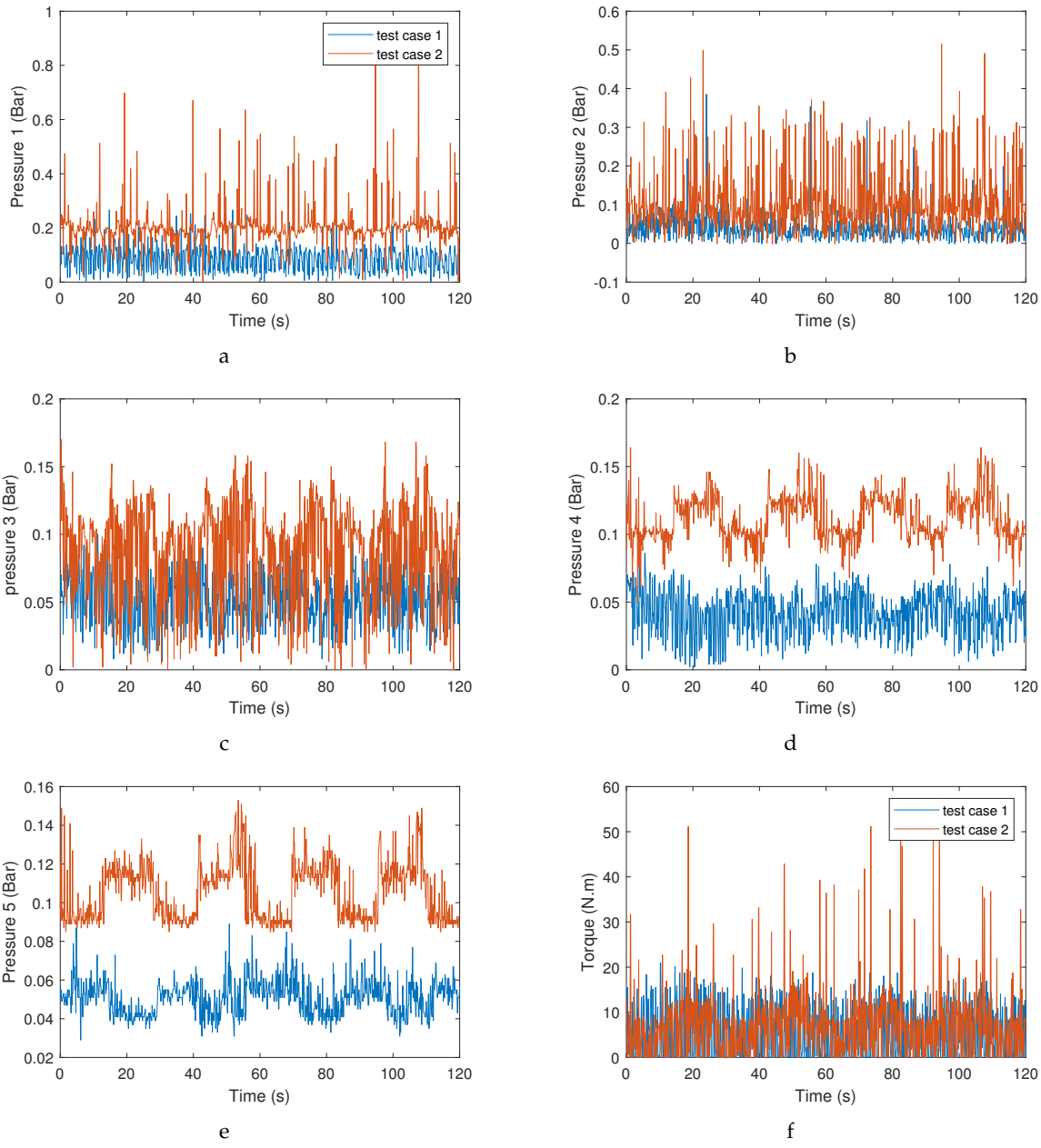

Figure 5.2: Time series plots of a) pressure 1, b) pressure 2, c) pressure 3, d) pressure 4, e) pressure 5, f) torque, g) flow rate, and h) rotational rate from test cases with 1) low rotational rate and torque, and 2) high rotational rate and torque with throttle valve 100% (fully) open for the scaled laboratory rig.

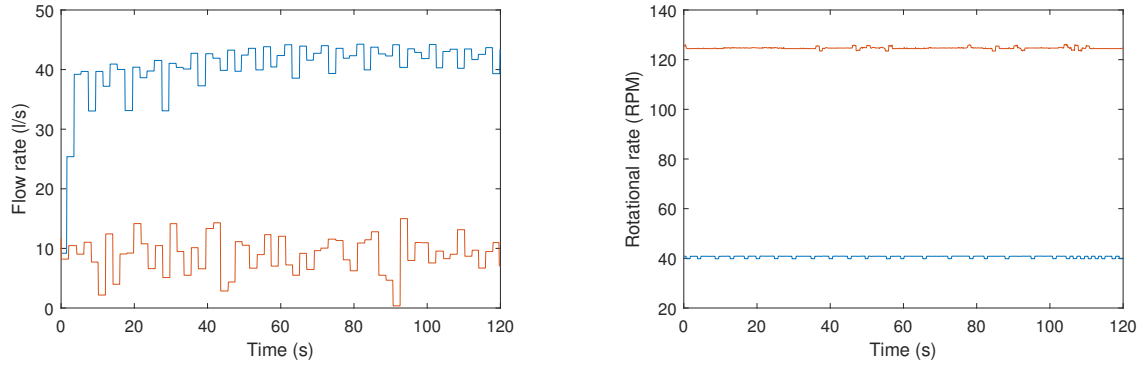

g h

Figure 5.2: Time series plots of a) pressure 1, b) pressure 2, c) pressure 3, d) pressure 4, e) pressure 5, f) torque, g) flow rate, and h) rotational rate from test cases with 1) low rotational rate and torque, and 2) high rotational rate and torque with throttle valve 100% (fully) open for the scaled laboratory rig.

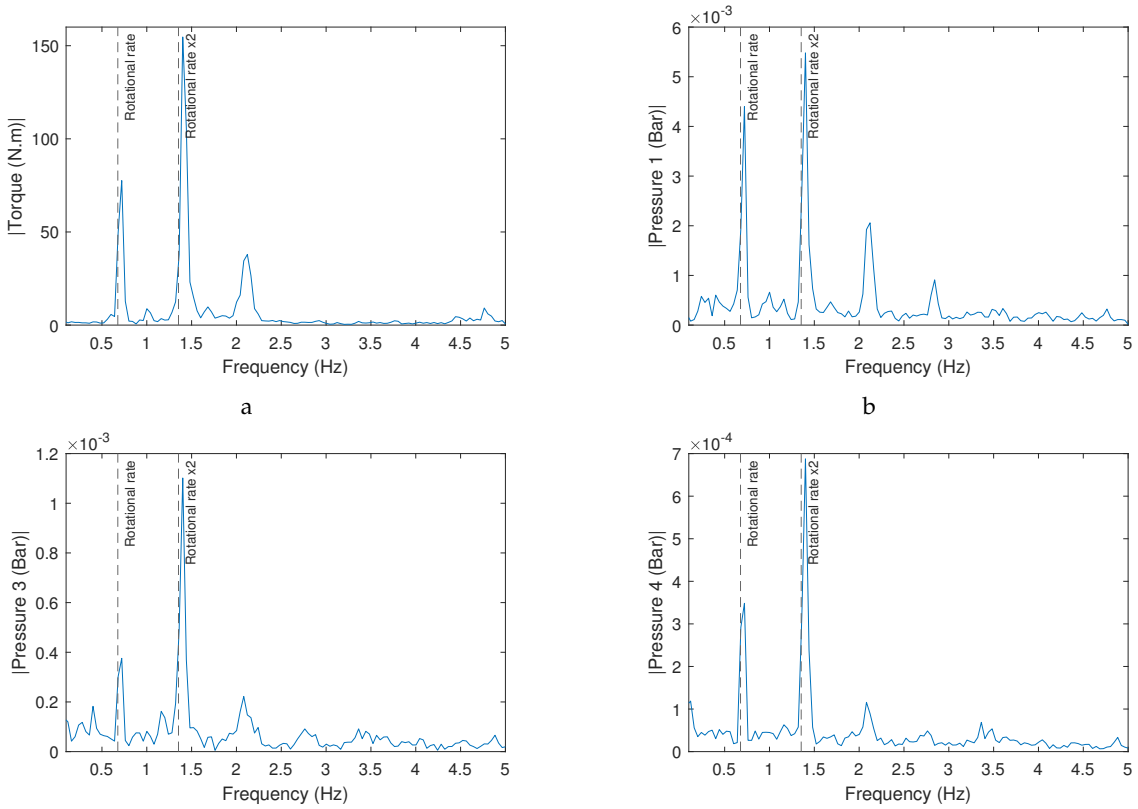

a b c d

Figure 5.3: Welch frequency domain plots of a) torque, b) pressure 1, c) pressure 3, and d) pressure 4 for test cases 1 (low rotational rate and torque with throttle valve 100% (fully) open) for the scaled laboratory rig.

5.2.2.2 Whole test campaign

Figure 5.4 is a plot of average rotational rate against flow rate for the whole test range. There is no clear correlation between rotational and flow rate. It is expected that the flow rate would increase with rotational rate. It is hypothesised that the system is not fully primed, thus a mixture of air and water is being pumped and that the percentage of water to air in the system increases with rotational rate. The flow rate sensor measures the volumetric flow rate, which for a constant rotational rate, would be higher for a system with a greater percentage of air.

Figure 5.5 shows a plot of mean torque, flow rate, throttle valve position, and pressure 3 with standard deviation error bands against rotational rate for the whole test range of the scaled laboratory rig. There is a clear correlation seen between throttle valve position and pressure 3 - higher pressure 3 is seen with lower throttle valve opening. Also, torque is proportional to pressure 3 and throttle valve position. When the rotational rate is kept constant, both torque and pressure 3 increase with closing the throttle valve.

A contour plot of rotational rate and pressure 3 against torque is shown in Figure 5.6. It shows that there is a strong positive correlation between pressure 3 and torque, and a weak positive correlation between rotational rate and torque. It was not possible to conduct

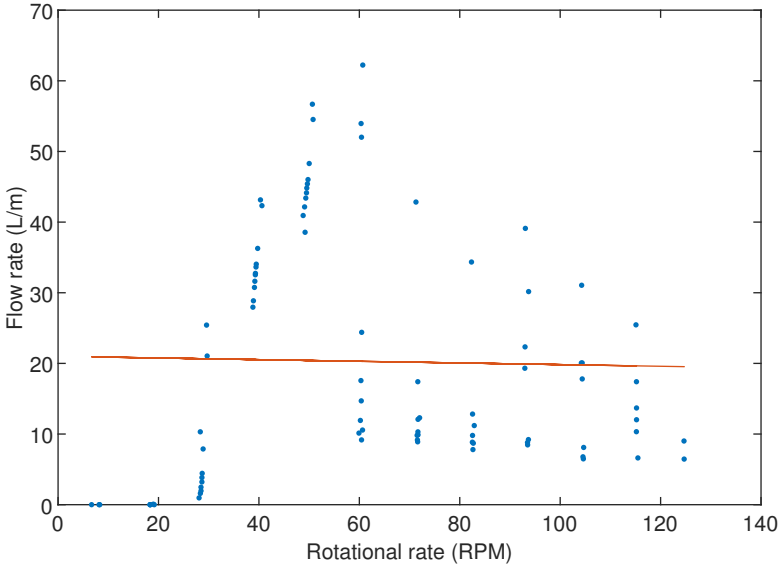

Figure 5.4: Plot of average rotational rate vs flow rate for the whole test range of the scaled laboratory rig.

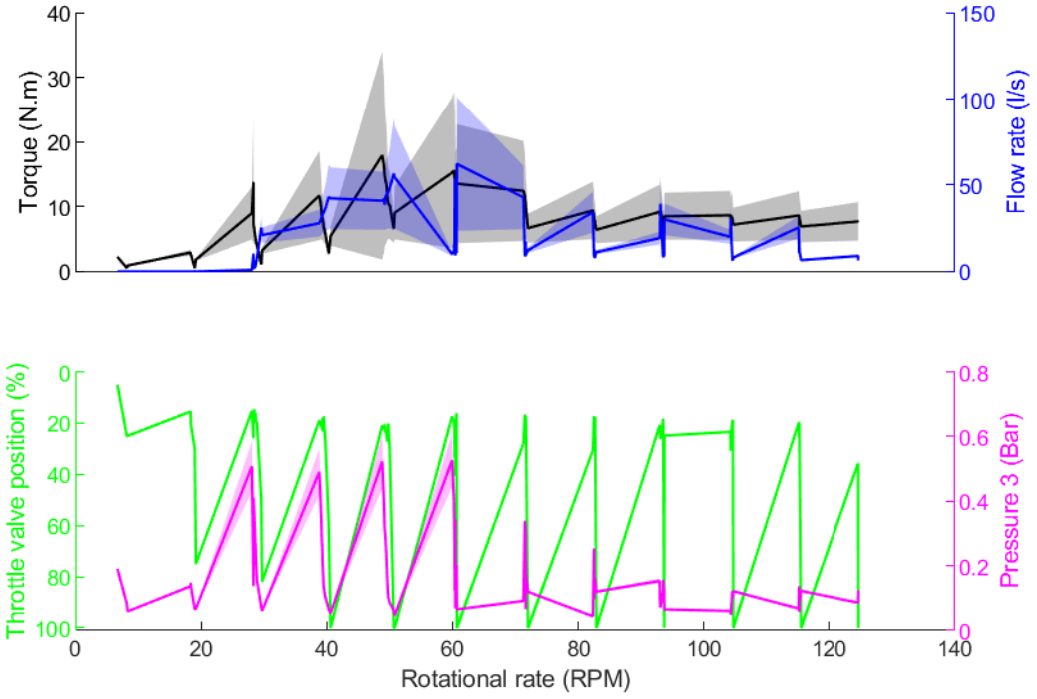

Figure 5.5: Plot of mean torque, flow rate, throttle valve position, and pressure 3 with standard deviation error bands against rotational rate for the whole test range for the scaled laboratory rig.

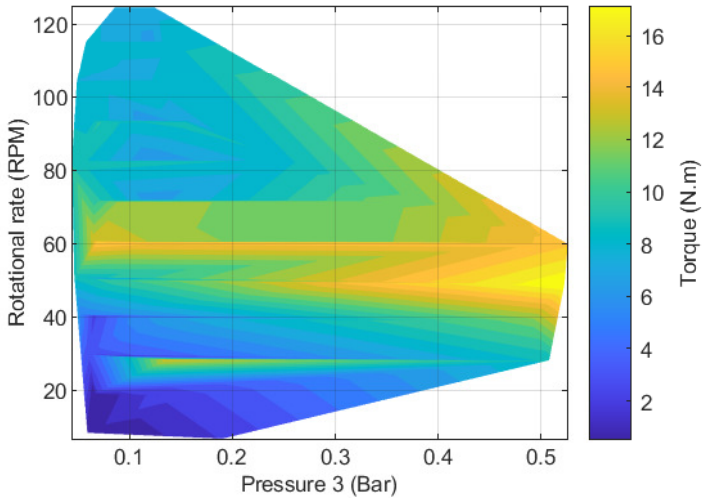

Figure 5.6: Contour plot of rotational rate and pressure 3 against torque for the scaled laboratory rig.

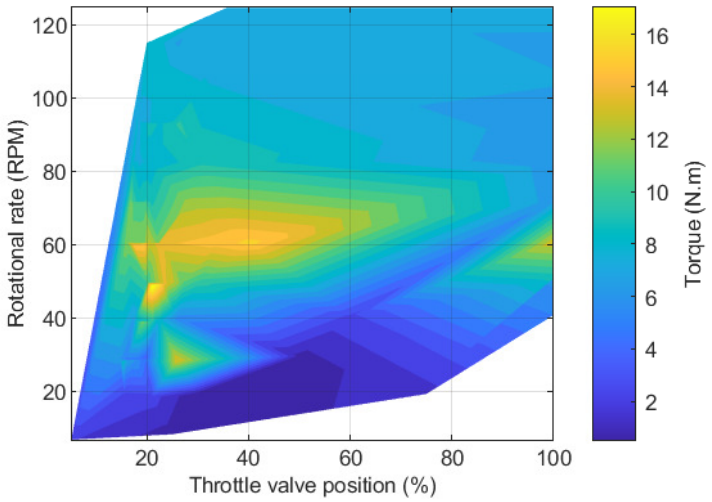

Figure 5.7: Contour plot of rotational rate and throttle valve position against torque for the scaled laboratory rig.

tests which had high pressure and rotational rate (i.e. top right corner of Figure 5.6), due to limitations of the electrical motor output torque. It is hypothesised that a test with high rotational rate and pressure 3 would require higher torque than possible with the electrical motor.

Similarly to Figure 5.6, Figure 5.7 is a contour plot of rotational rate and throttle valve position against torque. The plot shows that the throttle valve position between 50-100% makes very little difference to the torque. It is only when the throttle valve position is below 50% closed that it makes a noticeable difference to torque. This matches the findings made with the rotational rate and flow rate results seen in Figure 5.4. It indicates that the system is not fully primed, i.e. full of water, and a significant proportion of the volumetric flow is air. Figure 5.7 is trimmed for throttle valve position $<$40% in Figure 5.8 to improve its readability. As is seen in Figure 5.8, the greatest distribution of high torque is seen toward the smallest trottle valve position.

Average pressure at location 4 and 5 for each test case against rotational rate is shown in Figure 5.9. An orifice plate is located between location 4 and 5, which extracts energy from the fluid causing the large drop in pressure. The mean pressure drop across the orifice plate, i.e. between location 4 and 5, is 0.11 Bar. There is no significant difference in pressure drop across the orifice plate with various rotational rate. The average pressure drop across the orifice plate (p4 - p5) is plotted against flow rate for each test case in

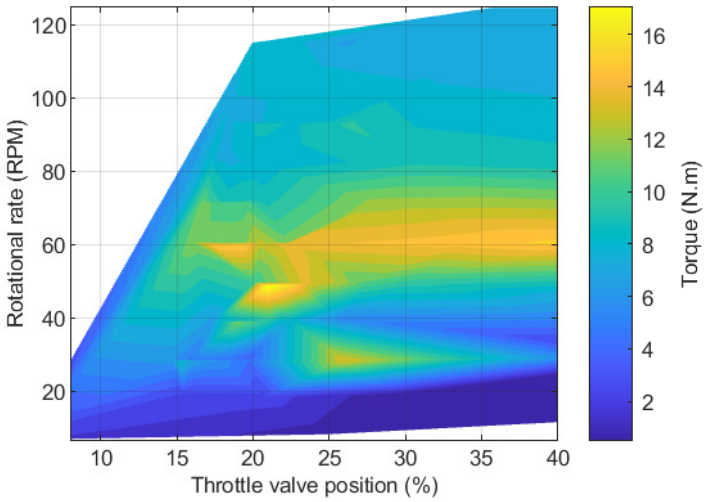

Figure 5.8: Contour plot of rotational rate and throttle valve position (<40%) against torque for the scaled laboratory rig.

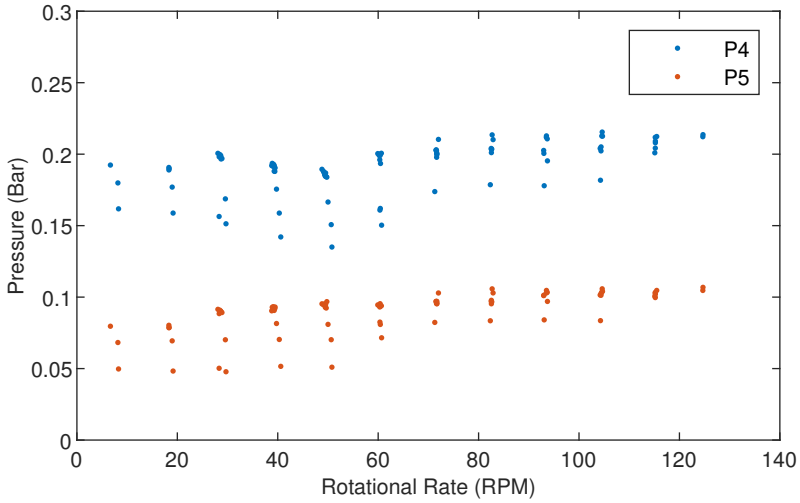

Figure 5.9: Average pressure at location 4 and 5 for each test case against rotational rate for the scaled laboratory rig.

Figure 5.10. As is clear from Equation 5.7, there should be a positive correlation between pressure drop and flow rate. A positive correlation between the pressure drop and flow rate is not seen due to inaccurate flow rate measurements as previously discussed.

A plot of pressure drop across the throttle valve (p3 - p4) against throttle valve position is shown in Figure 5.11. Throttle valve position (%) is plotted on the x axis which is the

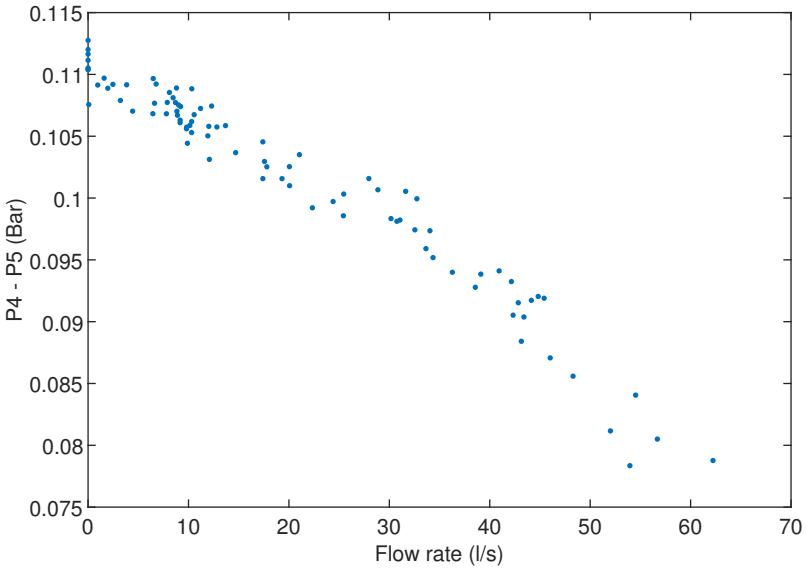

Figure 5.10: Average pressure drop across the orifice plate (p4 - p5) against flow rate for each test case for the scaled laboratory rig.

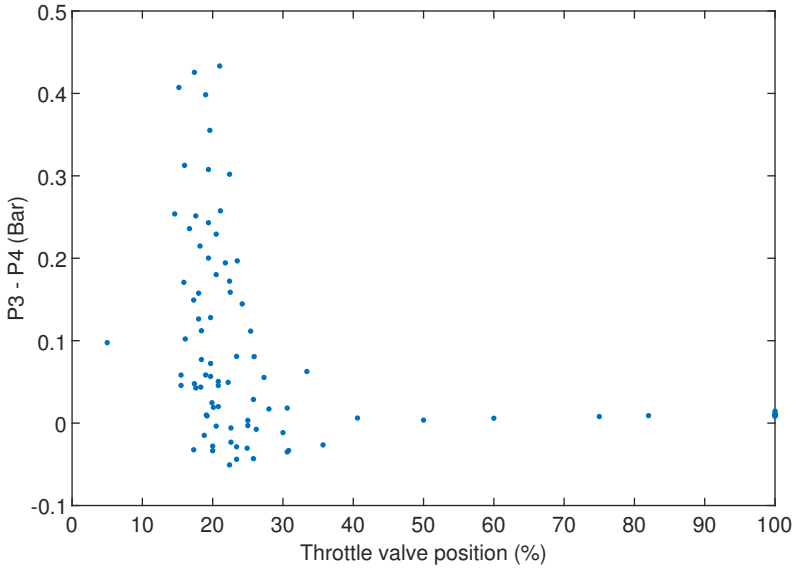

Figure 5.11: Plot of pressure drop across the throttle valve (p3 - p4) against throttle valve position for the scaled laboratory rig.

percentage of valve position from fully closed at 0%, and fully open at 100%. As expected, the pressure drop across the throttle valve is a function of throttle valve position. As the throttle valve closes, the pressure drop increases. There are a few test cases which show very little, or negative pressure drop across the throttle valve. These are test cases with low rotational rate and torque which means that the flow rate of water is also low. A low water flow rate gives less accurate pressure readings and is less affected by the change in throttle valve position.

Calculating the energy loss across the one way ball valves requires trimming of the pressure data. The pump is a dual stroke piston system and thus pumps water in both stroke direction. The pressure sensors at locations 1 and 2 record the pressure of the intake and exhaust phase. In order to estimate the energy loss across the one way ball valve, only the pressure data of the exhaust phase is needed. The pressure recording from p1 and p2 is trimmed to $>$50% of values (i.e. using only the pressure readings during the exhaust phase), as the exhaust phase will have the a larger pressure than the intake phase. Figure 5.12 is a plot of trimmed mean $>$50% for p1 and p2 against torque across all test cases for the scaled laboratory rig. The mean pressure drop between p1 and p2 (i.e. across the one way ball valve) is 0.064 Bar, and is essentially constant across torque inputs. Simplifying Bernoulli's equation by assuming no change in height or flow velocity between 1 and 2, gives a head loss of 0.652m. Multiplying the mean pressure loss by the mean flow rate through the one way ball valve gives the mean energy loss of 65J/s across the one way ball valve.

Power can be calculated at various locations on the laboratory test rig from measured data. The input power, $\boldsymbol{P}_{\text{Input}}$, is calculated at the torque sensor using Equation 5.6, and the power at location 3, $\boldsymbol{P}_3$, can be calculated using Equation 5.5. The efficiency of the PTO and pump can thus be calculated and is plotted against rotational rate in Figure 5.13. There best efficiency is seen between rotational rate 30-50RPM, with a significant decrease with higher rotational rate. It is important to note that the calculation of efficiency is only as accurate as the measured parameters. There is good confidence in the accuracy of the measured pressure at location 3 and torque, but not the flow rate.

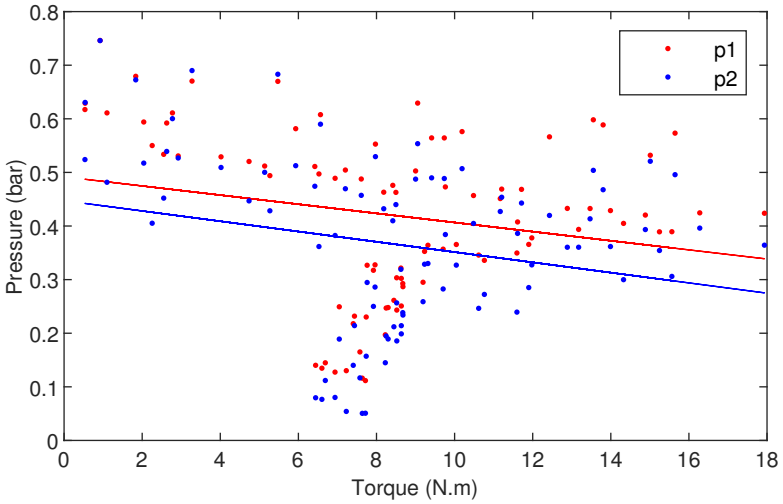

Figure 5.12: Comparison of pressure at locations 1 and 2, i.e across one way ball valve (Trimmed mean >50%) against torque for the scaled laboratory rig.

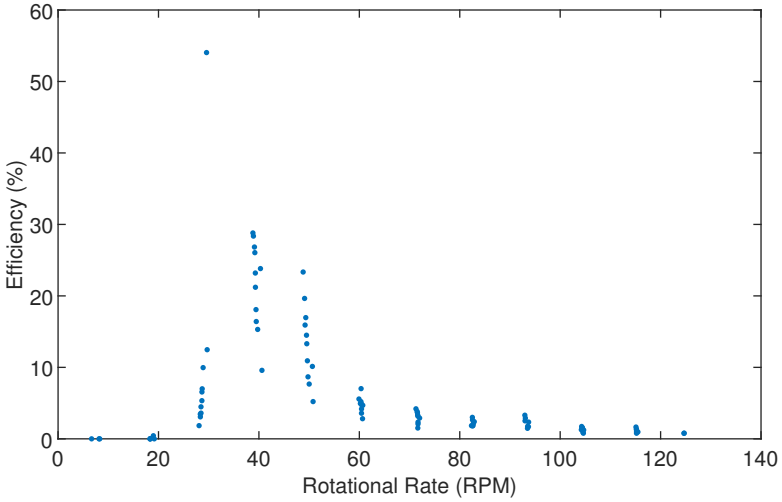

Figure 5.13: Plot of the PTO and pump assembly efficiency against rotational rate for the scaled laboratory rig.

5.2.3 Full scale laboratory rig: Results & Discussion

5.2.3.1 Individual cases

Following testing and review of the scaled laboratory rig minor design refinements were incorporated into the full scale version. These were mostly material choices of components, e.g. pump head was changed from 3D printed acrylic to machined stainless steel, and additional support for the PTO, pump and pipe system assemblies. Testing of the full scale RRES laboratory rig followed a similar procedure to the scaled version.
Torque, pressure 3, pressure 4, pressure 5, flow rate, and rotational rate are the parameters recorded by various sensors for the full scale laboratory rig. Using the same procedure as the scaled version, each test case lasts 180s; 30s start-up followed by 30s of settling time, before 120s of steady-state. Recorded data from two test cases for the full scale laboratory rig are plotted in Figure 5.14. To improve the readability only 20s of recorded data is plotted, taken from the middle of the 120s steady-state running. Figure 5.14 shows 20s time series of torque, pressure 3, pressure 4, pressure 5, flow rate, and rotational rate from test cases with 5) low rotational rate and high torque, and 6) high rotational rate and high torque. The two test cases used in Figure 5.14 both had the throttle valve at 20% open.
Plots of p3 and p4 from Figure 5.14 shows that p4 occasionally peaks higher than p3 for cases with low rotational rate and torque. This indicates that the flow direction changes for these instances. Test cases with low rotational rate and torque have low pressures which results in the one way ball valves not working as designed. It is suspected that the one way ball valves do not open for these cases where the pressures are low, causing the pressure in p3 to drop below p4.

Similarly to the scaled version, the recorded data from the full scale laboratory test rig is plotted in the frequency domain using the Welch overlapped segment averaging estimator function to validate the functionality of the various components. Figure 5.15 shows Welch frequency domain plots of torque, pressure 3, pressure 4, and pressure 5 from a test cases with high rotational rate with throttle valve 20% open.
The torque and pressure 3 frequency plots have two main peaks at frequency of rotational rate and rotational rate x2 which is as expected. The pressure 3 frequency plot has the strongest peak at frequency of rotational rate x2. This is due to the pump being a dual action type (i.e. water is pumped in both stroke direction). Both pressure 4 and pressure 5 frequency plots have also got peaks at frequency of rotation rate and rotational rate x2,

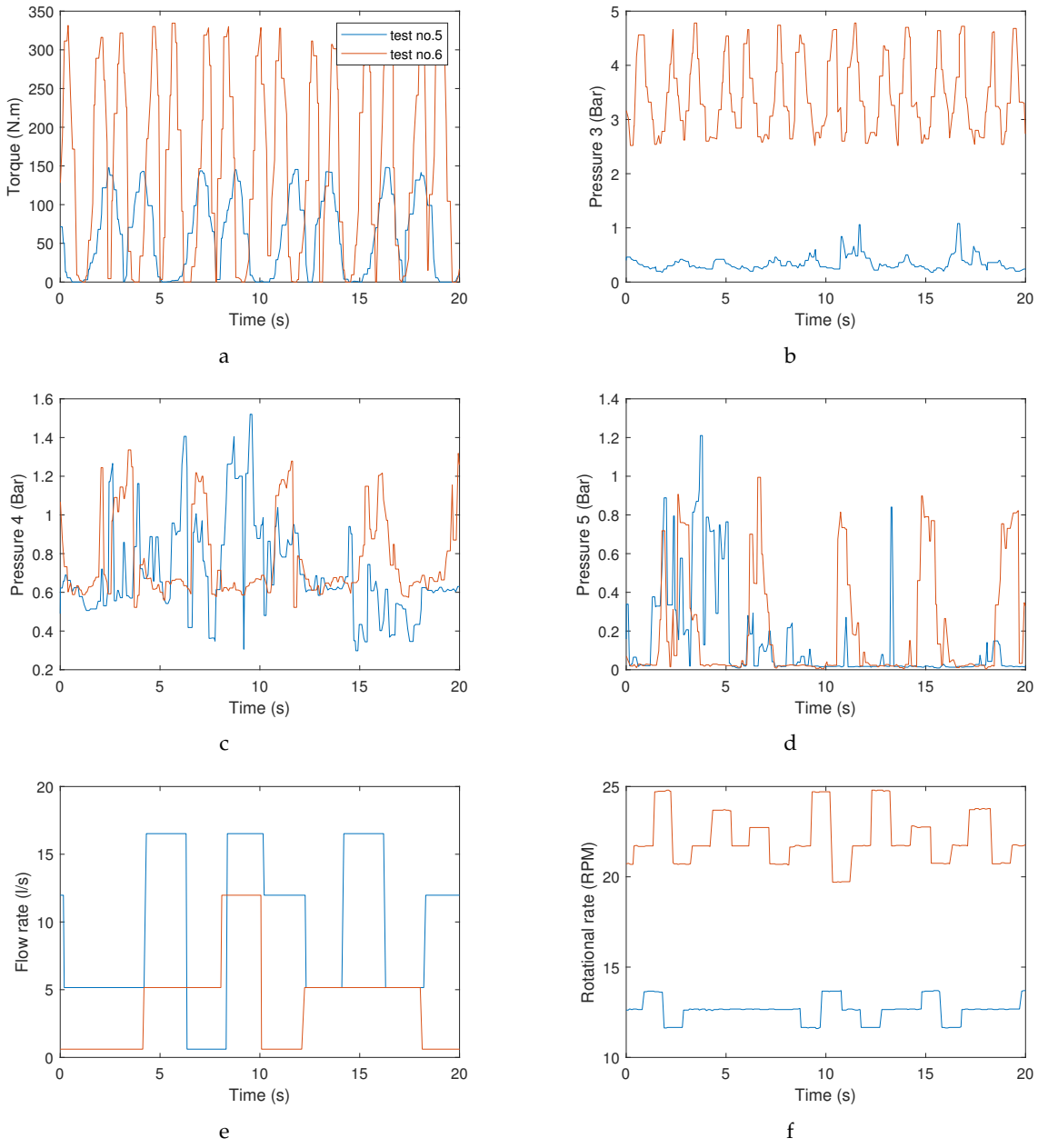

Figure 5.14: 20s time series plots of a) torque, b) pressure 3, c) pressure 4, d) pressure 5, e) flow rate, and f) rotational rate from test cases with 5) low rotational rate and high torque, and 6) high rotational rate and high torque, both with throttle valve 20% open.

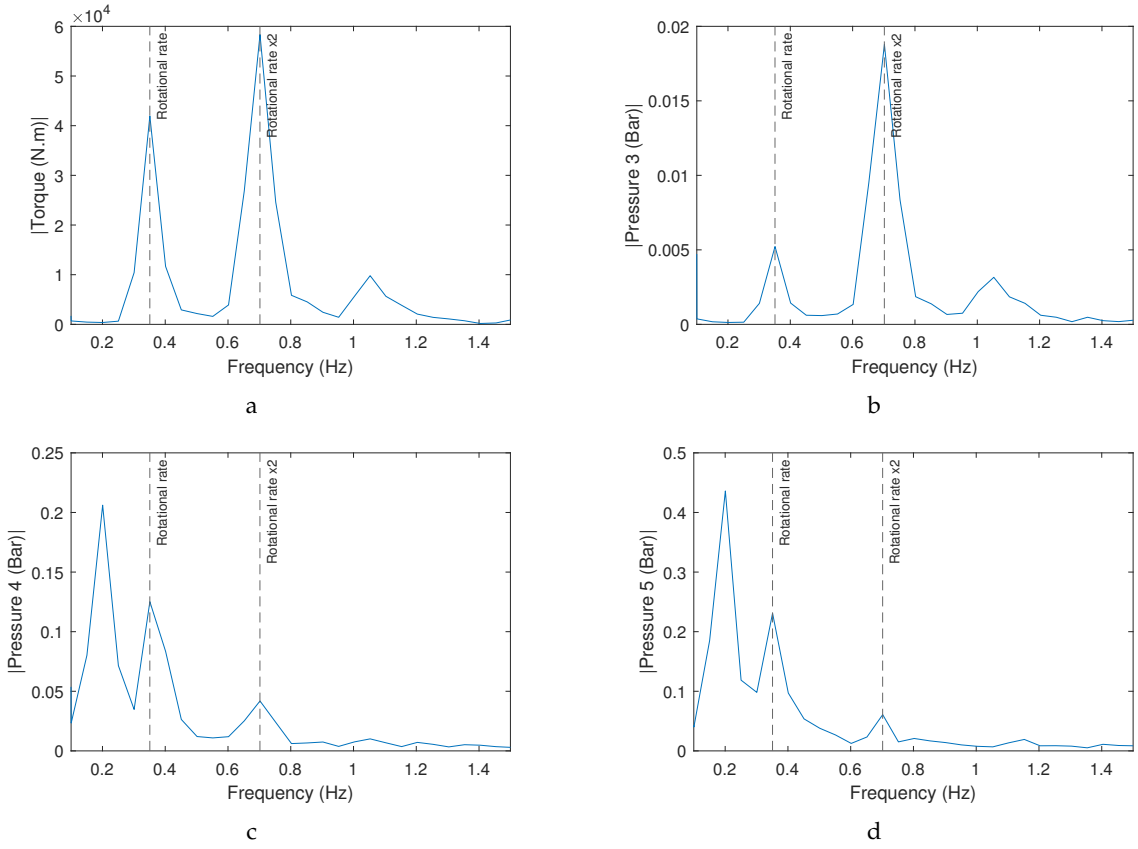

Figure 5.15: Welch frequency domain plots of a) torque, b) pressure 3, c) pressure 4, and d) pressure 5 from a test cases with high rotational rate with throttle valve 20% open.

but have a main peak at a lower frequency. This is due to the test case having the throttle valve 20% open which significantly alter/dampen the flow.

5.2.3.2 Whole test campaign

Figure 5.16 is a plot of average flow rate against rotational rate for the whole test range of the full scale lab rig. There is an inverse correlation between rotational rate and flow rate which is non-physical. It is expected that the flow rate would increase with rotational rate. Similarly to the scaled version, the flow rate sensor revealed that the full scale system was also not fully primed during testing. It was hoped that using components with better quality (e.g. tighter tolerances, less deficiencies, satisfy their stated or implied needs, etc.) in the full scale version would solve the issue of not priming, but it did not. Future iterations of the laboratory rig should consider alternative orientation of components and location of the water tank to fully prime the system.

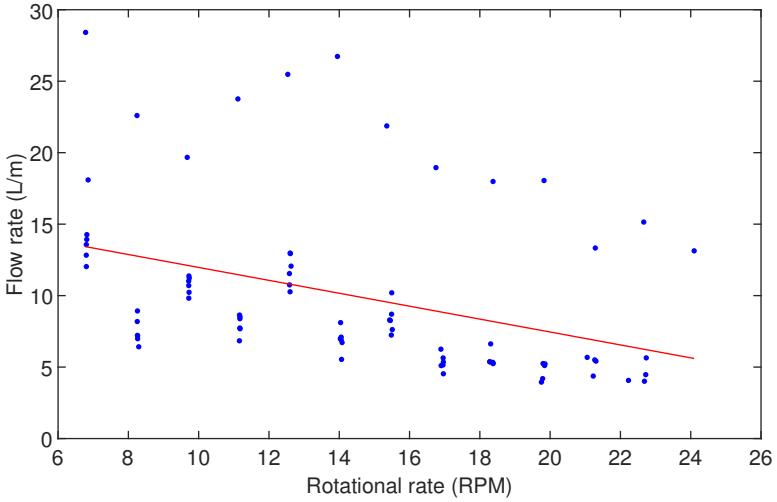

Figure 5.16: Plot of average flow rate against rotational rate for the whole test range of the full scale laboratory rig.

Figure 5.17 shows a plot of mean torque, flow rate, throttle valve position, and pressure 3 with standard deviation error bands against rotational rate for the whole test range. Similarly to the scaled laboratory test rig, an increase in torque and pressure 3 is seen with closing of throttle valve.

A contour plot of rotational rate and pressure 3 against torque is shown in Figure 5.18. As expected, torque has a strong positive correlation to pressure 3 and rotational rate. Pressure 3 is increased by closing the throttling valve, narrowing the outlet pipe. If the rotational rate is kept constant and the pressure 3 is increased, the torque also increases. Similarly, if the pressure 3 is kept constant and the rotational rate is increased, the torque also increases.

Similarly to Figure 5.18, Figure 5.19 is a contour plot of rotational rate and throttle valve position against torque. The plot shows that the throttle valve position between 50-100% makes very little difference to the torque. It is only when the throttle valve position is below 50% closed that it makes a noticeable difference to torque. This matches the findings made with the rotational rate and flow rate results seen in Figure 5.16. It indicates that the system is not fully primed, i.e. full of water, and a significant proportion of the volumetric flow is air. Figure 5.20 shows throttle valve position $<$40%.

Average pressure at location 4 and 5 against rotational rate for each test case is plotted in Figure 5.21. An orifice plate is located between location 4 and 5, which extracts energy from the fluid causing the large drop in pressure. The mean pressure drop across the

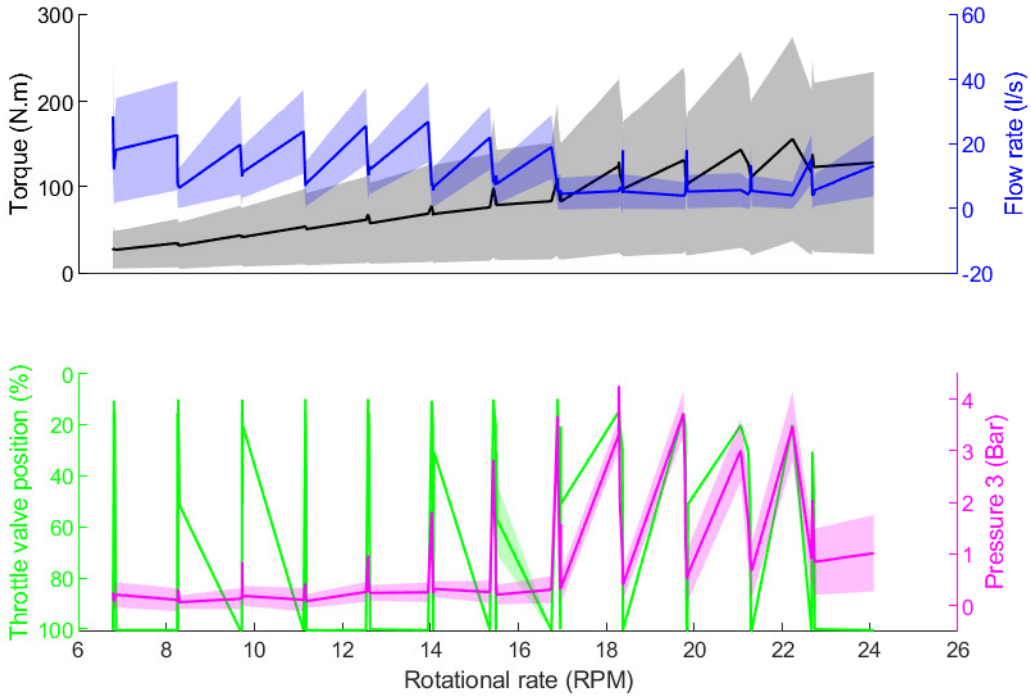

Figure 5.17: Plot of mean torque, flow rate, throttle valve position, and pressure 3 with standard deviation error bands against rotational rate for the whole test range for the full scale laboratory rig.

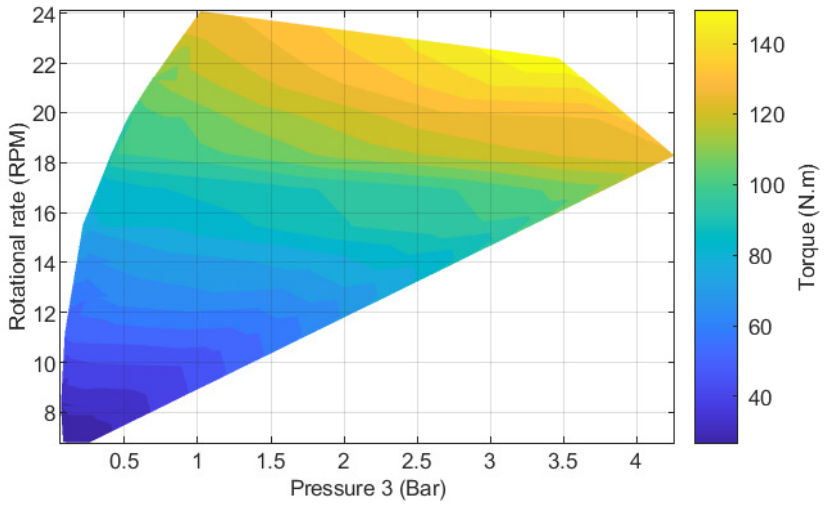

Figure 5.18: Contour plot of rotational rate and pressure 3 against torque for the full scale laboratory rig.

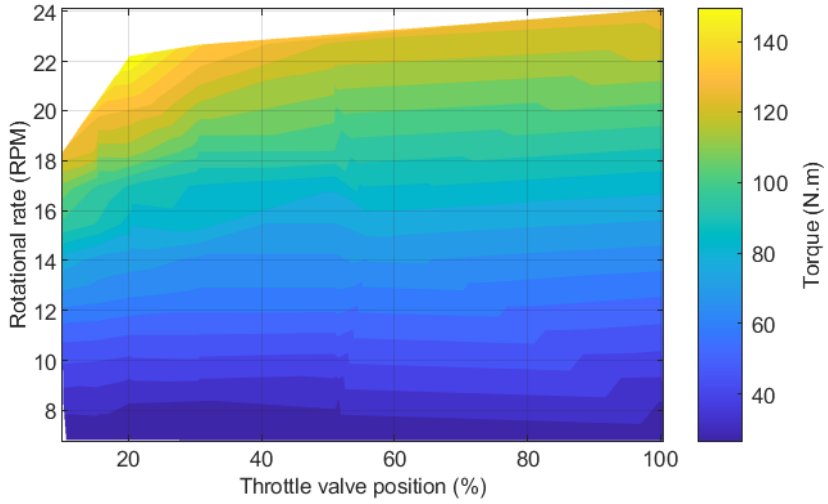

Figure 5.19: Contour plot of rotational rate and throttle valve position against torque for the full scale laboratory rig.

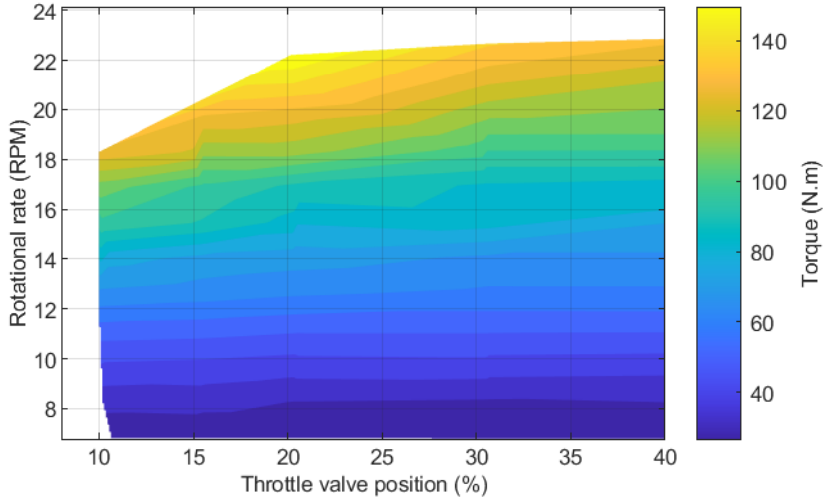

Figure 5.20: Contour plot of rotational rate and throttle valve position (<40%) against torque for the full scale laboratory rig.

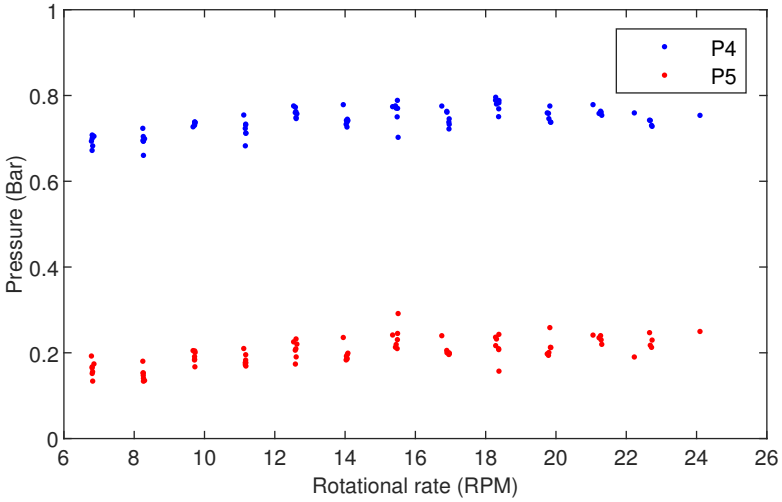

Figure 5.21: Average pressure at location 4 and 5 against rotational rate for each test case for the full scale laboratory rig.

orifice plate, i.e. location 4 and 5, is 0.54 Bar across the whole range of rotational rates. The average pressure drop across the orifice plate (p4 - p5) is plotted against flow rate for each test case in Figure 5.22. As is clear from Equation 5.7, there should be a positive correlation between pressure drop and flow rate. A strong correlation between the pressure drop and flow rate is not seen due to inaccurate flow rate measurements as previously discussed.

A plot of pressure drop across the throttle valve (p3 - p4) against throttle valve position is shown in Figure 5.23. As expected, the pressure drop across the throttle valve is a function of throttle valve position. As the throttle valve closes, the pressure drop increases. There are a few test cases which show very little, or negative pressure drop across the throttle valve. These are test cases with low rotational rate and torque which means that the flow rate of water is also low. A low water flow rate give less accurate pressure readings and is less effected by the change in throttle valve position.

Power can be calculated at various locations on the laboratory test rig from measured data. The input power, $\boldsymbol{P}_{\text{Input}}$, is calculated at the torque sensor using Equation 5.6, and the power at location 3, $\boldsymbol{P}_3$, can be calculated using Equation 5.5.

The efficiency of the PTO and pump can thus be calculated and is plotted against rotational rate in Figure 5.24. There are no strong correlations between efficiency and rotational rate. The calculation of efficiency is only as accurate as the measured parameters. There is good confidence in the accuracy of the measured pressure at location 3 and torque,

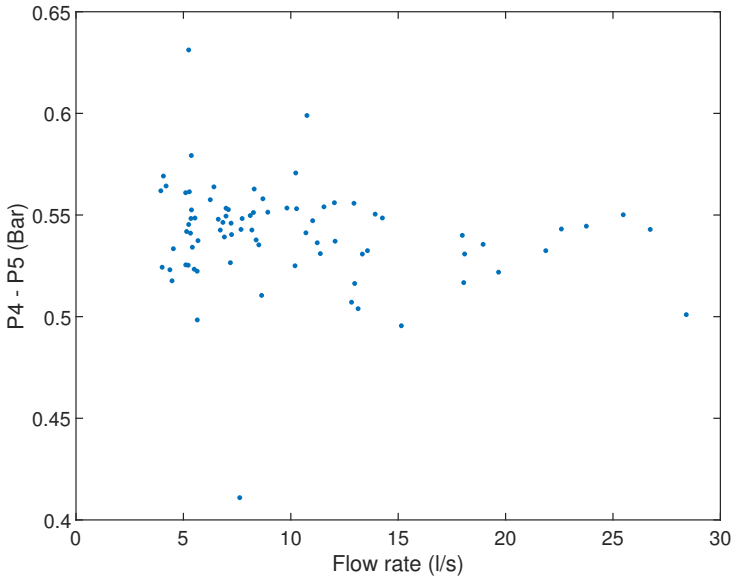

Figure 5.22: Average pressure drop across the orifice plate (p4 - p5) against flow rate for each test case for the full scale laboratory rig.

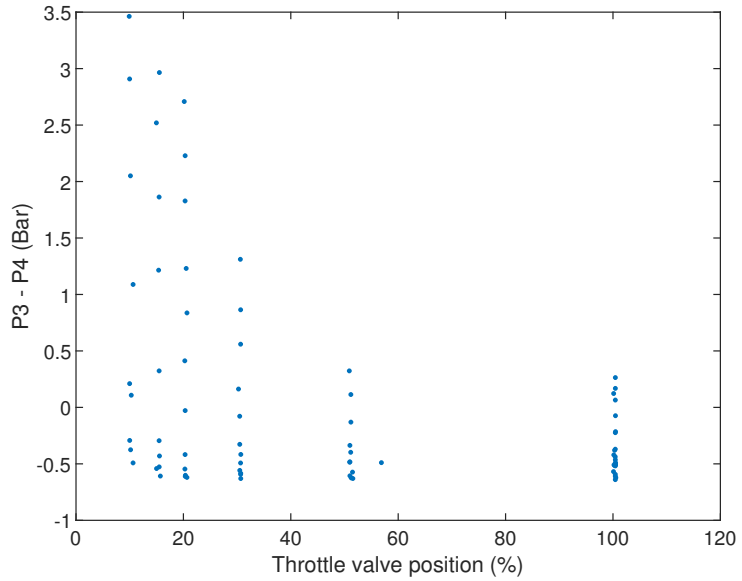

Figure 5.23: Plot of pressure drop across the throttle valve (p3 - p4) against throttle valve position for the full scale laboratory rig.

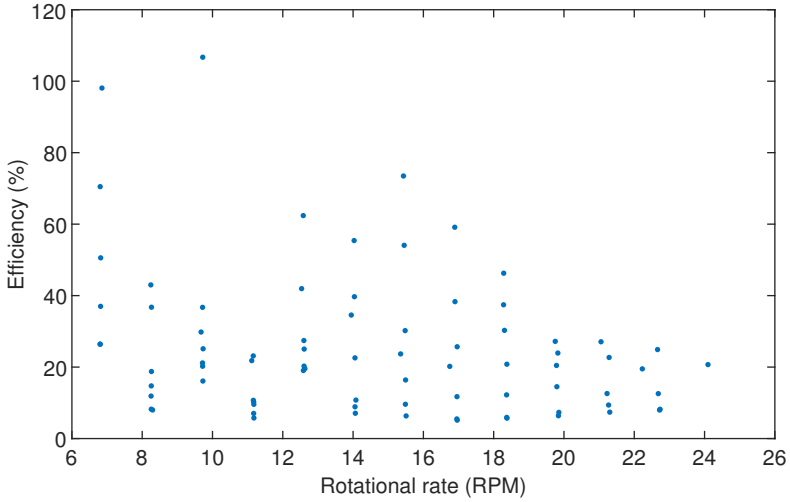

Figure 5.24: Plot of the PTO and pump assembly efficiency against rotational rate for the full scale laboratory rig.

but not the flow rate. The spikes in efficiency are likely due to over-estimations of flow rate, exaggerated by large volume of air in the system.

5.3 Full scale deployment

Photos of the RRES deployed at META Warrior Way test site are given in Figure 5.25 and the RRES on the slipway is given in Figure 5.26.

5.3.1 Test procedure

The rotor blades are pitched by 10° for rotor start-up. This is done as resistive bearing friction is unknown and due to low Reynolds number on a stationary blade, the torque available is also unknown.

The total torque is twice the measured value on the blade root bending sensor axis 1, as there are two rotor blades on the turbine. The total rotor thrust, F_T, is calculated from the blade root bending moment sensor axis 2 by using Equation 5.8. The bending moment is divided by half the length of the rotor blade as it the centre of load is at this location. TSR, $\boldsymbol{\lambda}$, is calculated using Equation 3.7.

$$\boldsymbol{F}_T = \frac{\text{blade root bending moment axis 2} \times \mathbf{2}}{\frac{\text{blade length}}{\mathbf{2}}} \tag{5.8}$$

Figure 5.25: RRES deployed at META Warrior Way.

Figure 5.26: RRES prior to deployment at META Warrior Way on slipway.

The turbine rotor power, $\boldsymbol{P}$, is calculated by multiplying torque, $\boldsymbol{T}$, by rotational rate, $\boldsymbol{\Omega}$, Equation 5.9.

$$\boldsymbol{P} = \boldsymbol{T\Omega} \tag{5.9}$$

Numerical prediction of rotor power, $\boldsymbol{P}$, and thrust, $\boldsymbol{F}_{\mathrm{T}}$, can be calculated using Equations 3.1 and 3.4 previously described in Chapter 3.

5.3.2 Field testing: Results & Discussion

5.3.2.1 Recorded data

Figure 5.27 shows a 9 minute time series of current velocity components in the x, y, and z direction (i.e. longitudinal, lateral, and vertical), two blade root bending moments, and rotor rotational rate. The velocity components were measured by an ADV which was located in line of the rotor rotational plane at hub height. A blade root bending moment from each blade at perpendicular directions to each other, are also shown. Axis one is in the same plane as the rotation of the rotor blades (i.e. torque) and axis two is perpendicular to the rotor rotation (i.e. thrust).

During testing, the RRES was dragged into shallow water where the rotor blades hit the river-bed. The first impact occurred at 11:25:05 and the second at 11:27:45. This is clearly seen in blade 1 axis 1, blade 2 axis 2, and Vx plots where there are significant spikes. Prior to the impacts, there was 2.5 minutes of the rotor operating in steady-state.

The data from Figure 5.27 is clipped from 11:22:33 to 11:24:50, and is shown in Figure 5.28. The average relative flow velocity perpendicular to the rotor blades rotation plane (i.e. Vx) and rotor rotational rate are 1.24m/s and 48.7rpm respectively. The average bending moment for axis 1 and 2 are 43.96N.m and 866.38N.m respectively. The average values are summarised in Table 5.4.

Between 11:22:33 and 11:24:50 the TSR remains fairly consistent, with an average of 6.2. The optimum TSR for this rotor blade is 3.0, thus it was operating at runaway in the

Table 5.4: Average values for the current velocity components, rotor rotational rate, and blade root bending moments between 11:22:33 and 11:24:50 from field testing of the RRES.

Parameter	Value.	Units
Vx	1.240	m/s
Vy	0.086	m/s
Vz	0.284	m/s
Rotational rate	48.68	rpm
Blade 1 axis 1 moment (torque)	43.96	Nm
Blade 2 axis 2 moment (thrust)	866.38	Nm

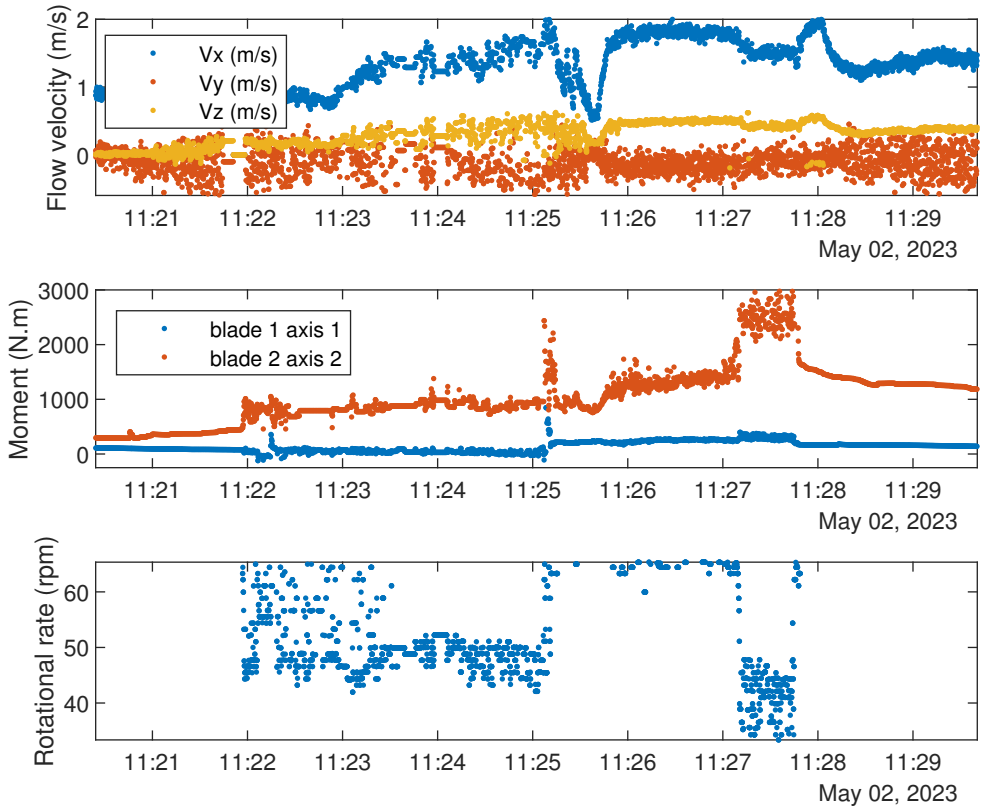

Figure 5.27: 9 minute time series plot of current velocity components in the x, y, and z direction, two blade root bending moments, and rotor rotational rate for the field testing of the RRES.

overspeed region. The rotor went straight to runaway because there was limited control over the rotational speed during this period as the pump system was still priming (i.e. filling with water). When the system is not fully primed, the method of using the throttle valve to control rotor speed by applying backwards torque does not work.
Four 30s segments are extracted from the recorded data between 11:22:33 and 11:24:50. Average measured rotational speed, current flow velocity, and blade root bending moments for the 30s segments are given in Table 5.5. The rotor performance is calculated from the 30s segments measured parameter and are given in Table 5.6.

5.3.2.2 Field campaign

Invaluable knowledge was gained throughout the whole field campaign of the RRES; particularly in manufacturing & assembly, planning, logstics, & consents, and testing.

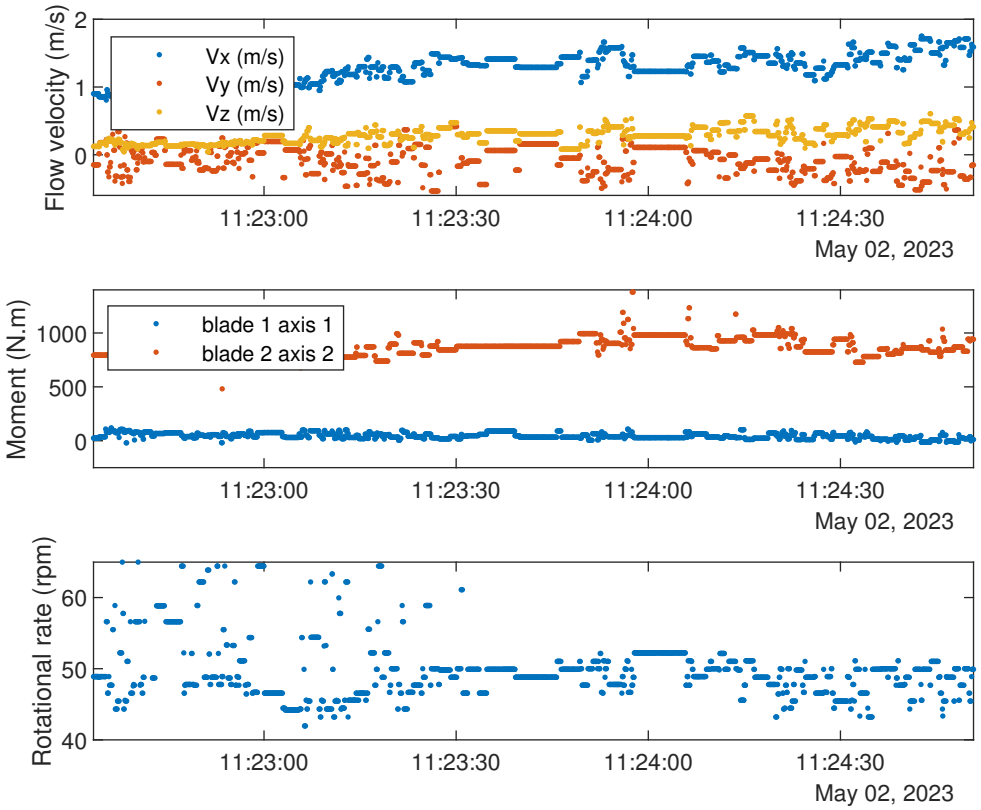

Figure 5.28: Time series plot between 11:22:33 and 11:24:50 of current velocity components in the x, y, and z direction, two blade root bending moments, and rotor rotational rate for the field testing of the RRES.

Table 5.5: 30s segment averages of measured rotor rotational rate, current flow velocity, and blade root bending moments from the field testing of the RRES.

Time (hh:mm:ss)	Rotational rate (RPM)	Vx (m/s)	Blade 1 axis 1 moment (torque) (Nm)	Blade 2 axis 2 moment (thrust) (Nm)
11:22:40 - 11:23:10	47.52	0.89	57.71	813.97
11:23:10 - 11:23:40	49.37	1.30	50.43	840.20
11:23:40 - 11:24:10	49.94	1.34	38.93	932.50
11:24:10 - 11:24:40	48.30	1.38	35.86	890.62

Table 5.6: Average rotor performance for the 30s segments between 11:22:40 and 11:24:40 from the field testing of the RRES.

Time (hh:mm:ss)	TSR	Torque (Nm)	Thrust (N)	Power (W)
11:22:40 - 11:23:10	8.39	115.42	2,504.52	574.36
11:23:10 - 11:23:40	5.97	100.86	2,585.23	521.45
11:23:40 - 11:24:10	5.85	77.86	2,869.23	407.18
11:24:10 - 11:24:40	5.50	71.72	2,740.37	362.76

The follow section will give an accurate and self-critical evaluation of the field campaign and how future testing of the RRES (and other tidal turbines) should be conducted to improve its design.

Manufacturing / assembly A test platform has been constructed from two modular pontoons (connected by steel beans at both ends) which offers the flexibility to be used by various turbine designs. The test platform has a submersible arm which is controlled by a hydraulic arm, giving control over the depth and pitch of the rotor blades. This designed was very stable in the water and was easy to assemble and disassemble.
The assembly of most components and sub-assemblies were achieved with ease, but some components caused difficulties. One such challenging assembly was the drive train, which is a relatively complex sub-assembly comprising of numerous components with precise tolerances. These components were sourced from various suppliers, all with different manufacturing standards, resulting in components not being compatible with each other. The necessary rectifying work took much time and added significantly to the timescale. Future projects should be careful which suppliers are used and that the standard of work which is required made very clear.

Planning, Logistics, & Consents A successful development of a tidal turbine takes years and requires meticulous planning. The most important planning lesson which was learned during the development of the RRES is that each stage will take longer than anticipated. There are numerous factors which contributed to these delays, e.g. design changes, manufacturing, consents, weather, contractors, and COVID. A plan can not account for all unforeseen factors, but it should include some slack to mitigate for these inevitable delays. This will allow for long term goals (i.e. deployment of tidal turbine) to be planned with certainty, which is crucial for a successful outcome.
Gaining the neseccary consent from various authorities (i.e. Crown estate, Port authority,

and Natural Resources Wales) is a teadious process which takes a great deal of time and effort. I believe that change is needed to reduce the complexity and extent of this process. This would reduce the burden on developers, making it easier to test and thus progress tidal turbine projects.

Tetsing A mooring design for a 7kW tidal turbine device has been designed and verified. The mooring system would be easily replicated by developers of similar devices in similar test areas. This mooring system was not used for the preliminary testing of the RRES which is presented in this thesis but will be used in successive testing. Due to a strict testing window at META Warrior Way (January - March), it was not possible to install the mooring infrastructure in time. Instead, a tow experiment was used to test the RRES. The tow vessel was a 11m workboat (8839) which was joined to the RRES by two 10m long tug rope fastened to its front corners. This proved to be a viable option to test a floating tidal turbine device in the absence of mooring. It is important to note that the tow test presented unique challenges which are not seen in static (mooring) tests. One of the most important lessons gained from the RRES tow test was the impact of the dynamic loads produced by the rotor on the test platform and subsequently the tow vessel. The lateral loads produced by the rotor were not anticipated to have such a drastic effect on the control of the tow vessel, limiting the maneuverability of the RRES test platform. Future tow tests should ensure that adequate tow vessel and tow links are used, and that a rigourous plan is in placed which has been overseen by an experienced captain familiar with the test area.

5.4 Remote river energy system testing: Conclusions

Three stages (2-4) of the RRES have been successfully tested; scaled laboratory test rig, full scale laboratory test rig, and full scale deployment. Testing of each stage has provided much valuable information on the performance of the RRES, and helped to improve its design. The complexity of the design and testing of the RRES increases substantially with the progression through the stages.

Testing of the scaled RRES laboratory rig has validated the design of the PTO, pump and pipework system functioned to an acceptable level and could be used on the full scale version. A wide range of input rotational speeds and torque were applied to the system from an electrical motor which matched the expected rotor performance at test site. Pressure, flow rate, rotational rate, and torque were all measured using various sensors.

Time series and frequency domain plots of these parameters have given much insight into the operation and performance of the scaled laboratory rig.

- Rotational power is successfully transferred through the power take off system to the pump assembly. No slipping of gears is seen even at the extremities of the operating conditions.
- The one way ball valves works as designed and water is pumped in both stroke directions.
- Pressure at location 3 has a strong positive correlation to torque and rotational rate.
- Orifice plate is working as an energy extraction device, with a mean drop of 0.11 Bar.
- The pressure drop across the one way ball valves is 0.064 Bar.
- The system does not fully prime, i.e. the pipe system contains a mixture of water and air.
  - The throttle valve affects the flow at positions <40%.
  - Efficiency of the PTO and pump assembly is approximated to be 10% across all test cases. This value is likely to be inaccurate due to the inaccuracy in the flow rate measurement.

Testing of the full scale RRES laboratory rig followed similar procedure to the scaled version and showed that the PTO, pump, and pipe system worked as to an acceptable level at full scale. The tests showed that the full scale RRES rig could be used on the sea deployment RRES. Similarly to the scaled version, key parameters of pressure, flow rate, rotational rate, and torque were all measured and then analysed in time and frequency domain to evaluate the operation and performance of the full scale RRES rig.

- Torque and pressure 3 have a frequency response at rotational rate and rotational rate x2.
- Pressure at location 3 has a possitive correlation to torque and rotational rate.
- Orifice plate is working as an energy extraction device, with an average drop of 0.54 Bar.

- Similarly to the scaled version, the system does not fully prime for the majority of cases, i.e. the pipe system contains a mixture of water and air. Again, the system is fully primed when the rotational rate and torque is high, but fails to fully prime at low values. The orientation of the rig will be different in the field deployment to ensure full priming at all operating conditions.
  - The throttle vale affects the flow at positions <40%.
  - Efficiency of the PTO and pump assembly is approximated to be 20% across all test cases. This value is likely to be inaccurate due to the inaccuracy in the flow rate measurement.

A great deal was learned during full scale deployment of the RRES at META in Warrior Way; e.g. deployment logistics, mooring, platform build, drive train, sensors, rotor performance.

- The logistical procedures which are required for deployment of a tidal energy device is very extensive.
  - Gaining consents from several parties such as NRW, port authorities, and crown estates.
  - Dry storage of device.
  - Planning and risk assessment methods statement documents.
- A mooring system has been designed for a 7kW tidal energy device.
  - 4 mooring lines attached to gravity anchors.
  - Mooring verified by a 3^{rd} party naval architects.
- Platform was constructed from two modular pontoons which kept the costs and ease of assembly to a minimum. A hydraulic arm successfully lowered and raised the rotor in and out of the water. The whole platform was stable and robust and provided a suitable base for the rotor to be submerged from.
- The drive train successfully transferred the rotational power from the rotor blades to the PTO. The difficulty of assembling the drive train was substantially increased by the additional complexity added by the slip ring. The slip ring was necessary to transfer data from the blade root bending moment sensors to the platform, which

provided invaluable data on rotor performance. In future devices where scientific data is not needed, the drive train can be significantly simplified which will drastically reduce the complexity of manufacture and assembly, and the cost.

- Many sensors were used on the deployment of the RRES. They were used as safety monitors, performance measurements, and flow field measurements.
  - Load shackles were located at the mooring line join to the platform and monitored the mooring loads, ensuring that they stayed within a safe limit.
  - The pressure and flow rate sensors of the laboratory rig are included in the RRES deployment version. The pressure sensors worked as expected during field testing providing valuable data.
  - The blade root bending moment sensors successfully measured strain in the plane of rotor rotation, and perpendicular to the rotation of the rotor, which were used to calculate torque and thrust respectively.
  - An ADV sensor was used to measure the flow velocity in line with the rotor rotational plane at hub height.
- Initial testing of the RRES has been completed, proving that the RRES can capture energy from the kinetic energy of the current. It has shown that the majority of components / sub-assemblies performed as expected. The second round of testing will commence in January 2024 where extensive tests will be carried out across the whole operating range of the RRES.

Chapter 6

Conclusions and Future Work

6.1 Conclusions

This thesis contributes towards the development of tidal stream turbines. Firstly, the BEMT numerical model which is used to predict the loads and performance of tidal stream turbines has been studied. Improvements have made to the numerical model by incorporating 1. element foil shape and Reynolds number dependency, and 2. transient features, and validation has been made to laboratory experiments. Secondly, the development of a 3m diameter tidal stream turbine has been presented, from laboratory rig to the deployed RRES (stages 2-4), using load predictions from the BEMT numerical model to govern its design. Lastly, testing of the RRES is presented where measured data is used to validate the design and the BEMT numerical model.

6.1.1 BEMT

In Chapter 3, validation and quantifying the improvements from the implementations of 1. element foil shape and Reynolds number dependency, and 2. transient features in the BEMT numerical model have been achieved by carrying out case studies of five different rotor blades. Each rotor blade has been extensively tested in laboratory scaled experiments which provided empirical data for validation of the BEMT numerical model. The rotor blades have different hydrofoil profiles, and twist and chord distribution which aim to test the limits of the BEMT numerical model.

Foil shape & Reynolds number dependence

A study has been conducted which looked at the effect of assigning each element across the rotor blades with individual lift and drag polars based on their hydrofoil shape

and Reynolds number. The BEMT model prediction of maximum rotor performance to laboratory results has improved by an average of 20.0% and 4.6% respectively for the Magallanes ATIR and Sabella D12 turbine rotor blades whilst it has decreased by 3.0% for the IFREMER turbine rotor with the inclusion of the improved blade geometry modelling. Comparing BEMT versions 2.gx and 3.xr (i.e. 2.gx hydrofoil shape dependence only, and 3.xr Reynolds number dependence only), it is clear that including geometry dependence has significantly greater impact on the BEMT model than that of Reynolds Number dependence. Including geometry dependence compared to Reynolds Number dependence has an average of 40% greater improvement in BEMT rotor performance prediction to laboratory. This is unsurprising as there is a more significant change in geometry compared to Reynolds Number across the rotor blades. Introducing the improved blade geometry modelling to the BEMT model has increased the computational time by approximately 10%. This is an acceptable increase in computational time in respect to added accuracy of the blade geometry modelling and the BEMT model prediction of rotor performance.

Uniform flow with turbulence

Five steady-state case studies have been carried out, where the performance of five rotor blades (Oxford, ATIR, D12, IFREMER, and Barltrop) were predicted by the BEMT numerical model in flow fields with constant mean current flow velocity with varying levels of turbulence. The BEMT numerical model is best at predicting rotor blade performance in stall and optimum operating region, with larger deviation in the overspeed operating region. The five tested rotor blades have different twist and chord distribution along their radial length, but all have decreasing chord and twist towards the tip. The location of optimum performance TSR is generally correlated to the twist along the rotor blade. A trend of decreasing optimum TSR with increasing maximum twist is seen with the rotor blades, with the exception of the Oxford rotor blade. The ATIR, D12, IFREMER, and Barltrop rotor blades all have very similar hydrofoil profile, but the profile of the Oxford rotor blade is significantly different, causing the difference seen in optimum TSR and twist correlation. If the maximum twist of the Oxford rotor blade was increased (i.e. pitching up of rotor blade), then the optimum TSR would decrease. This would be true for any rotor blade. Another observation of the power curves is that the maximum C_P increases with higher optimum TSR.

The C_T curves are all very similar with good comparison from the BEMT numerical model to laboratory experiments across the whole TSR for the majority of rotor blades.

There is a significant difference in C_T from the BEMT numerical model and the laboratory experiments in the overspeed region of for the Magallanes ATIR rotor blade. Many factors could be responsible for this discrepancy in the BEMT numerical model (e.g. inaccurate lift and drag polars, correction factors, or flow field representation). The discrepancies could also be due to limitations of the laboratory experiments (e.g. inaccurate measurement of flow conditions or manufacture of rotor blades).
Future work is needed to study the effects of the correction factors on the accuracy of the predicted turbine performance (i.e. C_t in the overspeed operating range). Identifying which elements of the BEMT model are contributing to the greatest inaccuracy of rotor performance requires a highly instrumented laboratory test campaign, such as the one conducted for the Oxford turbine. The predicted elemental forces from the BEMT model matched well to the measured Oxford laboratory tests across the whole rotor radius. The laboratory tests for all other turbines presented in this thesis measured only blade root forces, thus it is not possible to defer which elements are causing the inaccuracy between the BEMT model and laboratory testing.

Transient

A case study to establish the sensitivity of the IFREMER rotor blade to added mass (i.e. acceleration forces) in the BEMT numerical model has been conducted. It showed that the added mass has negligible contribution to the rotor torque, with the torque from the added mass being 2% of the hydrodynamic term. The contribution of the added mass on the rotor thrust is greater (as the waves travel perpendicular to the rotor rotation plane), with the thrust from the added mass being an average of 4.9% of the hydrodynamic term. The hydrodynamic and added mass terms are 90° out of phase. The added mass terms are dependent on the fluid acceleration and the hydrodynamic terms are dependent on the fluid velocity. There is a linear correlation between added mass thrust to both turbulence intensity and wave height of the flow field.
Transient case studies of four rotor blades (ATIR, D12, IFREMER, and Barltrop) have been completed. The flow fields of the transient case studies included waves and turbulence. The BEMT numerical model successfully captures the key parameters of the wave cycle of the flow fields. Similar to the steady-state cases, the BEMT numerical model is best at predicting rotor blade performance in stall and optimum operating region, with larger deviation in the overspeed operating region. The standard deviation of power and thrust of the BEMT numerical model is within an average of >95% across all cases ,to laboratory experiments,

validating that the BEMT is accurately accounting for the waves in the flow fields. Rotor performance is positively correlated to free stream velocity whilst turbulence intensity has a relative negligible effect due to the relatively large waves used in the experiments.

6.1.2 RRES design

In Chapter 4, the design process of a 3m diameter tidal stream turbine (named RRES) is presented. It's aimed to be used by a developing remote community to produce up to 7kW of power. The design process follows guidance of IEC TS 62600-202:2022 which gives best practice and recommendations on early stage development of tidal stream converters. The design process is accomplished over 4 stages, with stages 2-4 completed in this thesis; stage 2. Laboratory test rig, stage 3. At sea deployment of 0.9m diameter RRES, and stage 4. At sea deployment of full scale (3.0m diameter) RRES. The BEMT numerical model which has been improved and validated in Chapter 3 was used to predict the loads and performance of the RRES rotor blades which governed the design process.
A laboratory rig has been designed and manufactured which is capable of testing a wide range of power take off (PTO) and pump configurations. Rotational power produced by the rotor blades in the water is replicated by an electric motor which is capable of achieving input torque <1500Nm and rotational speeds >20rpm.
The RRES test platform is constructed from two modular pontoons connected by steel beams at both ends and has a submersible arm pivoting on the rear steel beam which is raised and lowered by a hydraulic arm. Two blade root bending moment sensors have been designed and manufactured which measure axial and tangential loads at the root of both rotor blades. These measurements are used to calculate the thrust and torque of the rotor blades. A mooring configuration has been designed for the deployment of the RRES at META Warrior Way following the standards and guidance of DNVGL-ST-N001.

6.1.3 RRES testing

Chapter 5 presents results from three stages (2-4) of the RRES testing; scaled laboratory test rig, full scale laboratory test rig, and full scale deployment. Testing of each stage has helped to improve its design. The complexity of the design and testing of the RRES increases substantially with the progression through the stages.
Testing of the scaled RRES laboratory rig has validated that the design of the PTO, pump and pipework system functioned to a satisfactory level and could be used on the full scale version. A wide range of input rotational speeds and torque were applied to the system from an electrical motor which match the expected rotor performance at test site.

Pressure, flow rate, rotational rate, and torque were all measured using various sensors. Time series and frequency domain plots of these parameters have given much insight into the operation and performance of the scaled laboratory rig. The flow rate sensor revealed that the system was not fully primed during testing (i.e. the pipe system contained a mixture of water and air).

Following testing and review of the scaled laboratory rig, minor design refinements were incorporated into the full scale version. These were mostly material choices and structural considerations. Testing of the full scale RRES laboratory rig followed similar procedure to the scaled version and showed that the PTO, pump, and pipe system worked to a satisfactory level at full scale. The tests showed that the full scale RRES rig could be used on the sea deployment RRES. Similarly to the scaled version, key parameters of pressure, flow rate, rotational rate, and torque were all measured and then analysed in time and frequency domain to evaluate the operation and performance of the full scale RRES rig. Similarly to the scaled version, the flow rate sensor revealed that the full scale system was also not fully primed during testing. It was hoped that using components with better quality (e.g. tighter tolerances, less deficiencies, satisfy their stated or implied needs, etc.) in the full scale version would solve the issue of not priming, but it did not. Future iterations of the laboratory rig should consider alternative orientation of components and location of the water tank to fully prime the system.

A great deal was learned during full scale deployment of the RRES at META in Warrior Way; e.g. deployment logistics, mooring, platform build, drive train, sensors, and rotor performance. The logistical procedures which are required for deployment of a tidal energy device are very extensive; e.g. gaining consents from several parties such as NRW, port authorities, and crown estates, dry storage of device, and planing and risk assessment methods statement documents. A mooring system which has been verified by a 3^{rd} party naval architect, has been installed for a 7kW tidal energy device which has 4 mooring lines attached to gravity anchors. The platform was constructed from two modular pontoons which kept the costs and ease of assembly to a minimum. A hydraulic arm successfully lowered and raised the rotor in and out of the water. The whole platform was stable and robust and provided a suitable base for the rotor to be submerged from. The drive train successfully transferred the rotational power from the rotor blades to the PTO. Many sensors were used on the deployment of the RRES, used as safety monitors, performance measurements, and flow field measurements. The blade root bending moment sensors

successfully measured strain in the plane and perpendicular to the rotor rotation, which were used to calculate torque and thrust respectively. Initial testing of the RRES has been completed, proving that the RRES can capture energy from the kinetic energy of the current. It has shown that the majority of components / sub-assemblies performed as expected. In the initial testing, the rotor was operating in the overspeed region due to limited control over the rotational speed during this period as the pump system was still priming.
A complete field test campaign of the RRES was not completed in time to be included in this thesis. The complete field campaign will produce vast amount of data which will be used to; 1. evaluate the performance of the RRES, 2. validate the BEMT numerical model (and others).

6.2 Future Work

A second deployment of RRES is planned for January 2024 where extensive testing of the RRES across its whole operating range in various flow conditions will be done. This will produce vast amount of performance data which will help future developments of tidal stream turbines and provide valuable scope for validation of numerical models.
To accurately predict the efficiency of the PTO and pump a better method for measuring the flow rate is needed. This could either be accomplished with a different flow rate sensor which is better suited for the operating conditions, or to modify the design of the piping system to ensure it can be fully primed.
Correction factors are used in the BEMT numerical model to account for omitted physical phenomena. The case studies of the BEMT show that the numerical model is least accurate in matching laboratory empirical data in the overspeed region. It is in this operating range where the correction factors are most influential. Further studies should look at the implementation of these correction factors and quantify their effect on the BEMT numerical model performance predictions of tidal stream turbines.

The original aims of the work were;

1. Improve the BEMT numerical model prediction of tidal stream turbines loads and performances through the implementation of 1. element foil shape and Reynolds number dependency, and 2. transient features.

2. Development and testing of the RRES, (stages 2-4 (scaled design model - full scale prototype device)), using the BEMT numerical model throughout as a design tool.

which have all been met.

References

[1] Ian Masters, Alison Williams, T. Nick Croft, Michael Togneri, Matt Edmunds, Enayatollah Zangiabadi, Iain Fairley, and Harshinie Karunarathna. A comparison of numerical modelling techniques for tidal stream turbine analysis. *Energies*, 8:7833–7853, 2015.

[2] XFOIL. Xfoil subsonic airfoil development system.

[3] (EMEC) European Marine Energy Centre. Tidal devices, 9 2023.

[4] HydroQuest. Ocean quest.

[5] Zhibin Zhou, Mohamed Benbouzid, Jean Frédéric Charpentier, Franck Scuiller, and Tianhao Tang. Developments in large marine current turbine technologies – a review, 2017.

[6] A. Roberts, B. Thomas, P. Sewell, Z. Khan, S. Balmain, and J. Gillman. Current tidal power technologies and their suitability for applications in coastal and marine areas. *Journal of Ocean Engineering and Marine Energy*, 2:227–245, 5 2016.

[7] Flumill. Harvesting energy from natural flow of water.

[8] Minesto. Innovation and design: tidal kite.

[9] T Burton, D Sharpe, N Jenkins, and E Bossanyi. *Wind energy handbook*. 2001.

[10] C.N. Lock, H Batemen, and H.C. Townsend. An extension of the vortex theory of airscrews with applications to airscrews of small pitch, including experimental results. *Aeronautical Research Committee Reports and Memoranda*, 1926.

[11] H Karadeniz, M.P Saka, and V Togan. Water wave theories and wave loads, 2012.

[12] A. V Garrel. *Development of wind turbine aerodynamics simulation module*. Energy research Centre of the Netherlands, 2003.

[13] Michael Togneri, Elaine Buck, Alasdair Macleod, Erwann Nicolas, José Nuño, and Michael O Connor. Multi-model analysis of tidal turbine reliability. *European Wave and Tidal Energy Conference*, 2019.

[14] N Barltrop, K S Varyani, A Grant, D Clelland, and Xuan Pham. Wave-current interactions in marine current turbines. *Proceedings of the Institution of Mechanical Engineers, Part M: Journal of Engineering for the Maritime Environment*, 220:195–203, 2006.

[15] N A Barltrop, K S Varyani, A Grant, D Clelland, and X P Pham. Investigation into wave – current interactions in marine current turbines. *Proceedings of the Institution of Mechanical Engineers, Part A: Journal of Power and Energy*, 221:233–242, 2007.

[16] P Mycek, B Gaurier, G Germain, G Pinon, and E Rivoalen. Experimental study of the turbulence intensity effects on marine current turbines behaviour. part 1: One single turbine. *Journal of Renewable Energy*, 66:729–746, 2014.

[17] Benoît Gaurier, Clément Carlier, Grégory Germain, Grégory Pinon, and Elie Rivoalen. Three tidal turbines in interaction: An experimental study of turbulence intensity effects on wakes and turbine performance. *Renewable Energy*, 148:1150–1164, 4 2020.

[18] Warrior way predictive habitat modelling. envision mapping ltd meta report, 2021.

[19] R.M. Warwick. Milford haven waterway sediment macrobenthos data analysis and review 2008-15. meta report, 2016.

[20] Net zero strategy: Build back greener. hm goverment, 2021.

[21] Robin Pelc and Rod M. Fujita. Renewable energy from the ocean. *Marine Policy*, 26:471–479, 11 2002.

[22] Mehmet Melikoglu. Current status and future of ocean energy sources: A global review. *Ocean Engineering*, 148:563–573, 1 2018.

[23] Meygen, 9 2023.

[24] C.M Johnstone, D Pratt, J.A Clarke, and A.D Grant. A techno-economic analysis of tidal energy technology. *Renew Energy*, 49:101–106, 2013.

[25] S Astariz, A Vazques, and G Iglesias. Evaluation and comparison of the levelized cost of tidal, wave and offshore wind energy. *Journal of Renewable Sustainable Energy*, 7, 2015.

[26] A.D Sagar and B Van Der Zwaan. Technological innovation in the energy sector: R and d, deployment and learning-by-doing. *Energy Polivy*, 34:2601–2608, 2006.

[27] S. Ordonez-Sanchez, R. Ellis, K.E. Porter, M. Allmark, T. O'Doherty, A. Mason-Jones, and C. Johnstone. Numerical models to predict the performance of tidal stream turbines working under off-design conditions. *Ocean Engineering*, 181:198–211, 6 2019.

[28] I. Masters, J. C. Chapman, M. R. Willis, and J. A.C. Orme. A robust blade element momentum theory model for tidal stream turbines including tip and hub loss corrections. *Journal of Marine Engineering and Technology*, 10:25–35, 2011.

[29] Brian Mannion, Seán B. Leen, and Stephen Nash. Development and assessment of a blade element momentum theory model for high solidity vertical axis tidal turbines. *Ocean Engineering*, 197:106918, 2 2020.

[30] Brian Mannion, Vincent McCormack, Seán B. Leen, and Stephen Nash. A cfd investigation of a variable-pitch vertical axis hydrokinetic turbine with incorporated flow acceleration. *Journal of Ocean Engineering and Marine Energy*, 5:21–39, 2019.

[31] W.M.J. Batten, A.S. Bahaj, A.F. Molland, and J.R. Chaplin. Experimentally validated numerical method for the hydrodynamic design of horizontal axis tidal turbines. *Ocean Engineering*, 34:1013–1020, 5 2007.

[32] EI Houghton and AE Brock. *Aerodynamics for engineering students*. Arnold, 1960.

[33] PJ Moriarty and AC Hansen. *AeroDyn theory manual. NREL/TP-500-36881*. NREL, 2005.

[34] J.C. Chapman, I. Masters, M. Togneri, and J.A.C. Orme. The buhl correction factor applied to high induction conditions for tidal stream turbines. *Renewable Energy*, 60:472–480, 12 2013.

[35] Ian Masters, Joshua Bird, Benjamin Birch, Maximilian Reader, William Turner, Tom Holland, Thomas Lake, and Alison J. Williams. Remote river energy system: An open source low maintenance turbine design for remote areas. *Proceedings of Institution of Civil Engineers: Energy*, pages 1–17, 2021.

[36] Fergal O. Rourke, Fergal Boyle, and Anthony Reynolds. Tidal energy update 2009. *Applied Energy*, 87:398–409, 2010.

[37] Yulin Si, Xiaodong Liu, Tao Wang, Bo Feng, Peng Qian, Yong Ma, and Dahai Zhang. State-of-the-art review and future trends of development of tidal current energy converters in china. *Renewable and Sustainable Energy Reviews*, 167, 10 2022.

[38] N. Khan, A. Kalair, N. Abas, and A. Haider. Review of ocean tidal, wave and thermal energy technologies. *Renewable and Sustainable Energy Reviews*, 72:590–604, 2017.

[39] Daniel Coles, Charles Greenwood, Arne Vogler, Tom Walsh, and David Taaffe. Assessment of the turbulent flow upstream of the meygen phase 1a tidal stream turbines. *AWTEC2018*, 2018.

[40] Syed shah Khalid, Liang Zhang, Xue wei Zhang, and Ke Sun. Three-dimensional numerical simulation of a vertical axis tidal turbine using the two-way fluid structure interaction approach. *Journal of Zhejiang University science and applied physics and engineering*, 14:574–582, 2013.

[41] Ahmed Gharib Yosry, Aitor Fernández-Jiménez, Eduardo Álvarez Álvarez, and Eduardo Blanco Marigorta. Design and characterization of a vertical-axis micro tidal turbine for low velocity scenarios. *Energy Conversion and Management*, 237, 6 2021.

[42] Pablo Ouro, Paul Dené, Patxi Garcia-Novo, Tim Stallard, Yusaku Kyozuda, and Peter Stansby. Power density capacity of tidal stream turbine arrays with horizontal and vertical axis turbines. *Journal of Ocean Engineering and Marine Energy*, 9:203–218, 5 2023.

[43] Mitchell G. Borg, Qing Xiao, Steven Allsop, Atilla Incecik, and Christophe Peyrard. A numerical performance analysis of a ducted, high-solidity tidal turbine. *Renewable Energy*, 159:663–682, 10 2020.

[44] C Belloni. Hydrodynamics of ducted and open-centre tidal turbines. *University of Oxford*, 2013.

[45] G H Huxham, S Cochard, and J Patterson. Experimental parametric investigation of an oscillating hydrofoil tidal stream energy converter. *18th Australasian Fluid Mechanics Conference*, 2006.

[46] S. R Waters. Analysing the performance of the archimedes screw turbine within tidal range technologies. *Lancaster University*, 2015.

[47] Koki Kishinami, Hiroshi Taniguchi, Jun Suzuki, Hiroshi Ibano, Takashi Kazunou, and Masato Turuhami. Theoretical and experimental study on the aerodynamic characteristics of a horizontal axis wind turbine. *Energy*, 30:2089–2100, 8 2005.

[48] R Mikkelsen. Actuator disk methods applied to wind turbines. *Dissertation for Technical University of Denmark*, 2003.

[49] W Shen, R Mikkelsen, J Sorensen, and C Bak. Tip loss corrections for wind turbine computations. *Wind Energy*, 8:457–475, 2005.

[50] WZ Shen, T Mikkelsen, J Sorensen, and C Bak. Evaluation of the prandtl tip correction for wind turbine computations. *Global Windpower Conf. Paris*, 2002.

[51] KY Maalawi and MTS Badawy. A direct method for evaluating performance of horizontal axis wind turbines. *Renewable and Sustainable Energy Reviews*, 5:175–190, 2001.

[52] HA Madsen, R Mikkelsen, S Oye, C Bak, and J Johansen. A detailed investigation of the blade element momentum (bem) model based on analytical and numerical results and proposal for modifications of the bem model. *Journal of Physics*, 75, 2007.

[53] Saeed A. El-Shahat, Lei Fu, and Guojun Li. Linear and non-linear wave theories coupled with a modified bem model for quantifying dynamic loads of a tidal stream turbine. *Ocean Engineering*, 243, 1 2022.

[54] Larissa Perez, Remo Cossu, Alistair Grinham, and Irene Penesis. An investigation of tidal turbine performance and loads under various turbulence conditions using blade element momentum theory and high-frequency field data acquired in two prospective tidal energy sites in australia. *Renewable Energy*, 201:928–937, 12 2022.

[55] John C. Chapman. Tidal energy device hydrodynamics in non-uniform transient flows. *Swansea University*, 2008.

[56] S Goldstein. On vortex theory of screw propeller. *Proceedings of the Royal Society*, pages 123–440, 1929.

[57] H Glauert. *Airplane propellers. Aerodynamic Theory*, volume 4. 1963.

[58] M.L.J. Buhl. A new empirical relationship between thrust coefficient and induction factor for the turbulent windmill state. nrel/tp-500-36834. *NREL*, 2005.

[59] Michael Togneri, Grégory Pinon, Clément Carlier, Camille Choma Bex, and Ian Masters. Comparison of synthetic turbulence approaches for blade element momentum theory prediction of tidal turbine performance and loads. *Renewable Energy*, 145:408–418, 2020.

[60] PS Veers. Three-dimensional wind simulation - sandia method. *Journal of Geophysical Research*, 92:2289, 1987.

[61] IA Milne, RN Sharma, RG Flay, and S Bickerton. Characterisatics of the turbulence in the flow at a tidal stream power site. *Phil. Trans. Roy, Soc, Lond. A Math. Phys. Eng. Sci.*, 371, 2013.

[62] I Milne, A Day, R Sharma, and R Flay. The characterisation of the hydrodynamic loads on tidal turbines due to turbulence. *Renew Sustain Energy*, pages 851–864, 2016.

[63] Clement Carlier. Simulation du comportement d'hydroliennes : modelisation de i'influence de la turbulence ambiante et des effets d'interaction, 2017.

[64] C Carlier, G Pinon, B Gaurier, G Germain, and E Rivoalen. A synthetic-eddy-method to represent the ambient turbulence in numerical simulation of marine current turbine. 2015.

[65] R E Baddour and S Song. On the interaction between waves and currents. *Ocean Engineering*, 17:1–21, 1990.

[66] T Stallard, R Collings, T Feng, and J Whelan. Interactions between tidal turbine wakes: experimental study of a group of three-bladed rotors. *Philos Trans R Soc*, 2013.

[67] T Blackmore, W Batten, and A Bahaj. Influence of turbulence on the wake of a marine current turbine sinulator. *The royal society*, 470, 2014.

[68] P Pyakurel, JH VanZwieten, M Dhanak, and N Xiros. Numerical modeling of turbulence and its effect on ocean current turbines. *International Journal of Marine Energy*, 17:84–97, 2017.

[69] M Togneri, I Masters, C Carlier, C Choma Bex, and G Pinon. Comparison of synthetic turbulence approaches for two numerical tidal turbine models. *Proceedings of the Twelfth European Wave and Tidal Energy Conference*, 2017.

[70] N. Jarrin, S. Benhamadouche, D. Laurence, and R. Prosser. A synthetic-eddy-method for generating inflow conditions for large-eddy simulations. *International Journal of Heat and Fluid Flow*, 27:585–593, 2006.

[71] N Jarrin. Inflow boundary conditions for the numerical simulation of turbulence. *University of Manchester*, 2008.

[72] J.B Herbich. Linear wave theory. handbook of coastal engineering, 2000.

[73] J.A.C. Orme. Dynamic performance modelling of tidal stream turbines in ocean waves. *Swansea University*, 2006.

[74] J.N. Newman. *Marine Hydrodynamics*. 1977.

[75] J.I. Whelan. A fluid dynamic study of free-surface proximity and inertia effects on tidal turbines. *Imperial College London*, 2010.

[76] Matt Edmunds, Alison J. Williams, Ian Masters, Arindam Banerjee, and James H. VanZwieten. A spatially nonlinear generalised actuator disk model for the simulation of horizontal axis wind and tidal turbines. *Energy*, 194:116803, 2020.

[77] H.G Weller, G Tabor, H Jasak, and C Fureby. A tensorial approach to computational continuum mechanics using object-oriented techniques. *Computational Physics*, 12:620–631, 1998.

[78] V Yakhot, S. A Orszag, S Thangam, T. B Gatski, and C. G Speziale. Development of turbulence models for shear flows by a double expansion technique. *Physics of Fluids and fluid dynamics*, 4:1510–1520, 1992.

[79] T O'Doherty, A Mason-Jones, D. M O'Doherty, C. B Byrne, I Owen, and Y. X Wang. Experimental and computational analysis of a model horizontal axis tidal turbine. *Proceedings of the 8th European wave and tidal energy conference*, pages 833–841, 2009.

[80] M. Edmunds, A. J. Williams, I. Masters, and T. N. Croft. An enhanced disk averaged cfd model for the simulation of horizontal axis tidal turbines. *Renewable Energy*, 101:67–81, 2017.

[81] J. D Anderson. *Fundamentals of aerodynamics*. 2010.

[82] Grégory Pinon, Paul Mycek, Grégory Germain, and Elie Rivoalen. Numerical simulation of the wake of marine current turbines with a particle method. *Renewable Energy*, 46:111–126, 2012.

[83] R Lewis. Vortex element methods for fluid dynamic analysis of engineering systems. *Cambridge University Press*, 1991.

[84] Myriam Slama, Camille Choma Bex, Grégory Pinon, Michael Togneri, and Iestyn Evans. Lagrangian vortex computations of a four tidal turbine array: An example based on the nepthyd layout in the alderney race. *Energies*, 14:1–23, 2021.

[85] G Cottet and P Koumoutsakos. Vortex methods: Theory of particle. *Cambridge University Press*, 2000.

[86] P Sagaut. Large eddy simulation for incompressible flows: An introduction. *Scientific Computation*, 2006.

[87] N Mansour, J Ferziger, and W Reynolds. Large-eddy simulation of a turbulent mixing layer. *Technical Report, Report TF-11. Stanford University, USA*, 1978.

[88] P. G Saffman. Vortex dynamics. *Cambridge University Press*, 1992.

[89] J.N. Sorensen and W.Z. Shen. Numerical modeling of wind turbine wakes. *Journal of Fluids Engineering*, 124:393–399, 2002.

[90] L Prandtl. *Applications of Modern Hydrodynamics to Aeronautics*. 1921.

[91] J.D. Anderson. *Fundamentals of Aerodynamics*. 5th edition, 2011.

[92] Hao Cheng and Hua Wang. Prediction of lift coefficient for tandem wing configuration or multiple-lifting-surface system using prandtl's lifting-line theory. *International Journal of Aerospace Engineering*, 2018:1–15, 7 2018.

[93] J The and H Yu. A critical review on the simulations of wind turbine aerodynamics focusing on hybrid rans-les methods. *Energy*, 138:257–289, 2017.

[94] S.H. Park and J.H. Kwon. Implementation of kw turbulence models in an implicit multigrid method. *AIAA J*, 42:1348–1357, 2004.

[95] P.C. Rocha, H.B. Rocha, F.M. Carneiro, M.V. da Silva, and A.V. Bueno. kw sst (shear stress transport) turbulence model calibration: a case study on a small scale horizontal axis wind turbine. *Energy*, 65:412–418, 2014.

[96] M.J. Lawson, J Melvin, S Ananthan, K.M. Gruchalla, J.S. Rood, and M.A. Sprague. Blade-resolved, single-turbine, simulations under atmospheric flow. *NREL*, 2019.

[97] P Weihing, J Letzgus, G Bangga, T Lutz, and E Kramer. Hybrid rans/les capabilities of the flow solver flower-application to flow around wind turbines. *Notes on Numerical Fluid Mechanics and Multidisciplinary Design, Springer*, pages 369–380, 2016.

[98] R Willden, S T Harvey, and X Chen. Unsteady loading tidal turbine benchmarking study.

[99] R H J Willden, X Chen, S W Tucker Harvey, H Edwards, C R Vogel, K Bhavsar, T Allsop, J Gilbert, H Mullings, D Apsley, T Stallard, I Benson, A Young, P Schmitt, F Zilic De Arcos, M.-A Dufour, C Choma Bex, G Pinon, A I Evans, M Togneri, I Masters, L H Da, Silva Ignacio, C A R Duarte, F J Souza, S Gambuzza, Y Liu, I M Viola, M Rentschler, T Gomes, G Vaz, R Azcueta, H Ward, F Salvatore, Z Sarichloo, D Calcagni, T T Tran, H Ross, M Oliveira, R Puraca, and B S Carmo. Tidal turbine benchmarking project: Stage i-steady flow blind predictions. *PROCEEDINGS OF THE 15TH EUROPEAN WAVE AND TIDAL ENERGY CONFERENCE*, pages 3–7, 2023.

[100] Grégory Pinon, Charifa El Hadi, Myriam Slama, José Nuno, Pablo Mansilla, Erwann Nicolas, Julie Marcille, Jean-Valéry Facq, Inès Belarbi, Benoît Gaurier, Grégory Germain, André Pacheco, and Michael Togneri. Influence of turbulence and wave flow conditions on different scaled tidal turbines. *13th European Wave and Tidal Energy Conference*, pages 1–11, 2019.

[101] Hai Bo Jiang, Yan Ru Li, and Zhong Qing Cheng. Relations of lift and drag coefficients of flow around flat plate. *Applied Mechanics and Materials*, 518:161–164, 2 2014.

[102] T Blackmore, L.E Myers, and A.S Bahaj. Effects of turbulence on tidal turbines: Implications to performance, blade loads, and condition monitoring. *International Journal of Marine Energy*, 14:1–26, 2016.

[103] F Maganga, G Germain, J King, G Pinon, and E Rivoalen. Experimental characterisation of flow effects on marine current turbine behaviour and on its wake properties. *IET Renewable Power Generation*, 4:314–327, 2010.

[104] O.D Medina, F.G Schmitt, R Calif, G Germain, and B Gaurier. Turbulence analysis and multiscale correlations between synchronized flow velocity and marine turbine power production. *Renewable Energy*, 112:314–327, 2017.

[105] P Stansby, S Draper, S Way, T Adcock, and T Stallard. Laboratory scale experiments and preliminary modelling to investigate basin scale tidal stream energy extraction. *European Wave and Tidal Energy Conference 2013*, 2013.

[106] J.I Whelan, Graham, J.M.R, and J Peiro. A free-surface and blockage correction for tidal turbines. *Journal of Fluid Mechanics*, 624:281–291, 2009.

[107] Myriam Slama, Gregory Pinion, Charifa El Hadi, Michael Togneri, Benoit Gaurier, Gregory Germain, Jean Valery Facq, Jose Nuno, Pablo Mansilla, Erwann Nicolas, Julie Marcille, and Andre Pacheco. Turbine design dependency to turbulence : an experimental study of three scaled tidal turbines. *Ocean Engineering*, 2020.

[108] M Dufour, G Pinon, B Gaurier, G Germain, J Facq, F Represas, Magallanes Renovables, Prego De Montaos, E Nicolas, J Marcille, S A Sabella, Rue Felix, and Le Dantec. Comparison of the experimental response of two horizontal axis tidal turbines to wave and current from a frequency dependency point of view. *RENEW 2022*, 2021.

[109] Hannah C Buckland, Ian Masters, James AC Orme, and Tim Baker. Cavitation inception and simulation in blade element momentum theory for modelling tidal stream turbines. *Proceedings of the Institution of Mechanical Engineers, Part A: Journal of Power and Energy*, 227:479–485, 6 2013.

[110] I Masters, I Evans, D George, D Glasby, J.H Caraballa, T Lake, M Togneri, and A.J Williams. Remote river energy system: Field trial experiments in a tidal estuary. *Preprint submitted to Elseivier*, 2023.

Appendix A

Supplementary Data

A summary and complete details of twist and chord distribution for the benchmark rotor blade are given in Table A.1 and Table A.2 respectively.

Table A.1: Summary twist and chord distribution for the benchmark rotor blades.

Normalised Radial Position (r/R)	Twist Angle (deg)	Chord length (m)
1.250000000000000000e-01	3.411040508341999811e+01	1.204334471418919972e-01
1.499999999999999944e-01	3.140910569775969918e+01	1.384201415120160095e-01
2.000000000000000111e-01	2.426431711123359847e+01	1.473706997801519925e-01
2.500000000000000000e-01	1.868261635321950109e+01	1.442492313565109929e-01
2.999999999999999889e-01	1.474212996002900056e+01	1.352520981482789875e-01
3.499999999999999778e-01	1.195037898126859943e+01	1.232471836807149945e-01
4.000000000000000222e-01	9.900544017192750346e+00	1.105313364362660034e-01
4.500000000000000111e-01	8.255074198253860018e+00	9.966075276561449370e-02
5.000000000000000000e-01	6.899168299952989969e+00	9.049824005735780663e-02
5.500000000000000444e-01	5.774468405708529595e+00	8.279525204741440547e-02
5.999999999999999778e-01	4.824750066151779926e+00	7.624225280362660617e-02
6.500000000000000222e-01	4.012841784150439572e+00	7.060137127280050051e-02
6.999999999999999556e-01	3.311623124110139926e+00	6.567525400308929506e-02
7.500000000000000000e-01	2.692731132210380185e+00	6.129257348710900194e-02
8.000000000000000444e-01	2.149116697758139960e+00	5.740564475568649822e-02
8.499999999999999778e-01	1.660622860066830020e+00	5.385959009012109694e-02
9.000000000000000222e-01	1.212285131822000039e+00	5.051328797914920316e-02
9.499999999999999556e-01	7.749049987593059630e-01	4.701934759594710023e-02
1.000000000000000000e+00	3.159099615384580173e-01	4.308996380769229695e-02

Table A.2: Full twist and chord distribution for the benchmark rotor blades.

Normalised Radial Position (r/R)	Twist Angle (deg)	Chord length (m)
1.25000000000000000e-01	3.411040508341999811e+01	1.204334471418919972e-01
1.30000000000000044e-01	3.405070264059249752e+01	1.255483457905409994e-01
1.35000000000000089e-01	3.374579881188120112e+01	1.317327710181520062e-01
1.40000000000000133e-01	3.301549685608439688e+01	1.346185802132910114e-01
1.44999999999999900e-01	3.222197325978189753e+01	1.367370030660680080e-01
1.49999999999999944e-01	3.140910569775969918e+01	1.384201415120160095e-01
1.54999999999999989e-01	3.060121276129530088e+01	1.398799831723870069e-01
1.60000000000000033e-01	2.980945230033249871e+01	1.411388521457329903e-01
1.65000000000000078e-01	2.904054536752289906e+01	1.422639493383180131e-01
1.70000000000000122e-01	2.829571606232200054e+01	1.432851633139549941e-01
1.74999999999999889e-01	2.756740394974029940e+01	1.443128329403589871e-01
1.79999999999999933e-01	2.687584423073240103e+01	1.451537803987550113e-01
1.84999999999999978e-01	2.620614524479560004e+01	1.458855072333989922e-01
1.90000000000000022e-01	2.554855145296669860e+01	1.465385159273520088e-01
1.95000000000000067e-01	2.489631556295219994e+01	1.471328777218519901e-01
2.00000000000000111e-01	2.426431711123359847e+01	1.473706997801519925e-01
2.04999999999999878e-01	2.364093597715940120e+01	1.474654298332900015e-01
2.09999999999999922e-01	2.302495202300289989e+01	1.474388585139390084e-01
2.14999999999999967e-01	2.242355934891860159e+01	1.473108950185020027e-01
2.20000000000000011e-01	2.183326214977969926e+01	1.471230018712940124e-01
2.25000000000000056e-01	2.125901104845819845e+01	1.468484394233839918e-01
2.30000000000000100e-01	2.070701767218509914e+01	1.464904372034240010e-01
2.34999999999999867e-01	2.016329842964049845e+01	1.461014169063389878e-01
2.39999999999999911e-01	1.965760558488119969e+01	1.455123295103669945e-01
2.44999999999999956e-01	1.915670604669820065e+01	1.449088600337380128e-01
2.50000000000000000e-01	1.868261635321950109e+01	1.442492313565109929e-01
2.55000000000000044e-01	1.821454381477130013e+01	1.435689465322750047e-01
2.60000000000000089e-01	1.777610077431679869e+01	1.427869473158979996e-01
2.65000000000000133e-01	1.734145540578359856e+01	1.419979378250930124e-01
2.70000000000000178e-01	1.693291529384330119e+01	1.411607395974809886e-01
2.75000000000000222e-01	1.652437518190300025e+01	1.403235413698689926e-01
2.80000000000000266e-01	1.614890325633049883e+01	1.393673949937810075e-01
2.84999999999999756e-01	1.577400321190580001e+01	1.384091915286539964e-01
2.89999999999999800e-01	1.542137278558129942e+01	1.373803686794720091e-01

Continued on next page

Table A.2 – continued from previous page

Normalised Radial Position (r/R)	Twist Angle (deg)	Chord length (m)
2.949999999999999845e-01	1.507689571670329975e+01	1.363256906459640039e-01
2.999999999999999889e-01	1.474212996002900056e+01	1.352520981482789875e-01
3.049999999999999933e-01	1.442401367346280061e+01	1.341460779210250087e-01
3.099999999999999978e-01	1.410589738689660066e+01	1.330400576937710022e-01
3.150000000000000022e-01	1.381222619801980045e+01	1.318674446500119890e-01
3.200000000000000067e-01	1.352168164356439917e+01	1.306863140950960123e-01
3.250000000000000111e-01	1.323768091440680017e+01	1.294970433393030085e-01
3.300000000000000155e-01	1.297044058109790043e+01	1.282869234650249879e-01
3.350000000000000200e-01	1.270320024778889945e+01	1.270768035907459959e-01
3.400000000000000244e-01	1.244642552589749940e+01	1.258240376611320099e-01
3.449999999999999734e-01	1.219840225358309915e+01	1.245356106709240018e-01
3.499999999999999778e-01	1.195037898126859943e+01	1.232471836807149945e-01
3.549999999999999822e-01	1.172041838708580030e+01	1.219465321915360057e-01
3.599999999999999867e-01	1.149728169252230003e+01	1.206412624085869967e-01
3.649999999999999911e-01	1.127414499795879976e+01	1.193359926256380016e-01
3.699999999999999956e-01	1.106596127857620004e+01	1.180319764914709996e-01
3.750000000000000000e-01	1.086183904889190011e+01	1.167283008702480057e-01
3.800000000000000044e-01	1.065771681920750069e+01	1.154246252490259972e-01
3.850000000000000089e-01	1.046413935043650056e+01	1.141782762632640030e-01
3.900000000000000133e-01	1.027306111000670086e+01	1.129455143425120017e-01
3.950000000000000178e-01	1.008198286957689938e+01	1.117127524217600004e-01
4.000000000000000222e-01	9.900544017192750346e+00	1.105313364362660034e-01
4.050000000000000266e-01	9.721073903022160678e+00	1.093604072891870005e-01
4.099999999999999756e-01	9.541603788851579893e+00	1.081894781421089968e-01
4.149999999999999800e-01	9.371265059771660688e+00	1.070691717658830006e-01
4.199999999999999845e-01	9.202507504365350144e+00	1.059576311345870048e-01
4.249999999999999889e-01	9.033749948959030718e+00	1.048460905032909951e-01
4.299999999999999933e-01	8.873581655876430219e+00	1.037833060401610052e-01
4.349999999999999978e-01	8.714647136064469279e+00	1.027275249790459977e-01
4.400000000000000022e-01	8.555712616252520775e+00	1.016717439179320032e-01
4.450000000000000067e-01	8.404922754331769497e+00	1.006635012545329944e-01
4.500000000000000111e-01	8.255074198253860018e+00	9.966075276561449370e-02
4.550000000000000155e-01	8.105225642175959422e+00	9.865800427669579875e-02
4.600000000000000200e-01	7.963093434788450331e+00	9.770137994519810520e-02
4.650000000000000244e-01	7.821646826326389856e+00	9.674885375312289315e-02

Continued on next page

Table A.2 – continued from previous page

Normalised Radial Position (r/R)	Twist Angle (deg)	Chord length (m)
4.69999999999999734e-01	7.68020021786434004 0e+00	9.57963275610476949 8e-02
4.74999999999999778e-01	7.54608481370047012 9e+00	9.48887700464740996 3e-02
4.79999999999999822e-01	7.41243404137004979 8e+00	9.39840625246474020 7e-02
4.84999999999999867e-01	7.27878326903961969 7e+00	9.30793550028207045 1e-02
4.89999999999999911e-01	7.15206439774329982 8e+00	9.22178578960305972 4e-02
4.94999999999999956e-01	7.02561634884814001 4e+00	9.13580489766941950 0e-02
5.00000000000000000e-01	6.89916829995298996 9e+00	9.04982400573578066 3e-02
5.05000000000000044e-01	6.77932622592344014 1e+00	8.96802065329752040 6e-02
5.10000000000000089e-01	6.65958747508395010 3e+00	8.88628264120887023 7e-02
5.15000000000000133e-01	6.53988989556749000 8e+00	8.80457111222968935 6e-02
5.20000000000000178e-01	6.42638922397581957 6e+00	8.72684569248489000 5e-02
5.25000000000000222e-01	6.31288855238415003 2e+00	8.64912027274009065 4e-02
5.30000000000000266e-01	6.19955412189388965 8e+00	8.57150341102752982 8e-02
5.35000000000000311e-01	6.09186607622566000 9e+00	8.49757372667561961 0e-02
5.40000000000000355e-01	5.98417803055741970 3e+00	8.42364404232370939 1e-02
5.45000000000000400e-01	5.87676289865682033 3e+00	8.34989451300201940 3e-02
5.50000000000000444e-01	5.77446840570852959 5e+00	8.27952520474144054 7e-02
5.55000000000000488e-01	5.67217391276023974 5e+00	8.20915589648086030 4e-02
5.60000000000000533e-01	5.57024295614506037 6e+00	8.13902564163867942 0e-02
5.64999999999999467e-01	5.47295585070517010 0e+00	8.07194908018804974 1e-02
5.69999999999999512e-01	5.37566874526527982 4e+00	8.00487251873741034 7e-02
5.74999999999999556e-01	5.27882118992612969 8e+00	7.93808810678310681 e-02
5.79999999999999600e-01	5.18618049147077986 3e+00	7.87410795104097061 0e-02
5.84999999999999645e-01	5.09353979301544956 8e+00	7.81012709140363053 9e-02
5.89999999999999689e-01	5.00140218166554984 0e+00	7.74647900769643987 8e-02
5.94999999999999734e-01	4.91307612390866044 2e+00	7.68535214402955024 8e-02
5.99999999999999778e-01	4.82475006615177992 6e+00	7.62422528036266061 7e-02
6.04999999999999822e-01	4.73679804633979718 e+00	7.56346668871726024 5e-02
6.09999999999999867e-01	4.65266382075218043 5e+00	7.50499691034250959 7e-02
6.14999999999999911e-01	4.56834783687038026 3e+00	7.44652713196777005 2e-02
6.19999999999999956e-01	4.48463105601075007 2e+00	7.38845410246473932 6e-02
6.25000000000000000e-01	4.40404609966419968 7e+00	7.33245474047683060 1e-02
6.30000000000000044e-01	4.32346114331765996 0e+00	7.27645537848892048 9e-02
6.35000000000000089e-01	4.24351035576600033 0e+00	7.22087346152193027 0e-02
6.40000000000000133e-01	4.16639839391497002 2e+00	7.16716021684464937 9e-02

Continued on next page

Table A.2 – continued from previous page

Normalised Radial Position (r/R)	Twist Angle (deg)	Chord length (m)
6.450000000000000178e-01	4.089286432063939714e+00	7.113446972167369875e-02
6.500000000000000222e-01	4.012841784150439572e+00	7.060137127280050051e-02
6.550000000000000266e-01	3.938988191134990213e+00	7.008393608139690256e-02
6.600000000000000311e-01	3.865134598119539966e+00	6.956650088999330461e-02
6.650000000000000355e-01	3.791968259368700078e+00	6.905363665533920114e-02
6.700000000000000400e-01	3.721144887978510063e+00	6.855635559422429415e-02
6.750000000000000444e-01	3.650321516588309834e+00	6.805907453310949817e-02
6.800000000000000488e-01	3.580203607656149867e+00	6.756650270960380678e-02
6.850000000000000533e-01	3.512215696306249857e+00	6.708814945238410210e-02
6.899999999999999467e-01	3.444227784956349847e+00	6.660979619516460559e-02
6.949999999999999512e-01	3.376958248354600123e+00	6.613616602458030624e-02
6.999999999999999556e-01	3.311623124110139926e+00	6.567525400308929506e-02
7.049999999999999600e-01	3.246287999865680174e+00	6.521434198159839490e-02
7.099999999999999645e-01	3.181681041101410035e+00	6.475826705936869876e-02
7.149999999999999689e-01	3.118832820819339879e+00	6.431387518562800554e-02
7.199999999999999734e-01	3.055984600537270168e+00	6.386948331188720129e-02
7.249999999999999778e-01	2.993604847987469952e+00	6.342804864319280533e-02
7.299999999999999822e-01	2.932244771708779840e+00	6.299305068637199578e-02
7.349999999999999867e-01	2.870884695430090172e+00	6.255805272955120011e-02
7.399999999999999911e-01	2.810467123960119995e+00	6.212933869852180213e-02
7.449999999999999956e-01	2.751599128085250090e+00	6.171095609281539857e-02
7.500000000000000000e-01	2.692731132210380185e+00	6.129257348710900194e-02
7.550000000000000044e-01	2.635099831790229885e+00	6.088247526708599755e-02
7.600000000000000089e-01	2.578867589228920121e+00	6.048174906735460238e-02
7.650000000000000133e-01	2.522635346667609912e+00	6.008102286762320027e-02
7.700000000000000178e-01	2.467544772227990180e+00	5.968777451662460320e-02
7.750000000000000222e-01	2.413098060041559911e+00	5.929874341969720158e-02
7.800000000000000266e-01	2.358651347855130087e+00	5.890971232276979996e-02
7.850000000000000311e-01	2.305718340606250027e+00	5.853042835743790112e-02
7.900000000000000355e-01	2.252874110886000203e+00	5.815171605322219661e-02
7.950000000000000400e-01	2.200559587628870162e+00	5.777611808247420239e-02
8.000000000000000444e-01	2.149116697758139960e+00	5.740564475568649822e-02
8.050000000000000488e-01	2.097673807887419972e+00	5.703517142889869690e-02
8.100000000000000533e-01	2.047431210069590168e+00	5.667244620809350208e-02
8.149999999999999467e-01	1.997273980067020061e+00	5.631027205223820137e-02

Continued on next page

Table A.2 – continued from previous page

Normalised Radial Position (r/R)	Twist Angle (deg)	Chord length (m)
8.19999999999999512e-01	1.947819384719470026e+00	5.59523475506946053e-02
8.24999999999999556e-01	1.898822000631430029e+00	5.55971883408803907e-02
8.29999999999999600e-01	1.850221991380130104e+00	5.52442160239651665e-02
8.34999999999999645e-01	1.802247187932179973e+00	5.48946844335512013e-02
8.39999999999999689e-01	1.754526334659370024e+00	5.45466729671804979e-02
8.44999999999999734e-01	1.707467657384390103e+00	5.42026252297364799e-02
8.49999999999999778e-01	1.660622860066830020e+00	5.38595900901210694e-02
8.54999999999999822e-01	1.614367638680030081e+00	5.35193462513575968 2e-02
8.59999999999999867e-01	1.568359988486839995e+00	5.31803655049341988 9e-02
8.64999999999999911e-01	1.522810098135970014e+00	5.28437202198464989 2e-02
8.69999999999999956e-01	1.477581852981810107e+00	5.25083563921252966 0e-02
8.75000000000000000e-01	1.432642295072529937e+00	5.21741427149435971 2e-02
8.80000000000000044e-01	1.388108523936169902e+00	5.18411602872339977 2e-02
8.85000000000000089e-01	1.343741104581799961e+00	5.15086391901255977 2e-02
8.90000000000000133e-01	1.299746308287849983e+00	5.11769714657952026 8e-02
8.95000000000000178e-01	1.255935953751829981e+00	5.08452047643608989 7e-02
9.00000000000000222e-01	1.212285131822000039e+00	5.05132879791492031 6e-02
9.05000000000000266e-01	1.168863637279599965e+00	5.01802198291352030 7e-02
9.10000000000000311e-01	1.125532681263780033e+00	4.98460705851579977 1e-02
9.15000000000000355e-01	1.082269511879049961e+00	4.95104274470841987 4e-02
9.20000000000000400e-01	1.039045969762419919e+00	4.91724491996297016 8e-02
9.25000000000000444e-01	9.957555793907969521e-01	4.88302173707063982 8e-02
9.30000000000000488e-01	9.523378052389870341e-01	4.84834443049838026 4e-02
9.35000000000000533e-01	9.086998180032139771e-01	4.81310999401678985 0e-02
9.39999999999999467e-01	8.647161275318829832e-01	4.77716098327082006 0e-02
9.44999999999999512e-01	8.202019165189999850e-01	4.74022639497932960 e-02
9.49999999999999556e-01	7.749049987593059630e-01	4.70193475959471002 3e-02
9.54999999999999600e-01	7.290054950372210074e-01	4.66264092171215990 8e-02
9.59999999999999645e-01	6.831059913151360519e-01	4.62334708382960979 4e-02
9.64999999999999689e-01	6.372064875930509853e-01	4.58405324594705967 9e-02
9.69999999999999734e-01	5.913069838709660297e-01	4.54475940806451997 3e-02
9.74999999999999778e-01	5.454074801488819624e-01	4.50546557018196985 9e-02
9.79999999999999822e-01	4.995079764267970068e-01	4.46617173229941974 4e-02
9.84999999999999867e-01	4.536084727047119958e-01	4.42687894416870324 e-02
9.89999999999999911e-01	4.077089689826279839e-01	4.38758405653432020 9e-02

Continued on next page

Table A.2 – continued from previous page

Normalised Radial Position (r/R)	Twist Angle (deg)	Chord length (m)
9.949999999999999956e-01	3.618094652605419737e-01	4.348290218651779809e-02
1.000000000000000000e+00	3.159099615384580173e-01	4.308996380769229695e-02

The polars used in the Oxford blind test were lift and drag provided by the project co-ordinators, and are given in Table A.3.

Table A.3: Lift and drag polars used for the benchmark case study. Hydrofoil profile NACA 63-415 at Reynolds number 288,888 and turbulence intensity 0.01%.

AoA (°)	Cl	Cd
0.000000000E+00	3.170053000E-01	1.481117000E-02
1.000000000E+00	4.289612000E-01	1.518466000E-02
2.000000000E+00	5.394359000E-01	1.572911000E-02
3.000000000E+00	6.479287000E-01	1.645465000E-02
4.000000000E+00	7.537792000E-01	1.738608000E-02
5.000000000E+00	8.561177000E-01	1.855998000E-02
6.000000000E+00	9.538070000E-01	2.002199000E-02
7.000000000E+00	1.045151000E+00	2.184680000E-02
8.000000000E+00	1.128008000E+00	2.414781000E-02
9.000000000E+00	1.200536000E+00	2.709434000E-02
1.000000000E+01	1.260667000E+00	3.097677000E-02
1.100000000E+01	1.305415000E+00	3.619467000E-02
1.200000000E+01	1.333081000E+00	4.312438000E-02
1.300000000E+01	1.343772000E+00	5.200547000E-02
1.400000000E+01	1.339028000E+00	6.293608000E-02
1.500000000E+01	1.321425000E+00	7.591979000E-02

Table A.4 gives the normalised chord and twist distribution along the radial length of the Magallanes ATIR rotor. The summary of the polars for angle of attack of 0-15° of the NACA-63(3)418 aerofoil at Reynolds number of $\mathbf{5 \times 10^5}$ are given in Table A.5 produced by the XFOIL tool.

Table A.6 gives the normalised chord and twist distribution along the radial length of the Sabella D12 rotor. Table A.7 gives the summary of the polars for angle of attacks of 0-15° of the NACA-63(3)418 aerofoil at Reynolds number of $\mathbf{2.5 \times 10^5}$ produced by the XFOIL tool.

Table A.8 gives the chord and twist distribution along the radial length of the laboratory scale Barltrop rotor. Table A.9 gives the summary of the lift and drag polars for angle

Table A.4: Summary twist and chord distribution for the Magallanes ATIR rotor blades.

Normalised Radial Position (r/R)	Twist Angle (deg)	Chord length (c/C)
0.133333333333333	61.5000000000000	0.812500000000000
0.166666666666667	65.5000000000000	0.812500000000000
0.222222222222222	72.1000000000000	0.875000000000000
0.333333333333333	77.5000000000000	1
0.444444444444444	79.5000000000000	1
0.555555555555556	81.4000000000000	0.937500000000000
0.666666666666667	82.9000000000000	0.762500000000000
0.777777777777778	84	0.593750000000000
0.888888888888889	84.8000000000000	0.450000000000000
0.972222222222222	85.3000000000000	0.362500000000000
1	85.7000000000000	0.306250000000000

Table A.5: Lift and drag polars for angle of attack of 0-15° for the NACA-63(3)418 aerofoil at a Reynolds number of $\mathbf{5 \times 10^5}$ used in the numerical modelling of the Magallanes ATIR turbine, produced by the XFOIL tool [2].

Angle of attack (°)	Cl	Cd
0	0.365500000000000	0.00940000000000000
1	0.490800000000000	0.0101000000000000
2	0.612900000000000	0.0102000000000000
3	0.732400000000000	0.0105000000000000
4	0.848300000000000	0.0110000000000000
5	0.963800000000000	0.0113000000000000
6	1.07740000000000	0.0117000000000000
7	1.18480000000000	0.0122000000000000
8	1.29130000000000	0.0127000000000000
9	1.38010000000000	0.0136000000000000
10	1.42610000000000	0.0173000000000000
11	1.36990000000000	0.0291000000000000
12	1.22450000000000	0.0392000000000000
13	1.19530000000000	0.0590000000000000
14	1.20810000000000	0.0880000000000000
15	1.18600000000000	0.104500000000000

of attacks of 0-15° of the NREL S814 aerofoil profile of the Barltrop rotor blade. The polars were produced from wind tunnel testing.

Table A.10 gives the chord and twist distribution along the radial length of the IFREMER turbine. The summary of the polars for angle of attack of 0-15° of the NACA-63(3)418 aerofoil at Reynolds number of $\mathbf{3.5 \times 10^5}$ produced by the XFOIL tool is given in Table A.11.

Table A.12 gives the twist, chord, and thickness distribution along the radial length of the 3.0m diameter IFREMER modified turbine. Similarly, Table A.13 gives the twist,

Table A.6: Summary twist and chord distribution for the Sabella D12 rotor blades.

Normalised Radial Position (r/R)	Twist Angle (deg)	Chord length (c/C)
0.320833333333333	66.9980000000000	1
0.332150000000000	68.2800000000000	0.949235872526952
0.354800000000000	70.8440000000000	0.847707617580855
0.377433333333333	72.8020000000000	0.775619002487857
0.400066666666667	74.4150000000000	0.719346049046322
0.422700000000000	75.7930000000000	0.673261461912096
0.445350000000000	76.9980000000000	0.634285037317853
0.467983333333333	78.0770000000000	0.600225091813766
0.490633333333333	79.0500000000000	0.570074635706670
0.513266666666667	79.9360000000000	0.543063618054733
0.535900000000000	80.7450000000000	0.518718161355290
0.558550000000000	81.4900000000000	0.496505153417842
0.581183333333333	82.1780000000000	0.476128420803222
0.603816666666667	82.8160000000000	0.457351024760100
0.626466666666667	83.4100000000000	0.439995261224973
0.649100000000000	83.9640000000000	0.423883426134344
0.671733333333333	84.4750000000000	0.409074754176046
0.694366666666667	84.9500000000000	0.395450775974411
0.717016666666667	85.3950000000000	0.382715318090274
0.739650000000000	85.8140000000000	0.370927615211468
0.762283333333333	86.2030000000000	0.360028432650160
0.784933333333333	86.5610000000000	0.350254709157683
0.807566666666667	86.8970000000000	0.341251036607037
0.830200000000000	87.2140000000000	0.332958180310390
0.852850000000000	87.5000000000000	0.325850017770406
0.875483333333333	87.7680000000000	0.319511906172255
0.898116666666667	88.0190000000000	0.313825376140268
0.920766666666667	88.2450000000000	0.309323539864945
0.943400000000000	88.4540000000000	0.305591754531454
0.966033333333333	88.6490000000000	0.302570785451961
0.988683333333333	88.8190000000000	0.300793744816965
1	88.9040000000000	0.299905224499467

chord, and thickness distribution along the radial length of the 0.9m diameter IFREMER modified turbine.

Table A.7: Lift and drag polars for angle of attack of 0-15° for the NACA-63(3)418 aerofoil profile at a Reynolds number of $\mathbf{2.5 \times 10^5}$ used in the numerical modelling of the Sabella D12 turbine, produced by the XFOIL tool [2].

Angle of attack (°)	Cl	Cd
0	0.229600000000000	0.0206000000000000
1	0.533200000000000	0.0194000000000000
2	0.737800000000000	0.0181300000000000
3	0.800000000000000	0.0183700000000000
4	0.843400000000000	0.0186800000000000
5	0.908600000000000	0.0193200000000000
6	0.986100000000000	0.0202600000000000
7	1.05750000000000	0.0214100000000000
8	1.12440000000000	0.0226700000000000
9	1.16400000000000	0.0239100000000000
10	1.17440000000000	0.0264800000000000
11	1.19200000000000	0.0301200000000000
12	1.19200000000000	0.0355500000000000
13	1.15030000000000	0.0468000000000000
14	1.12470000000000	0.0599800000000000
15	1.11520000000000	0.0724900000000000

Table A.8: Summary twist and chord distribution for the laboratory scale Barltrop rotor blades.

Normalised Radial Position (r/R)	Twist Angle (deg)	Chord length (m)
0.1500	58.0000	0.0665
0.2000	62.0000	0.0650
0.2500	70.0000	0.0620
0.3000	75.0000	0.0600
0.3500	79.0000	0.0580
0.4000	82.0000	0.0560
0.4500	84.0000	0.0540
0.5000	85.0000	0.0520
0.6000	88.0000	0.0470
0.7000	89.0000	0.0430
0.8000	90.0000	0.0390
0.9000	90.8000	0.0340
1.0000	91.5000	0.0300

Table A.9: Lift and drag polars for angle of attack of 0-15° for the NREL S814 aerofoil at a Reynolds number of $\mathbf{3 \times 10^6}$ used in the numerical modelling of the laboratory scale Barltrop turbine, produced by wind tunnel experiments.

Angle of attack (°)	Cl	Cd
0	0.176695070000000	0.00911433000000000
1	0.292689620000000	0.00932998000000000
2	0.409485540000000	0.00960901000000000
3	0.526405560000000	0.00991795000000000
4	0.643500340000000	0.0102965900000000
5	0.761169800000000	0.0107417300000000
6	0.876927620000000	0.0114216800000000
7	0.988909590000000	0.0124883700000000
8	1.09433487000000	0.0140193900000000
9	1.19197068000000	0.0161173900000000
10	1.27288047000000	0.0188391600000000
11	1.32707551000000	0.0221652000000000
12	1.35828127000000	0.0265960300000000
13	1.36842959000000	0.0323363400000000
14	1.35652280000000	0.0407436000000000
15	1.31880195000000	0.0527348100000000

Table A.10: Summary twist and chord distribution for the laboratory scale IFREMER rotor blades.

Normalised Radial Position (r/R)	Twist Angle (deg)	Chord length (m)
0.128881215469613	60.4328000000000	0.0198450000000000
0.145027624309392	60.4328000000000	0.0198450000000000
0.149861878453039	60.4328000000000	0.0198450000000000
0.191726519337017	64.3727000000000	0.0532350000000000
0.233687845303867	67.8509000000000	0.0865900000000000
0.275552486187845	70.6969000000000	0.0831250000000000
0.317417127071823	73.0263000000000	0.0790650000000000
0.359378453038674	74.9462000000000	0.0749350000000000
0.401243093922652	76.5428000000000	0.0710150000000000
0.443107734806630	77.8831000000000	0.0673750000000000
0.485069060773481	79.0185000000000	0.0640150000000000
0.526933701657459	79.9886000000000	0.0610050000000000
0.568798342541437	80.8239000000000	0.0582750000000000
0.610759668508287	81.5484000000000	0.0557900000000000
0.652624309392265	82.1809000000000	0.0535150000000000
0.694488950276243	82.7362000000000	0.0514850000000000
0.736450276243094	83.2265000000000	0.0496300000000000
0.778314917127072	83.6613000000000	0.0479500000000000
0.820179558011050	84.0486000000000	0.0463750000000000
0.862140883977901	84.3950000000000	0.0449750000000000
0.904005524861879	84.7059000000000	0.0436450000000000
0.945870165745857	84.9857000000000	0.0424550000000000
1	85.1257000000000	0.0237110000000000

Table A.11: Lift and drag polars for angle of attack of 0-15° for the NACA-63(3)418 aerofoil at a Reynolds number of $\mathbf{3.5 \times 10^5}$ used in the numerical modelling of the laboratory scale IFREMER turbine, produced by the XFOIL tool [2].

Angle of attack (°)	Cl	Cd
0	0.286650000000000	0.0143280000000000
1	0.390690000000000	0.0146520000000000
2	0.494550000000000	0.0147780000000000
3	0.597150000000000	0.0152460000000000
4	0.699930000000000	0.0155340000000000
5	0.801270000000000	0.0158580000000000
6	0.901350000000000	0.0163440000000000
7	0.999450000000000	0.0168300000000000
8	1.09413000000000	0.0176400000000000
9	1.17342000000000	0.0198900000000000
10	1.22184000000000	0.0242100000000000
11	1.24011000000000	0.0293940000000000
12	1.24380000000000	0.0380340200000000
13	1.23732000000000	0.0449604200000000
14	1.22994000000000	0.0591509000000000
15	1.21848635000000	0.0744624800000000

Table A.12: Summary twist, chord, and thickness distribution for the IFREMER modified rotor blades used for the 0.9m diameter remote river energy system.

Radius (m)	Twist (deg)	Chord (m)	Thickness (m)
0.108765	67.85	0.166995	0.035569935
0.12825	71.7	0.1603125	0.034306875
0.147735	73.03	0.1524825	0.033088703
0.167265	74.95	0.1445175	0.03179385
0.18675	76.54	0.1369575	0.030404565
0.206235	77.88	0.1299375	0.029106
0.225765	79.02	0.1234575	0.027777938
0.24525	79.99	0.1176525	0.026471813
0.264735	80.82	0.1123875	0.0251748
0.284265	81.55	0.107595	0.02388609
0.30375	82.18	0.1032075	0.022602443
0.323235	82.74	0.0992925	0.021347888
0.342765	83.23	0.095715	0.020004435
0.36225	83.66	0.092475	0.01867995
0.381735	84.05	0.0894375	0.017440313
0.401265	84.39	0.0867375	0.016133175
0.42075	84.71	0.0841725	0.01515105
0.440235	84.99	0.0818775	0.01473795
0.45	84.13	0.0442125	0.011053125

Table A.13: Summary twist, chord, and thickness distribution for the IFREMER modified rotor blades used for the 3.0m diameter remote river energy system.

Radius (m)	Twist (deg)	Chord (m)	Thickness (m)
0.36255	67.85	0.56	0.12
0.4275	70.70	0.53	0.11
0.49245	73.03	0.51	0.11
0.55755	74.95	0.48	0.11
0.6225	76.54	0.46	0.10
0.68745	77.88	0.43	0.10
0.75255	79.02	0.41	0.09
0.8175	79.99	0.39	0.09
0.88245	80.82	0.37	0.08
0.94755	81.55	0.36	0.08
1.0125	82.18	0.34	0.08
1.07745	82.74	0.33	0.07
1.14255	83.23	0.32	0.07
1.2075	83.66	0.31	0.06
1.27245	84.05	0.30	0.06
1.33755	84.39	0.29	0.05
1.4025	84.71	0.28	0.05
1.46745	84.99	0.27	0.05
1.5	84.13	0.15	0.04